



POLITECNICO

MILANO 1863

School of Civil, Environmental and Land Management Engineering

Polo territoriale di Lecco

M.Sc. programme in Civil Engineering for Risk Mitigation

Mitigating Scouring Around Bridge Piers Using Geosynthetics (Geo-carpets): An Experimental Study on the Effectiveness of Protective Measures

Supervisor: **Dr. Alessio Radice**

Master Dissertation of:

Mohammad Reza Kalhori 974795

Sina Fotoohi 970814

Academic Year 2022-23

Acknowledgments

We would like to extend our gratitude to all those who supported us in the completion of this master's thesis.

We want to express our special appreciation to Professor Alessio Radice for his valuable time, support, and guidance throughout this journey.

We are also thankful to the staff and professors at the Politecnico di Milano for their guidance and assistance during our master's degree program, as well as the staff of the Hydraulic Lab G. Fantoli for their cooperation during the experiments.

Lastly, we would like to acknowledge and thank our families and friends for their continuous support and encouragement over the years.

Table of Contents

Acknowledgments	I
Table of contents	II
Abstract (English)	IV
Astratto (Italiano)	V
چکیده (فارسی)	VI

Chapter 1: Introduction 1

1.1. Bridge's failure and the contributing factors	1
1.2. Objectives, and structure of the work	4

Chapter 2: Literature review 5

2.1. Sediment transport in open channel and bridge pier scour	5
2.1.1. Sediment Transport.....	5
2.1.1.1. Physical properties of sediments	5
2.1.1.2. Bed load transport.....	7
2.1.2. Pier scour	11
2.1.2.1. Local scour	11
2.1.2.2. Clear water and live-bed scour.....	14
2.1.2.3. Steady-flow scour studies.....	17
2.2. Pier scour countermeasures: A review of existing methods	25
2.2.1. Rip-Rap.....	25
2.2.2. Wire gabion	27
2.2.3. Collar	28
2.3. Pier scour countermeasures with Geosynthetics	30
2.3.1. Geosynthetics.....	30
2.3.2. Pier scour protection with geosynthetics	31
2.3.2.1. Geosynthetic containers	31
2.3.2.2. Armed soil by geotextile	36

Chapter 3: Laboratory description 40

3.1. Experimental facilities and measuring equipment	40
---	----

3.1.1. Water circulation components	42
3.1.2. Scour measuring tool and its accuracy	45
3.1.3. Sediment particles' properties	46
3.2. Geo-Carpets properties.....	46
3.2.1. Utilized Carpets	46
3.2.2. Weight of Carpets	48
3.2.3. Density test	49
3.3. Experimental Campaign.....	50
3.3.1. Threshold conditions and calibration	50
3.3.2. Experimental set up, procedure, and methods of data acquisition	52
Chapter 4: Experimental analysis and prospects	59
4.1. Unprotected Experiments.....	63
4.1.1. Unprotected tests: 3-hour and 6-hour Durations	63
4.1.2. Results, analysis, and comparison of unprotected tests.....	65
4.1.3. Validating a new scour predictor through two unprotected tests	67
4.2. Protected Experiments.....	68
4.2.1. Rigid Geo-Carpets	68
4.2.1.1. Coarse mesh nets	69
4.2.1.2. Results, analysis, and comparison of coarse mesh nets and the reference test	71
4.2.1.3. Fine mesh nets.....	79
4.2.1.4. Results, analysis, and comparison of fine mesh nets and the reference test	82
4.2.1.5. Comparison among rigid (coarse and fine mesh) nets	89
4.2.2. Flexible Geo-Carpets	91
4.2.2.1. Coarse mesh nets	91
4.2.2.2. Results, analysis, and comparison of coarse mesh nets and the reference test	93
4.2.2.3. Fine mesh nets.....	102
4.2.2.4. Results, analysis, and comparison of fine mesh nets and the reference test.....	104
4.2.2.5. Comparison among flexible (coarse and fine mesh) nets.....	111
4.2.3. Rigid VS Flexible Geo-Carpets	113
4.2.3.1. Dimensionless analysis and comparison of the results from all performed tests.	113
4.3. Comparing two analogous geosynthetic approaches	129
4.3.1. Comparing geo-carpets and geotextile layers.....	129
4.3.1.1. Two general comparisons: coverage area and location of scour hole.....	130
4.3.1.2. Comparing scour depth downstream over a 6-hour time period.....	130
4.4. Future research and improvements	131
Chapter 5: Summary and conclusions.....	134
References.....	137

Abstract (English)

Pier scouring, being a devastating natural event, is recognized as one of the major contributing factors responsible for the collapse of hydraulic structures. Its destructive potential poses a significant threat, leading to severe consequences including economic losses and casualties. Therefore, this phenomenon has garnered substantial attention, prompting the implementation of diverse countermeasures. Both active and passive approaches have been explored, encompassing techniques that modify flow patterns and solutions that reinforce the bed against scour.

This thesis centers on a comprehensive investigation of the geo-carpet, a novel countermeasure system, aiming to evaluate its effectiveness in mitigating scour. The experimental tests were conducted in a controlled environment simulating clear-water scour conditions at a cylindrical pier in free-surface flow. Each test had a duration of 6 hours, designed to be completed within a single day.

The experimental campaign encompassed a total of 30 tests at the Hydraulic Lab G.Fantoli, located in the Leonardo campus of the Politecnico di Milano. This included one preliminary test, two unprotected tests, and 27 tests utilizing various types of geo-carpets. The geo-carpets were varied based on three key parameters: coverage area, mesh size, and material flexibility. In addition to observing the scouring phenomenon during the tests, comprehensive quantitative data was collected.

The thorough data collection and subsequent surveys enabled an examination of various factors, such as changes in the channel bed, depths of maximum scouring, and alterations in scour volumes. These findings facilitated a dimensionless analysis and comprehensive comparison of all the protected tests, leading to the identification of the most effective geo-carpet configurations. Based on the case study findings, it was observed that fine-flexible nets with optimized coverage area were suitable for mitigating scour upstream of the pier, while coarse-flexible-extended nets proved to be effective in minimizing channel bed changes downstream.

The study provides valuable recommendations based on observed trends, obviously constrained to a relatively limited range of conditions explored.

Keywords: pier scouring, countermeasures, geo-carpet, clear water, cylindrical pier, free-surface flow, coverage area, mesh size, material flexibility, dimensionless analysis.

Astratto (Italiano)

L'erosione localizzata alla base delle pile dei ponti è uno dei fattori maggiormente responsabili del crollo delle strutture in alveo. Il suo potenziale distruttivo rappresenta una minaccia con severe conseguenze, tra cui perdite economiche e di vite umane. Il fenomeno è stato oggetto di attenzione e ha stimolato la ricerca di contromisure sia attive che passive, riguardando strategie per la modifica del campo di moto o per il rinforzo del letto.

La tesi comprende un'indagine sperimentale del "geo-carpet" per valutarne la capacità di mitigare i livelli di erosione. Prove sperimentali sono state condotte in laboratorio per erosione in acque chiare a una pila circolare sotto l'azione di un flusso a superficie libera. Ogni esperimento ha avuto una durata di 6 ore, con questo potendo essere completato in un giorno.

La campagna sperimentale ha compreso 30 esperimenti, svolti presso il laboratorio di idraulica Fantoli del Politecnico di Milano. Un esperimento preliminare per la ricerca delle condizioni di prova è stato seguito da 2 esperimenti con pila non protetta e 27 esperimenti con diverse configurazioni del geo-carpet in termini di area coperta, dimensione delle maglie, e flessibilità del materiale.

I dati quantitativi misurati durante gli esperimenti sono stati analizzati in termini di profondità di erosione e volume di sedimento coinvolto. Tutti gli esperimenti sono stati confrontati tramite un'opportuna analisi adimensionale, identificando le configurazioni più promettenti. Un geo-carpet a maglia fine, flessibile e di area opportunamente determinata mitiga efficacemente lo scavo a monte della pila, mentre un geo-carpet a maglia grossolana, flessibile è efficace per ridurre lo scavo a valle.

Lo studio offre indicazioni preliminari, da considerarsi ovviamente valide nel campo sperimentale indagato.

Parole chiave L'erosione localizzata, contromisure, geo-carpet, acque chiare, pila circolare, flusso a superficie libera, area coperta, dimensione delle maglie, flessibilità del materiale, analisi adimensionali.

چکیده (فارسی)

آبشستگی رسوبات پایه ستون، به عنوان یک رویداد طبیعی ویرانگر، به عنوان یکی از عوامل اصلی فروپاشی سازه‌های هیدرولیکی شناخته می‌شود. قدرت پتانسیل ویرانگری آن تهدید قابل توجهی را به ارمغان می‌آورد و منجر به عواقب شدیدی از جمله ضررهای اقتصادی و تلفات جانی می‌شود. بنابراین این پدیده توجه چشمگیری را به خود جلب کرده و منجر به اجرای تدابیر متقابل متنوعی شده است. هر دو روش‌های فعال و غیرفعال مورد بررسی قرار گرفته‌اند که شامل تکنیک‌هایی هستند که الگوی جریان را تغییر می‌دهند و راهکارهایی که به تقویت بستر در برابر آبشستگی رسوبات می‌پردازند.

این پایان‌نامه بر بررسی جامع سیستم مقاومتی جدید ژئو-کارپت متمرکز است که هدف آن ارزیابی کارایی آن در کاهش آبشستگی رسوبات است. آزمایش‌های تجربی در یک محیط کنترل شده با شبیه‌سازی شرایط آبشستگی رسوبات در جریان آب شفاف (بدون رسوبات معلق) در اطراف یک پایه ستون استوانه‌ای در جریان سطح آزاد انجام شده است. هر آزمایش به مدت ۶ ساعت انجام و طراحی شده است تا در یک روز به اتمام برسد.

این کمپین آزمایشی در مجموع شامل ۳۰ آزمایش بود که در آزمایشگاه هیدرولیک جی.فانتولی واقع در پردیس لئوناردو در دانشگاه پلی تکنیک میلان انجام شده است. این کمپین آزمایشی شامل یک آزمایش مقدماتی، دو تست محافظت نشده (بدون ژئو-کارپت) و ۲۷ آزمایش با استفاده از انواع مختلف ژئو-کارپت بوده است. ژئو-کارپت‌ها بر اساس سه پارامتر کلیدی متفاوت هستند: منطقه پوشش، اندازه شبکه و انعطاف پذیری مواد. علاوه بر مشاهده پدیده آبشستگی رسوبات در طول آزمایشات، داده‌های کمی جامع جمع‌آوری شده است.

جمع‌آوری کامل داده‌ها و در ادامه برداشت داده‌ها، بررسی عوامل مختلف مانند تغییرات بستر کانال، حداکثر عمق آبشستگی و تغییرات در حجم رسوبات دچار آبشستگی را فراهم کرد. این یافته‌ها تجزیه و تحلیل غیر ابعادی و مقایسه جامع همه آزمایش‌های محافظت‌شده را تسهیل می‌کند و منجر به شناسایی ژئو-کارپت‌ها با مؤثرترین پیکربندی‌ها می‌شود. بر اساس یافته‌های این مطالعه، مشاهده شد که ژئو-کارپت‌های منعطف مشبک ریز با منطقه تحت پوشش بهینه برای کاهش آبشستگی بالادست ستون مناسب هستند، در حالی که ژئو-کارپت‌های منعطف مشبک درشت که منطقه تحت پوشش آن‌ها به سمت پایین دست ستون گسترش یافته است، برای کاهش تغییرات بستر کانال در پایین دست مؤثر بوده‌اند.

این مطالعه توصیه‌های ارزشمندی را بر اساس روندهای مشاهده شده ارائه می‌کند، که بدیهی است محدود به طیف نسبتاً محدودی از شرایط بررسی شده است.

کلید واژه‌ها: آبشستگی رسوبات پایه ستون، اقدامات متقابل، ژئو-کارپت، جریان آب شفاف، پایه ستون استوانه‌ای، جریان سطح آزاد، منطقه پوشش، اندازه شبکه، انعطاف پذیری مواد، تجزیه و تحلیل غیر ابعادی.

Chapter 1

Introduction

1.1. Bridge's failure and the contributing factors

Since ancient times, civil infrastructure systems have served as a tangible reflection of societal progress and temporal development, holding immense significance in the realm of engineering. In contemporary times, civil infrastructure systems have emerged as a critical concern with multifaceted impacts on society, particularly in terms of connectivity, which directly influences economic growth. Modern engineers are increasingly devoted to the research, development, design, and construction of a wide array of infrastructural components, seeking optimal solutions at reduced costs. However, one aspect that often receives inadequate attention is the maintenance of these infrastructure systems, which plays a pivotal role in the overall framework of any infrastructure management strategy, irrespective of geographic location. Consequently, engineers have innovatively designed materials to mitigate the challenges associated with maintenance endeavors.

Civil infrastructure systems are invariably exposed to numerous environments, thereby exposing them to risks that may lead to failure. Consequently, it becomes imperative to manage the repercussions of such failures in terms of connectivity, social implications, and economic consequences for society or communities. As delineated in the latest definition proposed by the United Nations International Strategy for Disaster Reduction (UNISDR) in 2017, risk can be conceptualized as a function of three interconnected factors: hazard, exposure, and vulnerability. While hazard and exposure are often beyond direct control, certain infrastructure elements can be fortified by implementing a range of tools or systems that enhance and sustain their performance over time, primarily targeting vulnerability reduction. A prominent illustration of infrastructure vulnerable to risks is found in bridges situated in hostile environments such as rivers or, worse yet, coastal areas.

In the past 30 years, over 1,000 bridge collapses have been recorded in the United States, with 60% of these failures attributed to river hydraulics processes, including pier scour ([Deng and Cai, 2010](#)). Additionally, ([Foti and Sabia, 2011](#)) identified more than 26,000 bridges in the United States as being susceptible to scour-related issues.

The Federal Highway Administration's research on bridge scour highlighted those major regional floods in 1964 and 1972 resulted in damages totaling approximately US\$100 million per event ([Brice and Blodgett, 1978](#)). Similarly, in New Zealand, a survey conducted among roading authorities revealed that river-induced scouring leads to annual roading expenditures of NZ\$36 million ([Macky, 1990](#)).

Although the dynamics of bridge scouring are well understood, and numerous studies exist in the literature regarding scour processes and predicting maximum scour depth ([Graf and Yulistiyanto, 1998](#)) and ([Melville and Coleman, 2000](#)), several bridge failures during river floods over the past decades have raised concerns within the scientific community. This has prompted engineers and researchers to enhance scour prediction models and develop improved scour measurement techniques ([Brandimarte et al., 2012](#)). Notably, an examination of the database compiled by ([Imhof, 2004](#)) indicates an increasing percentage of bridge collapses in recent decades, while collapses resulting from limited knowledge or design errors have declined over time, those attributed to natural hazards have shown an upward trend.

A comprehensive compilation of bridge failure data from around the world in 2004 substantiates the assertion that natural hazards are the primary cause of bridge collapses, as depicted in Figure 1.1, with scour emerging as one of the most prominent contributors, as elucidated in Figure 1.2. These statistics reinforce the central idea within modern engineering that constantly strives to devise innovative methods aimed at fortifying bridges against potential hazards in the future.

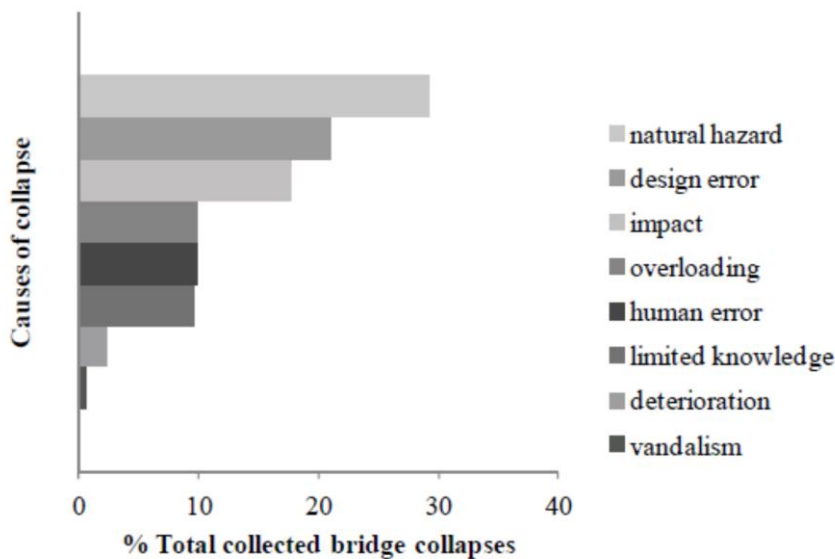


Figure 1.1. Main causes of bridge collapse ([Imhof, 2004](#)).

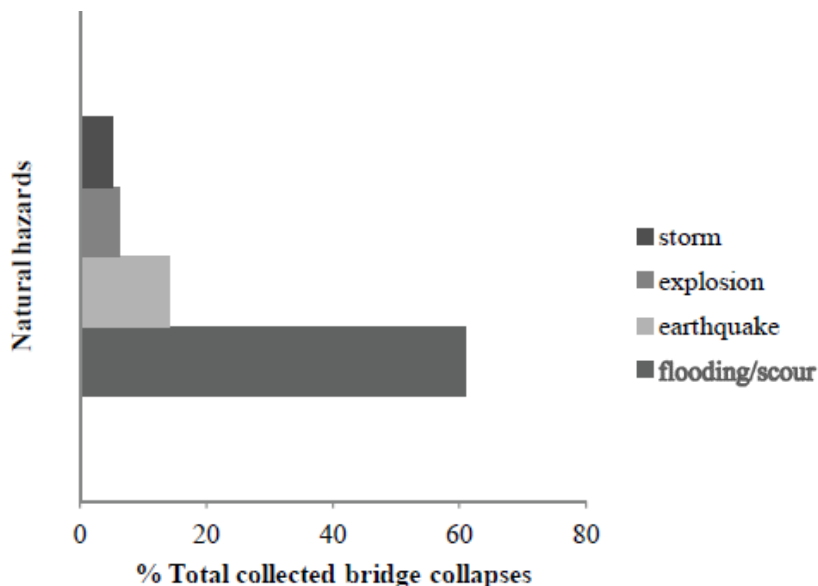


Figure 1.2. Different natural hazards causing bridge collapse ([Imhof, 2004](#)).

In the case of infrastructural entities like bridges, although the factors of hazard and exposure are inherently intertwined with geographical location and are difficult to alter, the reduction of vulnerability assumes paramount importance from a systemic perspective encompassing the entire territory. Adequate preparedness for diverse flood events or scour phenomena in representative bridges assumes significance as it augments the likelihood of maintaining their structural integrity during the post-emergency phase, thereby ensuring the preservation and even augmentation of redundancy in such territories following hydrogeological events that endanger densely populated areas.

Bridge failures are most observed during floods when there is a high flow velocity (v) compared to the critical velocity (v_c) required to initiate sediment particle motion. Even in rivers with flat terrain, the flow velocity typically exceeds 5 m/s during severe flood events. As a result, if the riverbed contains fine sand with a critical velocity of approximately 0.25 m/s, the flow intensity (v/v_c) can reach or exceed 20 ([Ettmer et al., 2015](#)).

Several researchers have studied clear-water scour, including ([Laursen and Toch, 1956](#)), ([Larras, 1963](#)), ([Breusers, 1965](#)), ([Shen et al., 1969](#)), ([Coleman, 1981](#)), ([Coleman, 1972](#)), ([Hancu, 1971](#)), ([Neill, 1973](#)), ([Breusers et al., 1977](#)), ([Jain, 1981](#)), ([Chitale, 1988](#)), ([Melville and Sutherland, 1988](#)), ([Breusers and Raudkivi, 1991](#)), ([Johnson, 1992](#)), ([Johnson and Ayyub, 1992](#)), ([Ansari and Qadar, 1994](#)), ([Melville, 1997](#)), and ([Oliveto and Hager, 2002](#)). They have examined the phenomenon extensively. For flow velocities with a range of $0.5 < v/v_c < 1.0$, maximum scour depth (d_s) in relation to pier diameter (b) has been reported to vary widely from 0.75 to 2.5. In most cases, a peak in scour depth was observed at $v/v_c = 1$.

The presence of pile foundations has a significant impact on flow patterns and increases turbulence around them ([Rasaei et al., 2020](#)) and ([Jia et al., 2018](#)). When the current is obstructed by a pile, it leads to the formation of a horseshoe vortex, which erodes and transports bed particles, ultimately causing scour ([Zhang et al., 2017](#)) and ([Xiong et al., 2017](#)). ([Lagasse et al., 1997](#)) reported that in the United States alone, there are 488,750 bridges spanning rivers prone to scour-related failures, resulting in an annual cost of \$30 million. Hydraulic failure modes, including scour in pile foundations, account for approximately 60% of the 823 identified bridge failures in the past 30 years ([Shirole and Holt, 1991](#)).

Noteworthy bridge collapse incidents linked to excessive scouring under pile foundations, as shown in Figure 1.3, include the Schoharie Creek Bridge collapse in New York State Thruway on April 5, 1987, where five vehicles plunged into the river, resulting in 10 fatalities ([Lebeau and Wadia-fascetti, 2007](#)). Similarly, in Taiwan, the collapse of the Houfeng Bridge on September 14, 2008, claimed six lives during extreme weather conditions with strong winds and heavy rain ([Hong et al., 2012](#)). These incidents emphasize that scouring is a common and potential cause of failure for bridge pile foundations, leading to loss of life, as well as economic and environmental impacts. Therefore, it is imperative to monitor and assess the depth of scour around bridge pile foundations during design, operation, and maintenance of hydraulic structures ([Chris and Norbert, 2003](#)).

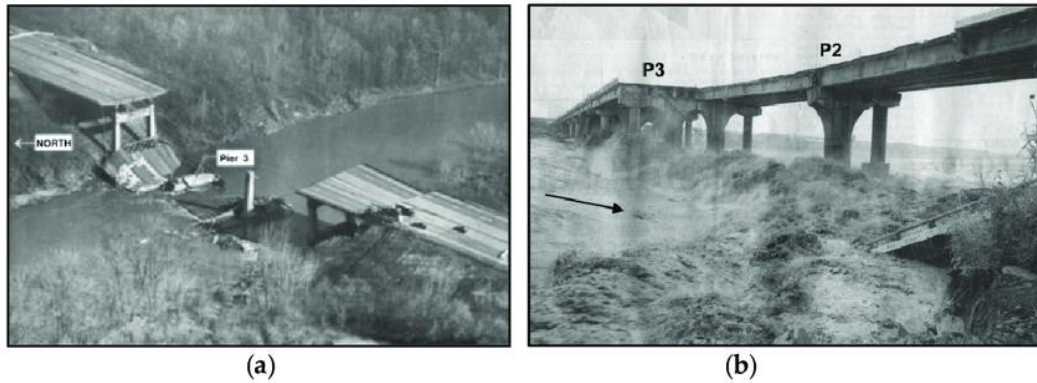


Figure 1.3. Collapses of bridge pile foundations: (a) Schoharie Creek Bridge; (b) Houfeng Bridge.

1.2. Objectives, and structure of the work

The main goal of this thesis is to evaluate the effectiveness of a novel countermeasure known as "Geo-carpet" for mitigating pile scour in clear water conditions. The study involves an extensive experimental campaign comprising multiple tests to preliminarily analyze the performance of the proposed countermeasure. The primary objective is to assess various parameters and their behavior in relation to the effectiveness of the Geo-carpet. Furthermore, the study aims to compare the results with existing research studies on similar countermeasures.

The present dissertation composes of five chapters:

Chapter 1

Introduction of the bridge's failure and the contributing factors.

Chapter 2

An explanation of sediment transport in open channel and pier scouring. Moreover, specification of the traditional countermeasure approaches and geosynthetics as contemporary countermeasure.

Chapter 3

The description of the laboratory equipment used in the experiments, the methods for data acquisition, and a brief description of the experimental procedures are presented.

Chapter 4

Conducting various types of experiments and comparing different combinations to examine their effectiveness and identify the most suitable approach. The objective is to gain a comprehensive understanding of the experimental outcomes and determine the optimal combination that yields the desired results. Moreover, some suggestions for future research and improvements.

Chapter 5

The summary and conclusion of the study.

Chapter 2

Literature Review

2.1. Sediment transport in open channel and bridge pier scour

2.1.1. Sediment Transport

Sediment transport is a physical process that pertains to the movement of sedimentary particles within various hydrodynamic environments such as rivers, streams, and coastal regions, among others.

This phenomenon encompasses two distinct categories of sediment transport, namely bed load and suspended load, each signifying distinct modes of particle displacement.

Bed load represents the motion of grains as they roll along the riverbed or channel bottom, while suspended load denotes the transportation of particles that remain in suspension within the fluid medium.

2.1.1.1. Physical properties of sediments

Two categories exist for sediments: cohesive, encompassing clay and silt particles, and non-cohesive, comprising sand and gravel particles. Sediments can be distinguished by their relative density and size, as illustrated in Table 2.1.

The relative density is determined by the equation:

$$S = \frac{\rho_s}{\rho} \quad (2.1)$$

Here, (ρ_s) denotes the density of the sediment, while (ρ) represents the density of the surrounding fluid.

Class name (1)	Size range (mm) (2)	Phi-scale (ϕ) (3)	Remarks (4)
Clay	$d < 0.002$ to 0.004 mm	$+8$ to $+9 < \phi$	
Silt	0.002 to $0.004 < d < 0.06$ mm	$+4 < \phi < +8$ to $+9$	
Sand	$0.06 < d < 2.0$ mm	$-1 < \phi < +4$	Silica
Gravel	$2.0 < d < 64$ mm	$-6 < \phi < -1$	Rock fragments
Cobble	$64 < d < 256$ mm	$-8 < \phi < -6$	Original rocks
Boulder	$256 < d$	$\phi < -8$	Original rocks

Table 2.1. Sediment size classification ([Chanson, 2004](#)).

Multiple definitions of sediment size are utilized in sedimentology. The sieve diameter refers to the particle size that can pass through a square mesh sieve of a specific size but not through the subsequent smaller-sized sieve. For instance, it can be expressed as $1\text{mm} < d < 2\text{mm}$, indicating a particle size between 1mm and 2mm.

The sedimentation diameter, on the other hand, represents the size of a quartz sphere that settles within the same fluid at an equivalent settling velocity as the actual sediment particle being studied.

Lastly, the nominal diameter denotes the size of a sphere with identical density and mass as the real sediment particle. This concept, introduced by (Chanson, 2004), allows for simplified analysis by considering an equivalent sphere in terms of density and mass when examining sediment characteristics.

➤ Particle size distribution

In natural sediment compositions, a multitude of particle sizes and shapes are present, creating a diverse mixture. The distribution of particle sizes is commonly represented by plotting the weight percentage of the total sample that is smaller than a specific size against the particle size itself.

Within this context, certain characteristic sediment sizes are defined. The (d_{50}) size, for instance, refers to the particle size at which 50% of the material's weight is comprised of finer particles. Similarly, the (d_{16}) and (d_{84}) sizes represent the grain sizes for which 16% and 84% of the material's weight, respectively, consists of finer particles.

The sediment size distribution's uniformity is characterized by the geometric standard deviation (σ_g), which is based on a log-normal distribution of grain sizes. A higher value of (σ_g) indicates a wider sediment size distribution, whereas a lower value implies a more uniform distribution.

$$\sigma_g = \sqrt{\frac{d_{84}}{d_{16}}} \quad (2.2)$$

Figure 2.1 illustrates a typical particle distribution curve, which displays the percentage of the sample as a function of the sedimentological size parameter (ϕ), as well as the cumulative percentage of particles passing as a function of the particle size (d).

The sedimentological size parameter (ϕ) is defined as follows:

$$\phi = -\frac{\ln(d)}{\ln(2)} \quad (2.3)$$

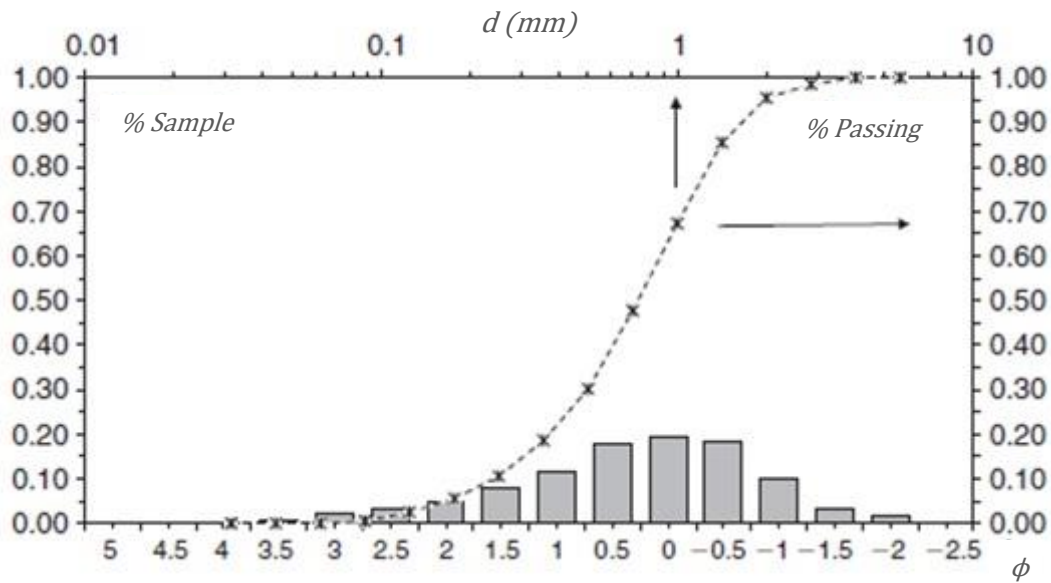


Figure 2.1. Sediment size distribution sample (Chanson, 2004).

➤ Angle of repose

When considering the stability of an individual particle on a horizontal plane, the threshold condition for particle motion is met when the center of gravity aligns vertically above the point of contact. This critical condition, at which motion commences, is referred to as the angle of repose, denoted as (ϕ_s). The angle of repose is influenced by the shape of the particle and, specifically on a flat surface, increases with angularity. Generally, the angle of repose varies between 26° and 42° , with sands typically exhibiting angles of repose ranging from 26° to 34° (Chanson, 2004).

Figure 2.2 provides illustrative examples of the angle of repose for various sediment particle shapes.

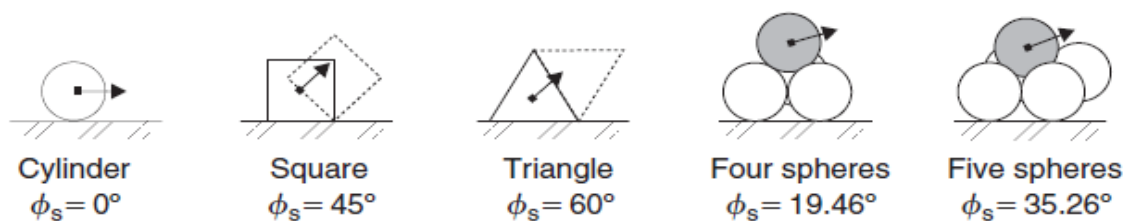


Figure 2.2. Examples of angle of repose (Chanson, 2004).

2.1.1.2. Bed load transport

➤ Threshold of sediment bed motion

The threshold of sediment bed motion refers to the condition at which sediment particles initiate movement from a state of rest. In practical scenarios, the transport of bed load commences at lower velocities compared to sediment suspension, given a specific bed geometry and particle size distribution.

In the context of open channel flow with a mobile bed, several forces act upon each sediment particle, as depicted in Figure 2.3.

These forces include:

$$\text{Gravity force} = \rho_s g V_s, \quad (2.4)$$

Where (ρ_s) represents the density of the sediment and (V_s) is the volume of the particle.

$$\text{Buoyancy force: } F_b = \rho g V_s, \quad (2.5)$$

Where (ρ) is the density of the surrounding fluid and (g) is the acceleration due to gravity.

$$\text{Drag force: } C_d = \frac{A_s v^2}{2}, \quad (2.6)$$

Where (C_d) denotes the drag coefficient, (A_s) is a characteristic particle cross-sectional area, and (v) is a characteristic velocity adjacent to the channel bed.

$$\text{Lift force: } C_L = \frac{A_s v^2}{2}, \quad (2.7)$$

Where (C_L) represents the lift coefficient.

Reaction forces from neighbouring grains.

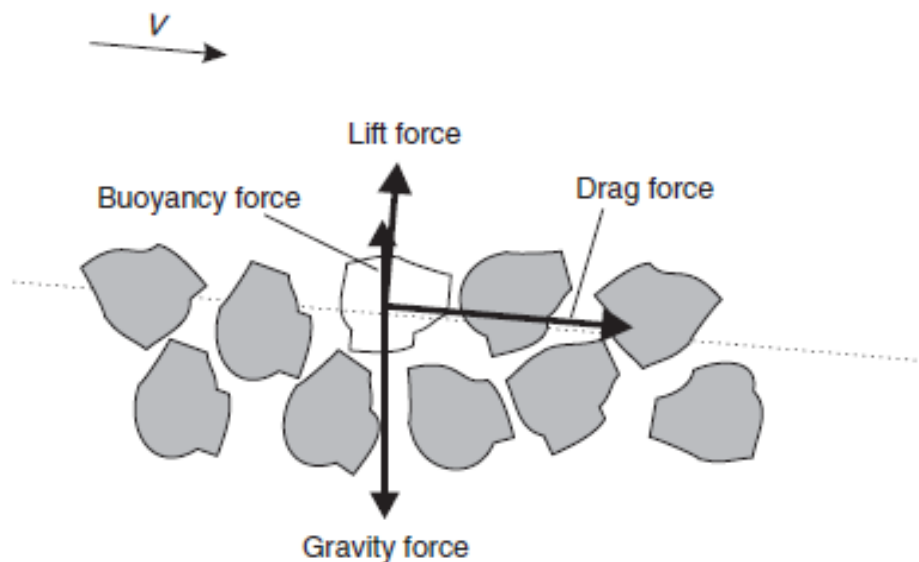


Figure 2.3. Forces acting on a sediment particle ([Chanson, 2004](#)).

The gravitational and buoyancy forces act vertically, while the drag force operates in the direction of flow and the lift force acts perpendicular to the flow direction. Inter-granular forces are influenced by the arrangement and packing of grains ([Chanson, 2004](#)).

Precisely defining the exact threshold of sediment transport is challenging, but numerous well-conducted experiments have provided consistent and reasonably accurate outcomes.

To analyse the sediment transport threshold in dimensionless terms, several pertinent parameters come into play, including the bed shear stress (τ_0), sediment density (ρ_s), fluid density (ρ), grain diameter (d_s), gravity acceleration (g), and fluid viscosity (μ) ([Chanson, 2004](#)).

$$f_2 \left(\frac{\tau_0}{\rho g d_s}; \frac{\rho_s}{\rho}; \frac{d_s \sqrt{\rho \tau_0}}{\mu} \right) = 0 \quad (2.8)$$

The shear velocity can be precisely defined as follows:

$$v_0 = \sqrt{\frac{\tau_0}{\rho}} \quad (2.9)$$

Hence, the preceding equation can be reformulated as:

$$f_3 \left(\frac{v_0}{\sqrt{g d_s}}; \frac{\rho_s}{\rho}; \rho \frac{d_s v_0}{\mu} \right) = 0 \quad (2.10)$$

The motion of particles transpires when the moments generated by the destabilizing forces (namely, drag, lift, and buoyancy) surpass the stabilizing moment generated by the gravitational force. This condition is contingent upon the angle of repose.

Empirical investigations have underscored the significance of the stability parameter (τ^*), which can be deduced through dimensional analysis. It is expressed as:

$$\tau^* = \frac{\tau_0}{\rho(s-1)g d_s} \quad (2.11)$$

$$\tau_0 = \rho g R_H S_{f,skin} \quad (2.12)$$

$$S_{f,skin} = \frac{n_{skin}^2 v^2}{R_H^{4/3}} \quad (2.13)$$

$$n_{skin} = \frac{d_{90}^{1/6}}{26} \quad (2.14)$$

In summary, the onset of bed load transport transpires when the bed shear stress (τ_0) surpasses a critical threshold:

$$(\tau_0)_c = \rho(s - 1)gd_s(\tau_0) \quad (2.15)$$

Notably, sediment particles in water, as depicted in Figure 2.4, exhibit distinct trends in the Shields diagram corresponding to different turbulent flow regimes:

- smooth turbulent flow ($Re^* < 4-5$) $0.035 < (\tau^*)_c$,
- transition regime ($4-5 < Re^* < 75-100$) $0.03 < (\tau^*)_c < 0.04$,
- fully rough turbulent flow ($75-100 < Re^*$) $0.03 < (\tau^*)_c < 0.06$.

It is noteworthy that for fully rough, turbulent flows, the critical Shields parameter $(\tau^*)_c$ remains relatively constant, and the critical bed shear stress required for initiating bed load motion becomes linearly proportional to the size of the sediment particles ([Chanson, 2004](#)).

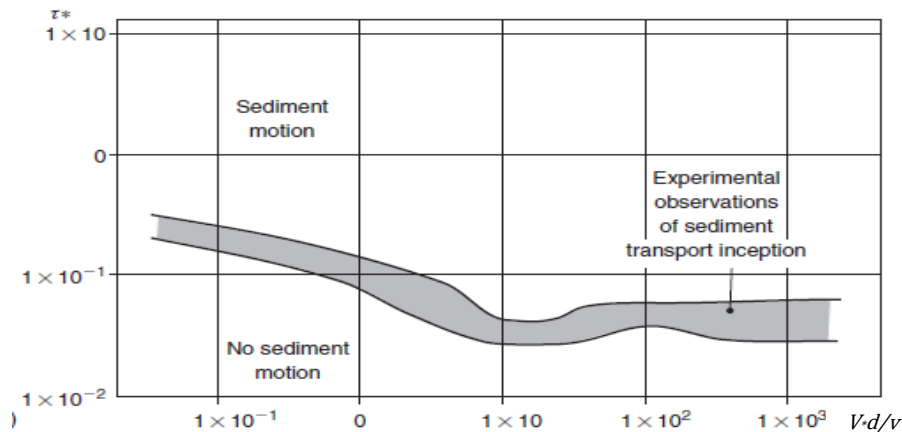


Figure 2.4. Shields parameter as a function of the particle Reynolds number for sediment in water ([Chanson, 2004](#)).

➤ Sediment bed motion

Figure 2.5 illustrates the mechanism of bed transport when the bed shear stress exceeds the critical threshold. Bed-load transport encompasses three primary modes of particle motion: rolling, sliding, and saltation, which involves the intermittent hopping and bouncing of sediment particles along the bed.

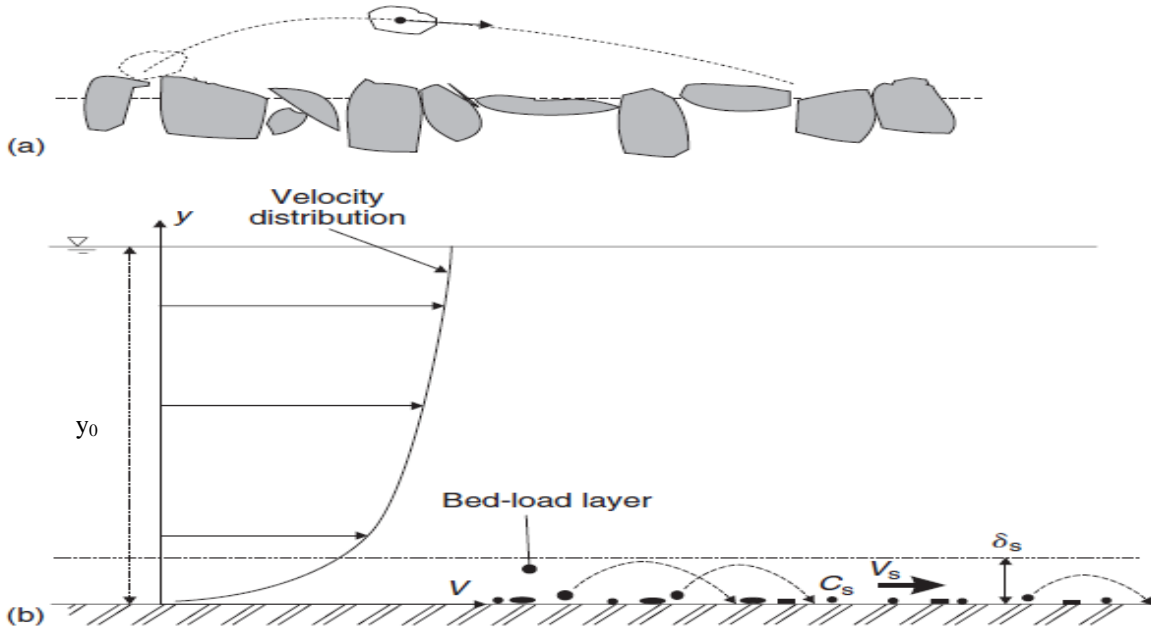


Figure 2.5. Bed-load motion: (a) sketch of saltation motion and (b) definition sketch of the bed-load layer (Chanson, 2004).

The rate of sediment transport, typically expressed in meter width, is commonly quantified using either mass or volume measurements (Chanson, 2004):

$$\dot{m}_s = \rho_s q_s \quad (2.16)$$

The mass sediment flow rate per unit width is denoted as (\dot{m}_s), while the volumetric sediment discharge per unit width is represented by (q_s). Furthermore, (ρ_s) signifies the specific mass of sediment. When the shear stress exceeds the threshold, it induces bed load transport, which can be determined based on the shear stress magnitude.

2.1.2. Pier scour

Scouring at bridge crossings is the consequence of the erosive impact exerted by flowing water, which possesses sufficient strength to excavate and carry away sediment from the surrounding areas encompassing bridge piers and abutments (Richardson and Davis, 2001). The scour depth represents the reduction in the level of the riverbed and serves as a measure of the potential for exposing the foundations of bridges (Melville and Coleman, 2000).

2.1.2.1. Local scour

In the presence of bridge crossings, the alteration in the cross-sectional geometry due to the bridge itself induces scour, commonly known as Local Scour. This type of scour occurs as a consequence of the flow disturbance caused by the obstruction of the flow around piers, abutments, and embankments (Richardson and Davis, 2001).

The presence of a bridge structure within a flow channel inevitably leads to significant changes in the flow pattern, subsequently resulting in alterations to the stream bed elevation. The flow modifications induced by the bridge piers give rise to the formation of scour holes at the piers, which have been extensively studied and recognized as potential causes of pier damage or failure (Richardson and Davis, 2001) and (Melville and Coleman, 2000).

The primary characteristic of the flow near a pier is the development of a system of vortices, which occurs when unidirectional flow in an erodible channel becomes three-dimensional ([Graf and Yulistiyan, 1998](#); [Melville and Coleman, 2000](#); [Shen et al., 1969](#)).

Depending on the geometry of the bridge and the flow conditions, this vortex system can consist of three distinct components, either individually or in combination, acting at the pier as depicted in figure 2.6:

a) the horseshoe-vortex system at the base of the pier; b) the wake-vortex system downstream of the pier; c) the surface roller ahead of the pier.

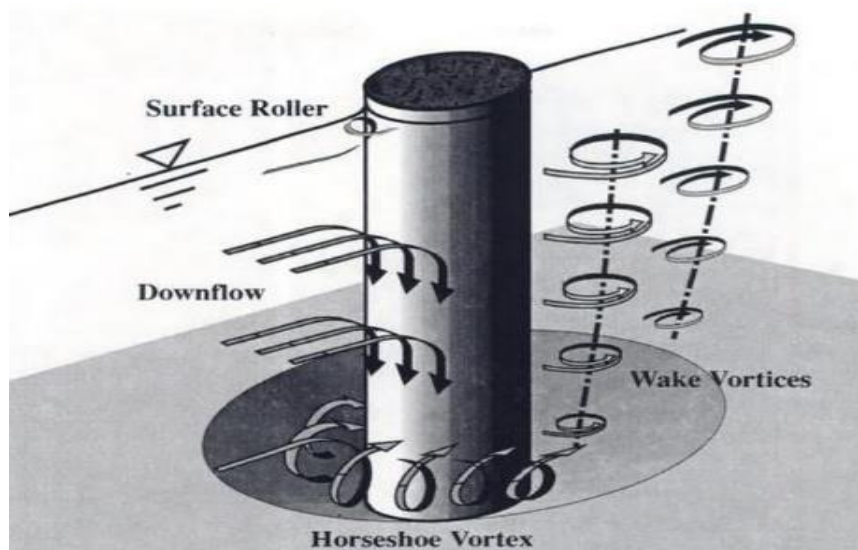


Figure 2.6. Illustration of the system of vortices at a bridge pier ([Melville and Coleman, 2000](#)).

The horseshoe-vortex is generated by the vertical component of the downward flow, observed in front of the pier as a result of the stagnating pressure gradient when the flow approaches the pier ([Breusers and Raudkivi, 1991](#)).

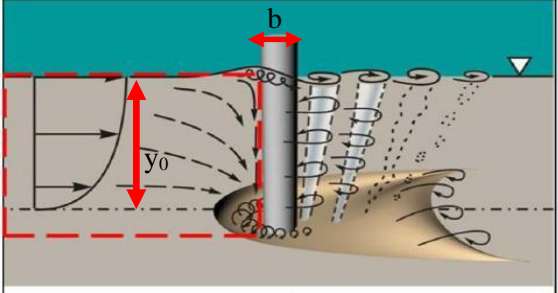
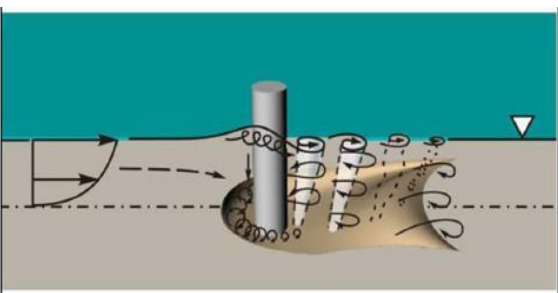
Although the lateral diversion of the flow by the pressure gradient around the pier is inevitable, it is generally acknowledged that it is the vertical component of the flow that primarily contributes to the removal of bed material ([Graf and Istiarto, 2002](#)). The presence of the stagnation pressure leads to an increase in the water surface, creating a surface roller upstream of the pier.

If the pressure field is sufficiently strong, it results in a three-dimensional separation of the boundary layer, and the horseshoe-vortex system forms at the base of the pier ([Graf and Istiarto, 2002](#); [Shen et al., 1969](#)). The downward flow impinging on the bed acts as a vertical jet, eroding a groove immediately adjacent to the front of the pier ([Melville and Coleman, 2000](#)).

The wake-vortex system is generated due to the rolling up of unstable shear layers at the surface of the pier ([Shen et al., 1969](#)). The wake vortices originate from both sides of the pier at the separation line and are subsequently carried downstream by the flow.

(Shen et al., 1969) observed that this vortex system remains stable for low Reynolds numbers ($3 < Re < 40$ to 50) and forms a standing system downstream of the pier. However, for Reynolds numbers of practical interest, the wake vortices become unstable, shed alternately from the pier, and are transported downstream. The wake-vortex system acts as a "vacuum cleaner," entraining and transporting downstream the sediment displaced by the downward flow and the horseshoe-vortex system (Melville and Coleman, 2000). The intensity of the wake vortices diminishes rapidly with increasing distance downstream of the pier, often leading to sediment deposition downstream of long piers (Richardson and Davis, 2001).

The scouring process can be better understood by examining the flow field around the pier, which provides insights into the sediment movement. This process is classified into three categories based on the ratio between the pier width (b) and the flow depth (y_0), as described by (Ettema et al., 2017). The values presented in Table 2.2 are derived from data trends that highlight variations in the relationship between scour depth and (y_0/b).

Narrow Piers ($y_0/b \geq 1.4$)	
 <p style="text-align: center;"><i>Scour typically is deepest at the pier face.</i></p>	<p>The flow dynamics around the pier are characterized by deceleration as the flow approaches, followed by impact against the pier's centerline. Subsequently, the flow strongly deflects both downward and upward along the pier's face. These vertical flows closely adhere to the pier's surface and move along its centerline, with one directed upward towards the free surface and the other downward towards the bed. The downward flow is driven by the downward gradient of stagnation pressure along the leading face of the pier, below the still water level. This gradient arises due to the velocity distribution of the approaching flow, which corresponds to a fully turbulent shear flow, resulting in a decrease in velocity towards the bed. As the scour hole forms, the downward flow is reinforced as the approaching flow diverges into the scour hole. Furthermore, when the flow passes around the sides of the pier, it contracts, leading to localized increases in flow velocity and bed shear stress around the pier's sides. These turbulence structures, combined with local flow convergence and contractions, play a crucial role as erosive flow mechanisms, particularly around the wide fronts and flanks of piers.</p>
Transition Piers ($0.2 \leq y_0/b < 1.4$)	
 <p style="text-align: center;"><i>Transitional pier.</i></p>	<p>For transition piers, the overall flow field does not undergo significant changes, but there are differences in the way it develops. The accompanying figures illustrate the adjustments in the flow field, which indicate a reduction in the scour capacity of the flow. The down-flow at the pier face becomes less pronounced as it has a shorter distance to develop, whereas the up-flow associated with the bow wave, known as flow stagnation, remains largely unaffected. The large-scale turbulence structures, such as the horseshoe vortex, which are horizontally aligned in the pier flow field, experience a weakening effect as the down-flow weakens. Similarly, the vertically aligned turbulence structures, referred to as wake vortices, also diminish in strength due to the increased influence of bed friction in shallower flow conditions. These changes occur as a consequence of the transition pier's altered geometry and the corresponding adjustments in the flow field characteristics.</p>

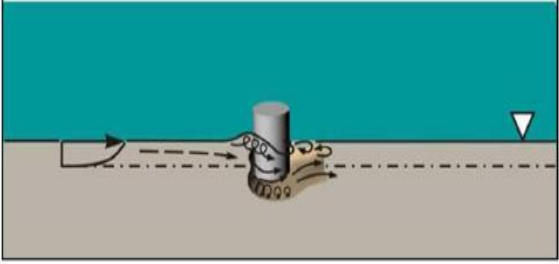
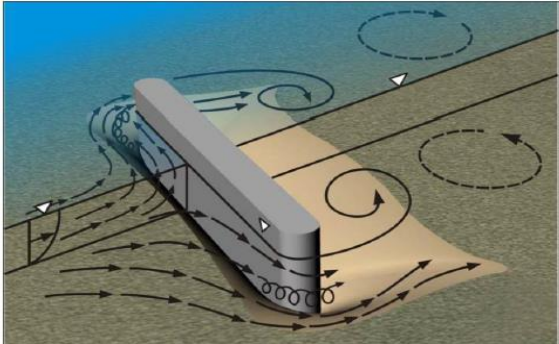
 <p style="text-align: center;"><i>Shallow transitional pier.</i></p>	
Wide Piers ($y_0/b < 0.2$)	
 <p style="text-align: center;"><i>Scour typically is deepest at the pier sides.</i></p>	<p>In the case of wide piers, the flow pattern undergoes distinct changes. As the flow approaches the pier, it decelerates and redirects, flowing laterally along the pier face before narrowing and passing around the sides of the pier. The down-flow at the pier face is relatively weak and causes minimal erosion at the center plane of the pier's foundation. However, the circulation of the necklace vortices reaches its maximum intensity in the vertical sections near the sides of the pier. The highest flow velocities are observed in the vicinity of the pier where the flow contracts around its sides.</p> <p>Erosive turbulence structures in this scenario primarily consist of wake vortices and the relevant portion of the horseshoe vortex system located in the scour region near each side of the pier. The deepest scouring takes place at the sides of the pier, where the erosive action is most pronounced. The flow dynamics and associated scour patterns are influenced by the wide pier geometry, resulting in distinct flow characteristics and erosion patterns compared to other pier configurations.</p>

Table 2.2. Scour processes and pier geometry variations (Ettema et al., 2017).

The scour process, similar to other natural phenomena, is influenced by various factors, such as variations in pier dimensions, shape, orientation, flow depth, and the presence of debris or ice. These factors have the potential to modify the flow field, thereby either amplifying or diminishing its erosive characteristics. Additionally, these variables can have an impact on the extent of scour, which refers to the reduction in riverbed level and serves as an indicator of the potential exposure of bridge foundations (Richardson and Davis, 2001).

Bridges are particularly susceptible to these phenomena due to the crucial role of bridge piers in supporting the superstructure and facilitating the transfer of both designed structural loads and flow-induced hydrodynamic forces. This transfer mechanism typically involves a configuration of end-bearing or friction-bearing piles connected to a pile cap, while the foundation material allows for the stable placement of the pier column on a slab footing. Failure of piers can occur when scouring, combined with structural and hydraulic loads, disrupts the stability of their foundations.

2.1.2.2. Clear water and live-bed scour

In order to effectively manage or control the scouring mechanism, it is crucial to understand the influence of sediment bed motion on the development of the scour hole. This understanding has led to the identification of two distinct scour regimes: clear-water scour and live-bed scour.

Clear-water scour refers to the process in which material is eroded from the scour hole without being replenished by the incoming flow. This occurs when the mean flow velocities remain below the threshold velocity required to entrain bed sediment. In such cases, the scour hole lacks sediment as the flow energy is insufficient to transport sediment particles.

On the other hand, live-bed scour occurs when the scour hole is continuously supplied with sediment by the approaching flow. This phenomenon arises when the flow velocity exceeds the threshold velocity necessary for bed sediment entrainment. Consequently, the scour hole remains filled with sediment due to the sustained transport of sediment particles.

In literature, the threshold between clear-water scour and live-bed scour is often determined based on the ratio between the two velocities mentioned. When this ratio is less than 1, it signifies a clear-water scour process. Conversely, if the ratio exceeds 1, it indicates a live-bed scour process. This threshold ratio serves as a crucial parameter in distinguishing between the two scour regimes, as illustrated in Figure 2.8.

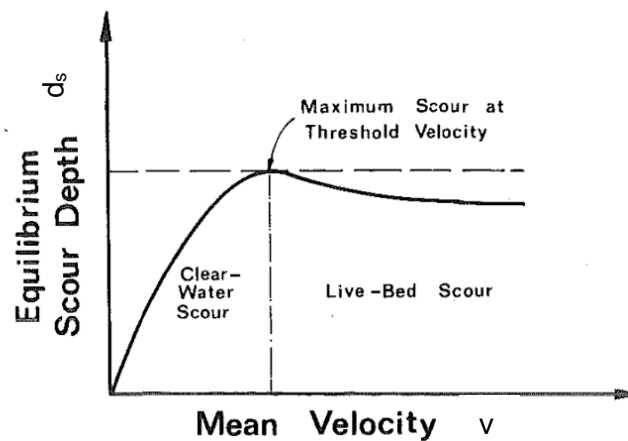


Figure 2.7. Equilibrium scour depth vs Mean velocity (Melville, 1984).

A noteworthy approach was proposed in the research conducted by (Melville, 1984), which examines the variation of scour depth parallel to the stage of sediment bed motion, as depicted in Figure 2.8. The study also emphasizes the temporal decrease in scour depth (normalized with respect to the pier diameter) beyond the critical threshold (v_c in the graph), attributed to lower velocities and the initial stage of bed motion, which contribute less to the erosion process.

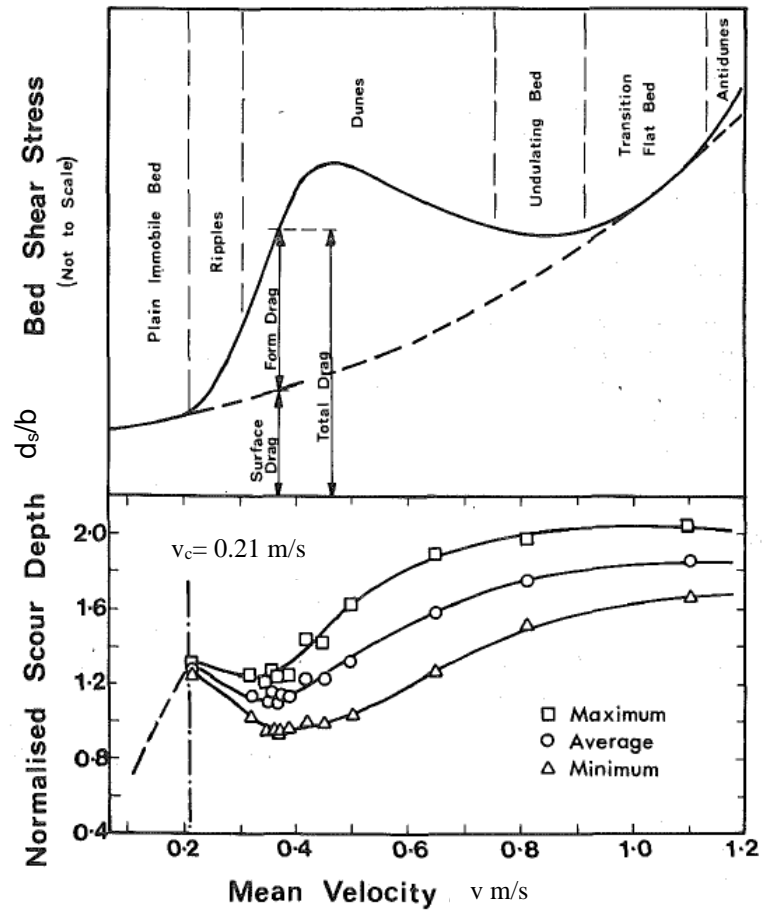


Figure 2.8. Bed motions vs Mean velocity (Melville, 1984).

Furthermore, distinct patterns of hole scouring are anticipated in these two scenarios. In clear-water conditions, the scour depth undergoes a gradual increment and eventually reaches a steady state. Conversely, in live-bed conditions, the scour depth experiences rapid growth and tends to fluctuate around a stable value due to the interplay between erosion and deposition processes (Brath and Montanari, 2000; Richardson and Davis, 2001). Figure 2.9 visually depicts the progression of scour in both clear-water and live-bed conditions.

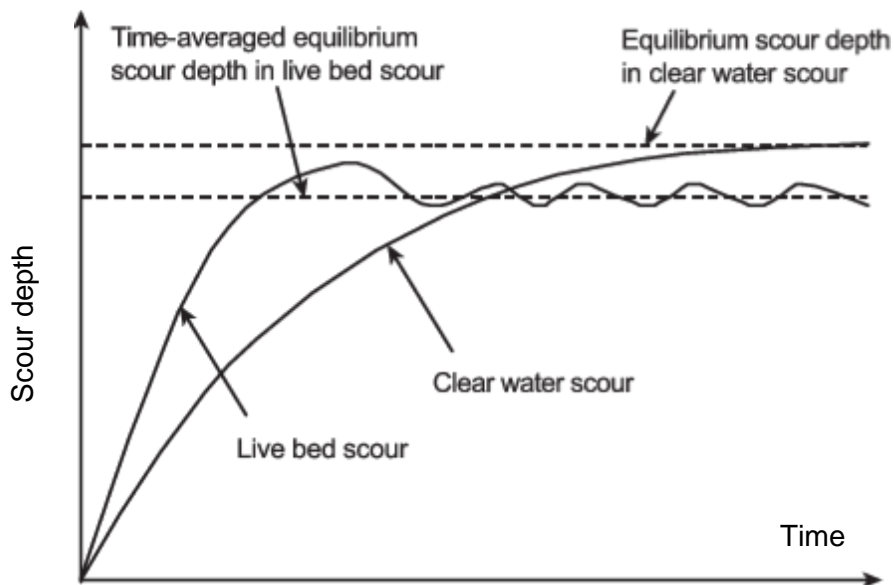


Figure 2.9. Temporal evolution of scour depth in clear-water and live-bed conditions (Brandimarte et al., 2012).

2.1.2.3. Steady-flow scour studies

Numerous investigations have been conducted to examine the relationship between scour depth and various parameters under steady conditions ([Chang et al., 2004](#); [Chiew and Melville, 1987](#)). This section focuses on highlighting some of these experiments along with their findings:

➤ Case study 1:

In this study, ([Chiew and Melville, 1987](#)) explored the sensitivity of scour depth to approaching velocity, sediment size, and water depth. They derived three empirical functions that establish a connection between equilibrium scour depth and the approach velocity, sediment size, and flow depth ([Chiew and Melville, 1987](#)). Transparent cylindrical piers, constructed from clear 17erspex tubes, were utilized for the experiments. A total of five uniformly graded sediments with varying sizes, as presented in Table 2.3, were carefully chosen. For each sediment size, three different pier sizes (b) were investigated, measuring 31.8 mm (1.3 in.), 40 mm (1.6 in.), and 45 mm (1.8 in.).

mean particle size, in millimeters (inches)	specific gravity	critical shear velocity, in metres per second (feet per second)	critical mean velocity, in metres per second (feet per second)	geometric standard deviation
0.24 (9.45×10^{-3})	2.65	0.013 (0.041)	0.27 (0.89)	1.33
0.60 (2.36×10^{-2})	2.65	0.019 (0.062)	0.34 (1.12)	1.18
0.85 (3.35×10^{-2})	2.65	0.022 (0.072)	0.39 (1.28)	1.23
1.45 (5.71×10^{-2})	2.65	0.028 (0.092)	0.45 (1.48)	1.24
3.20 (1.26×10^{-1})	2.65	0.049 (0.161)	0.73 (2.39)	1.28

Table 2.3. Properties of sediments used in experiments ([Chiew and Melville, 1987](#)).

By considering d_s as the average scour depth, b as the pier diameter, v as the mean approaching velocity, (v_c) as the critical velocity for sediment size (d_{50}), and (y_0) as the flow depth, the study revealed interesting findings. When the relative equilibrium scour depth, (d_s/b), is plotted against the velocity excess, (v/v_c), for subcritical approach flows with Froude numbers less than unity, certain patterns emerge. Initially, there is a decrease in scour depth as the velocity slightly exceeds the threshold velocity of the bed sediment. This reduction continues until a minimum scour depth is reached at $v/v_c = 2$. Subsequently, the local scour depth begins to increase again, albeit at a decreasing rate, until a second peak is observed at $v/v_c = 4$. This particular point corresponds to the formation of a transition flatbed, as depicted in Figure 2.10.

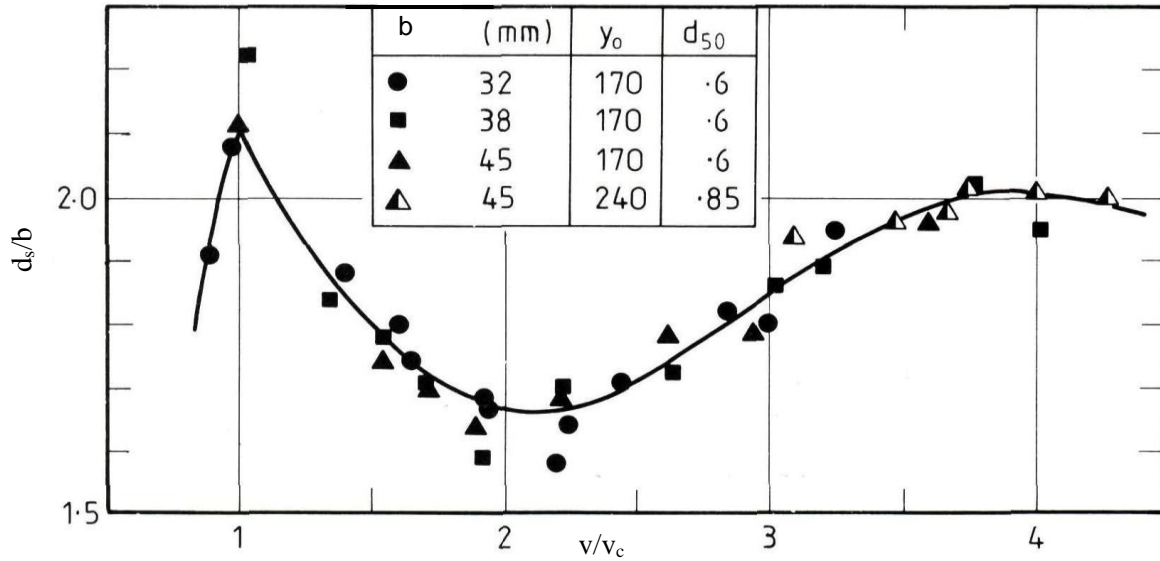


Figure 2.10. Relative equilibrium scour depth, d_s/b versus velocity excess, v/v_c for $d_{50} = 0.6$ and 0.85 mm (Chiew and Melville, 1987).

The equilibrium scour depth is influenced by the size of the bed sediment. (Ettema, 1980) conducted a study on clear-water scour and found that the scour depth is affected by the relative size of the pier to sediment, (b/d_{50}) .

It was observed that as the value of (b/d_{50}) decreases, the depth of scour also decreases. However, when (b/d_{50}) is greater than or equal to 50, the scour depth becomes independent of (b/d_{50}) . To illustrate this, Ettema's data, along with clear-water scour results from (Chee, 1982) and live-bed scour results from the present study, are plotted together in Figure 2.11. Each curve demonstrates that as (b/d_{50}) increases, the value of b/d_{50} also increases almost linearly until it reaches a maximum at $b/d_{50} = 50$. This indicates that the scour depth remains unaffected by the relative size of the pier to sediment when $b/d_{50} > 50$ (Chiew and Melville, 1987).

Considering the effect of water depth, it has been observed that in shallow flow conditions, the scour depth decreases primarily due to the weakening of the downflow. The erosion of the scour hole is driven by the momentum of the fluid flowing downward at the base of the scour hole. In shallow flows, this momentum is reduced, resulting in a lesser scour hole.

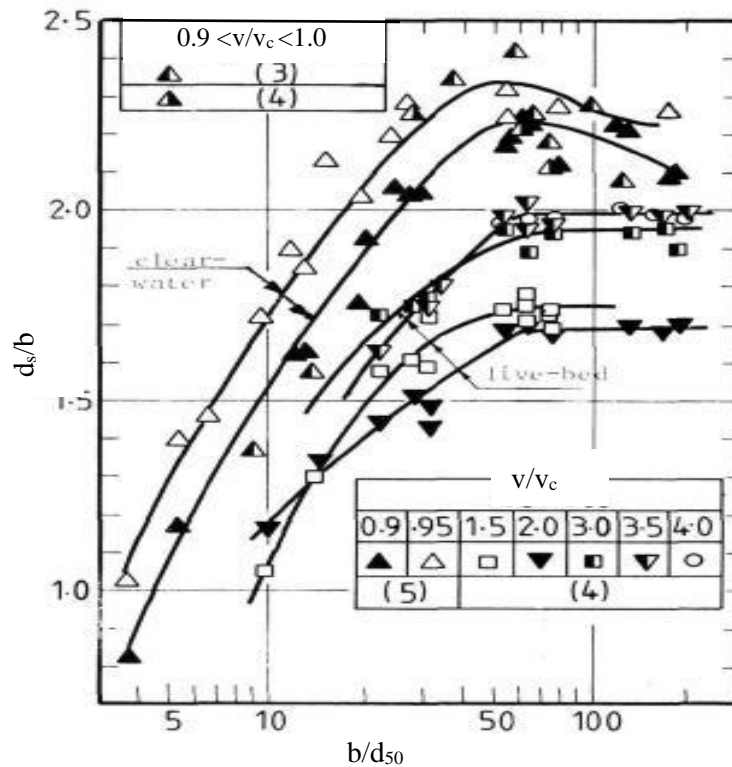


Figure 2.11. Relative equilibrium scour depth versus b/d_{50} at various values of v/v_c (Chiew and Melville, 1987).

➤ Case study 2:

This experiment conducted by (Chang et al., 2004), focused on investigating the effect of sediment uniformity on clear-water pier scour under steady conditions. The study aimed to explore how sediment size gradation influences the evolution of scour depth at the nose of a circular pier. The research employed both laboratory experiments and a simulation model to analyse the phenomenon.

The experiments involved the use of two types of sediments: uniform sediments with sizes measuring 1.0 and 0.71 mm, and nonuniform sediments with the same median sizes but varying standard deviations (σ_g) of 2.0 and 3.0, respectively. Notably, all the sediments utilized in the experiments had a specific gravity of 2.65. The diameter of the cylindrical pier (b) was 0.1 m, while the flow depth (y_0) was not specified. For detailed information regarding the experimental conditions, please refer to Table 2.4.

In a channel with a movable bed, the flow has the ability to entrain and transport materials that are located on or near the bed surface. The layer from which these materials can be entrained by the flow is known as the mixing layer. This layer can be seen as an active zone where the bed material is susceptible to erosion and movement.

During the process of erosion involving nonuniform sediment, it is observed that fine grains tend to be scoured and transported by the flow first, while the coarse grains are left behind. Over time, a significant portion of the finer grains gets washed out of the active zone. As a result, the bed materials covered by the remaining coarse grains become immobile and create a protective layer known as an armored layer. This armored layer serves to safeguard the underlying materials from further erosion by providing a barrier against the erosive forces of the flow.

Run number	d_0 (mm)	σ_g	y_0 (mm)	v (cm/s)	t (h)	d_s/b
S1	1.00	1.2	20.0	39.0	19	1.86
S2	1.00	1.2	20.0	28.0	19	1.18
S3	1.00	2.0	20.0	28.0	56	0.43
S4	1.00	3.0	20.0	28.0	28	0.29
S5	0.71	1.2	30.0	35.5	7	1.54
S6	0.71	1.2	15.0	22.7	7	0.66
S7	0.71	2.0	30.0	35.5	72	0.83
S8	0.71	2.0	15.0	22.7	47	0.24
S9	0.71	3.0	30.0	35.5	38	0.68
S10	0.71	3.0	15.0	22.7	27	0.15

Table 2.4. Experimental conditions ([Chang et al., 2004](#)).

➤ Case study 3:

([Ettmer et al., 2015](#)) focused on studying steady live-bed scour and measuring various parameters of scour depth, including maximum, minimum, and mean values. The experiments were performed in a sediment recirculating flume with a bed consisting of polystyrene particles.

The primary objective of the research was to investigate scour at bridge piers using live-bed experiments. The experiments were carried out until equilibrium conditions were achieved. The flow velocities (v) ranged from 0.8 to 8.5 times the critical velocity (v_c) required for the incipient motion of sediment particles. Continuous measurement of the maximum scour depth was performed using an endoscopic camera placed inside a plexiglass cylinder used as the pier structure.

The study observed that bed load transport with dunes was the dominant mode of sediment transport for flow velocity ratios of $1 < v/v_c < 4$. However, when the velocity ratio exceeded $v/v_c \geq 4$, the entrainment of sediment particles into suspension without the formation of bedforms became the predominant mode.

For detailed information regarding the experimental conditions, please refer to Table 2.5, where the pier diameter (b) was 7 cm. The critical velocity for the incipient motion of sediment particles (v_c) was experimentally determined in preliminary runs and found to be $v_c = 0.09$ m/s.

1	2	3	4	5	6	7	8
Number	t (min)	v (m/s)	F (dimensionless)	v/v_c (dimensionless)	$d_{s\ max}/b$ (dimensionless)	$d_{s\ min}/b$ (dimensionless)	$d_{s\ mean}/b$ (dimensionless)
S1	360	0.072	0.069	0.80	0.81	0.81	0.81
S2	360	0.077	0.074	0.85	1.10	1.10	1.10
S3	360	0.081	0.078	0.90	1.23	1.23	1.23
S4	360	0.086	0.082	0.95	1.34	1.34	1.34
S5	360	0.090	0.087	1.00	1.51	1.51	1.51
S6	60	0.135	0.130	1.50	1.67	1.31	1.54
S7	60	0.180	0.173	2.00	1.77	1.09	1.48
S8	60	0.225	0.217	2.50	1.96	1.53	1.79
S9	60	0.270	0.260	3.00	2.26	1.79	2.07
S10	60	0.315	0.303	3.50	2.37	1.97	2.22
S11	60	0.360	0.347	4.00	2.51	2.13	2.40
S12	60	0.405	0.390	4.50	2.64	2.44	2.57
S13	60	0.450	0.433	5.00	2.84	2.59	2.73
S14	60	0.495	0.477	5.50	3.01	2.73	2.88
S15	60	0.540	0.520	6.00	3.09	2.84	2.99
S16	60	0.585	0.563	6.50	3.21	2.99	3.10
S17	60	0.630	0.606	7.00	3.23	2.99	3.15
S18	60	0.675	0.650	7.50	3.29	2.94	3.18
S19	60	0.720	0.693	8.00	3.29	3.00	3.21
S20	60	0.765	0.736	8.50	3.33	2.99	3.22

Note: Flow depth was $y_0=0.11$ m during all runs.

Table 2.5. Experimental conditions ([Chang et al., 2004](#)).

In Figure 2.12, the equilibrium scour depth (d_s/b) overflow intensity (v/v_c) is depicted. Additionally, the fluctuation of scour depth is represented as minimum and maximum values for $v/v_c > 1$.

For $v/v_c < 1$, the minimum, average, and maximum scour depths coincide and increase with flow intensity until reaching a peak at $v/v_c = 1$.

In the range of $1 < v/v_c < 2$, the average scour depth initially decreases with flow intensity until reaching a local minimum, after which it continuously increases. The same trend is observed for the minimum scour depth. However, the maximum scour depths consistently increase with flow intensity for $v/v_c > 1$, reaching their highest value of 3.33 at $v/v_c = 8.5$. Notably, this value is significantly greater than the clear-water scour depth of 1.51 observed at $v/v_c = 1.0$.

The minimum and average scour depths exhibit a local minimum at $v/v_c = 2.0$, and the envelope curve of these depths aligns well with the findings of previous investigations, such as ([Melville and Coleman, 2000](#)).

Furthermore, it was observed that under bed-load conditions with $1 < v/v_c < 4$, the maximum scour depth is approximately 10-20% deeper than the average scour depth. However, for $v/v_c \geq 4$, the maximum scour depths are only around 5% deeper than the average. These results are consistent with the findings of ([Richardson and Davis, 2001](#)), who highlight that the maximum scour depth under sediment transport conditions can be significantly deeper compared to clear-water conditions.

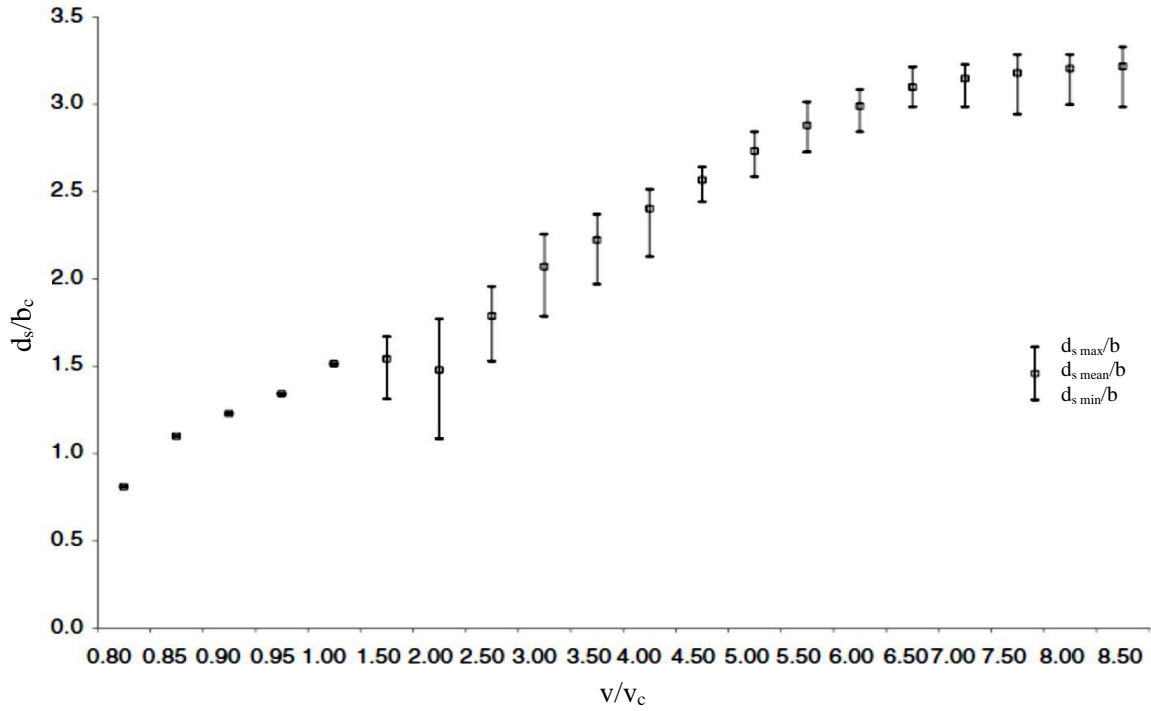


Figure 2.12. Measured equilibrium scour depth (d_s/b) overflow intensity (v/v_c) (Ettmer et al., 2015).

- Factors affecting the scour depth.

Multiple factors influence the magnitude of local scour at piers and abutments, including the width and length of the pier/abutment (especially if skewed to flow), the depth of flow, the velocity of the approach flow, the size and gradation of the bed material, the angle of attack of the approach flow, the shape of the pier/abutment, the bed configuration, and the presence of ice formation or debris (Radice and Lauva, 2017).

The dimensionless scour depth at a circular bridge pier with uniform sediment can be described by the following function:

$$\frac{d_s}{b} = F\left(\frac{y_0}{b}, \frac{b}{B}, \frac{y_0}{d}, \frac{Q}{Q_c}, \frac{tv}{b}\right) \quad (2.17)$$

where d_s represent the scour depth, (b) is the pier diameter, (y_0) is the water height, (B) is the channel width, (t) denotes time, and (v) is the flow velocity. The parameters on the right-hand side of the Eq. (2.17) correspond to the influence of pier slenderness, flow contraction, sediment coarseness, flow intensity, and dimensionless time (Radice and Lauva, 2017).

- Clear water scour at circular piers

Reference is made to a paper by (Franzetti et al., 2022), that focuses on Clear Water Scour at Circular Piers. The paper introduces a novel predictor for predicting the maximum scour depth at a circular pier under clear-water flow conditions. The authors argue that despite the existence of various approaches in scour research, a simple predictor based on data correlation still holds value, as in-depth studies of process dynamics have not significantly influenced

engineering practices. Moreover, focusing on the case of a circular pier allows for the consideration of various other factors.

To develop their predictor, the authors collected laboratory data from 30 different sources, comprising a total of 328 experiments conducted over 66 years. This data was utilized to establish a formula that incorporates five dimensionless parameters: pier slenderness, flow intensity, sediment coarseness, sediment uniformity, and time. The proposed predictor demonstrates strong predictive capabilities, surpassing the performance of 27 previously published equations from the literature.

In addition to presenting the new formula, the paper discusses several considerations regarding additional parameters and operational conditions that should be taken into account. It also includes an analysis of the uncertainty associated with computed scour values and provides recommendations for making conservative predictions of scour depth in engineering applications.

Overall, this paper introduces a promising new predictor for scour depth around circular piers, based on a comprehensive dataset spanning several decades. The proposed formula offers improved predictive performance compared to existing equations and is accompanied by valuable insights and recommendations for practical engineering applications.

The methodology involved employing a dimensionless framework and addressing related issues such as dimensionless analysis, bulk and central mean velocity, velocity and shear velocity, threshold conditions, and data selection. The scour function was derived, resulting in the proposed scour predictor in the form of an equation:

$$D_s = \tilde{F}(H, D_{50}, \sigma_g, U, T) = aF_1(H)F_2(D_{50})F_3(\sigma_g)F_4(U)F_5(T) \quad (2.18)$$

Where, the scour function employed in this study assumes a multiplicative relationship among functions of individual parameters, with D_s representing the ratio of d_s (scour depth) to b (pier width). This approach capitalizes on the notion of separate effects of various dimensionless parameters, as previously explored by several researchers ([Franzetti et al., 1994](#); [Kothyari et al., 1992](#); [Lauchlan et al., 2001](#); [Melville and Coleman, 2000](#); [Oliveto and Hager, 2002](#); [Radice et al., 2002](#)).

The proposed equation, denoted as Eq. (2.18), incorporates only five parameters, whereas other equations from which it was derived contained a larger number of parameters. Certain parameters were excluded from the equation based on specific criteria.

The functions for the individual parameters can be described as follows:

$$F_1(H) = 1 - 0.675e^{-1.451H} \quad (2.19)$$

$$F_2(D_{50}) = 0.849(D_{50}^{1.815} e^{-2.990D_{50}^{0.235}} + 0.511) \quad (2.20)$$

$$F_3(\sigma_g) = 0.740(e^{-0.066\sigma_g^{3.923}} + 0.416) \quad (2.21)$$

$$F_4(U) = \begin{cases} 1 - 2.017(1 - U)^3; & U \leq 1 \\ 1; & U > 1 \end{cases} \quad (2.22)$$

$$F_5(T) = (1 - e^{-0.083T^{0.231}}) \quad (2.23)$$

Based on the provided parameters' functions, where: $H = y_0/b$, $D_{50} = b/d_{50}$, $U = v/v_c$, and $T = tv/b\Delta^{0.5}$.

The dimensionless representation of the scour experiments can be depicted graphically. Figure 2.13 illustrates this representation, showcasing the dimensionless scour over dimensionless time.

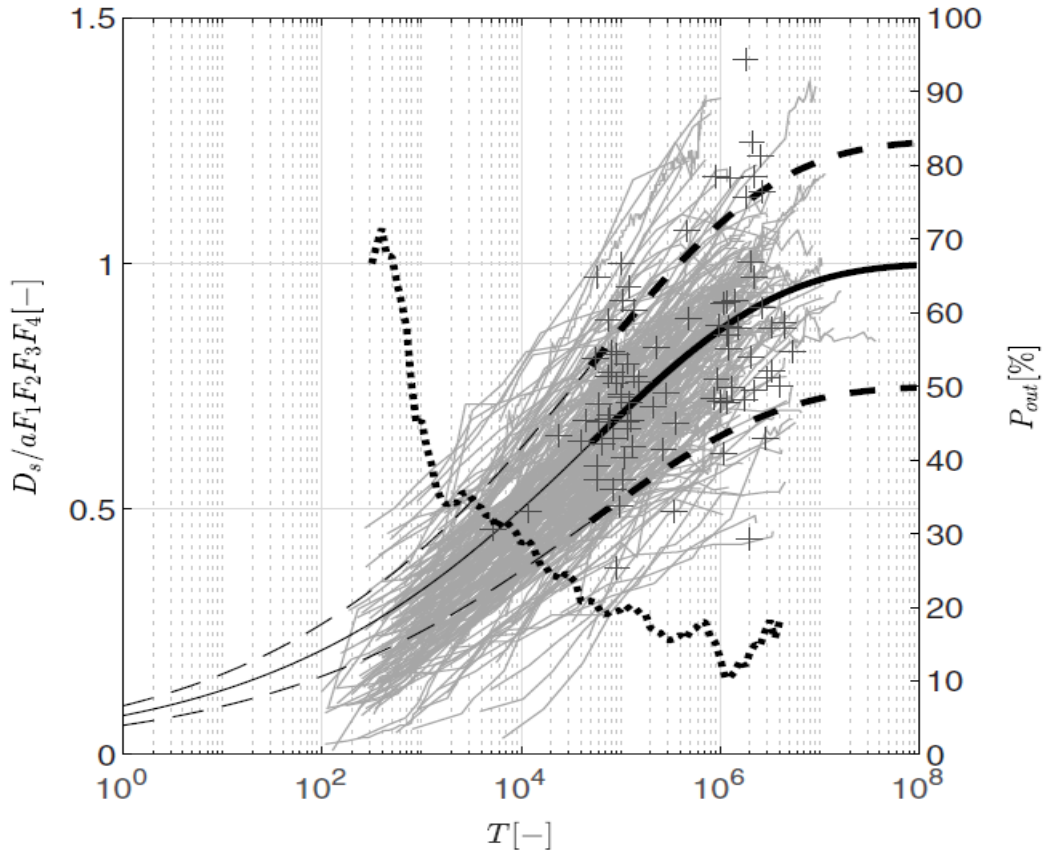


Figure 2.13. Dimensionless representation of the scour experiments. Black continuous line = Eq. (2.23); dashed lines = $\pm 25\%$ bounds. On the right axis: P_{out} (dotted line) ([Franzetti et al., 2022](#)).

To summarize, under steady conditions, the scour depth evolution is found to be more rapid and fluctuating in live-bed conditions compared to clear-water conditions. The fluctuation of scour depth decreases at higher velocities ($v/v_c > 4$) ([Ettmer et al., 2015](#)), as illustrated in Figure 2.14.

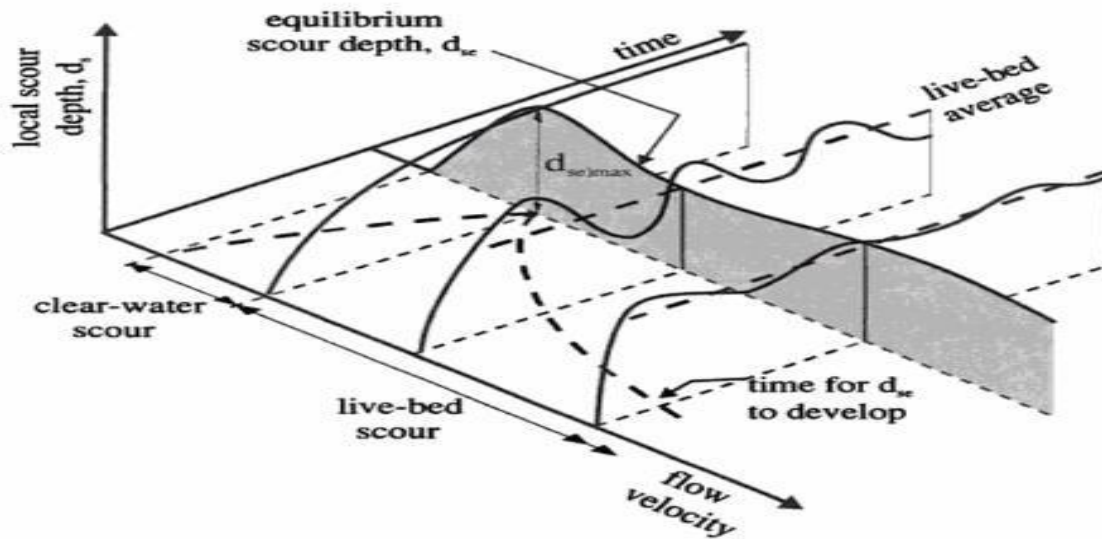


Figure 2.14. The temporal scour depth fluctuation changes with the flow velocity) (Melville and Coleman, 2000).

2.2. Pier scour countermeasures: A review of existing methods

The issue of scour around bridge piers has long posed a threat to the stability of bridges, necessitating the development of various systems to mitigate this problem. Traditional engineering approaches have introduced methods aimed at controlling scour, such as the use of rip-rap, wire gabion structures, and collars. These systems are designed to safeguard the integrity of bridges by providing protective measures against scour erosion.

2.2.1. Rip-Rap

Scour holes that form around bridge piers in various environments are primarily caused by the intense vortex motion and sediment-induced motion described earlier. To mitigate the erosional effects, engineers commonly employ a technique known as rip-rap, as depicted in Figure 2.15. Rip-rap involves placing a layer of coarse rock material along vulnerable areas to provide protection against scour and erosion. This system acts as a physical barrier, effectively resisting the erosive forces of the flowing water and shielding the foundation of the bridge pier from exposure.

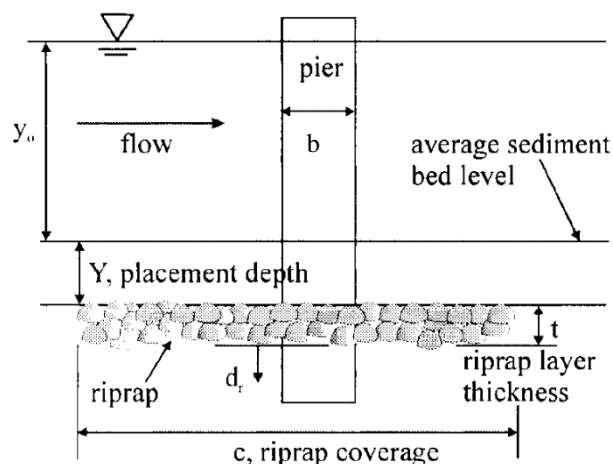


Figure 2.15. Rip-Rap scheme (Lauchlan and Melville, 2001).

Later research has focused on optimizing the Rip-Rap protection system, and studies by (Chiew, 1995) and (Chiew and Lim, 2000) have revealed potential failure mechanisms that can compromise the stability of the armor. It should be noted that these failure mechanisms differ depending on whether the Rip-Rap is exposed to clear-water or live-bed conditions.

In the case of clear-water conditions, the following failure mechanisms can occur:

1. Shear failure: This refers to the situation where the Rip-Rap stones are entrained and carried away by the flow due to shear forces.
2. Winning failure: This failure occurs when the finer bed material underlying the Rip-Rap stones is eroded by turbulence and seepage flows, leading to the displacement and removal of the stones.
3. Edge failure: This failure corresponds to scouring at the periphery of the Rip-Rap layer, which undermines the stability of the armor stones.

In live-bed conditions, the stability of the Rip-Rap layer is affected by the movement of bedforms around the pier. The migration of large dunes causes fluctuations in the bed level, which can lead to the instability and potential movement of Rip-Rap stones as they lose support from the underlying bed. There are two types of stone movement that can occur. If the trough of the bedform is deeper than the bottom of the Rip-Rap layer, the stones may be undercut and slide into the trough, possibly becoming embedded at a deeper level. Once a stone is removed, the erosion of the underlying sediment increases, making the adjacent stones more prone to movement. Alternatively, as the bedform approaches the pier, high turbulence and shear stresses are generated for short periods. This can result in Rip-Rap stones being plucked from the layer and transported downstream to the lee side of the pier.

The Figure 2.16 illustrates the potential failure mechanisms for both clear-water and live-bed conditions. It shows the regions of possible failure based on flow velocity and the median sizes of the Rip-Rap stones (D_{50}) and bed sediments (d_{50}). The (v^*) axis represents undisturbed shear velocity, (v_{cs}^*) represents the critical shear velocity for entrainment of sediment bed material, and (v_{cr}^*) represents the critical shear velocity for entrainment of Rip-Rap stones.

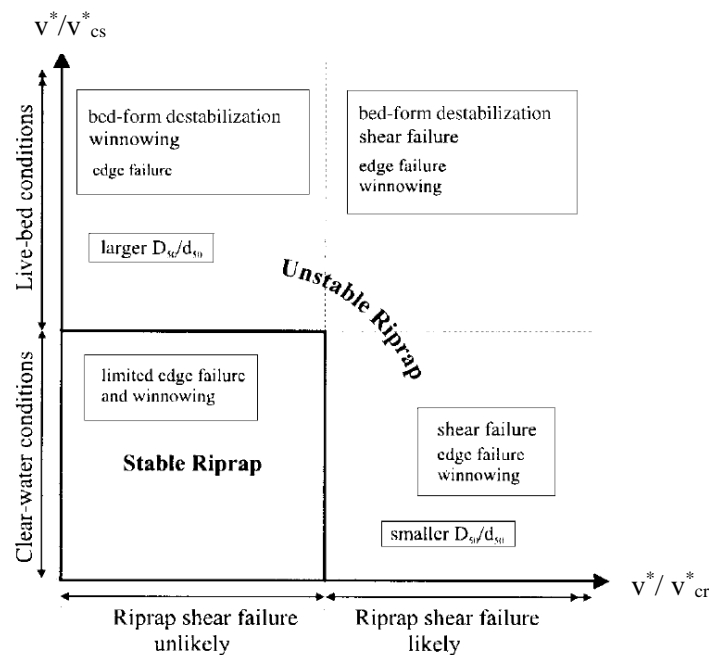


Figure 2.16. Rip-Rap failure mechanisms (Lauchlan and Melville, 2001).

Over time, the design procedures for Rip-Rap systems have evolved to incorporate the findings from various research studies. Several parameters have been identified as key influencers on the performance of Rip-Rap systems. These parameters are typically considered in the design process and include flow velocity, pier width, median grain size of the Rip-Rap stones, and median grain size of the sediments. Design procedures aim to determine the appropriate size of the Rip-Rap layer based on these parameters. However, there is still no universally accepted design approach. Different methods have been proposed, and their effectiveness may vary depending on specific conditions. In Table 2.6 of (Chiew, 1995), various design procedures are summarized, providing insights into the different approaches employed at that time. Recent research, such as the study referenced as (Lauchlan and Melville, 2001), focuses on refining the determination of the Rip-Rap layer thickness. This parameter is considered crucial as it significantly impacts the performance of the Rip-Rap system. A more precise estimation of the layer thickness can help establish the optimal design limits, ensuring better overall effectiveness and stability of the Rip-Rap system.

Method (1)	Minimum riprap size (2)	Extent of Riprap Layer		
		Length (3)	Width (4)	Thickness (5)
Gales (1938)	Not specified	$5.5b^a$	$5b$	Not specified
Bonasoundas (1973)	$D_{50}^b = 6 - 3.3U + 4U^2$ ($Ss^c = 2.65$)	$7b$, of which $2.5b$ is upstream of the upstream face of pier	$6b$	$b/3$
Neill (1973)	Presented in graphical form	Extend $1.5b$ in all directions from face of pier	Extend $1.5b$ in all directions from face of pier	$>2D_{50}$
Posey (1974)	Not specified	Extend $1.5-2.5b$ in all directions from face of pier	Extend $1.5-2.5b$ in all directions from face of pier	Not specified
Breusers et al. (1977)	$\frac{1.384U^2}{(Ss - 1)2g}$	Not specified	Not specified	Not specified
Richardson et al. (1991)	$\frac{0.692(KU)^2}{(Ss - 1)2g}$	Not specified	$2b$ from face of pier	$>3D_{50}$

Note: D_{50} is in cm; U (undisturbed mean flow velocity) is in m/s; and $K = 1.5$ for round-nose pier and $K = 1.7$ for rectangular pier.
^aPier width.
^bMedian grain size of riprap stone.
^cSpecific gravity of riprap stone.

Table 2.6. Design approaches for Rip-Rap (Chiew, 1995).

2.2.2. Wire gabion

Wire gabions, as shown in Figure 2.17, consisting of wire net baskets filled with stones, offer advantages such as flexibility, durability, permeability, and cost-effectiveness. However, limited research has been conducted on their effectiveness as an alternative to Rip-Rap in live-bed conditions. In comparison, numerous studies have been carried out in clear-water conditions, providing interesting comparisons between wire gabions and Rip-Rap systems. More research is needed to assess the performance of wire gabions in live-bed conditions and their ability to withstand erosion and provide stability.

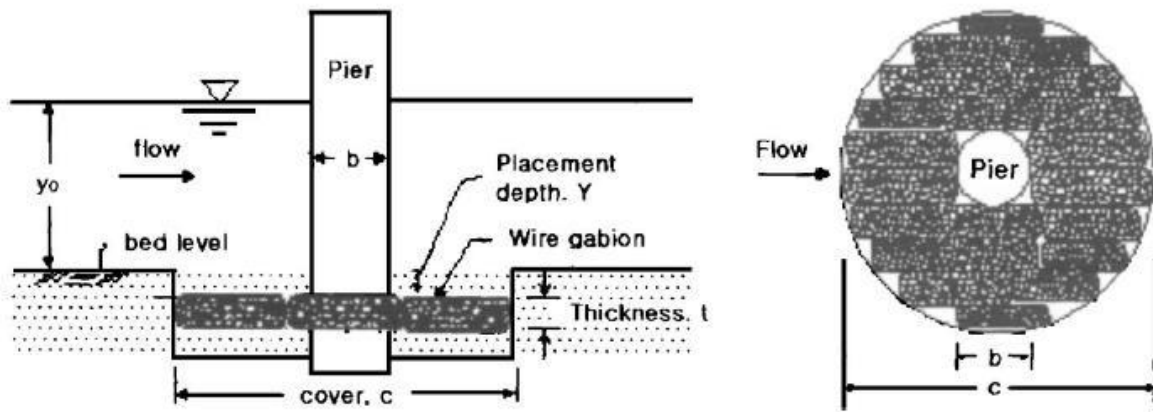


Figure 2.17. Wire gabion scheme (Yoon, 2005).

The research conducted by (Yoon, 2005) highlights leaching as a failure mechanism for wire gabions in clear-water conditions. The study demonstrates that bed sediment particles near the pier and in the upstream regions can be lifted through the interstices of the wire gabions, leading to the loss of material near the pier and causing the gabions to tilt towards it. The leached bed material is then deposited downstream beyond the coverage of the gabions. Additionally, at higher velocities, a secondary stage of failure can occur between the pier and a distance of half the pier diameter, resulting in jolted gabions. These jolted gabions can be dislodged and swept away downstream, leading to the displacement and disintegration of the gabion system.

Another factor influencing the performance of wire gabions is their classification as a coarse bed material and the potential risk of the peaking phenomenon of critical entrainment velocity. The scour depth or the ratio between critical velocities in wire gabions increases with flow depth up to a certain limit, beyond which flow depth has no influence. The peaking phenomenon, observed at depths below the limiting flow depth, is mainly attributed to the elongation of wire gabions and partly to complex flow conditions. It becomes more pronounced as the ratio of gabion length to thickness increases, contributing to improved stability.

Furthermore, the research by (Yoon, 2005) suggests that wire gabions smaller than Rip-Rap stones can provide equivalent protection. This finding implies cost-effectiveness, as a wire gabion with the same volume as a Rip-Rap stone offers higher protection, indicating improved performance. A comparison of the data from this study with Rip-Rap experiments in live-bed conditions by (Lauchlan and Melville, 2001) shows that a two-layer gabion system has higher critical entrainment velocities compared to a three-layer Rip-Rap system by approximately 30%, and higher compared to a three-layer gabion system by nearly 100%. These comparisons confirm that, under given flow conditions, wire gabions smaller than Rip-Raps can provide equivalent protection, making them a cost-effective solution. Wire gabions of the same size as Rip-Raps offer even better protection, indicating improved performance as a countermeasure for scour protection around piers.

2.2.3. Collar

A collar, as shown in Figure 2.18, is a countermeasure used to mitigate scouring around piers by diverting the downward flow. It functions as an obstruction to the flow, weakening the vortex and reducing its strength. The effectiveness of collars is influenced by their size and elevation. Specifically, decreasing the elevation of a collar enhances its efficiency as it limits

the flow penetration below the collar, leading to a weaker downward flow. Besides reducing the depth of scour, collars also help in decreasing the rate of scouring.

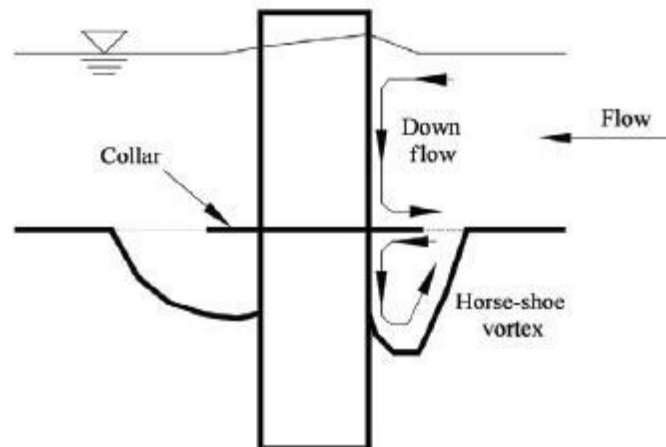


Figure 2.18. Collar scheme (Zarrati et al., 2010).

The research conducted by (Mashahir et al., 2004; Zarrati et al., 2004) demonstrates that the use of a collar not only reduces the depth of scour around bridge piers but also significantly decreases the rate of scouring. According to the study, a collar with an effective size equal to three times the diameter or width of the pier, installed at the bed level, was found to be highly effective. The results show that the scouring rate at the upstream face of the circular pier is notably slow in the initial 30 hours of the experiment. After this time period, only 30% of the maximum scouring occurred with the collar, whereas an unprotected pier experienced 98% of scouring within the same timeframe. Furthermore, the study highlights that a collar is more effective in reducing the scour rate compared to a pier foundation of similar width and elevation.

In some cases, researchers have employed a combination of different methods to protect bridge piers. For example, (Chiew, 1992) used a combination of a slot and Rip-Rap to mitigate bridge pier scouring, while (Zarrati et al., 2004) concluded that a combination of a collar and Rip-Rap could completely control the scour depth around a rectangular pier. Similarly, (Zarrati et al., 2010) studied the effectiveness of combining Rip-Rap and a collar to control local scour around cylindrical piers.

The aforementioned research sheds light on several important aspects of collars as a countermeasure for pier scour. It is observed that collars do not affect the reduction of the stable size of Rip-Rap. Consequently, collars appear to be more effective when combined with coarser Rip-Rap sizes, as they provide protection to the sides and upstream area of the pier. However, in the case of finer Rip-Rap sizes, the downstream area of the collar, subjected to wake vortices, becomes critical in terms of the removal of Rip-Rap stones. The study reveals various relationships between the parameters of both the collar and Rip-Rap systems. Lastly, the research establishes that the use of a collar reduces the extent of Rip-Rap required in the front and sides of the pier, and with collar widths double or triple the size of the pier width, the Rip-Rap volumes are respectively 31% and 57% less than those needed for an unprotected pier (Zarrati et al., 2010).

2.3. Pier scour countermeasures with Geosynthetics

2.3.1. Geosynthetics

Over time, advancements in materials technology have led to improvements in civil engineering systems for building and maintaining infrastructure. One significant innovation in this field is the development of geosynthetics, which are synthetic or natural polymeric materials used in conjunction with soil, rock, or other geotechnical materials.

Geosynthetics encompass various types such as geotextiles, geogrids, geocells, geonets, geomembranes, erosion control mats, geosynthetic clay liners, and geocomposites ([Imhof, 2004](#)). Geotextiles, in particular, find wide application in geotechnical engineering and serve functions such as separation, filtration, drainage, reinforcement, stabilization, barrier, and erosion protection.

Most geotextiles, around 98%, consist of non-degradable polymers from the polyolefin, polyester, or polyamide families. However, long-term usage of geotextiles can result in the disintegration of synthetic polymers due to environmental factors like wind, moisture, friction, and ultraviolet radiation. This can lead to the accumulation of microplastics in the surrounding environment. Additionally, geotextiles used in geotechnical engineering face complex environmental conditions, including acidic or alkaline settings, which necessitate higher performance requirements ([Wu et al., 2020](#)).

The development of geotextiles aims to achieve high performance and multifunctionality while embracing a green concept as a key factor. Recent research and development focus on utilizing natural geotextiles to replace at least 50% of synthetic geotextile applications. Furthermore, the integration of optical fiber sensors into geotextiles offers the potential for creating "intelligent geotextiles." These intelligent geotextiles can contribute to the development of monitoring systems for geotechnical structures, enabling early detection of high-risk areas prone to failure and damage ([Wu et al., 2020](#)).

Regarding the use of geosynthetics as scour countermeasures, they can be employed as layer armors. These armors consist of single elements such as permeable or impermeable mattresses or continuous blankets. Impermeable layers are acceptable when excess pore water pressure below the layer is not a concern. However, in cases where excess pore water pressure is caused by a high groundwater table compared to the surface water level or due to waves or drawdown, a permeable cover layer is recommended. Although permeable configurations may require more effort and cost, the overall benefit is positive in such cases.

When designing the armor layer of a scour countermeasure, it is essential to minimize the thickness of the layer to maximize cost-benefit ratios for certain configurations. Linear placement of geosynthetics with a minimum thickness is preferred, while ensuring the highest possible resistance against hydraulic forces. Connecting the elements of the layer can enhance its resistance. For instance, geosynthetic bags filled with sand or geosynthetic mattresses are suitable options, although the placement of mattresses without gaps can be challenging.

Complete prevention of scouring is often difficult, and small scour holes at the borders of the scour protection are sometimes unavoidable and accepted as long as they remain within acceptable thresholds. Hence, the scour protection system needs to be flexible to accommodate

changes at the edges. Rigid systems must ensure that erosion does not occur below or beside the armor layer, which can be challenging. This flexibility requirement applies to all elements of the armor layer, including the fill, filter, and armor. Figure 2.19 illustrates an example of a scour countermeasure consisting of geo-containers serving as a filter and filled with Rip-Rap as the cover layer. This system can adapt to the given geometry and withstand hydrodynamic forces ([Heibaum, 2000](#)).

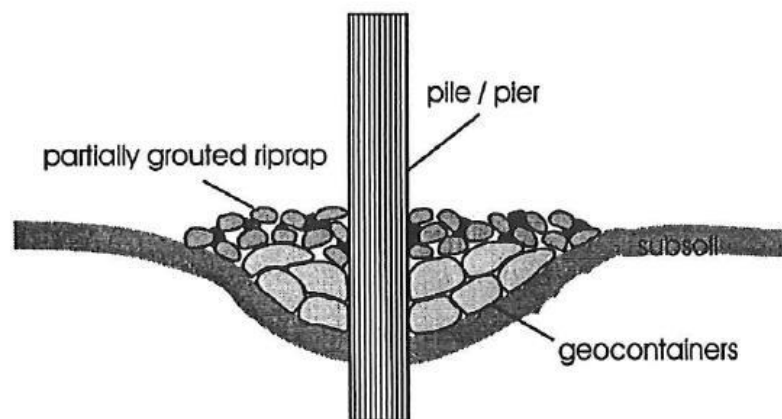


Figure 2.19. Example of flexible scour countermeasure ([Heibaum, 2000](#)).

It is important to note that each type of geosynthetic has its limitations and challenges when it comes to placement. For instance, geotextiles used as filters have a depth limitation of around 20 meters. Mattresses, on the other hand, are typically assembled in dry conditions and require specialized cranes for placement. Geosynthetic concrete mattresses can be filled on-site, but similar difficulties arise when placing the geotextile cover as with geotextile filters.

2.3.2. Pier scour protection with geosynthetics

If the anticipated development of scour exceeds an acceptable limit, countermeasures are necessary to prevent reaching this threshold. These countermeasures can be classified as either "active" measures, which reduce the action causing scour, or "passive" measures, which increase resistance to scour. Geosynthetics can play a beneficial role in both cases. However, an alternative approach is to modify the flow pattern in a way that prevents scouring. This can be achieved through river training works, which may incorporate geotextiles for functions such as filtration, reinforcement, and containment. Increasing resistance may be a more suitable solution when altering the flow pattern is not feasible or when cost comparisons favor this approach ([Heibaum, 2006](#)).

2.3.2.1. Geosynthetic containers

The primary application of geotextiles in scour protection is their use as a filter beneath an armor layer to withstand hydraulic forces. However, there are also geosynthetic solutions that do not require additional armor or provide their own armor, such as geosynthetic containers (see Figure 2.20).



Figure 2.20. Photograph of filling plant for geosynthetic containers ([Heibaum, 2006](#)).

Geosynthetic containers were developed to address the challenges of filter placement by combining filtration capabilities with sufficient weight to resist hydraulic actions. These containers are versatile and can be customized based on specific requirements such as raw material, size, shape, filtration capacity, and strength. The size of the container is chosen based on hydraulic demands and operational limitations, with larger containers being less prone to displacement.

To ensure safe placement and long-term durability, the material of the container must be carefully selected to withstand mechanical loads. This choice depends on the decision between using geosynthetic woven or nonwoven materials. Woven geosynthetics offer high tensile strength and large strain capacity, but they may be more susceptible to crack propagation if the containment is damaged. Nonwoven geosynthetics, on the other hand, have high strain capacity and can withstand impact loads by allowing for large deformations. They also provide better protection against abrasion, which is crucial when containers are used without additional armor and are exposed to sediment and bedload transport. Moreover, the fabric used in the containers should exhibit sufficient resistance to weathering, including UV radiation, especially if they are exposed to sunlight for extended periods. Modern geotextile solutions (refer to Figure 2.21), such as the Groynes in Australia, have demonstrated long-lasting performance without degradation over a period of 10 years ([Heibaum, 2006](#)).



Figure 2.21. Sea Groyne with geotextile containers ([Heibaum, 2006](#)).

Certain research studies have provided evidence supporting the effectiveness of geosynthetic containers in various applications. One such study, outlined in paper ([Korkut et al., 2007](#)), investigated the use of a geo-container system to protect bridge abutments in alluvial channels. The results indicated that geosynthetic containers show promise as an alternative to Rip-Rap systems for bridge abutment-scour countermeasures. The study emphasized the importance of connecting the geo-containers to enhance the overall system strength and prevent individual failures. Additionally, geo-containers were found to be beneficial in preventing sediment winnowing between bed-armor elements like Rip-Rap stones, offering easier placement compared to underlay cloths.

Combining different scour protection systems can yield favorable outcomes, as they can complement each other and address the limitations of individual systems. Research ([Akib et al., 2014](#)) examined the combination of geosynthetic containers and collars under clear water conditions (Figure 2.22), which is an intriguing combination as it involves both flow-altering and armoring devices.

The study focused on protecting four piers in a channel, initially employing collars made of different materials (steel, aluminum, and Perspex), as depicted in Figure 2.23, and subsequently using geosynthetic containers alone. A further improvement was achieved by simultaneously employing collars and geosynthetic containers filled with crushed concrete and palm shells (see Figure 2.23).

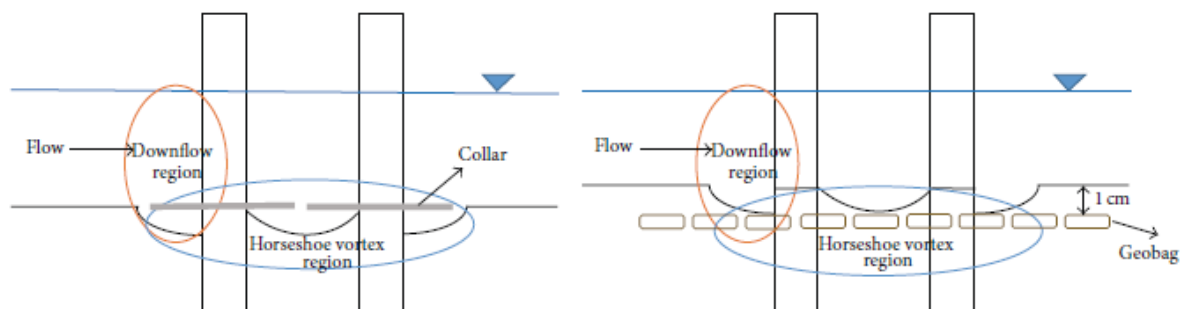


Figure 2.22. Scour around a pile protected by (left) collar and (right) geosynthetic container ([Akib et al., 2014](#)).

The collar countermeasures in the experiments involved installing collars at the sediment bed level with an effective width three times the diameter of the pier. Geosynthetic containers were also placed around the piles. The experiments were conducted over a 24-hour period, focusing on the threshold of motion of the bed material where maximum scour hole depth was expected. When collars were installed at the streambed level, no scouring or horseshoe vortex was observed at the upstream face of the piers initially. In contrast, unprotected piers experienced scouring starting downstream of the piers due to wake vortices. The scour holes then extended upstream and undermined the collars. The use of crushed concrete mixed with oil palm shells, which had greater strength and reduced voids due to improved bonding, effectively reduced scouring ([Akib et al., 2014](#)).

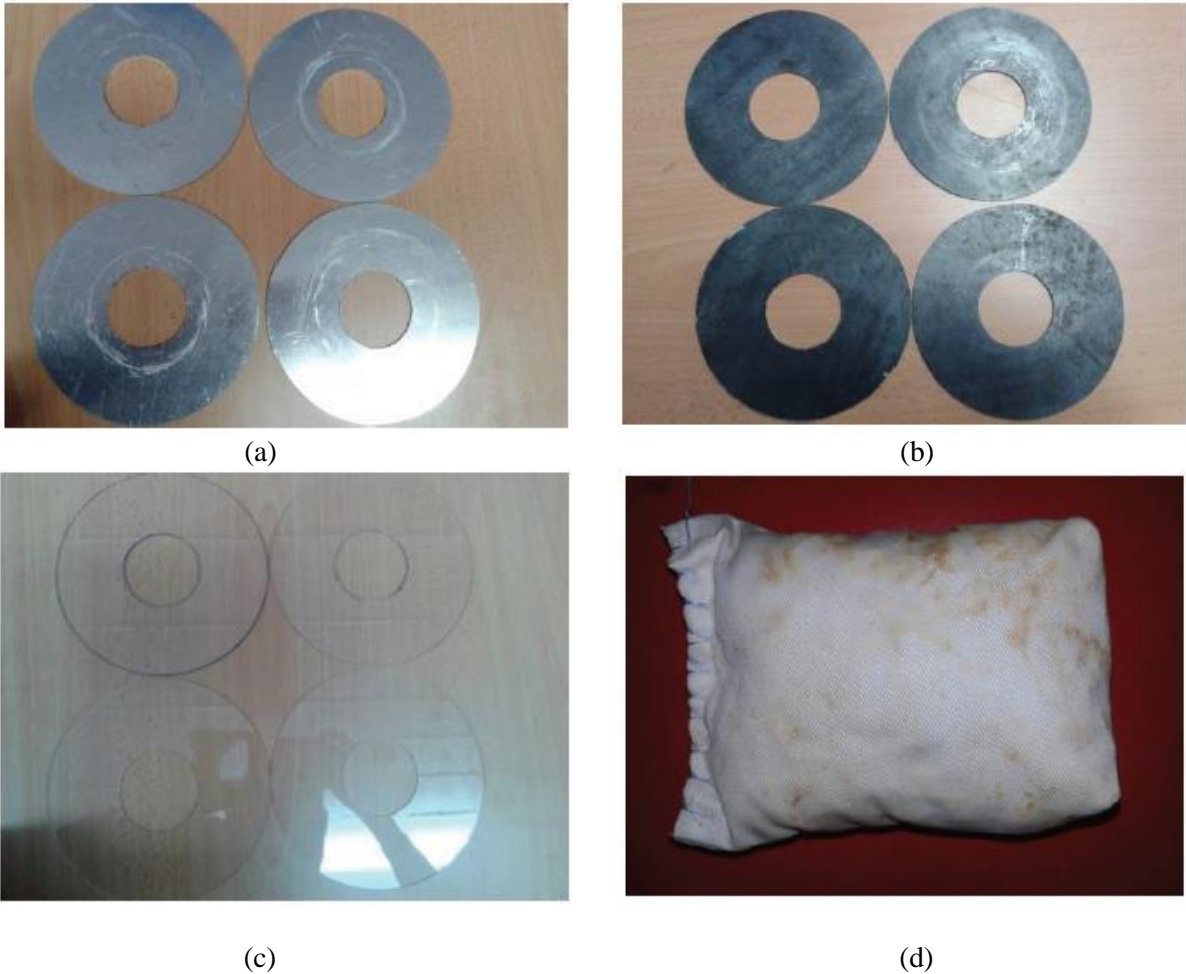


Figure 2.23. (a) Aluminium collar; (b) Steel collar; (c) Perspex collar; (d) Geocontainers with crushed concrete containing oil palm shell ([Akib et al., 2014](#)).

The Figure 2.24 illustrates the results of scour depth for different combinations of collars and protection methods, including the use of geosynthetic containers. The most effective outcome was observed when a steel collar and a geosynthetic container were employed together. The stiffness of the steel collar contributed to its rigidity, influencing the movement of the horseshoe vortex near the pile.

Additionally, the pile was shielded by a geo-container positioned 10 mm below the sediment, providing protection against scouring. Over the course of the three runs, the scour depth gradually increased, but the presence of countermeasures led to less scouring than for an unprotected pier.

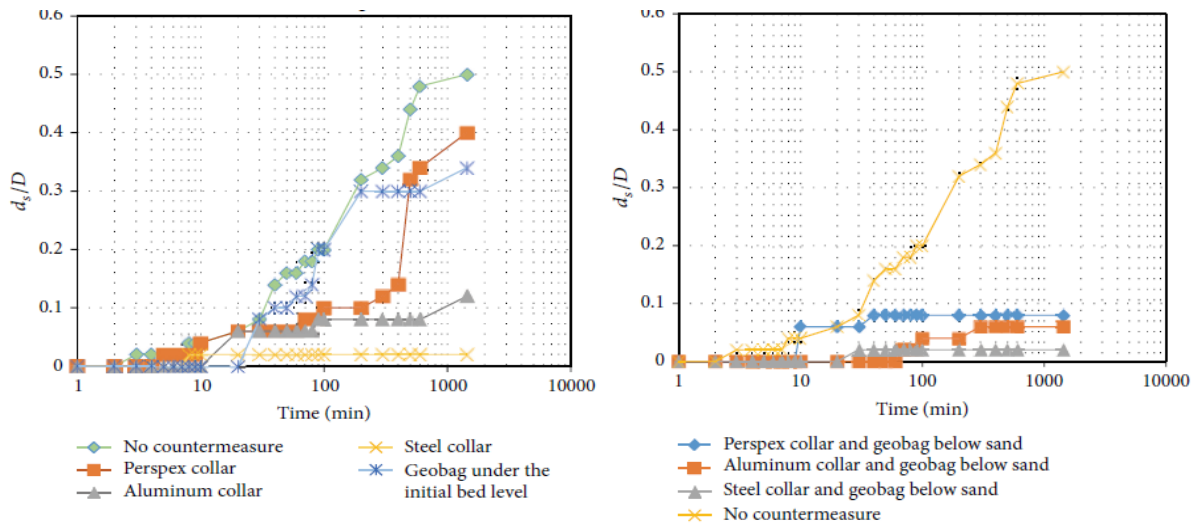


Figure 2.24. Dimensionless scour depth vs time for all the scenarios (Akib et al., 2014).

The table 2.7 presents the scour reduction achieved for the front and rear piles using different combinations of collars and geosynthetic containers as countermeasures. When a steel collar and a geo-container were combined, there was a significant 96% reduction in scouring for the rear pile, indicating the superior effectiveness of this combination compared to other countermeasures. Scouring occurred in 30 minutes for the steel collar and geo-container combination, while it took only 8 minutes for the single steel collar. The heavier and more rigid steel collar likely contributed to a weaker downflow at the upstream face of the rear pile, resulting in improved efficiency. The maximum scour depth was consistently observed at the upstream face of the front pile in all tests.

#	Type of countermeasure	Scour reduction after 24h (%)
1	None	-
2	Perspex collar	20
3	Aluminum collar	76
4	Steel collar	96
5	Geocontainers	44
6	Perspex collar and geocontainers below sediment	86
7	Aluminum collar and geocontainers below sediment	88
8	Steel collar and geocontainers below sediment	96

Table 2.7. Scour reduction scenarios (Akib et al., 2014).

Geosynthetic containers offer numerous advantages over standard engineering solutions and are suitable for various infrastructure projects. However, it is crucial to prioritize environmentally friendly practices and seek continuous improvement in these systems. Research conducted by (Akib et al., 2012) focused on assessing the use of fine and coarse crushed recycled concrete as fillers in geo-containers, replacing sand fillers and promoting green technologies. The experiments aimed to investigate the potential of these eco-friendly solutions in reducing scour impact on piers of skewed integral bridges during flooding conditions.

The analysis of the research results demonstrated that the ability to decrease scour depth was not affected, and the protective trend remained consistent with geo-containers. Lower velocities were found to be more effective in reducing scour depth, while higher velocities decreased their effectiveness. The experiments revealed that finer mixtures of crushed concrete exhibited greater flexibility, whereas coarse crushed recycled concrete resulted in slower scour rates (see Figure 2.25). By utilizing crushed concrete derived from recycled sources, these

findings highlight an environmentally friendly, cost-effective, and efficient solution for designing scour protection. Moreover, such an approach can contribute to waste management and create economic benefits by repurposing waste materials.



Figure 2.25. Geocontainers with fine crushed concrete and coarse crushed concrete ([Akib et al., 2012](#)).

2.3.2.2. Armed soil by geotextile

In addition to previous methods, recent research ([Nouri Imanzadehei et al., 2016](#)) has explored the effectiveness of geotextile layers in reducing local scour depth around a cylindrical single pier under clear water conditions.

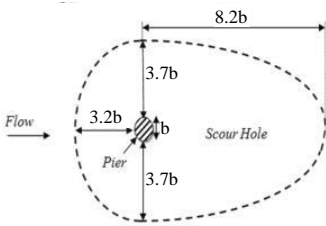
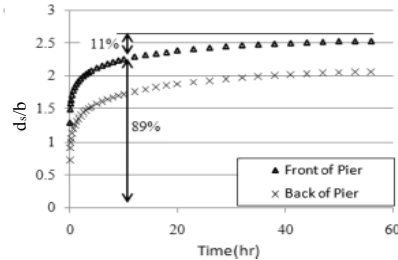
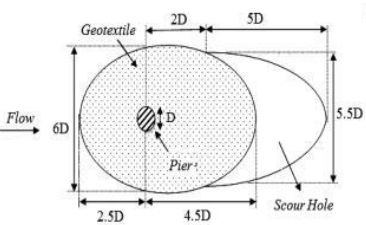
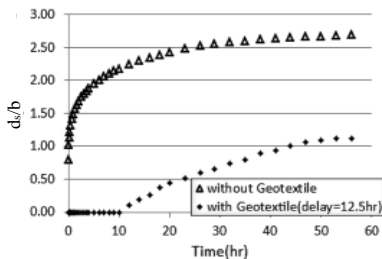
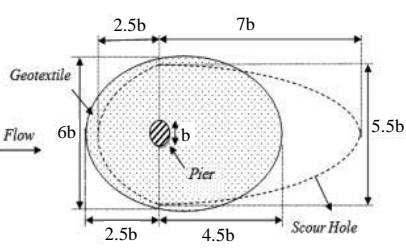
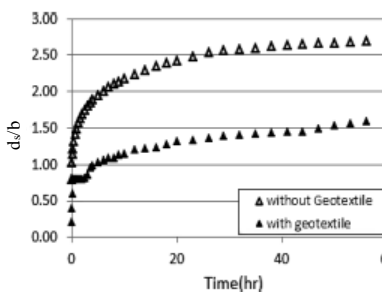
The experiment consisted of ten runs, each lasting 56 hours, with a critical velocity ratio (v/v_c) of 0.93. The sizes of the geotextile layers used in the experiment were based on patterns suggested by previous studies on Rip-Rap conducted by ([Gales and Bell, 1938](#)), ([Bonasoundas, 1973](#)), and ([Neill, 1973](#)). Tables 2.8 summarize the tests, providing information on the layer sizes, scour hole size, and the development of scour depth over time. It's important to note that in all the protected tests, the reported scour depth corresponds to the deepest point in the scour hole, rather than the scour depth in front of the pier, as observed in other research studies.

For instance, in Test 1, the change in scour depth after 8 hours was minimal. The maximum scour depth observed in front of the pier was 11.9 cm, which is approximately 2.6 times the pier diameter. Previous research by ([Ghorbani and Kells, 2008](#)) indicated that more than 70% of the scour occurs within the first 7 hours of testing. In this particular case, over 75% of the scour had occurred within the first 8 hours.

It is worth noting that tests 2, 4, and 5 were conducted with geotextile layers sized according to the referenced studies ([Gales and Bell, 1938](#)), ([Bonasoundas, 1973](#)), and ([Neill, 1973](#)). Test 3 used the same geotextile layer as test 2, but it was positioned at a depth of 0.8b (0.8 times the diameter of the pier), which corresponds to a placement 4 cm below the initial bed level. Only one test was conducted with this condition, even though it was performed for the other references as well.

All the tests exhibited similar behavior, with a rapid scouring rate observed until reaching the level of the geotextile layer. After reaching this level, the scour rate decreased, as depicted in the scour depth vs. time graph, where there was no delay compared to the other tests. Additionally, all the other tests were conducted with only a 2 mm cover.

Moreover, no scouring occurred in front of or at the sides of the pier during any of the tests, as it occurred in the downstream, which led the researchers to focus on reducing the extent of the scour hole. Tests 6 and 7 represent an optimization process based on trial and error, where the size of the geotextile layer was optimized (oval-shaped) in terms of its efficiency in reducing the scour hole. As a result, the geotextile layer in test 7 successfully reduced the scour depth and shifted the location of scouring 5.5 times the diameter of the pier downstream. The geotextile layer demonstrated its ability to reinforce scour protection by strengthening the bed and altering the flow pattern.

#	Layer size/scour hole size	Depth scour vs time
1		
2		
3		

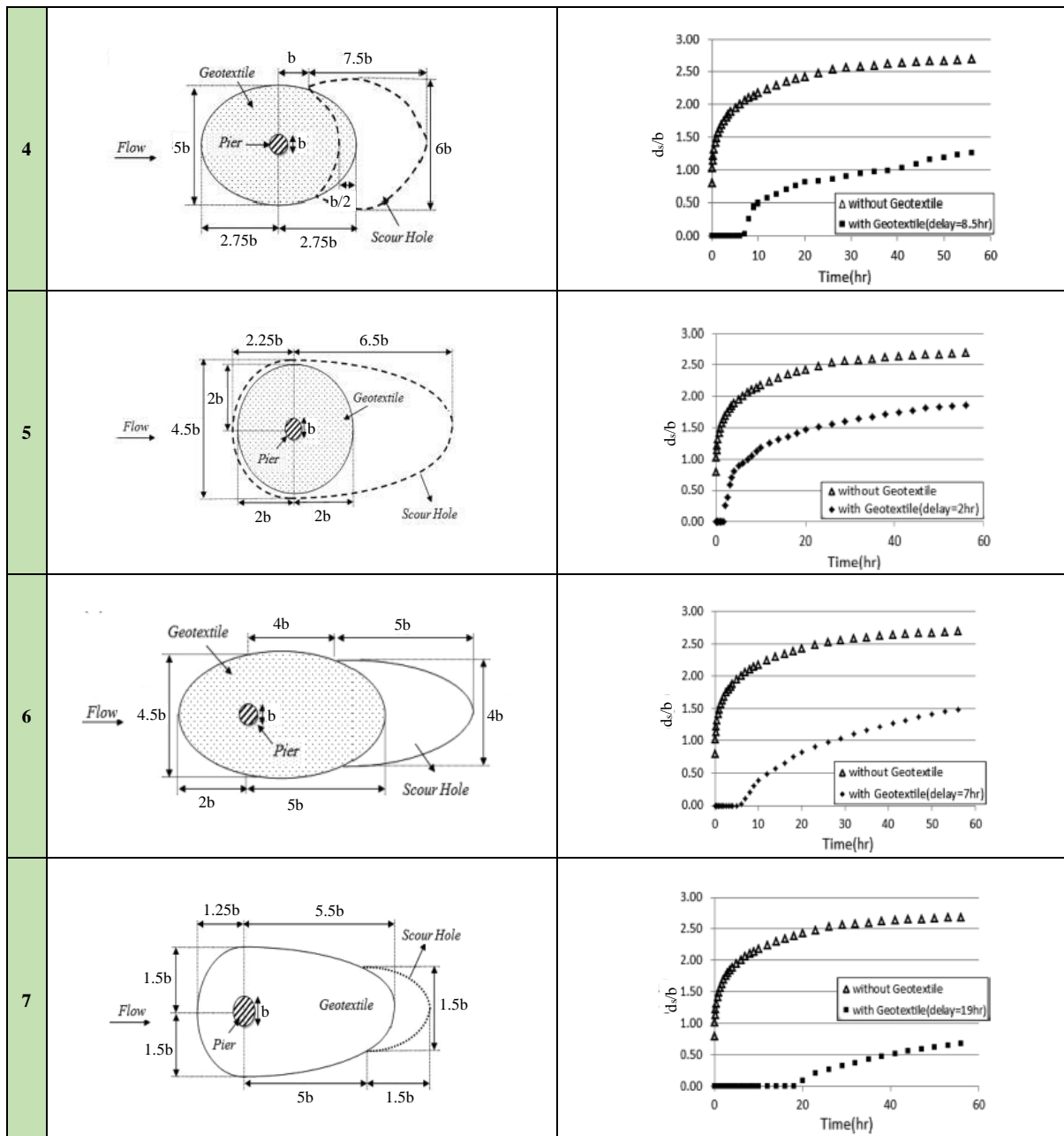


Table 2.8. Geotextile layer sizes and scour holes (Nouri Imamzadehei et al., 2016).

Figure 2.26 presents a summary of the scour depth results over time and highlights the suggested pattern as the most effective arrangement, with a delay of 19 hours before the first signs of scouring appear at the downstream edges. Additionally, another notable finding is that the circular pattern, although it serves as a coverage system, proved to be less suitable due to the intense vortex formation behind the pier. The circular layer of geotextile can be considered as an alternative to the collar system, and further studies are recommended to compare their performance.

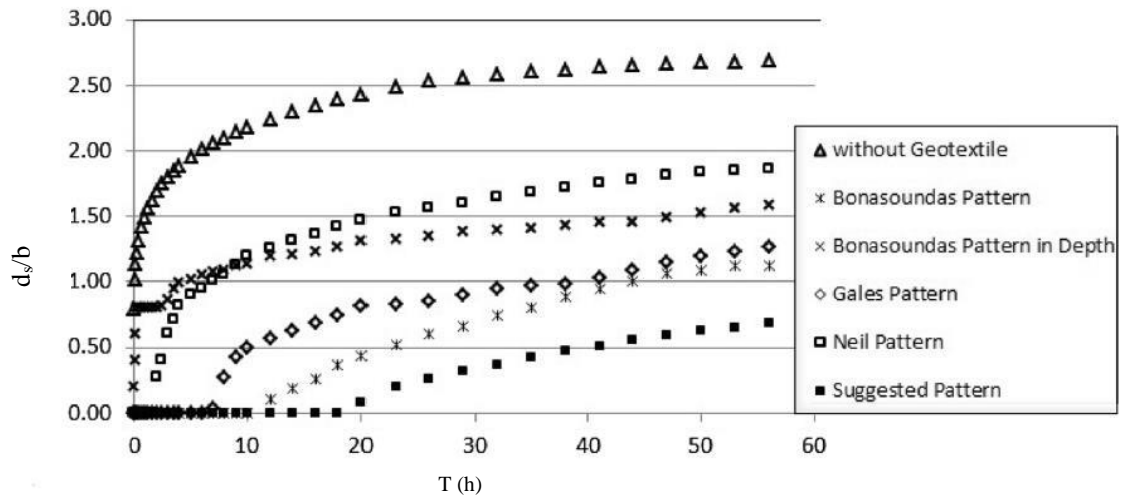


Figure 2.26. Scour depth vs time-geotextile layer system (Nouri Imamzadehei et al., 2016).

Chapter 3

Laboratory description

The research conducted in this study took place at the Hydraulic Lab G. Fantoli, situated in the 4A Building within the Leonardo Campus of the Politecnico di Milano in Milan, Italy that shown in Figure 3.1.

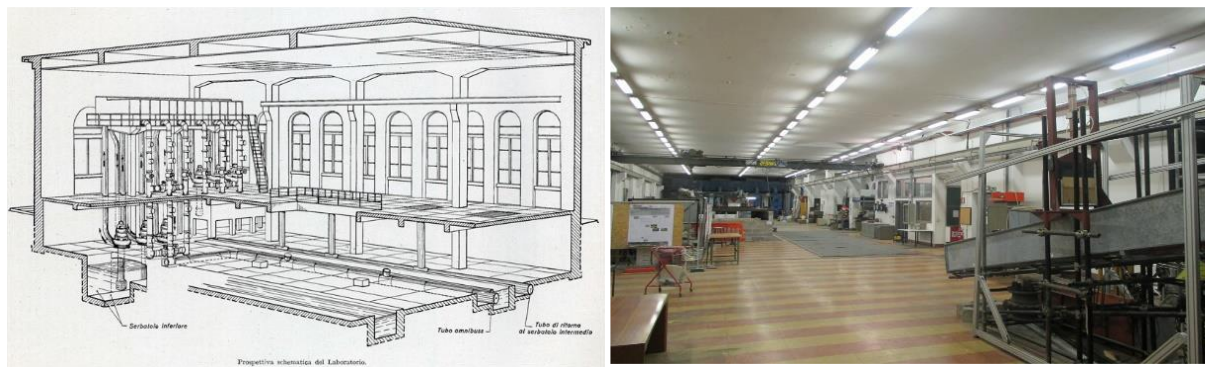


Figure 3.1. Hydraulics laboratory.

3.1. Experimental facilities and measuring equipment

The transparent flume (Figure 3.2(a)) with a rectangular section was utilized for conducting the experiments. The channel had specific dimensions, including a length of 5.8 meters, a width of 0.40 meters, and a height of 0.16 meters. Steel clamps were used to maintain the desired width of the channel, as depicted in Figure 3.2(b).

In the final segment of the channel, there exists a recessed section measuring 2 meters in length. To conduct scour runs in this area, a telescopic pier was utilized which was positioned at the channel axis, precisely 450 centimetres from the inlet. The outer part of the pier comprised a PVC pipe with internal and external diameters of 0.06 meters and 0.063 meters, respectively. The inner part consisted of a Plexiglas cylindrical bar that could slide within the outer pipe which is illustrated in Figure 3.3. This design allowed for simulating the presence of piles within the channel and assessing sediment behaviour around them.



(a)



(b)

Figure 3.2. (a) Experimental flume; (b) Experimental channel.

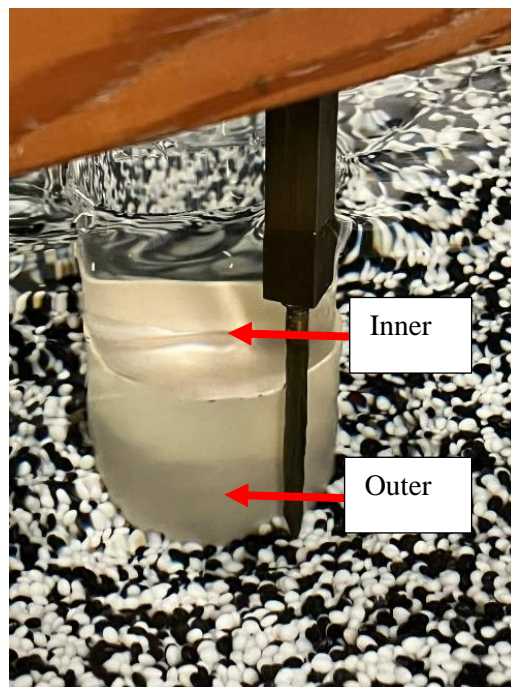


Figure 3.3. Inner and outer part of the Pier.

The experimental facilities employed in this study are capable of replicating both live-bed scour conditions and clear-water conditions.

The accompanying figure 3.4 illustrates a schematic depiction of the arrangement of all components installed in the facilities, specifically designed to operate under clear water and live bed conditions.

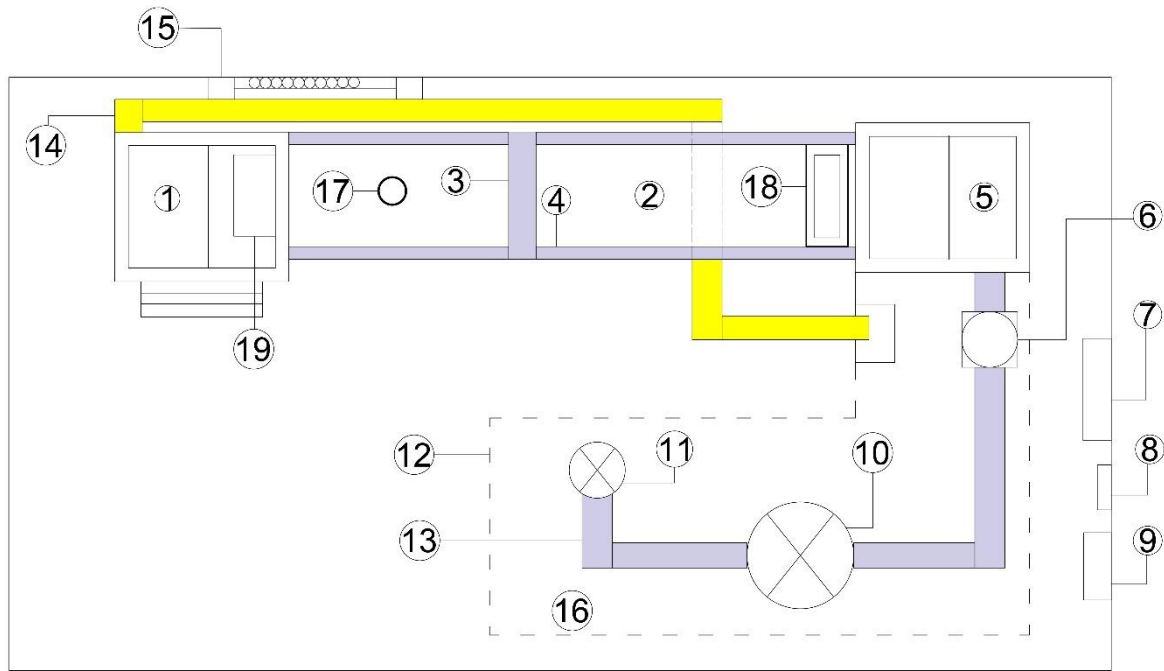


Figure 3.4. Plan view of experimental facilities.

1. The outlet tank
2. A rectangular duct (channel)
3. Transverse positioning system (not utilized in the present study)
4. Longitudinal positioning system (roller)
5. The inlet tank
6. Magnetic flow meter device
7. Hopper operator and time controller (not utilized in the present study)
8. Magnetic flow meter reader
9. Electric power controller
10. Main-stream valve
11. By-pass valve
12. Pumping and water discharge control unit.
13. Inlet-Pipe
14. Outlet plastic pipe to recirculate water
15. Gauges and piezometers (not utilized in the present study)
16. Underground water storage
17. Cylindrical pier.
18. Hopper for sediment feeding (not utilized in the present study)
19. Sediment's trap basket/sticks as boundary condition

3.1.1. Water circulation components

The measurement of flow rate Q is accomplished through the utilization of an electromagnetic flowmeter positioned on the supply pipe responsible for releasing water into the upstream tank. The entrance to the channel is rounded, and the initial section spanning 0.3 meters is equipped with a flow straightener, composed of an arrangement of pipes with a diameter of 1.6 cm.

The inlet units, depicted in figures 3.5 comprise an underground storage tank that serves as the source of discharged flow to the inlet tank. This flow is facilitated by a submerged pump connected to a steel pipe with a diameter of 15 cm, which includes a control valve regulating the discharge into the inlet tank. In the event that the submerged pump is operational, but the primary pipe valve does not permit flow passage, an auxiliary pipe is connected with a control valve to redirect excess flow back to the underground storage tank.



(a)



(b)



(c)

Figure 3.5. (a) Inlet pipes' connection; (b) Inlet tank; (c) Channel's inlet straightener pipes.

The operation of the magnetic flowmeter relies on the application of a magnetic field to the metering tube, generating a potential difference that is directly proportional to the velocity of flow perpendicular to the magnetic flux lines. This process is governed by the principle of electromagnetic induction. To measure and present the discharge, the magnetic flow meter consists of two components: the measuring device and the reader. These components are depicted in figure 3.6.

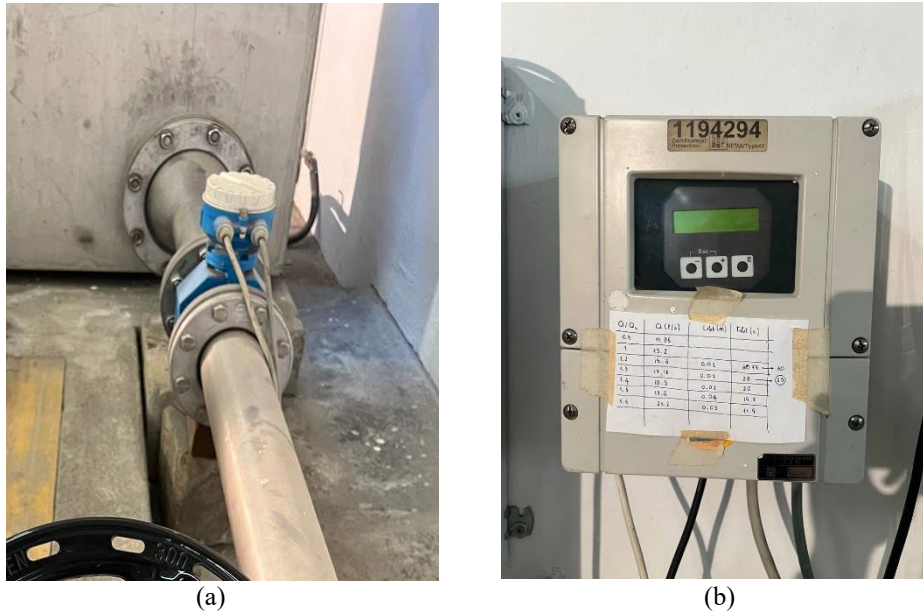


Figure 3.6. (a) Flow meter device; (b) Flow meter reader.

Figure 3.7 illustrates the presence of two control valves on the inlet and by-pass pipes. The primary control valve regulates the flow of discharge from the submerged pump to the inlet tank. Conversely, the other valve is positioned on the by-pass pipe and serves the purpose of preventing the supply of water to the inlet tank while the pump is operational, if such a situation is desired.



Figure 3.7. Control valves.

In the downstream section of the channel, an outflow tank is strategically positioned to capture sediment particles that are discharged from the channel and facilitate the recycling of water flow back into the underground storage tank that is illustrated in figure 3.8(a). The tank is divided into two compartments by a vertical metal sheet.

For each selected scour condition, the experimental facilities were modified or eliminated accordingly. In the case of the clear-water condition, the channel only needed a set of sticks placed as boundary conditions at the entrance of the outlet tank to regulate the water depth, as depicted in Figure 3.8(b).



(a)



(b)

Figure 3.8. (a) Outlet tank; (b) Series of sticks as boundary condition.

In the second part of the tank, the water is recirculated through a plastic pipe with a diameter of 200 mm, directing it back to the storage tank. From there, the water is pumped back into the system via the inlet tank. To ensure proper water level control downstream of the weir and to facilitate system drainage during shutdowns, a control valve with a diameter of 40 mm is installed at the outlet of the tank.

3.1.2. Scour measuring tool and its accuracy

Bed level measurements were performed manually using a point gauge, as illustrated in Figure 3.9, with the support of a transverse mechanism. The accuracy of these measurements was maintained at 0.5 mm.



Figure 3.9. Point gauge & transversal support.

3.1.3. Sediment particles' properties

The sediment used in this work was made of Polybutylene Terephthalate (PBT). Uniform, quasi spherical particles with an aspect ratio of 2 were used. Sediment' properties are listed in Table 3.1.

Sediment Properties	
Δ	0.27
d (m)	0.003
W_g (m ³)	1.41372E-08

Table 3.1. Sediment properties.

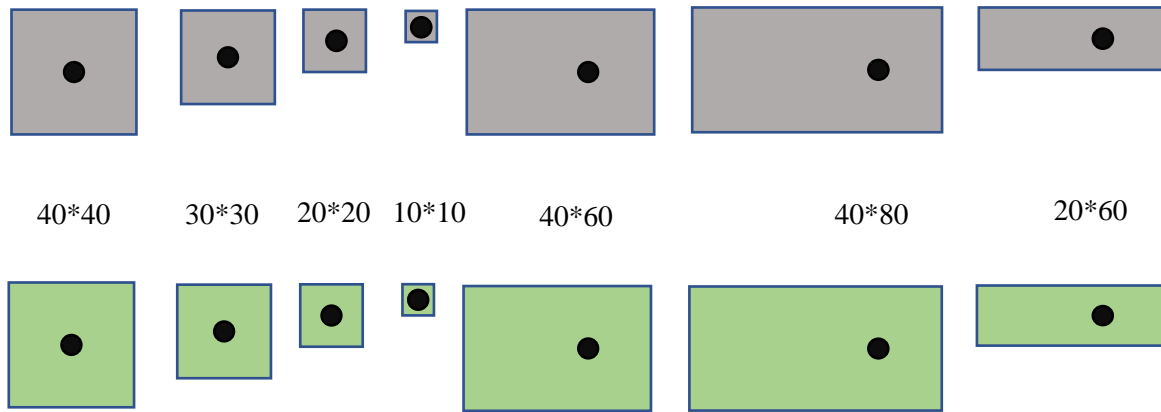
3.2. Geo-Carpets properties

3.2.1. Utilized Carpets

Different combinations of carpets were tested along the flume, including square-shaped and extended forms, as depicted in Figure 3.10. While all series of the experiments followed the same coverage areas, there were slight deviations in the selection of extended nets' coverage areas for the coarse flexible geo-carpets due to limited material availability. However, efforts were made to align the coverage area of the extended coarse flexible nets as closely as possible with those used in other series of experiments.

To create the desired coverage areas for the coarse flexible geo-carpets, except for the 20 cm by 20 cm and 10 cm by 10 cm nets, additional attachments were used. These attachments involved utilizing thread and sewing techniques to connect smaller pieces, thus achieving the intended configurations.

Rigid Configurations:



Flexible Configurations:

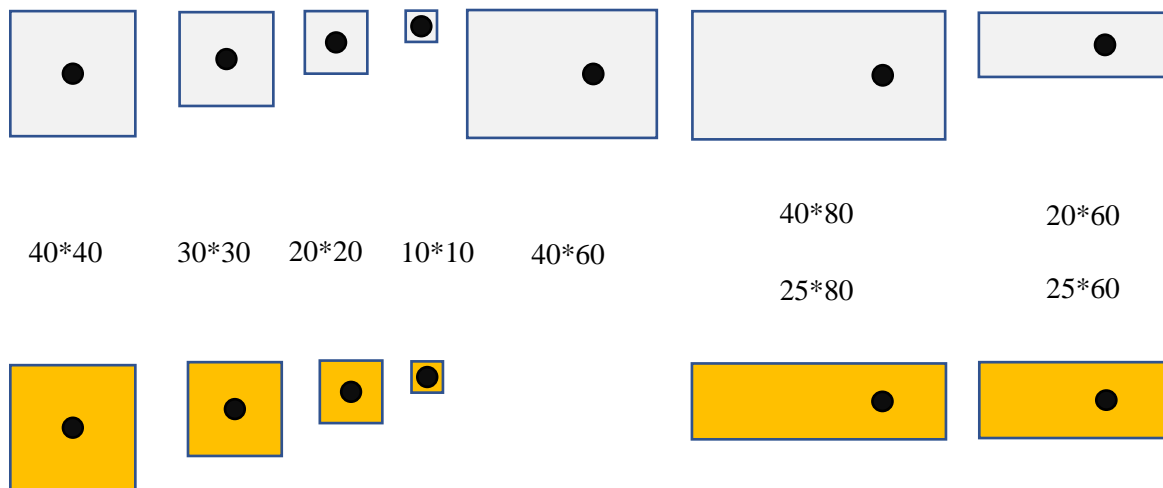


Figure 3.10. Nets' configuration.

In the experimentation process, two distinct materials, flexible and rigid, were utilized, and they were further classified into coarse and fine categories. These materials were employed with three different mesh sizes. Figure 3.11 illustrates this categorization.

For both rigid and flexible geo-carpets, a mesh size of 10 mm was chosen, as depicted in Figure 3.11(a) and (b) respectively. Additionally, a mesh size of 5 mm was considered as the fine rigid mesh, shown in Figure 3.11(c). However, due to the unavailability of this specific mesh size for the flexible nets in the market, a mesh size of 7 mm was adopted for the fine flexible geo-carpets, as depicted in Figure 3.11(d).

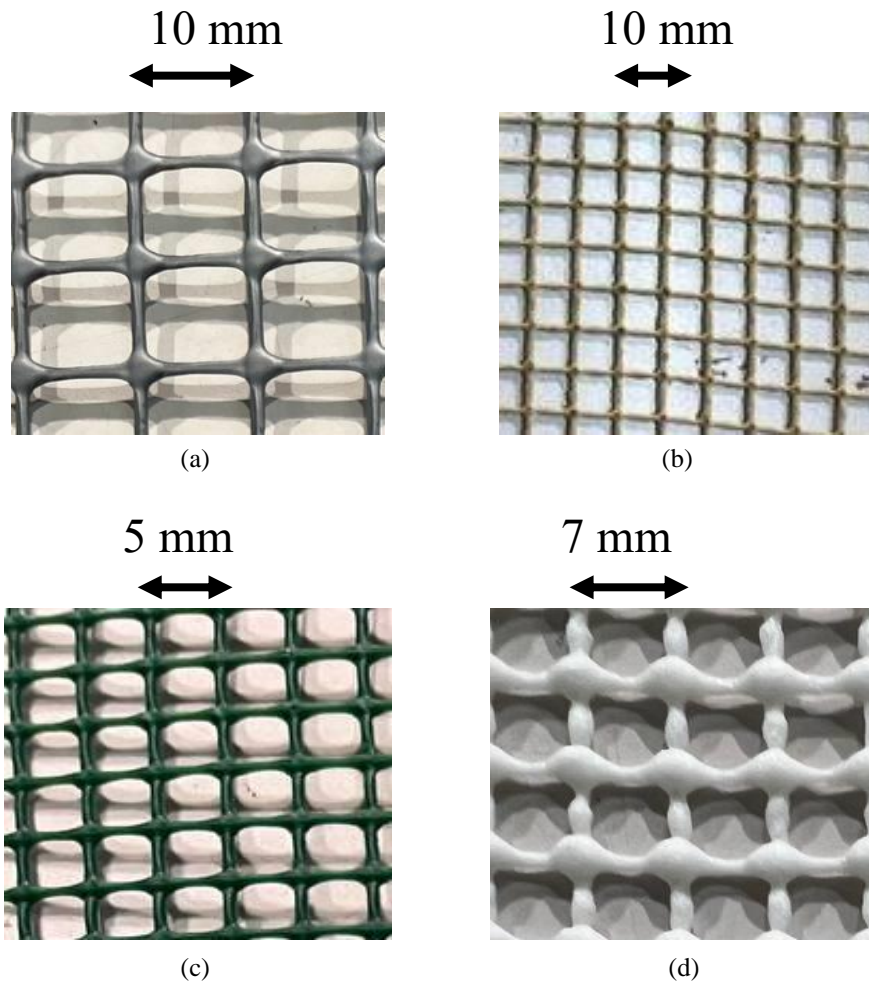


Figure 3.11. The mesh size of the geo-carpets: (a) & (b) coarse; (c) & (d) fine. The material of the geo-carpets: (a) & (c) rigid; (b) & (d) flexible.

3.2.2. Weight of Carpets

Rigid Coarse Mesh		
	Net Size	Weight (kg)
1	10*10	0.002
2	20*20	0.009
3	30*30	0.02
4	40*40	0.036
5	40*60	0.052
6	40*80	0.072
7	20*60	0.024
Rigid Fine Mesh		
	Net Size	Weight (kg)
1	10*10	0.002
2	20*20	0.011
3	30*30	0.024
4	40*40	0.042
5	40*60	0.062
6	40*80	0.084
7	20*60	0.033

Flexible Coarse Mesh		
	Net Size	Weight (kg)
1	10*10	0.002
2	20*20	0.008
3	30*30	0.018
4	40*40	0.034
5	25*60	0.032
6	25*80	0.042
Flexible Fine Mesh		
	Net Size	Weight (kg)
1	10*10	0.002
2	20*20	0.008
3	30*30	0.018
4	40*40	0.032
5	40*60	0.047
6	40*80	0.064
7	20*60	0.025

Table 3.2. Weight of different size of carpets.

3.2.3. Density test

A density test was conducted to examine the relationship between the density of various geo-carpets and water. The aim was to compare the densities of different materials by immersing nets in water and determining whether they would sink or float. This provided insights into the relative densities of the materials. The results indicated that the density of water was higher than that of the tested materials, resulting in all the geo-carpets floating on the water, as shown in Figure 3.12. Furthermore, the floating velocities of the nets were compared to gain a deeper understanding. Through careful analysis, it was observed that the flexible nets had a lower density compared to the rigid nets, as evidenced by their faster ascent to the water's surface.

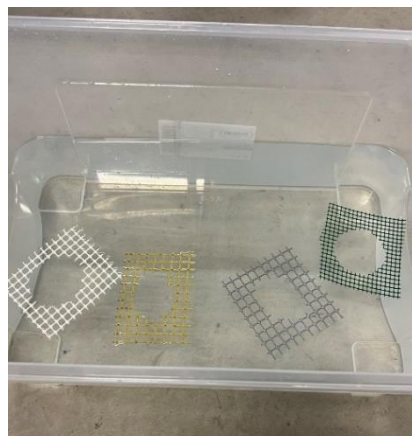


Figure 3.12. Density test.

3.3. Experimental Campaign

Initially, threshold conditions for bed load incipient motion have been defined. Then, setting up two experiments to explore the occurrence of clear-water pier scour. Following that, further experiments were conducted using geo-carpets as protective measures to reduce scouring around piers and determine the optimal solution.

3.3.1. Threshold conditions and calibration

In the initial phase of this study, a preliminary test was conducted to determine the appropriate discharge flow for the experimental campaign, the definition proposed by ([Radice and Ballio, 2008](#)). This definition establishes a relationship between the incipient motion and a dimensionless sediment transport rate per unit width. To put this definition into practical use, an experimental test was conducted to measure the motion of sediment at various flow discharges.

Table 3.3 presents the measurements of the number of particles, water discharge, and their corresponding mean values, which are crucial for calculating the reference water discharge. To determine the discharge value to be used in the experimental campaign, the number of particles in motion was counted at two specific zones along the channel (Upstream & Downstream) the position of zones is illustrated in Figure 3.13. The graphically represented outcome is depicted in the Figure 3.14.



Figure 3.13. Position of the plates, sediments passing over them.

#	Discharge (l/s)											
1	6.400	6.639	7.209	8.009	8.263	7.646	7.504	7.066	6.795	6.789	7.289	8.271
2	6.376	6.670	7.411	7.940	8.391	7.707	7.477	7.007	6.736	6.812	7.282	8.285
3	6.389	6.682	7.346	7.978	8.340	7.784	7.432	7.093	6.628	6.814	7.265	8.277
4	6.198	6.674	7.307	8.016	8.349	7.771	7.405	7.112	6.506	6.844	7.277	8.285
5	6.336	6.655	7.314	7.934	8.451	7.820	7.566	7.058	6.621	6.822	7.224	8.194

6	6.406	6.820	7.293	7.922	8.391	7.884	7.508	6.999	6.603	6.847	7.215	8.329
7	6.298	6.743	7.336	7.977	8.278	7.627	7.518	6.989	6.520	6.759	7.291	8.233
8	6.265	6.599	7.293	8.006	8.311	7.667	7.408	7.008	6.532	6.770	7.235	8.278
9	6.241	6.544	7.311	7.864	8.526	7.721	7.446	7.036	6.525	6.920	7.211	8.302
10	6.369	6.669	7.255	8.041	8.405	7.744	7.551	7.154	6.516	6.830	7.221	8.311
mean	6.328	6.670	7.308	7.969	8.371	7.737	7.482	7.052	6.598	6.821	7.251	8.277
Number of Particles (Upstream)	0	4	1	17	146	33	20	3	1	2	2	192
Number of Particles (Downstream)	0	0	5	46	132	23	10	2	1	0	5	140
Mean	0	2	3	31.5	139	28	15	2.5	1	1	3.5	166

Table 3.3. Measurements of the number of particles.

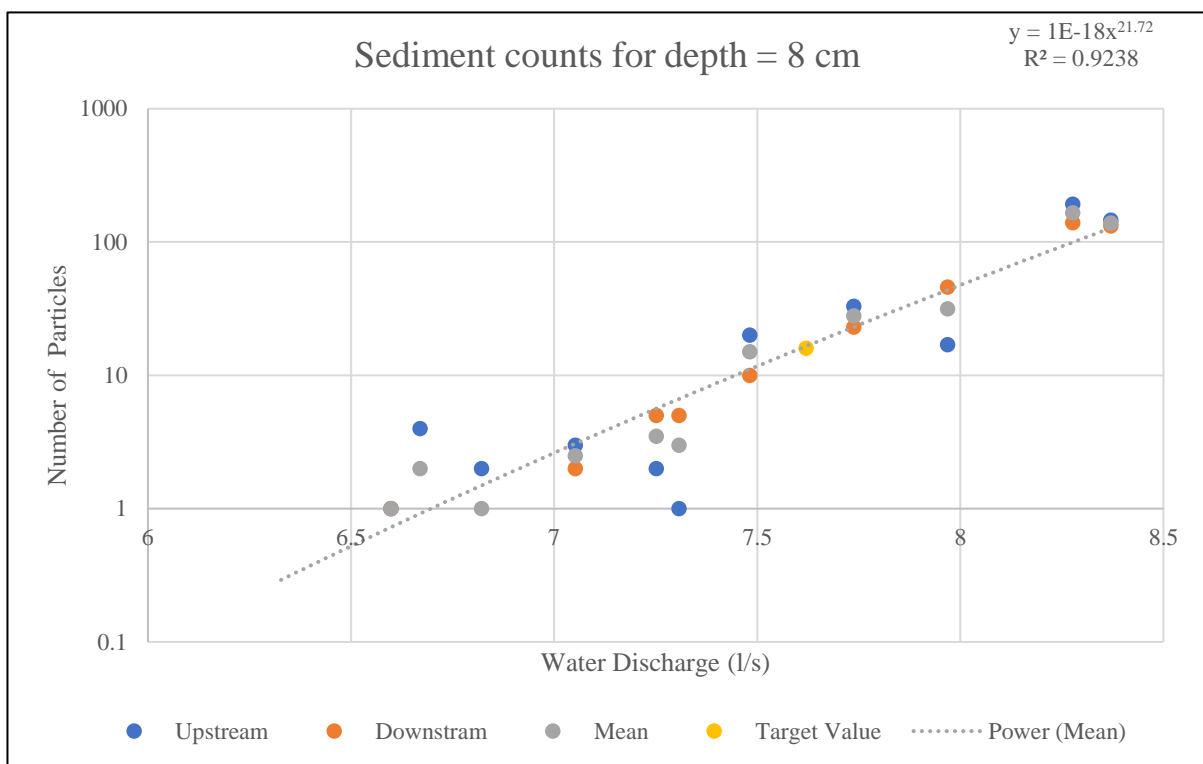


Figure 3.14. Representation of experimental results.

By applying the threshold conditions specified in Table 3.4 to Equation (3.1) and utilizing the data obtained during the preliminary test (refer to Table 3.3), it was established that a water discharge of 7.62 l/s was necessary to maintain a constant count of 16 particles passing over the plate within 180 s.

where:

q_s = Sediment transport rate per unit width,

B = Width of the plate,

T = Duration of each preliminary test

$$N = \frac{q_s \cdot S \cdot T}{w_g} \quad (3.1)$$

Threshold Conditions	
Φ	0.000056
q_s (m ² /s)	1.49757E-08
S (m)	0.085
T (s)	180
N	16

Table 3.4. Threshold conditions.

As noted by (Melville, 1984), the maximum scour depth occurs at the critical flow rate, where our critical discharge has been captured 7.62 l/s, in order to minimize upstream bed disturbances while remaining close to the critical flow rate and maximum scour depth, the obtained critical flowrate (7.62 l/s) was multiplied by a factor of 0.95. It is common practice to conduct experiments with a discharge of 0.9 or 0.95. Consequently, the final water discharge for the present study was determined to be 7.25 l/s.

3.3.2. Experimental set up, procedure, and methods of data acquisition

In the following illustration (Figure 3.15), a schematic representation of the experimental setup is provided, depicting the surveyed area where all measurements have been done before, during, and after the experiments.

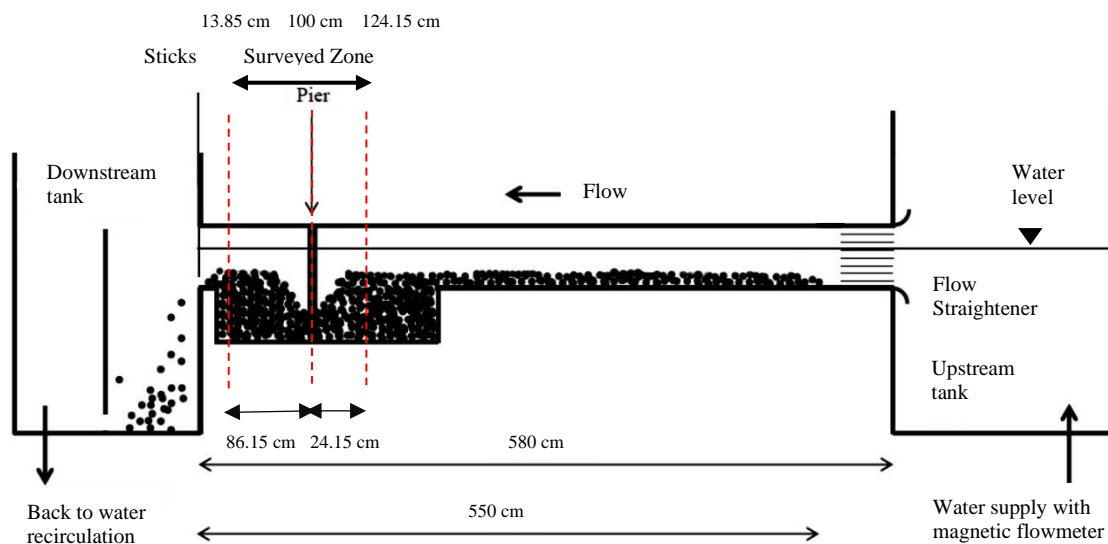


Figure 3.15. Schematic representation of the flume (specified surveyed zone).

The experimental workflow followed a methodical approach:

- Initially, a preliminary test was conducted to obtain the appropriate discharge, as explained thoroughly in the previous section.

- Subsequently, two unprotected tests have been carried out with different durations, 3-hour and 6-hour, the initial test sought to validate the repeatability of the subsequent test, which spanned a duration of three hours, the second test, lasting six hours, was specifically designated to be completed within a single day, as the reference test for this study. Notably, these two unprotected experiments also served the additional purpose of validating a novel scour predictor put forth by ([Franzetti et al., 2022](#)).
- Ultimately, 27 experiments have been accomplished, utilizing different geo-carpets, in order to find the proper solution.

Overall, the experimental workflow adhered to a systematic and rigorous approach, considering multiple factors such as coverage area, mesh size, and material properties of the geo-carpets. This meticulous approach facilitated a comprehensive evaluation of the countermeasure's effectiveness and provided valuable insights into the response of the geo-carpets under varying conditions.

The overall experimental procedure:

Prior to commencing each experiment, several preparatory steps are undertaken to ensure the proper setup of the flume. A specialized tool, depicted in Figure 3.16, is utilized to level the bed, and establish an initial bed profile characterized by uniformity. This meticulous preparation guarantees a consistent starting point for the test, enabling the identification of any significant changes throughout the experiment.

Additionally, it is worth noting that prior to the initiation of each test, a precautionary measure is implemented. A manual application of water, facilitated by a dedicated tool (refer to Figure 3.17), is carried out to prevent sediment suspension and the undesired floating of particles when the water gradually enters the channel.



Figure 3.16. Bed-straightening tools.



Figure 3.17. Spray tool.

The desired coverage area of the net was extracted from the available materials. To ensure the stability and secure fixation of the carpet on the channel's bed, a practical method utilizing nails was employed. These nails were specifically selected for their characteristics, measuring 3 cm in width and 12 cm in length, as illustrated in Figure 3.18.

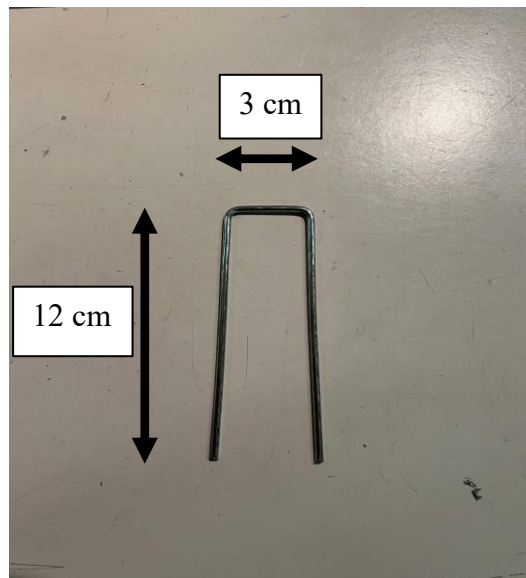


Figure 3.18. The sample nail utilized as anchorage.

To effectively secure the carpet, a systematic approach was followed. Four nails were consistently used around the pier to create a robust anchorage, strategically positioned to prevent any movement or displacement of the carpet, as it shown in Figure 3.19(a). By firmly fixing the carpet with these nails, its stability was ensured.

In addition to the area around the pier, careful attention was given to securing the border of the nets to the channel bed. The number of nails used varied depending on the size and dimensions of the nets, and their spacing was determined based on the specific requirements of each net. This tailored arrangement of nails provided optimal support and stability for the nets. An example of this nail positioning can be observed in Figure 3.19(b).

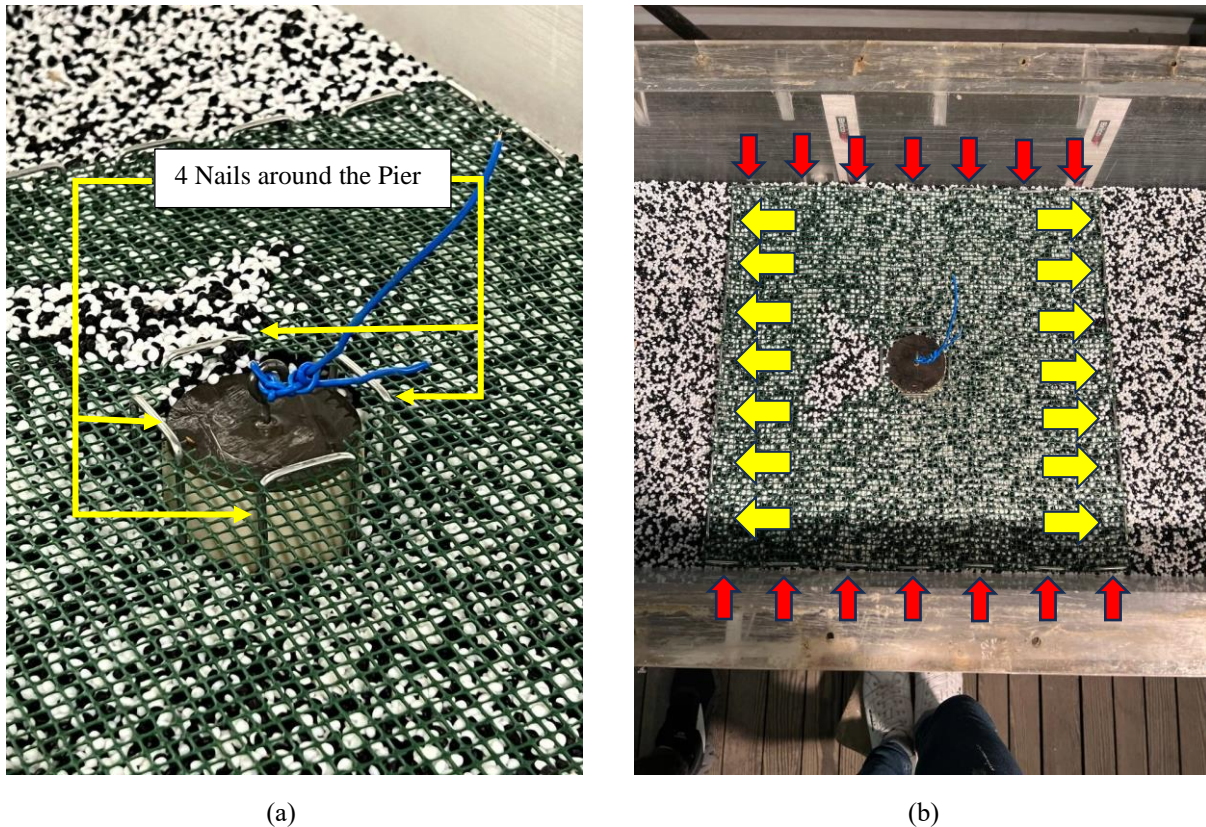


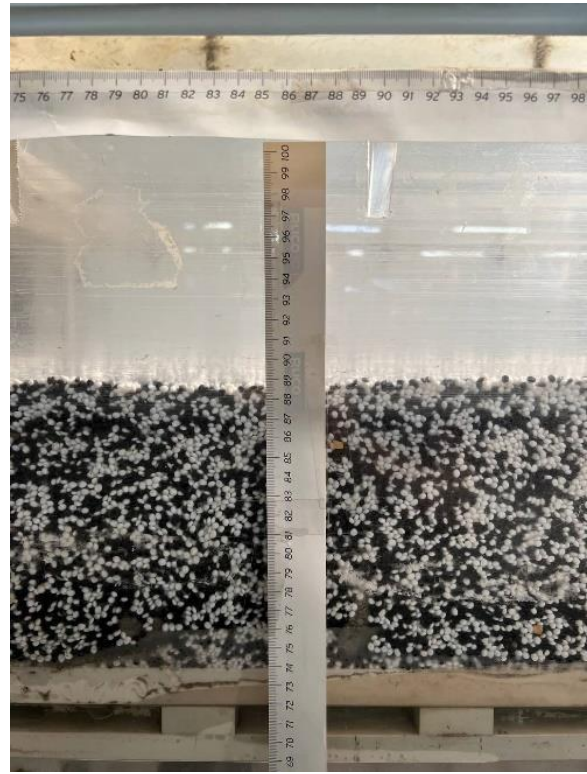
Figure 3.19. (a) Nail's Position on the Border of a Sample Net; (b) Nail's Position around the Pier.

To initiate the experiment, the electric power control, as shown in Figure 3.20(a), was activated to allow the water to enter the channel. The channel was initially filled with water at a low flow rate. Gradually, the flow rate was increased to raise the water depth incrementally.

At the same time, boundary sticks at the end of the channel were adjusted to maintain a constant water depth at the target value of 8 cm. A strip ruler, illustrated in Figure 3.20(b), was employed to control and measure the water depth. It was fixed to the side of the channel.



(a)



(b)

Figure 3.20. (a) Electric power controller; (b) Strip ruler.

The flow rate was carefully adjusted over time, ensuring a gradual increase in the water depth. Once the flow rate reached the approximate target value of 7.25 l/s and all the specified conditions were met, the experiment could proceed.

Prior to commencing the experiment, a transversal section was captured at the 1 cm upstream edge of the pier using a point gauge.

To run the experiment, the pier was lifted up, allowing it to integrate with the water flow. Simultaneously, the timer was started to track the duration of the experiment. During the first 30 minutes, temporal measurements of the scour depth were taken at a point located 1 cm upstream of the pier, with measurements recorded every few seconds. After the initial 30 minutes, the frequency of measurements was reduced, and readings were taken at regular intervals of 15 minutes until the execution of the experiment (6-hour).

At the same time, the flow rate was closely monitored. Initially, the flow rate was measured at the tenth minute and subsequently every 30 minutes until the end of the experiment (6-hour). To ensure accuracy, ten consecutive readings were averaged, and any deviations from the target discharge rate of 7.25 l/s were checked to be within a 5% tolerance. If deviations exceeded this acceptable range, adjustments were made using the Main-stream Valve to maintain the desired flow rate.

Throughout the experiments, it was crucial to constantly monitor and maintain the water depth and discharge at the target values to ensure consistent experimental conditions.

At the conclusion of the 6-hour period, the electric power control was deactivated, preventing further water entry into the channel. Subsequently, once the water was drained, specific points were selected for surveying.

Initially, a transversal cross-section was surveyed at the same location as the reference cross-section.

Furthermore, additional transversal sections were surveyed at specific locations along the channel. These sections were spread out along the surveyed zone, as depicted in Figure 3.15, from 75.85 cm downstream and 24.15 cm upstream of the pier.

Lastly, a longitudinal section was conducted along the middle of the channel.

Data collection, recording, and surveying were conducted throughout the entire experiment, encompassing the pre, during, and post-experiment phases. The collected data was meticulously recorded and organized, and the findings were presented in tables. Additionally, the data was visualized through the use of graphs and charts.

The collected survey data was utilized to generate various 2D and 3D maps using Surfer, a specialized software tool widely recognized and extensively used in scientific research for creating three-dimensional (3D) visualizations of geospatial data. The process of creating a 3D view using Surfer involved importing longitudinal and cross-section coordinates (x, y, z) and applying the Kriging method of interpolation to handle the point data.

The software provided options for wireframe, surface 3D maps, and contour 2D map, which were selected for visualization purposes. By employing the surveyed cross-sections, the five types of volumes were calculated using the midpoint method.

These included the positive scour volume, representing the sediment volume below the reference bed elevation ($Z=0$); the negative scour volume, indicating the accumulated sediment volume above the reference bed elevation ($Z=0$); the upstream scour volume, obtained by summing the positive and negative scour volumes in the upstream of the pier; the downstream scour volume, obtained by summing the positive and negative scour volumes in the downstream of the pier; and the total scour volume, representing the summation of positive and negative volumes or downstream and upstream volumes, in other words, it represents the sediment volume lost into the outlet tank.

The volume calculation process involved determining the area of each cross section by calculating the trapezoidal area between adjacent points and summing the trapezoidal areas within a cross section to obtain the total area. Subsequently, the distance between two consecutive cross sections was measured, and the volume was calculated using the formula:

$$V = \frac{(A_1 + A_2)L}{2} \quad (3.2)$$

where A_1 and A_2 represent the areas of the two consecutive cross sections, and L is the distance between the cross-sections.

In the upcoming chapter (experiments), there are informative graphical visualizations provided to facilitate comparisons, as well as additional data presented in tables, graphs, and generated maps. These valuable visual representations can be found in the appendix section of the document.

It is important to note that all the steps outlined in the experimental procedure were followed in the same manner across all series of experiments, with the exception of unprotected experiments where the use of geo-carpets was not employed.

Chapter 4

Experiments

Two distinct types of experiments were conducted: two unprotected experiments and 27 protected experiments, as exemplified by Figure 4.1. The relevant information regarding the experiments, including their key characteristics, is documented in Table 4.1.

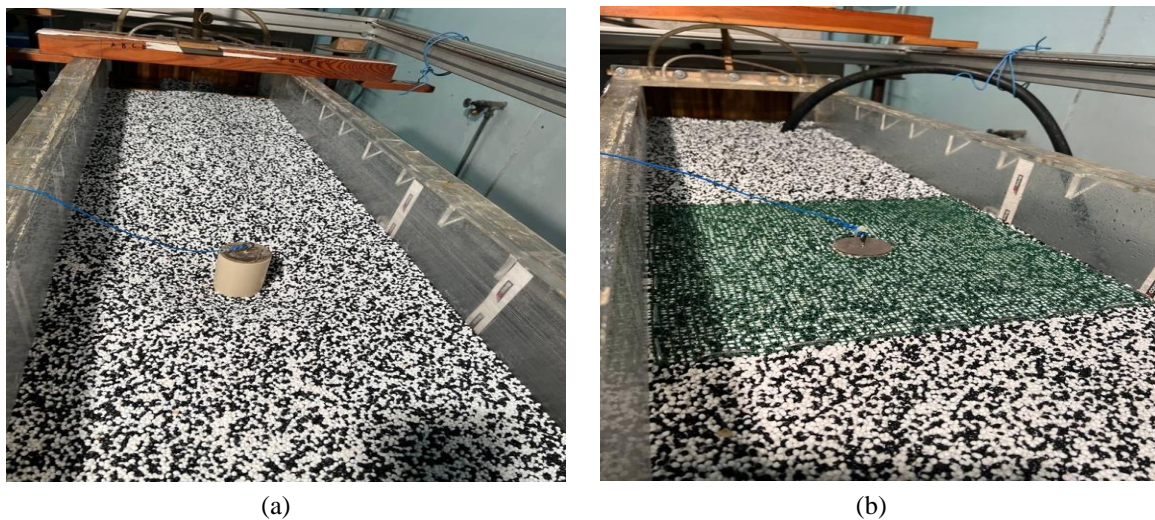
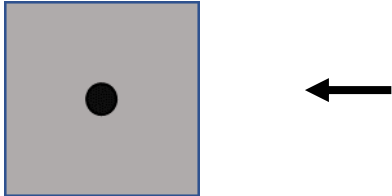



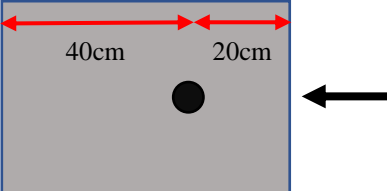
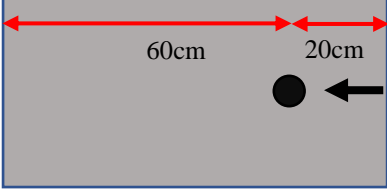
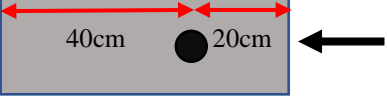
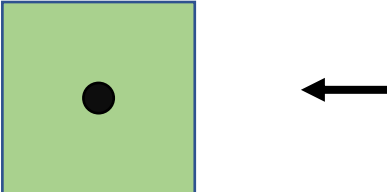



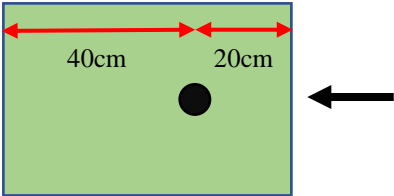
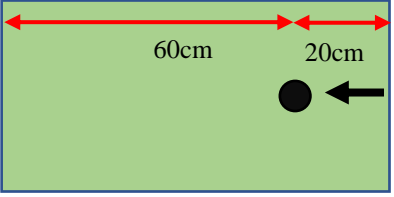
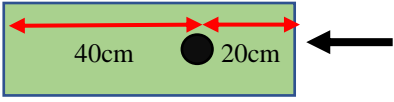




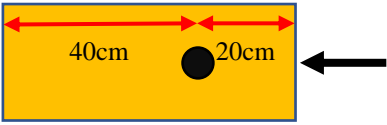
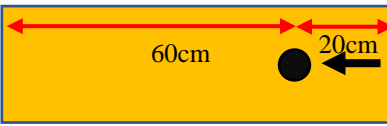
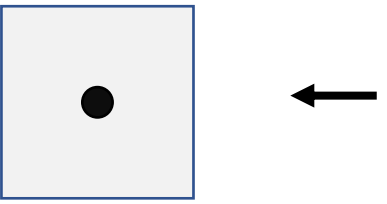



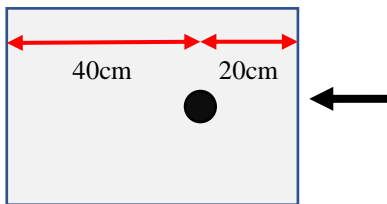


Figure 4.1. (a) Front view of an Unprotected Test. (b) Front view of a Protected Test.

Table of Experiments						
All experiments were conducted using a water discharge rate of 7.25 l/s and a water depth of 8 cm.						
Exp n°	Code	Duration (h)	Mesh Size(mm)	Coverage Area (cm ²)	Material	Net's Position
1	U 3h	3	-	-	-	-
2	U 6h	6	-	-	-	-
3	10-R-40	6	10	40*40	Rigid	

4	10-R-30	6	10	30*30	Rigid	
5	10-R-20	6	10	20*20	Rigid	
6	10-R-10	6	10	10*10	Rigid	
7	10-R-40*60	6	10	40*60	Rigid	
8	10-R-40*80	6	10	40*80	Rigid	
9	10-R-20*60	6	10	20*60	Rigid	
10	5-R-40	6	5	40*40	Rigid	
11	5-R-30	6	5	30*30	Rigid	

12	5-R-20	6	5	20*20	Rigid	
13	5-R-10	6	5	10*10	Rigid	
14	5-R-40*60	6	5	40*60	Rigid	
15	5-R-40*80	6	5	40*80	Rigid	
16	5-R-20*60	6	5	20*60	Rigid	
17	10-F-40	6	10	40*40	Flexible	
18	10-F-30	6	10	30*30	Flexible	
19	10-F-20	6	10	20*20	Flexible	

20	10-F-10	6	10	10*10	Flexible	
21	10-F-25*60	6	10	25*60	Flexible	
22	10-F-25*80	6	10	25*80	Flexible	
23	7-F-40	6	10	20*60	Flexible	
24	7-F-30	6	7	1600	Flexible	
25	7-F-20	6	7	900	Flexible	
26	7-F-10	6	7	400	Flexible	
27	7-F-40*60	6	7	100	Flexible	

28	7-F-40*80	6	7	1500	Flexible	
29	7-F-20*60	6	7	2000	Flexible	

Table 4.1. Experiments characteristics.

4.1. Unprotected Experiments

The subsequent section presents an explanation of the two unprotected experiments that were conducted, differing in durations of 3 hours and 6 hours, respectively.

The two primary reasons for conducting the unprotected experiments are twofold. Firstly, they serve as a reference for the comparison of the protected experiments, enabling a comprehensive analysis. Secondly, these experiments have been compared with prior unprotected experiments conducted on different flumes with a scour predictor by other authors.

By considering these unprotected experiments, valuable insights can be gained into the effectiveness and significance of incorporating geosynthetic carpets as a protective measure in subsequent experiments.

4.1.1. Unprotected tests: 3-hour and 6-hour Durations

Both experiments were conducted under conditions that were alike, as indicated in the experimental campaign, except for the difference in duration. The 6-hour test yielded comprehensive data, including various 2D and 3D figures, while limitations prevented the generation of similar visual presentations for the 3-hour test.

The initial experiment (3h), depicted in Figure 4.2(a), was conducted on November 9th, 2022.

The subsequent experiment (6h), shown in Figure 4.2(b) took place on November 15th, 2022:

It was chosen as the reference benchmark for the protected experiments due to its extended duration. Similar procedures and measurements were performed as in the 3-hour test.

Multiple cross-sections were taken along the channel, enabling the generation of some 2D and 3D figures, as shown in Figure 4.3 and calculation of scour volumes.



(a)

(b)

Figure 4.2. Unprotected tests: (a) Top view of the unprotected test 1; (b) Front view of the unprotected test 2.

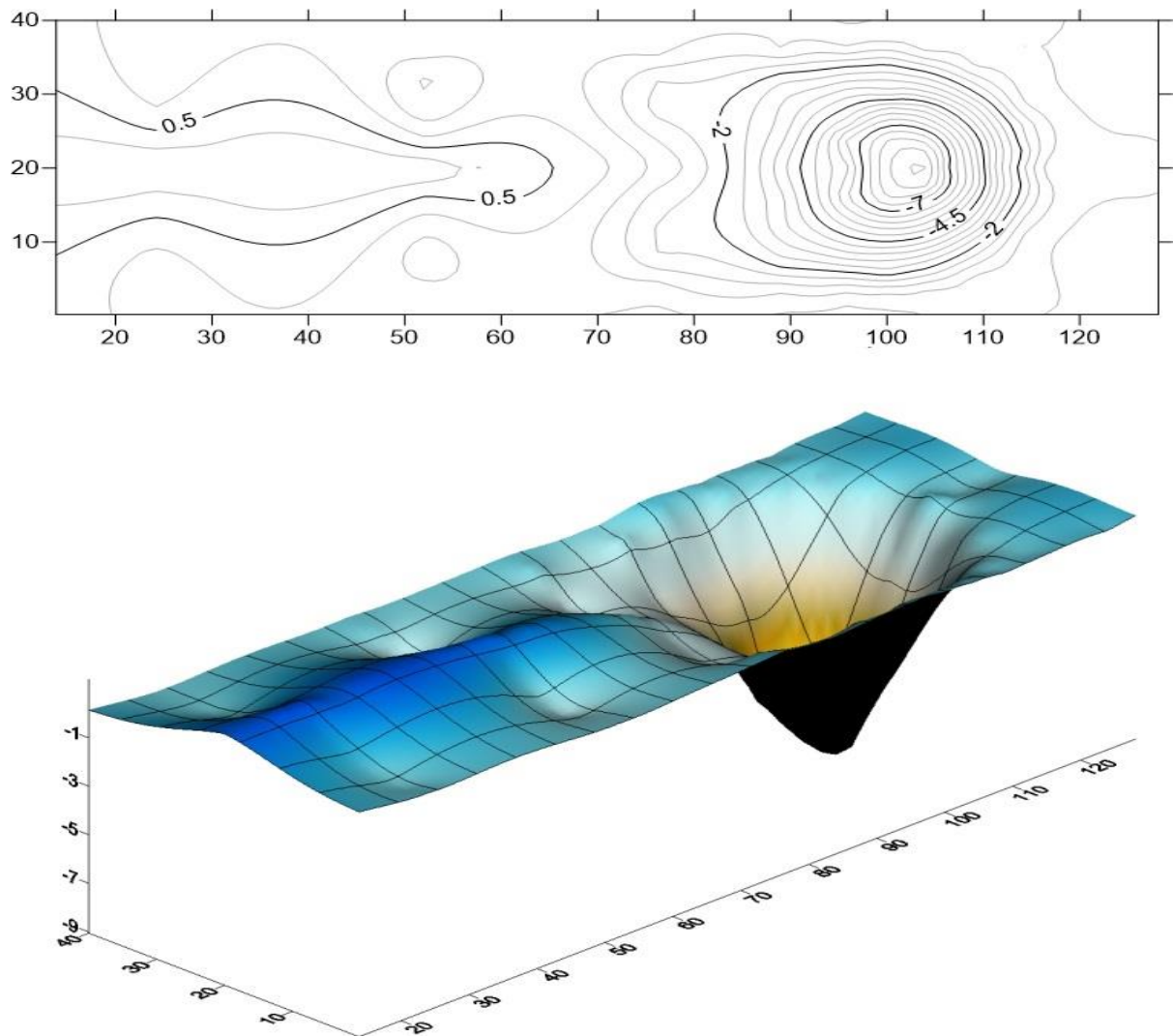


Figure 4.3. 2D counter map, followed by a 3D surface map.

4.1.2. Results, analysis, and comparison of unprotected tests

When analyzing and comparing the unprotected experiments, various perspectives can be considered:

➤ Temporal perspective:

Temporal observations, as depicted in Figure 4.4, indicated similarities in the behavior of both experiments during the initial three hours, thus providing mutual validation, as they reached approximately 89% and 88% of the final recorded scour depth within an hour, respectively.

This finding highlights the significance of the first hour in determining the most significant changes in scour depth.

In the second experiment (6h), there was slightly greater scouring observed from the 3rd to the 6th hour, although the rate of increasing scour depth decreased over time.

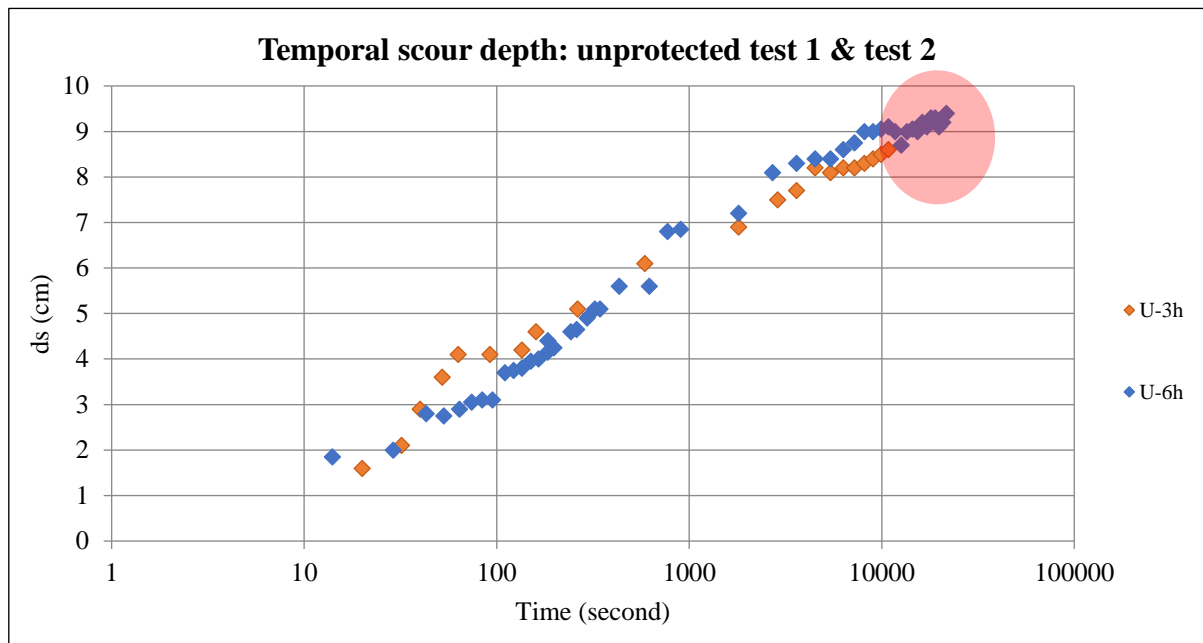


Figure 4.4. Temporal representation of unprotected tests. Red circle shows the occurrence of the slight difference of scouring after the 3rd hour.

➤ Longitudinal perspective:

The longitudinal analysis confirmed increased scouring near the upstream and downstream areas of the pier in the 6-hour test, which supports the previous findings mentioned in the earlier section (from a temporal perspective). However, there was relatively less sediment accumulation compared to the 3-hour test.

Figure 4.5 demonstrated, as the experiment progressed, the flow velocity, shear velocity, and other factors gradually transported sediments downstream, leading to reduced accumulation compared to the 3-hour test.

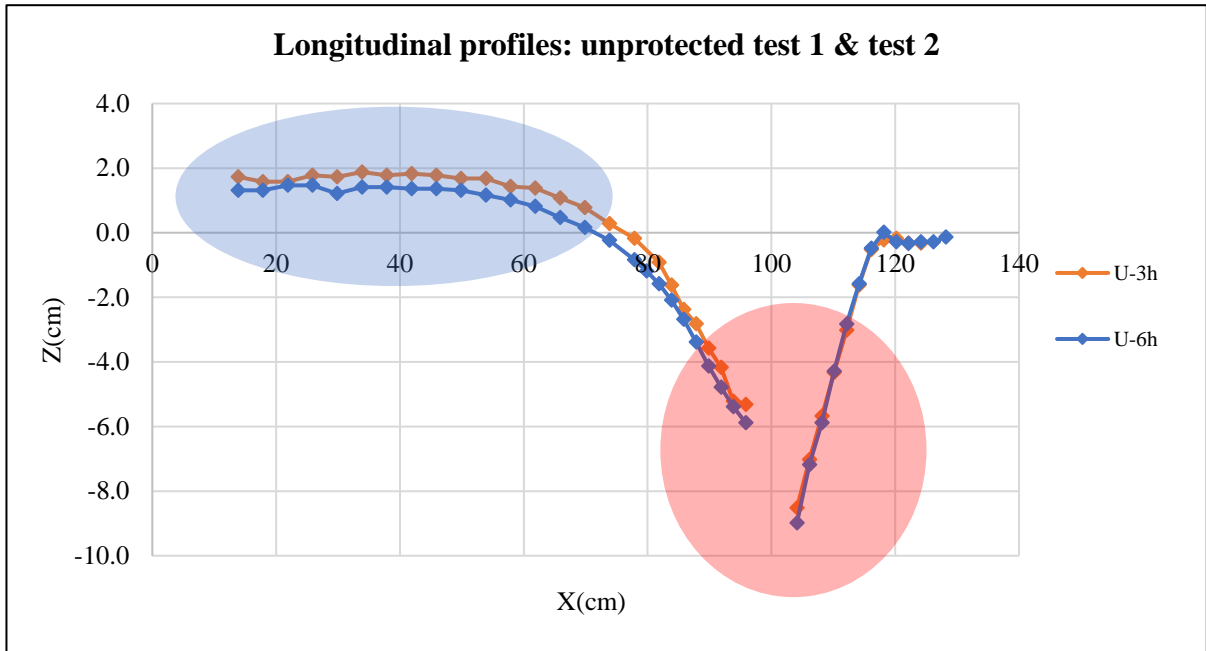


Figure 4.5. Longitudinal representation of the unprotected tests. The blue oval highlights the variation in accumulated sediment between different unprotected cases, while the red circle indicates the difference in scour depth between the upstream and downstream of the pier.

➤ Transversal perspective:

It is evident from Figure 4.6 that the second experiment exhibited more pronounced transverse scouring, as anticipated due to the longer duration.

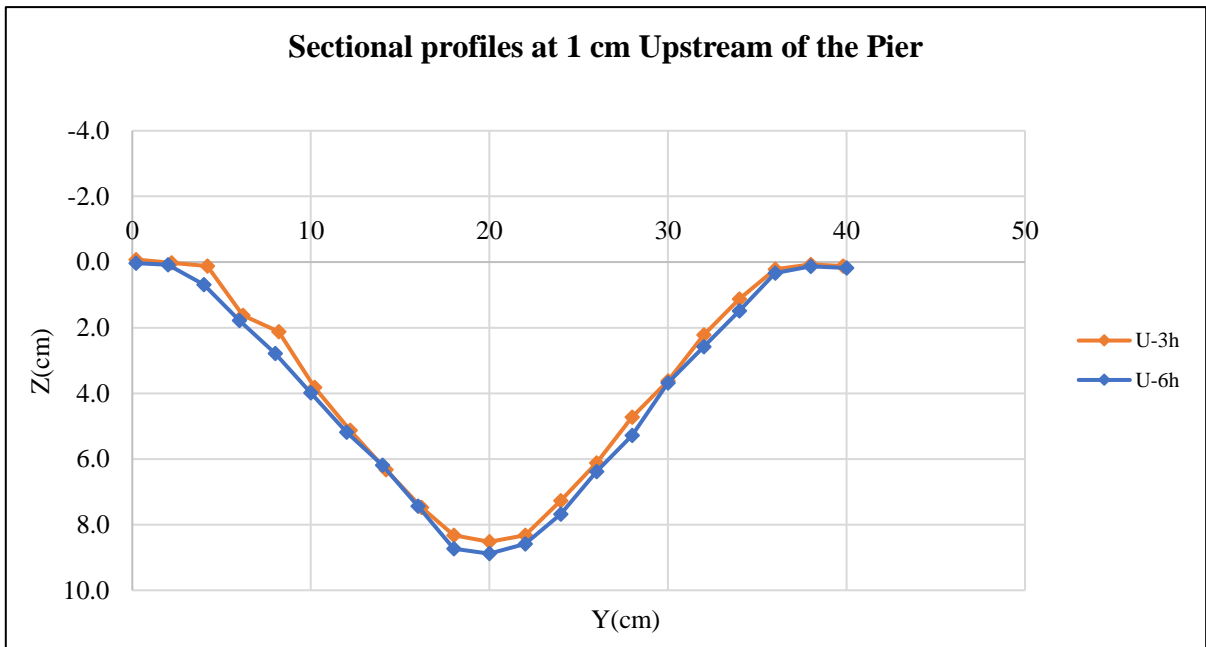


Figure 4.6. Sectional representation of the unprotected tests.

4.1.3. Validating a new scour predictor through two unprotected tests

The two completed unprotected tests have mutually validated each other and are being compared to previous unprotected tests conducted by other researchers, as presented in the reference ([Franzetti et al., 2022](#)). This comparison aims to determine whether they exhibit similar trends and findings.

In our specific case, the experimental parameters listed in Table 4.2 were the same for both unprotected tests.

Experimental Parameters	Value
v (m/s)	0.23
v_c (m/s)	0.24
v/v_c	0.95
Δ	0.27
b (cm)	6.3
a	2.57
F1	0.8931
F2	0.9049
F3	1.0006
F4	0.99975
aF1F2F3F4	2.077518746

Table 4.2. Parameters applied in this study for all the experiments.

By calculating the dimensionless scour and time based on the dimensional measurements obtained during the experiments, the dimensionless representations for both tests were constructed. Subsequently, the dimensionless representations of these two experiments were superimposed on the dimensionless representation of the previous 328 experiments ([Franzetti et al., 2022](#)), as shown in Figure 4.7.

Figure 4.7 indicates that the results of the two unprotected experiments align with the findings of previous studies conducted by different authors over a period of seventy years. This alignment serves to reinforce the coherence and consistency of our study's findings within the broader field of scour research. Furthermore, it provides validation for the newly introduced scour predictor proposed by ([Franzetti et al., 2022](#)), which was extensively discussed in the literature review chapter.

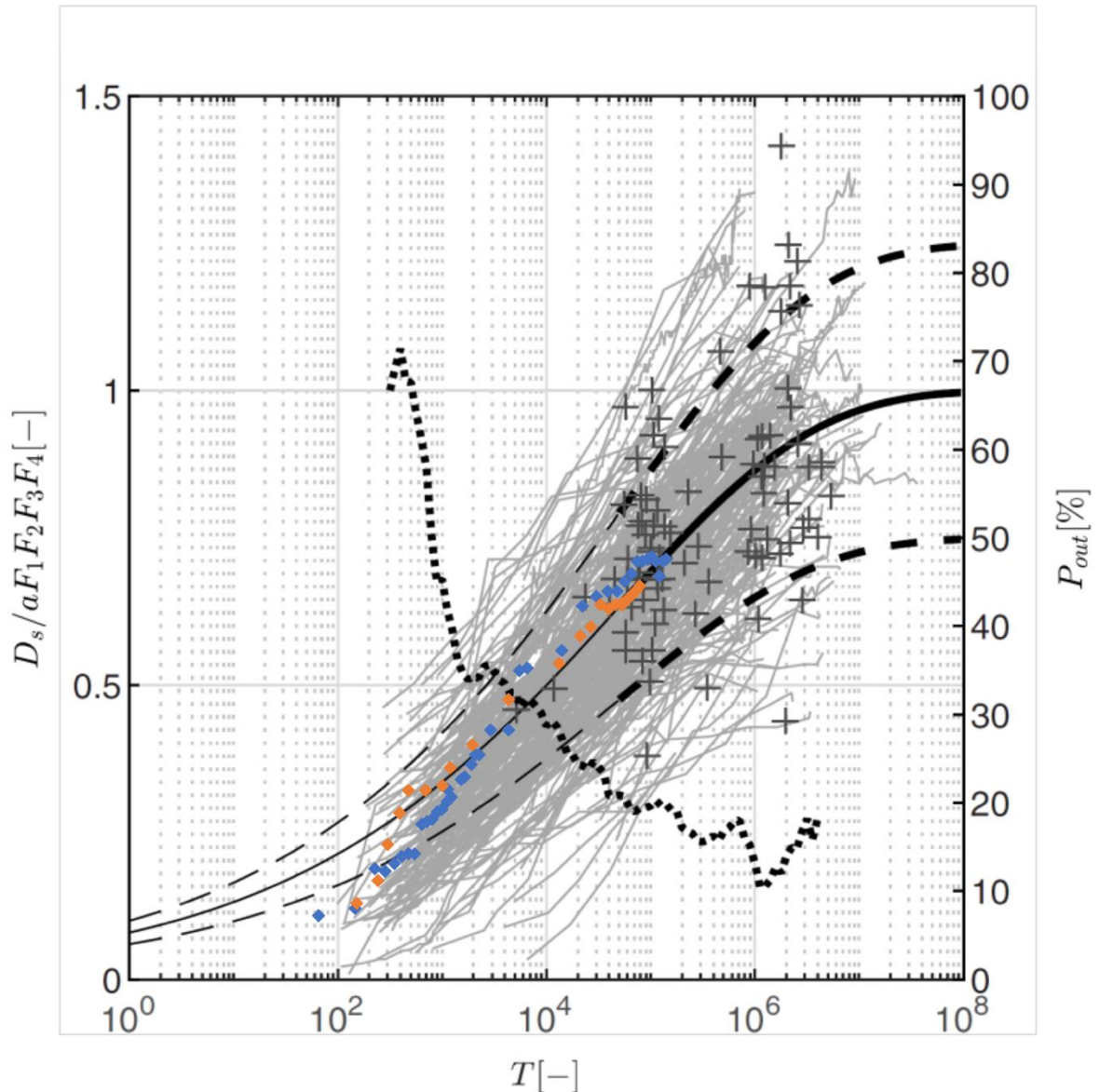


Figure 4.7. Superposition of the dimensionless representation of the two unprotected tests on the dimensionless representation of the previous 328 experiments ([Franzetti et al., 2022](#)).

4.2. Protected Experiments

To assess the effectiveness of Geo-carpets countermeasure, four rigorous series of protected experiments were conducted by considering three factors in rotation:

- Coverage area
- Mesh size (opening)
- Material flexibility

4.2.1. Rigid Geo-Carpets

Consisting of two series of nets, both series have the same coverage areas and material flexibility, with the only difference being the mesh size.

4.2.1.1. Coarse mesh nets

In this series of experiments, seven coarse rigid nets were employed, consisting of four square-shaped nets with different coverage dimensions ranging from the entire width of the channel (40 cm by 40 cm) to a smaller size of 10 cm by 10 cm, as exemplified in Figure 4.8.

Additionally, three extended nets were used, with two of them covering the entire width of the channel and one being a combination of two nets, as shown in Figure 4.8.

The 3D representation of these series of experiments can be found in Figure 4.9.

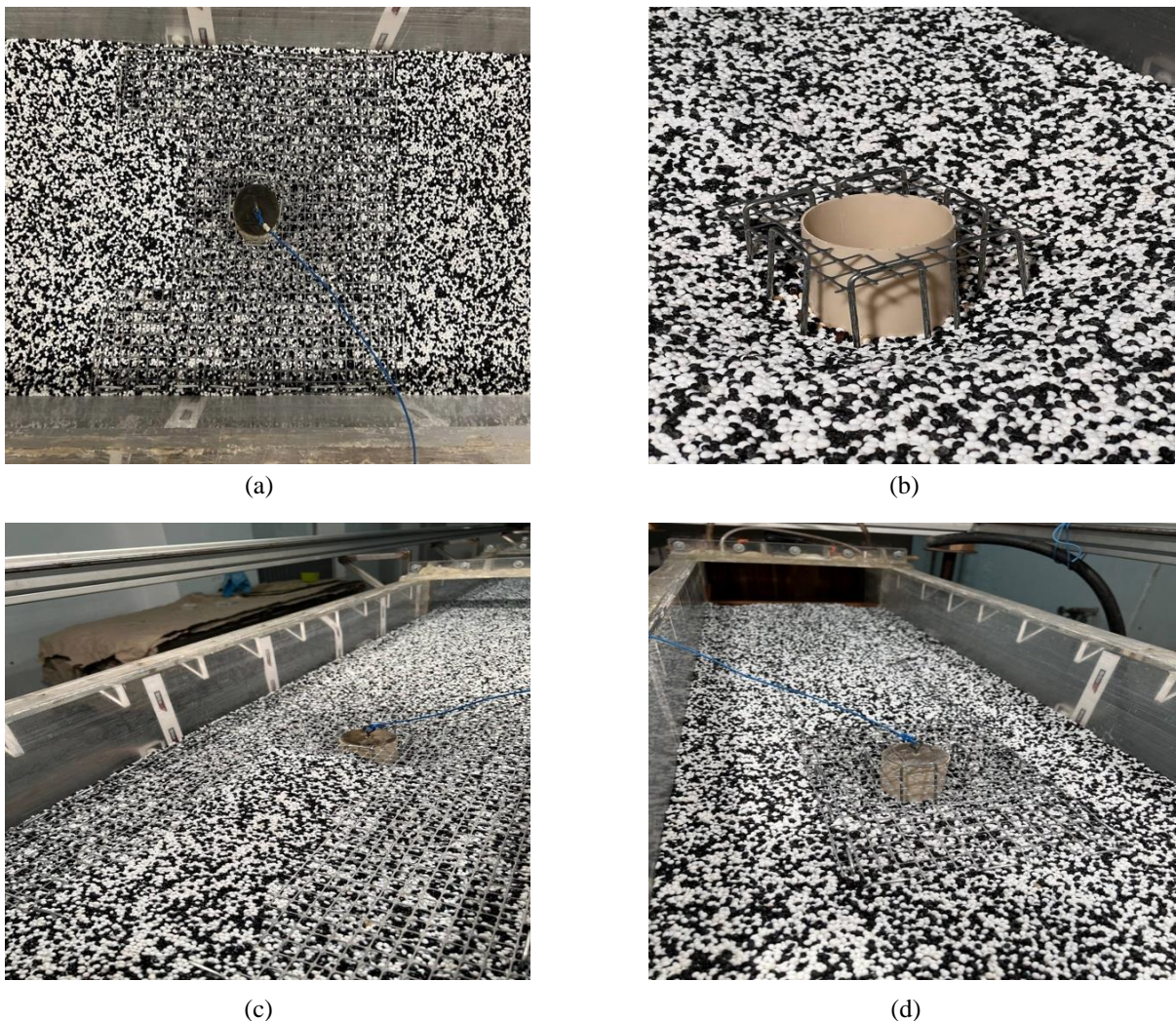


Figure 4.8. Exemplified applied coarse nets on the channel bed around the pier: (a) top view of the 40 cm by 40 cm net; (b) corner view of the 10 cm by 10 cm net; (c) back view of the 40 cm by 60 cm net; (d) front view of the 20 cm by 60 cm net.

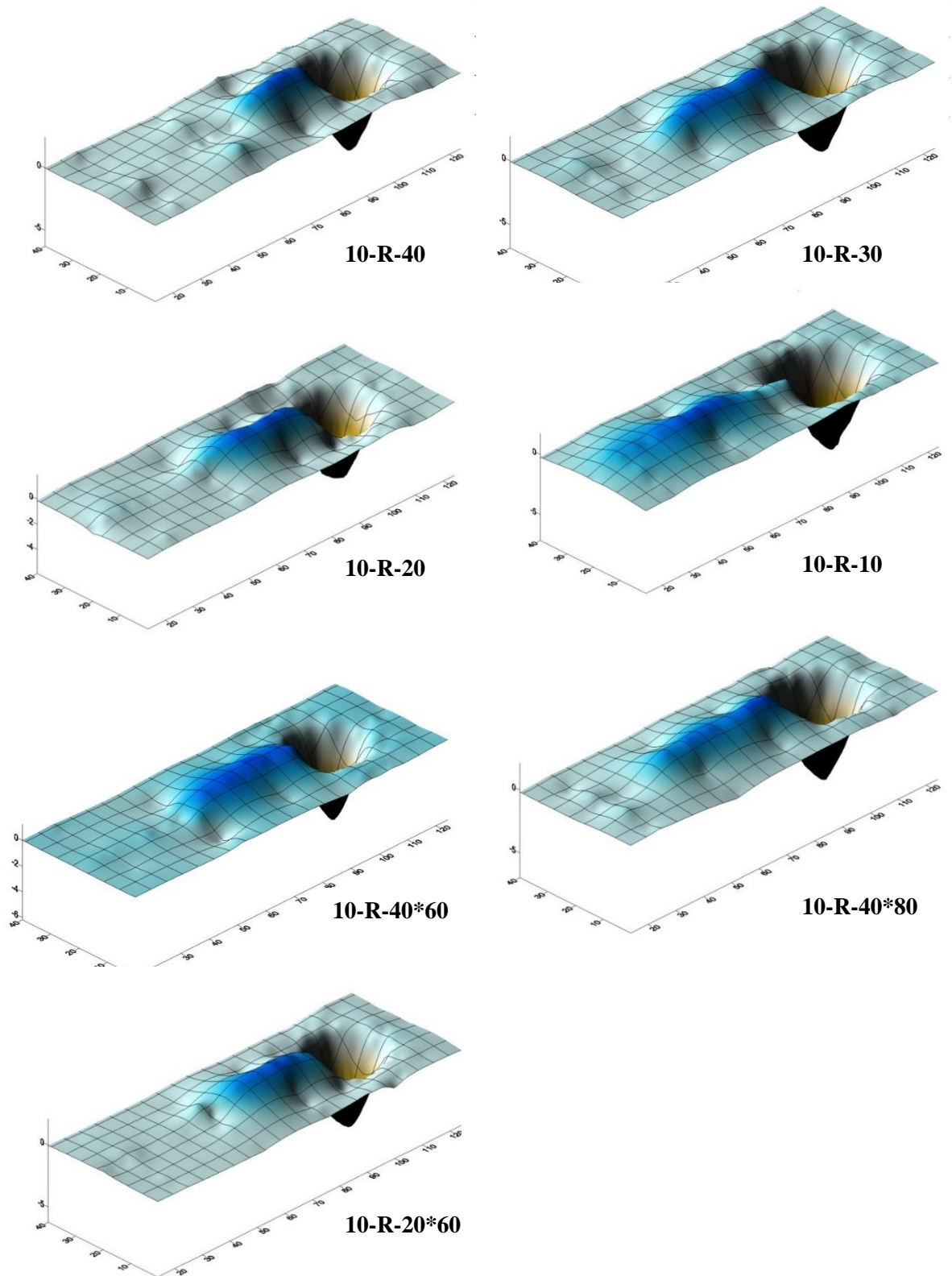


Figure 4.9. The sequence of maps presented 3D surface map.

4.2.1.2. Results, analysis, and comparison of coarse mesh nets and the reference test

In this section, the analysis of coarse rigid nets was performed by comparing them with unprotected reference test, focusing on the coverage area criterion.

The analysis is based on the results of specific graphical data and a dimensionless framework, which are as follows:

➤ Temporal perspective

The upstream edge of the pier is considered the most critical section of the channel bed, as it is highly susceptible to deep scouring caused by the downward flow led to formation of horseshoe vortices.

By examining the temporal measurements obtained during the experiments (refer to Figure 4.10), it becomes apparent that all seven experiments exhibit a similar trend characterized by an increasing scour depth.

Notably, the majority of the recorded scouring occurred within the initial hour of the experiments, followed by a gradual increase until the end of the 6-hour duration. A significant reduction of approximately 2.5 cm in scour depth is observed when comparing the protected experiments with unprotected reference case.

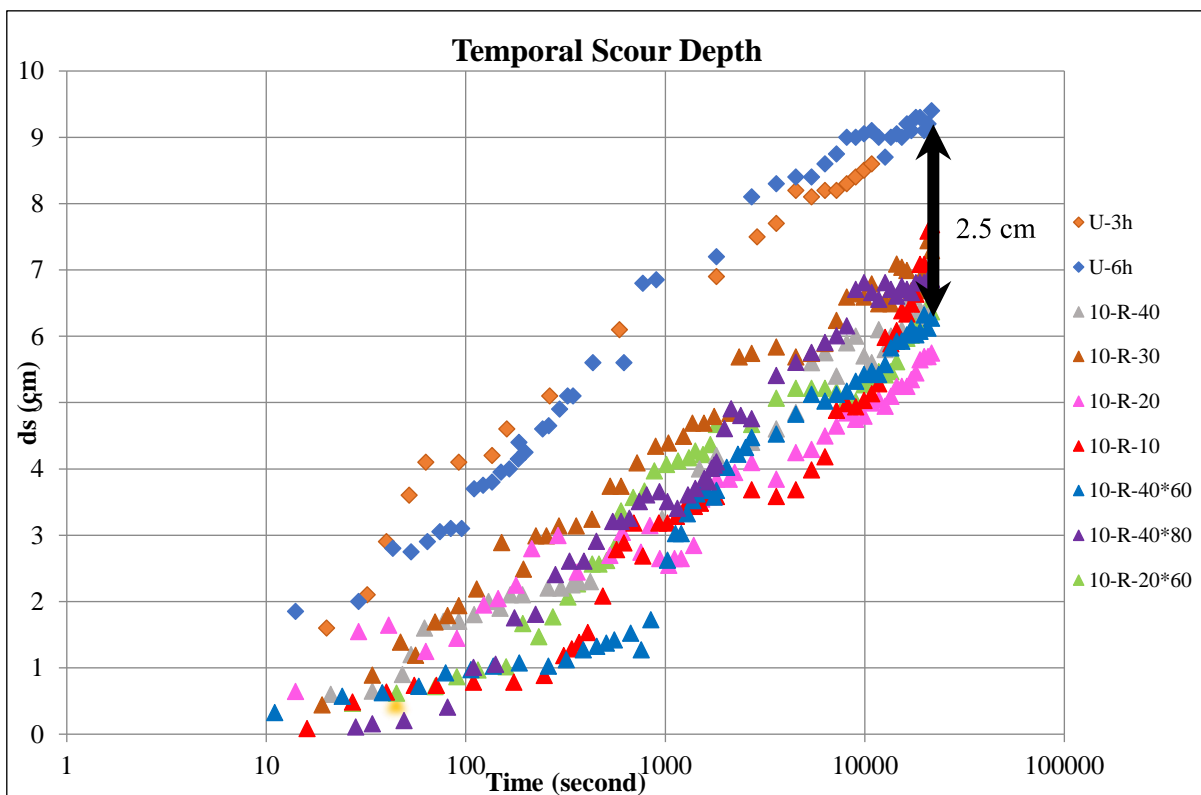


Figure 4.10. Temporal representation of the scour depth. The black arrow is indicating the mean scour depth difference btw the protected and unprotected tests.

➤ Longitudinal perspective:

A longitudinal analysis reveals that all experiments share the same trend in terms of longitudinal profiles (see Figure 4.11). The vicinity of the pier is identified as the most critical region for scouring, both upstream and downstream. Following this critical area, a substantial accumulation of sediment is observed, extending beyond the nets. Although the extension of the nets does not result in a consistent trend, it helps to disperse the accumulation and mitigate its concentration.

However, in the case of the 10 cm by 10 cm net, the accumulation extends until the end of the channel, resembling the unprotected scenario. The presence of coarse rigid nets reduces scouring in the critical region near the pier compared to the unprotected condition.

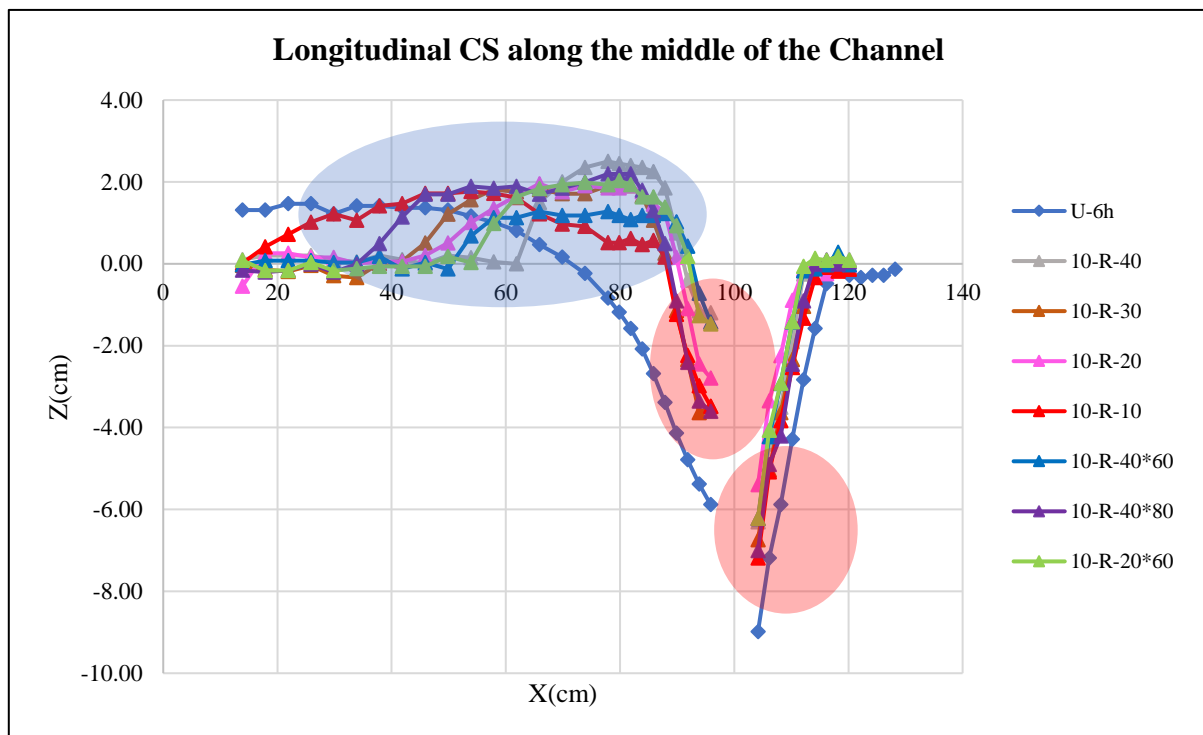


Figure 4.11. Visual representation of the longitudinal profiles. The red circles are indicating the critical area of scouring around the pier, up and downstream. the blue oval is indicating the accumulated eroded sediments in the downstream of the pier.

➤ Transversal perspective:

Figure 4.12 demonstrates that all experiments exhibit identical trend in terms of transversal profiles. Among the tested scenarios, the 20 cm by 20 cm net yielded the least amount of scouring, while the 10 cm by 10 cm net resulted in the highest level of scouring.

Furthermore, the middle part of the channel, where the pier is located, is the area most susceptible to scouring and is considered hazardous and vulnerable. In contrast, the sides of the channel experienced comparatively lower levels of scouring.

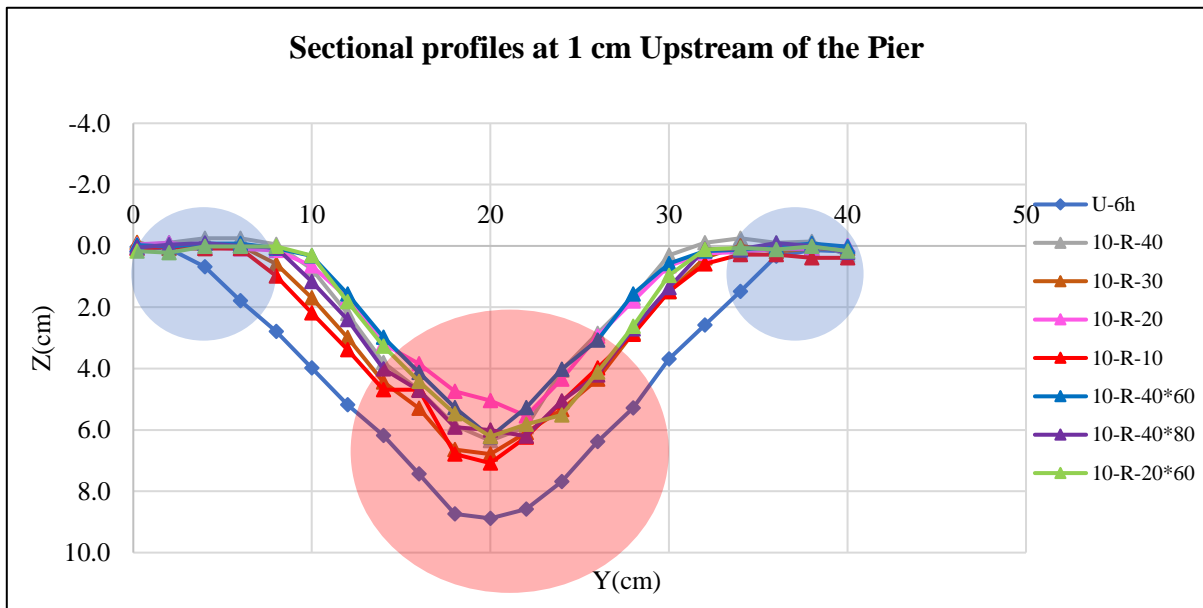


Figure 4.12. Visual representation of the transversal profiles. The blue circles are representing the side of the channel and the middle part of the channel is representing by the red circle.

➤ Location of Maximum Scouring in the Upstream and Downstream of the Pier:

Analyzing the longitudinal profile (refer to Figure 4.11) reveals that, in all cases of coarse rigid nets, the maximum scour depth is observed near the pier, both upstream and downstream, indicated by two red circles.

The subsequent comparative analyzes will rely on a dimensionless framework that involves four parameters. The first parameter is the ratio of scour depth to the pier diameter (d_s/b), which will be used to conduct a dimensionless comparative analysis of the maximum scour depths in both the upstream and downstream. The second parameter is the ratio of scour volume to the pier diameter raised to the power of three ($\text{scour volume}/b^3$), which will be employed to perform a dimensionless comparative analysis of various scour volumes, including total, positive, negative, downstream, and upstream volumes. Moreover, the geocarpet will be expressed in a dimensionless way, for the sake of being comparable with other experimental campaigns, consequently, the third parameter is the net' width-to-pier diameter ratio (W/b) for distinguishing the square-shaped nets and the fourth parameter is the net' length-to-net' width ratio (L/W) for discriminating the extended nets. The dimensionless framework described above will be maintained the same throughout the subsequent series of experiments as well. Table 4.3 depicts the ratio of different net sizes.

The net's width-to-pier's diameter ratio					
Square-shaped nets	10*10	20*20	30*30	40*40	
W/b	1.59	3.17	4.76	6.35	
The net's length-to-net's width ratio					
Extended nets	40*60	40*80	25*60	20*60	25*80
L/W	1.5	2	2.4	3	3.2

Table 4.3. Ratio of different net sizes.

- Upstream Maximum Scour Depth:

Figure 4.13 demonstrates that the 20 cm by 20 cm net ($W/b=3.17$) exhibits the best performance in terms of reducing scouring near the upstream edge of the pier, while the 10 cm by 10 cm ($W/b=1.59$) and 40 cm by 80 cm ($L/W=2$) nets represent the worst cases.

It is worth noting that the extension of the nets does not yield improvements in reducing upstream scouring.

- Downstream Maximum Scour Depth:

Figure 4.14 illustrates that as the coverage around the pier increases, there is a corresponding decrease in scouring downstream near the pier. This reduction in scouring continues up to a certain point, beyond which the 40 cm by 80 cm ($L/W=2$) net exhibits a higher level of scouring compared to the other net sizes.

However, extending the nets downstream does not contribute to a further reduction in scouring near the pier. The 40 cm by 40 ($W/b=6.35$) cm net performs the best in terms of minimizing downstream scouring, while the 10 cm by 10 cm ($W/b=1.59$) and 40 cm by 80 cm ($L/W=2$) nets represent the worst cases.

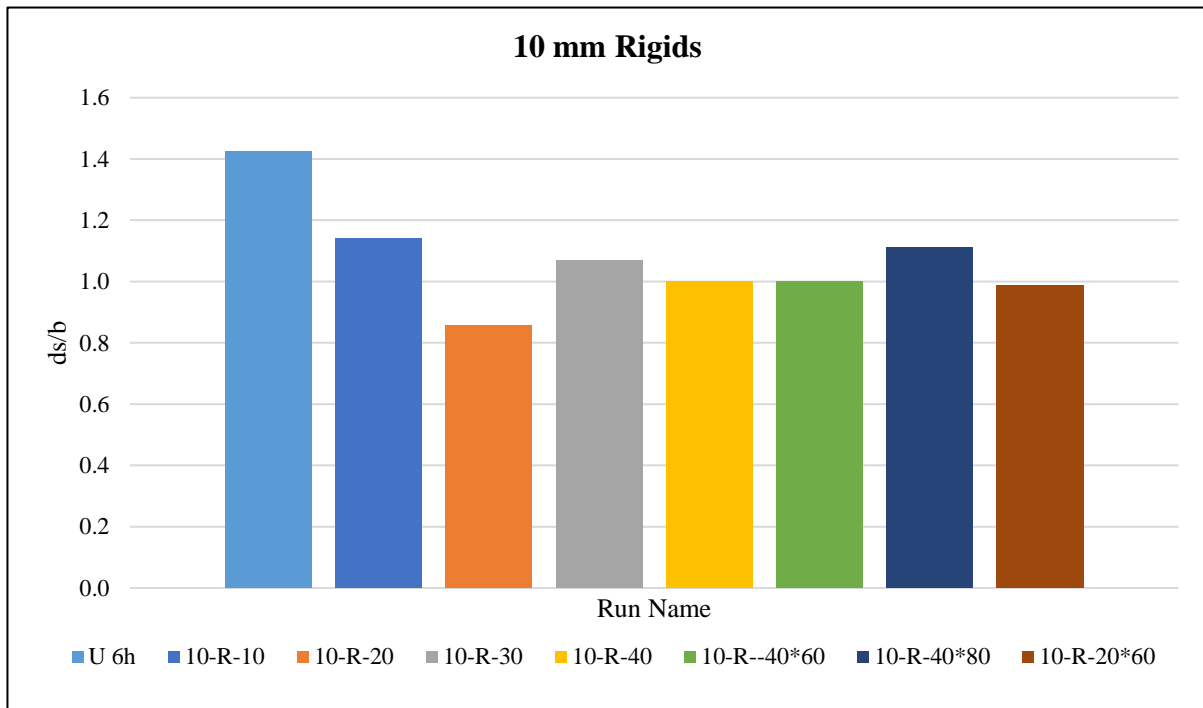


Figure 4.13. Histogram representation of the dimensionless upstream maximum scour depth.

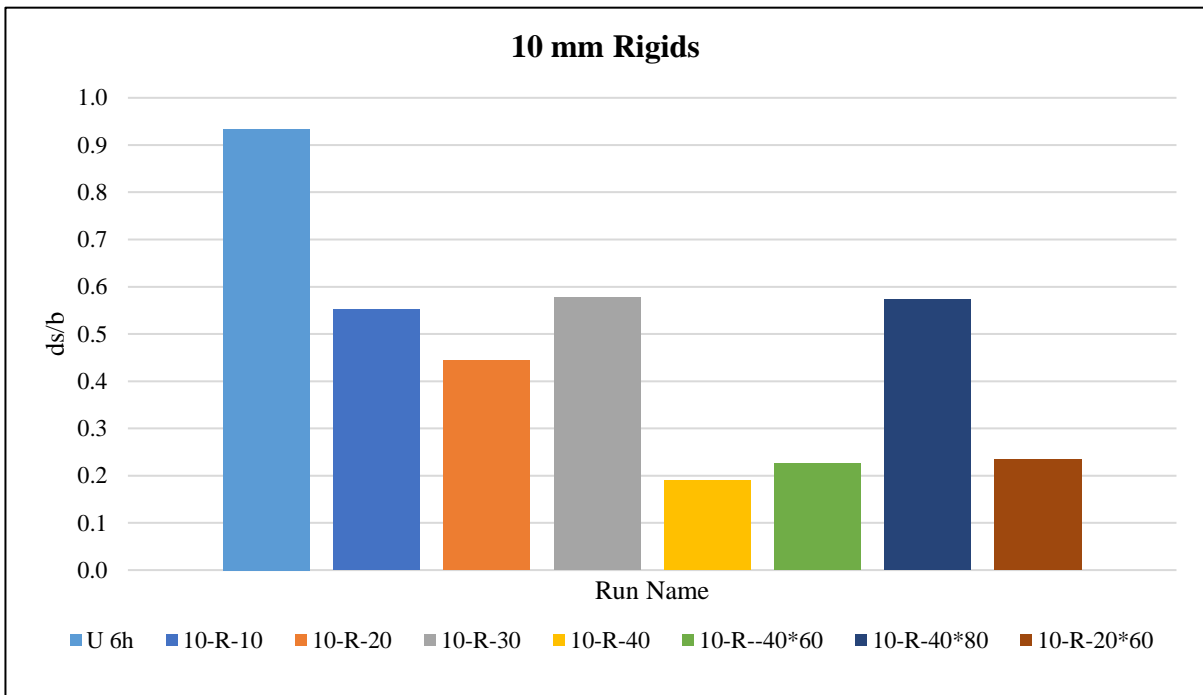


Figure 4.14. Histogram representation of the dimensionless downstream maximum scour depth.

➤ Scour Volumes Categorized into 5 Types:

- Total Scour Volume (Lost Sediments):

Figure 4.15 illustrates that increased coverage and extension of nets lead to a reduction in lost sediments. However, it should be noted that the unprotected test, which serves as the worst case, exhibits a significant difference with three times more sediment loss compared to the other cases where geo-carpets were employed as scouring countermeasures.

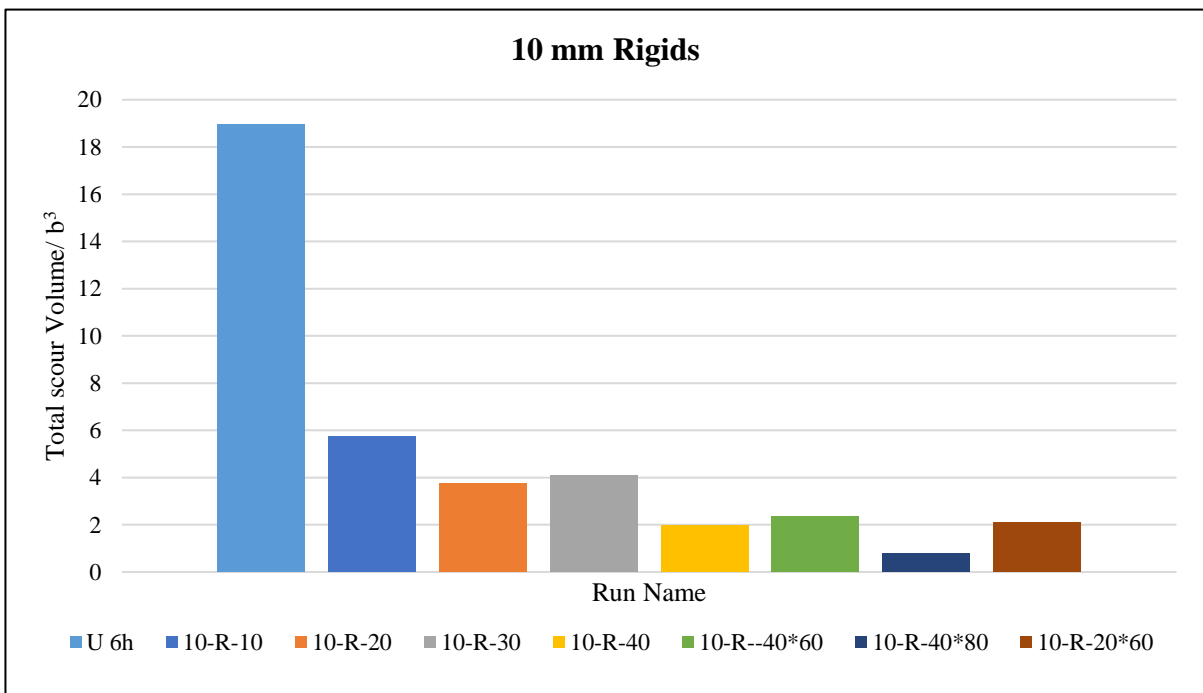


Figure 4.15. Histogram representation of the dimensionless total scour volume.

- Positive Scour Volume (Scoured Sediments):

Figure 4.16 demonstrates that the best-performing nets in terms of minimizing positive scour volume (i.e., sediments scoured) are the 20 cm by 20 cm ($W/b=3.17$), 40 cm by 60 cm ($L/W=1.5$), and 20 cm by 60 cm ($L/W=3$) nets, while the 10 cm by 10 cm ($W/b=1.59$) net represents the worst case.

Thus, less coverage results in higher positive scour volumes, while increased coverage and extension of nets lead to lower positive scouring up to a certain point. However, beyond that point [e.g., 40 cm by 80 cm ($L/W=2$)], an increase in positive scouring is observed. The unprotected test exhibits a substantial difference, with three times more sediment scouring than the other cases employing geo-carpets.

- Negative Scour Volume (Accumulated Sediments):

The unprotected test records a lower volume of sediment accumulation, as shown in figure 4.17, which is expected considering the significant sediment loss during the experiment.

Overall, it can be stated that greater coverage leads to higher accumulation. However, it is worth mentioning that the moderate square-shaped geo-carpets demonstrate lower accumulation volumes.

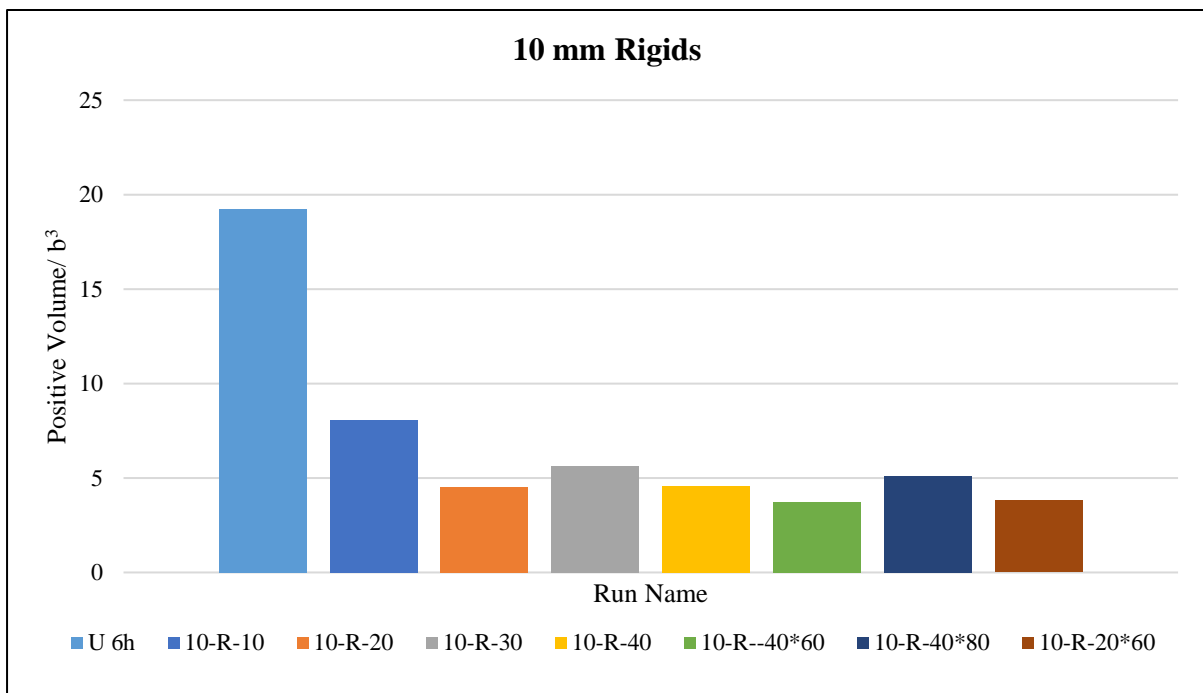


Figure 4.16. Histogram representation of the dimensionless positive scour volume.

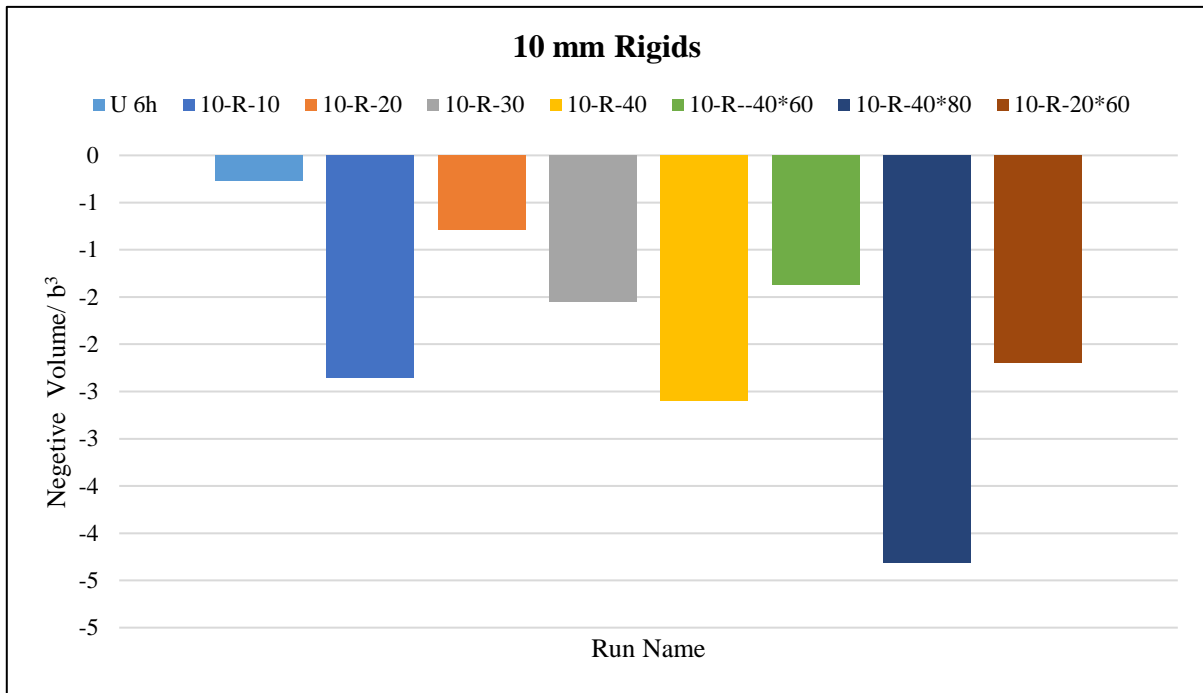


Figure 4.17. Histogram representation of the dimensionless negative scour volume.

- Downstream Scour Volume:

Figure 4.18 indicates that less coverage results in a higher positive scour volume, resulting in a positive downstream volume. On the other hand, extending the nets leads to a negative downstream volume due to increased accumulation. The unprotected test exhibits a substantial downstream scour volume, six times higher than the protected cases, highlighting the effectiveness of the protection measures.

- Upstream Scour Volume:

Figure 4.19 reveals that greater coverage with square-shaped nets leads to a lower positive scour volume, resulting in a lower upstream volume. However, extending the nets results in a worse performance, with an increase in upstream scour volume. The unprotected test exhibits a significantly higher upstream scour volume, twice as much as the protected cases, underscoring the effectiveness of the protection measures.

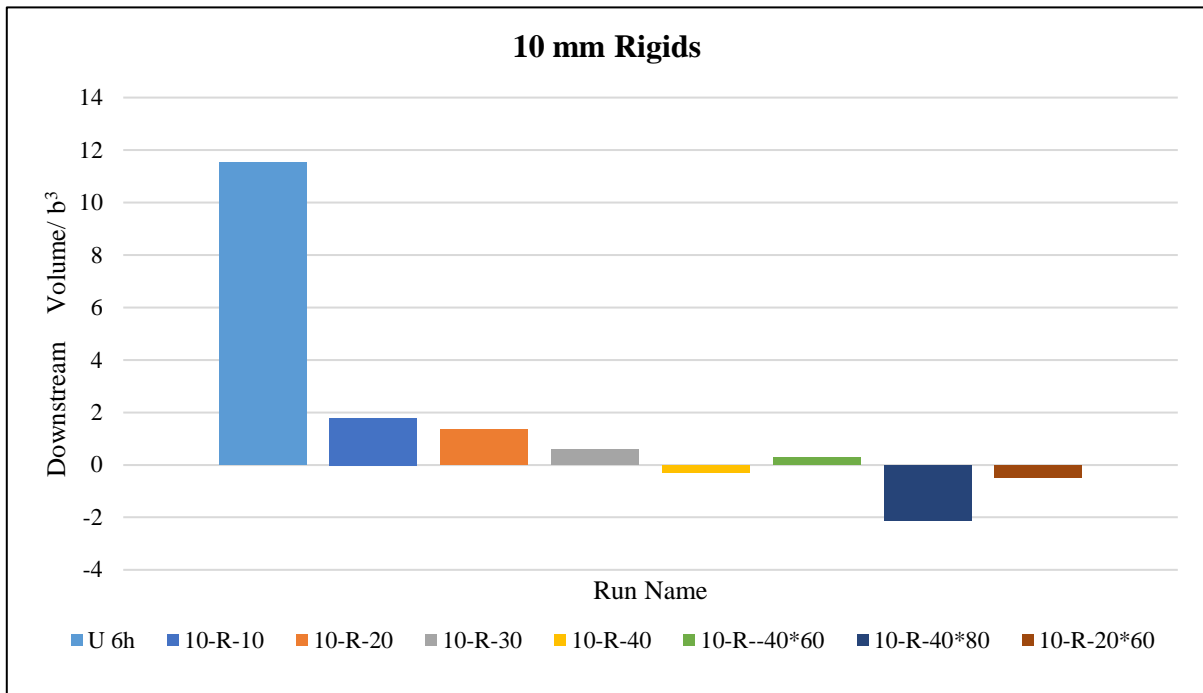


Figure 4.18. Histogram representation of the dimensionless downstream scour volume.

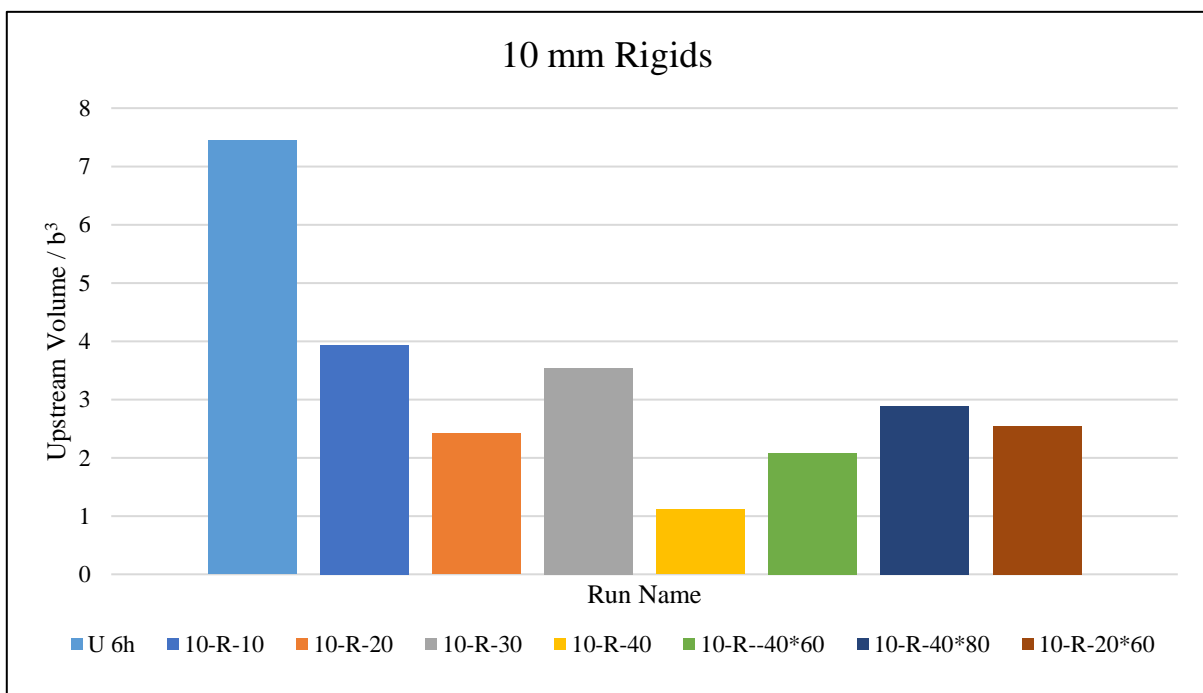


Figure 4.19. Histogram representation of the dimensionless upstream scour volume.

➤ Comparison between Upstream and Downstream Scour Volumes:

An analysis of upstream and downstream scour volumes does not reveal a clear trend (see Figure 4.20).

Nevertheless, it can be inferred that moderate coverage provides the best protection for the upstream volume of the pier, while extending the net downstream contributes to the downstream volume of the pier.

In summary, the comparison between coarse mesh nets and unprotected testing demonstrates that the implementation of various nets as scour protection measures has a significant impact on the coverage area and offers substantial improvements in terms of scour depth reduction, sediment accumulation, and positive scour volumes.

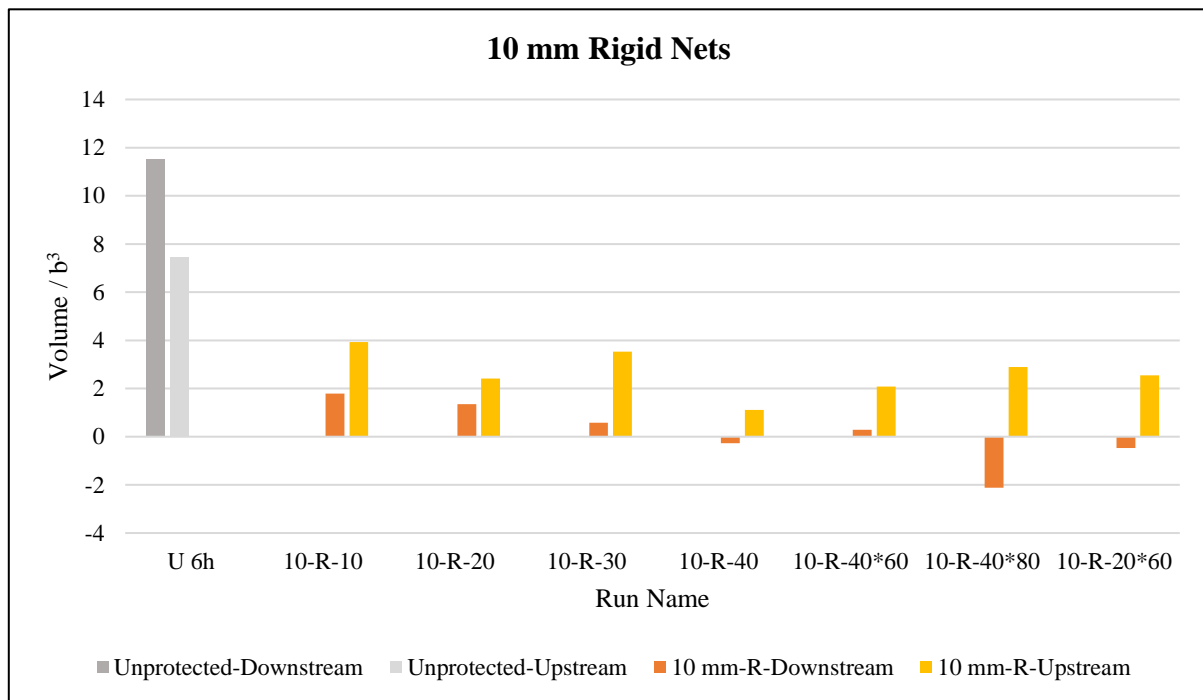
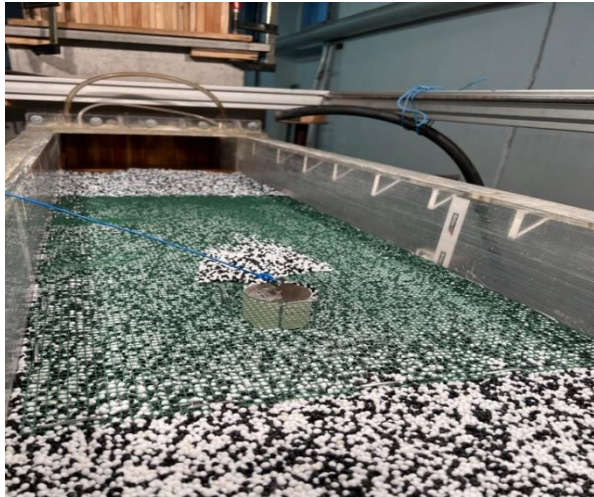


Figure 4.20. Histogram comparison of the dimensionless up and downstream scour volume.

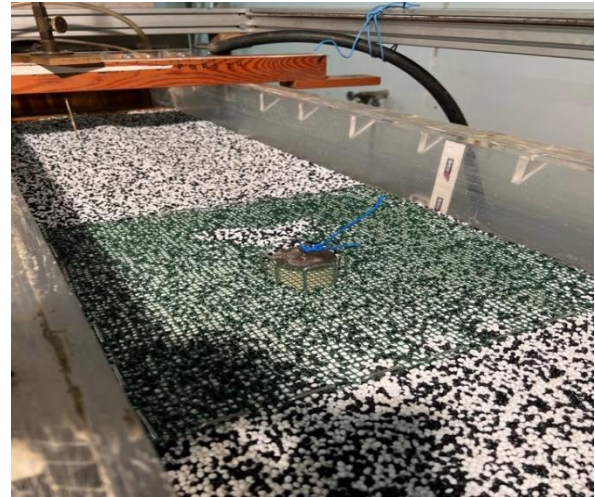
4.2.1.3. Fine mesh nets

In this series of experiments, a total of seven fine rigid nets were utilized, with coverage areas identical to those of the coarse rigid nets.

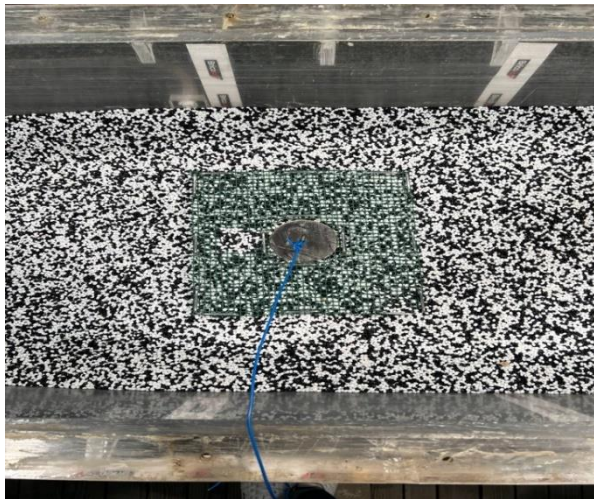
Examples of these fine rigid nets are presented in Figure 4.21, while the corresponding 3D schematics can be found in Figure 4.22.



(a)



(b)



(c)



(d)

Figure 4.21. Exemplified applied fine nets on the channel bed around the pier: (a) front view of the 40 cm by 80 cm net; (b) corner view of the 40 cm by 40 cm net; (c) top view of the 20 cm by 20 cm net; (d) front view of the 20 cm by 60 cm net.

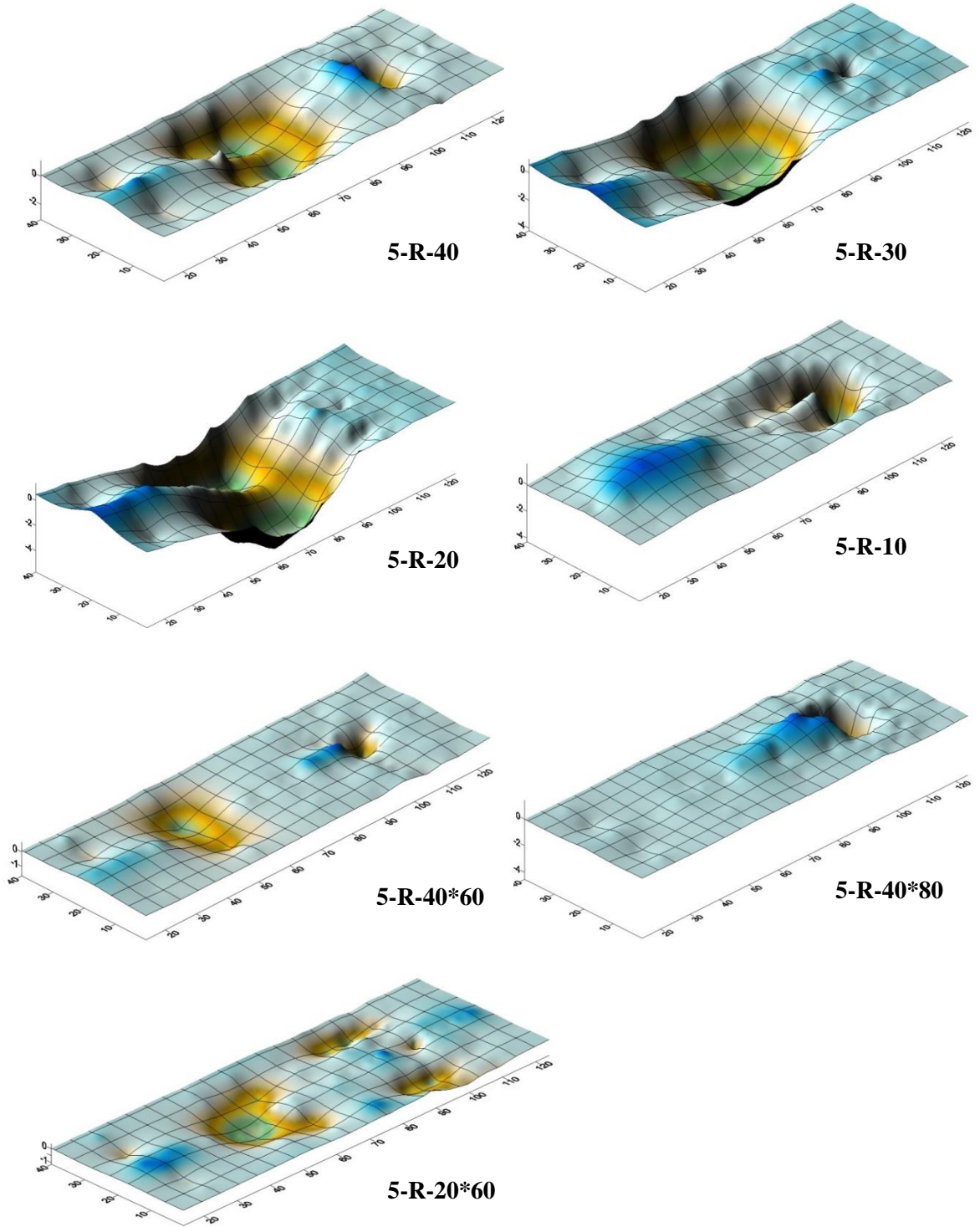


Figure 4.22. The sequence of maps presented 3D surface map.

4.2.1.4. Results, analysis, and comparison of fine mesh nets and the reference test

In this section, the analysis of fine rigid nets was performed by comparing them with unprotected reference test, focusing on the coverage area criterion.

The analysis is based on the results of specific graphical data, and a dimensionless framework, which are as follows:

➤ Temporal perspective

Examination of the temporal measurements obtained from the fine rigid experiments (see Figure 4.23) reveals a consistent trend among all seven experiments, characterized by an increasing scour depth over time. Most of the recorded scouring occurs within the initial hour, followed by a gradual increase throughout the 6-hour duration.

A remarkable outcome is the substantial average decrease of around 7 cm in scour depth. This observation underscores the noteworthy impact of the fine mesh nets in reducing scouring.

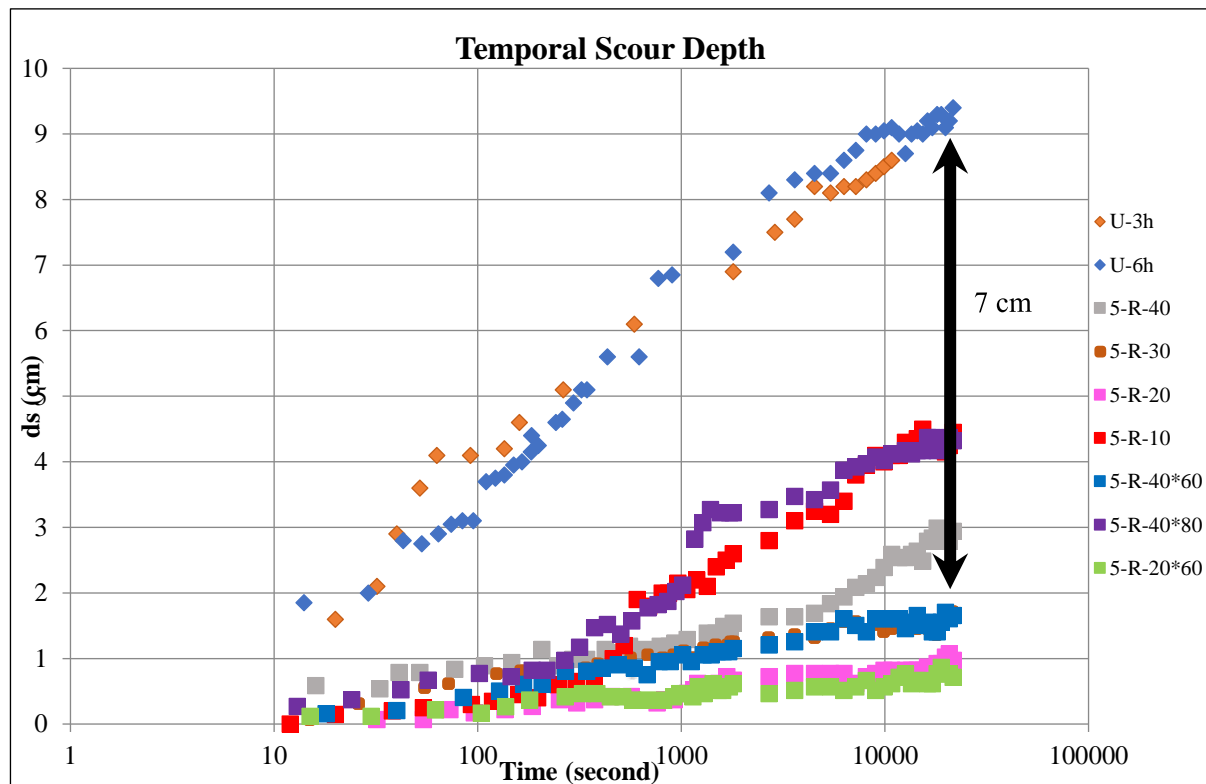


Figure 4.23. Temporal representation of the scour depth. The black arrow is indicating the mean scour depth difference btw the protected and unprotected tests.

➤ Longitudinal perspective:

The analysis of longitudinal cross-sections, as depicted in Figure 4.24, indicates that all experiments exhibit a consistent trend in terms of the shape of the longitudinal profile. The critical region for scouring is identified near the upstream of the pier, followed by sediment accumulation downstream, extending until the end of the nets. Beyond the nets, a notable scouring is observed in all cases. It is worth mentioning that less coverage leads to deeper

scouring beyond the net, while extending the nets downstream reduces the magnitude of scouring.

However, the behavior of the 10 cm by 10 cm net is different and does not follow the mentioned trend, resembling the unprotected scenario. The presence of fine rigid nets significantly reduces scouring near the pier compared to the unprotected condition.

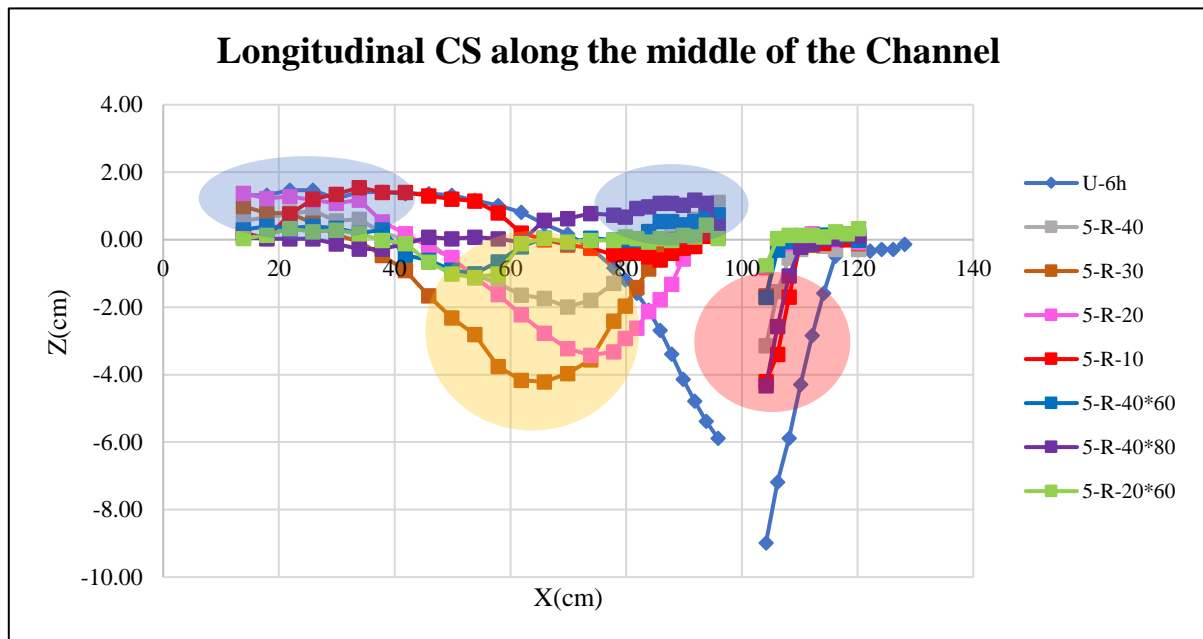


Figure 4.24. Visual representation of the longitudinal profiles. The red circle is indicating the critical area of scouring at 1 cm upstream edge of the pier, the blue ovals are indicating the accumulated eroded sediments in the downstream of the pier, the yellow circle is indicating the scouring after the nets.

➤ Transversal perspective:

Figure 4.25 demonstrates that all experiments exhibit identical trend in terms of transversal profiles.

Among the tested scenarios, the 20 cm by 20 cm and 20 cm by 60 cm nets yielded the least amount of scouring, while the 10 cm by 10 cm and 40 cm by 80 cm nets resulted in the highest level of scouring.

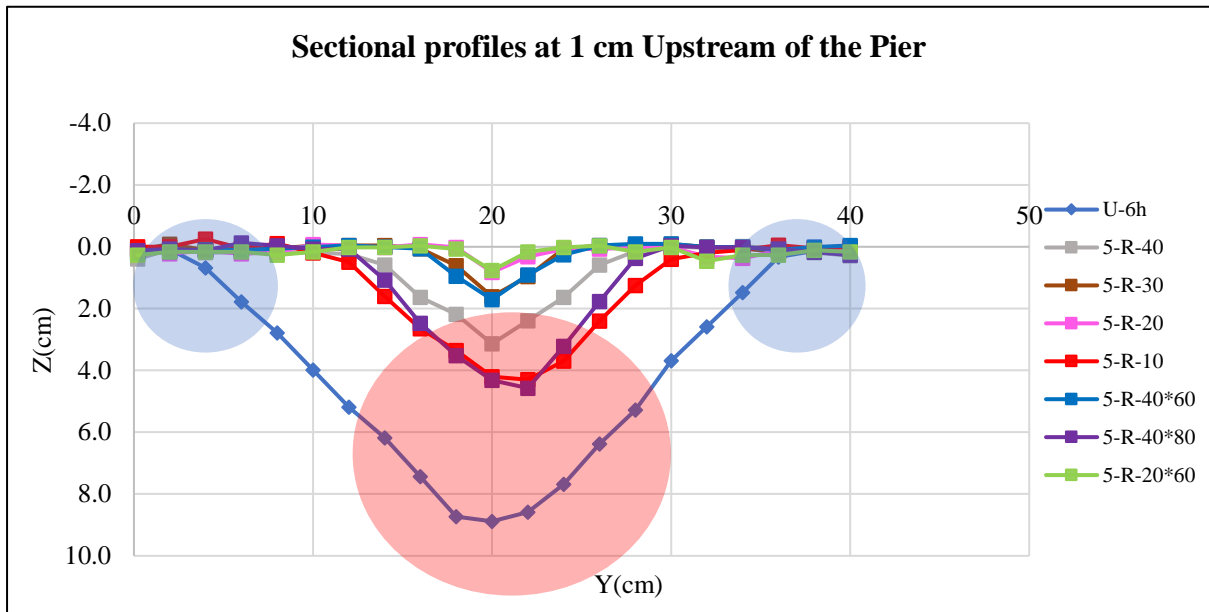


Figure 4.25. Visual representation of the transversal profiles. The blue circles are representing the side of the channel and the middle part of the channel is representing by the red circle.

➤ Location of Maximum Scouring in the Upstream and Downstream of the Pier:

Analyzing the longitudinal cross-sections (Figure 4.24) reveals that, in all cases of fine rigid nets, the maximum scour depth is observed near the pier in the upstream and beyond the net in the downstream.

- Upstream Maximum Scour Depth:

Figure 4.26 demonstrates that the 20 cm by 20 cm ($W/b=3.17$) and 20 cm by 60 cm ($L/W=3$) nets exhibit the best performance in reducing scouring near the upstream edge of the pier, while the 10 cm by 10 cm ($W/b=1.59$) and 40 cm by 80 cm ($L/W=2$) nets represent the worst cases. Extending the nets yields improvements in reducing upstream scouring, but the 40 cm by 80 cm ($L/W=2$) net does not perform as effectively.

It can also be noted that leaving the sides of the channel bed unprotected results in less scouring upstream, likely due to changes in flow patterns caused by covering the whole width of the channel. However, in all cases, the scour depth is significantly lower compared to the unprotected condition.

- Downstream Maximum Scour Depth:

Figure 4.27 indicates that increased square-shaped coverage area around the pier leads to increased scouring downstream near the pier, up to the point of covering the whole width of the channel, which results in a reduction in scouring. The 40 cm by 80 cm ($L/W=2$) net performs the best in terms of minimizing downstream scouring, while the 20 cm by 20 cm ($W/b=3.17$) and 30 cm by 30 cm ($W/b=4.76$) nets represent the worst cases.

Importantly, all protected cases exhibit lower scouring compared to the unprotected scenario.

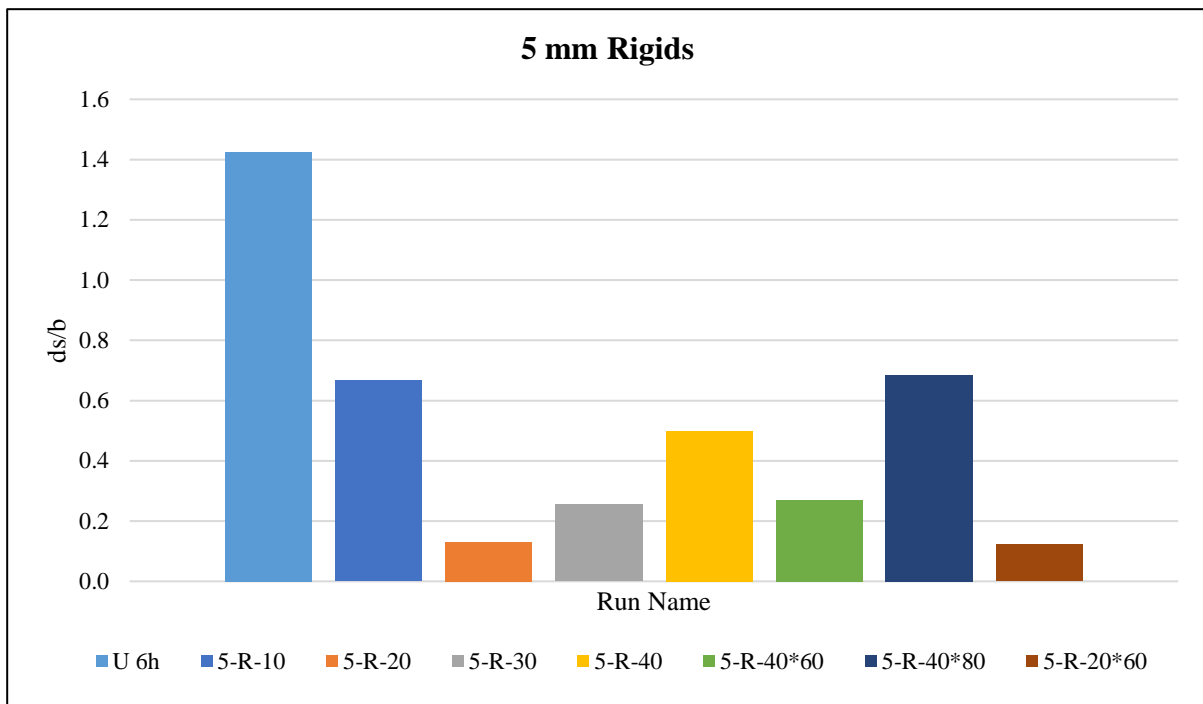


Figure 4.26. Histogram representation of the dimensionless upstream maximum scour depth.

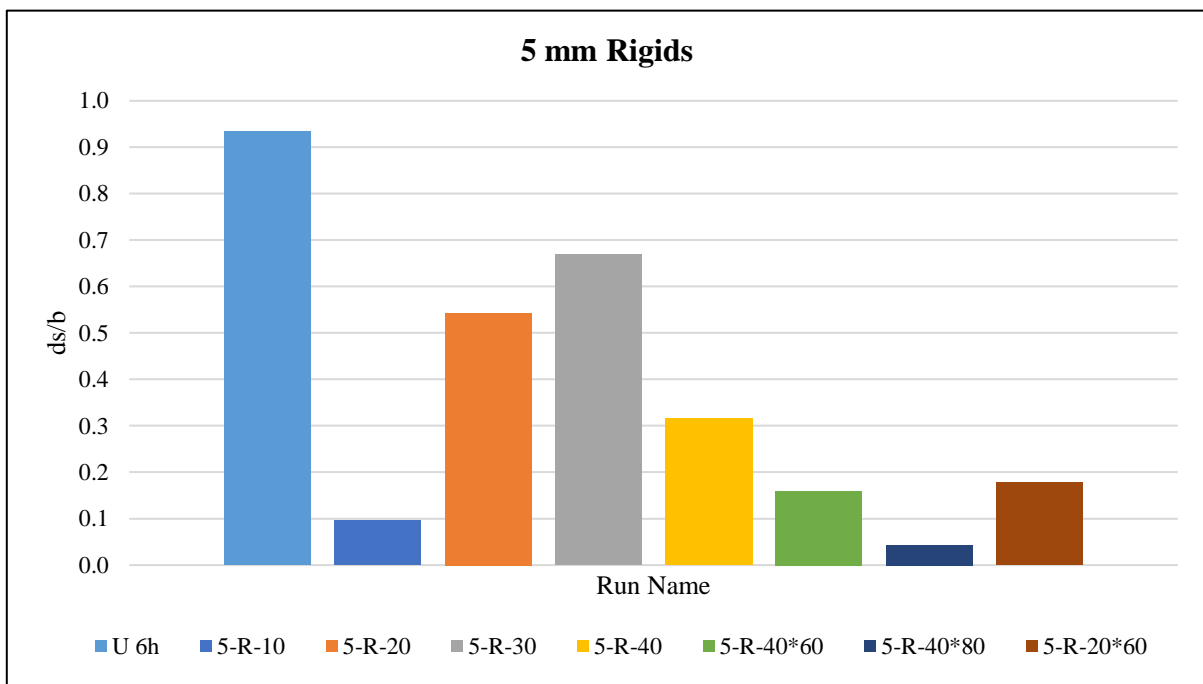


Figure 4.27. Histogram representation of the dimensionless downstream maximum scour depth.

➤ Scour Volumes Categorized into 5 Types:

- Total Scour Volume (Lost Sediments):

Figure 4.28 illustrates that increased coverage and extension of nets result in a reduction in lost sediments.

However, it should be noted that the trend observed with the 10 cm by 10 cm ($W/b=1.59$) net is inconsistent with the other nets, showing significantly lower lost sediments. It is notable that sediment loss occurs even in the protected tests, with some cases surpassing the sediment loss observed in the unprotected test, which is noteworthy. This suggests that sediment loss occurs after the protection provided by the net.

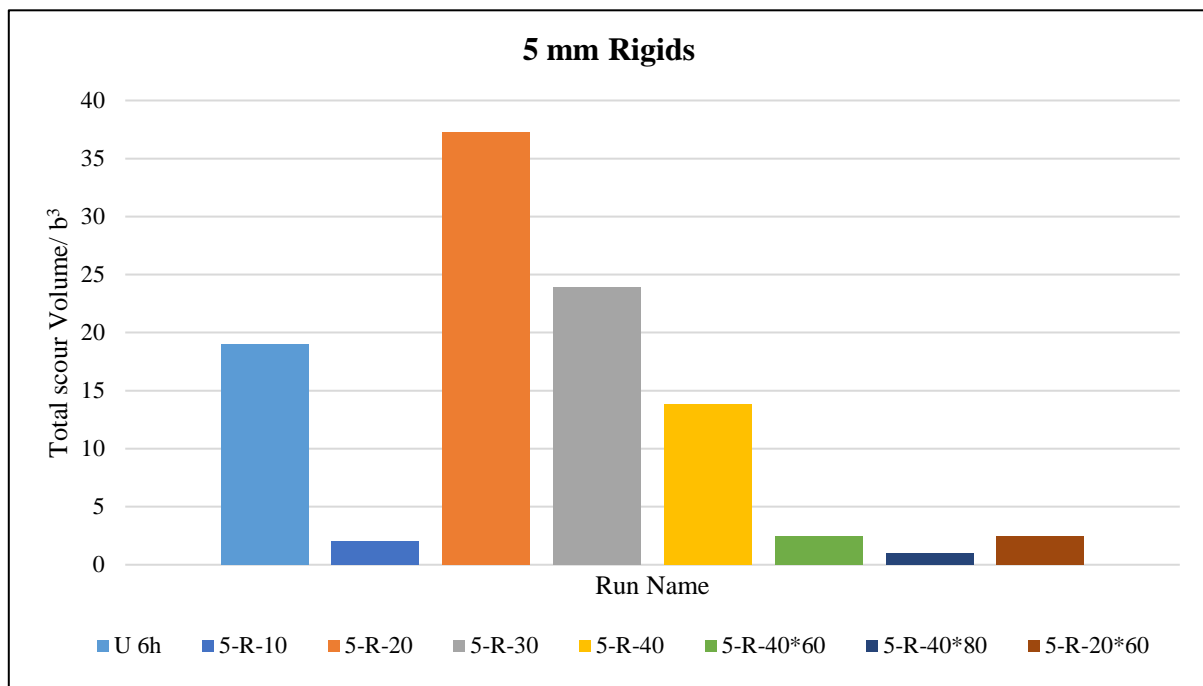


Figure 4.28. Histogram representation of the dimensionless total scour volume.

- Positive Scour Volume (Scoured Sediments):

Figure 4.29 demonstrates that the positive scour volume follows the same trend as the total scour volume, with minimal negative scour volume observed in these fine rigid cases.

- Negative Scour Volume (Accumulated Sediments):

As mentioned previously, a small accumulation of sediment is observed in these protected cases, as shown in figure 4.30. Among the comparisons, the 10 cm by 10 ($W/b=1.59$) cm and 40 cm by 80 ($L/W=2$) cm nets exhibit the highest accumulation.

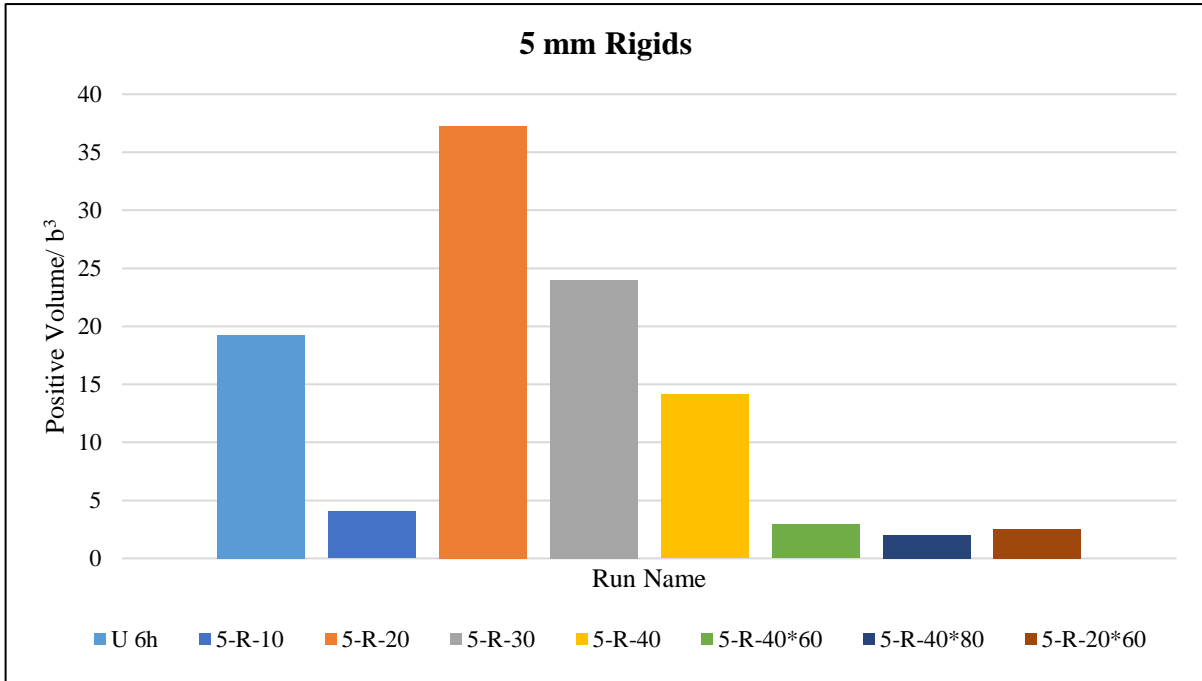


Figure 4.29. Histogram representation of the dimensionless positive scour volume.

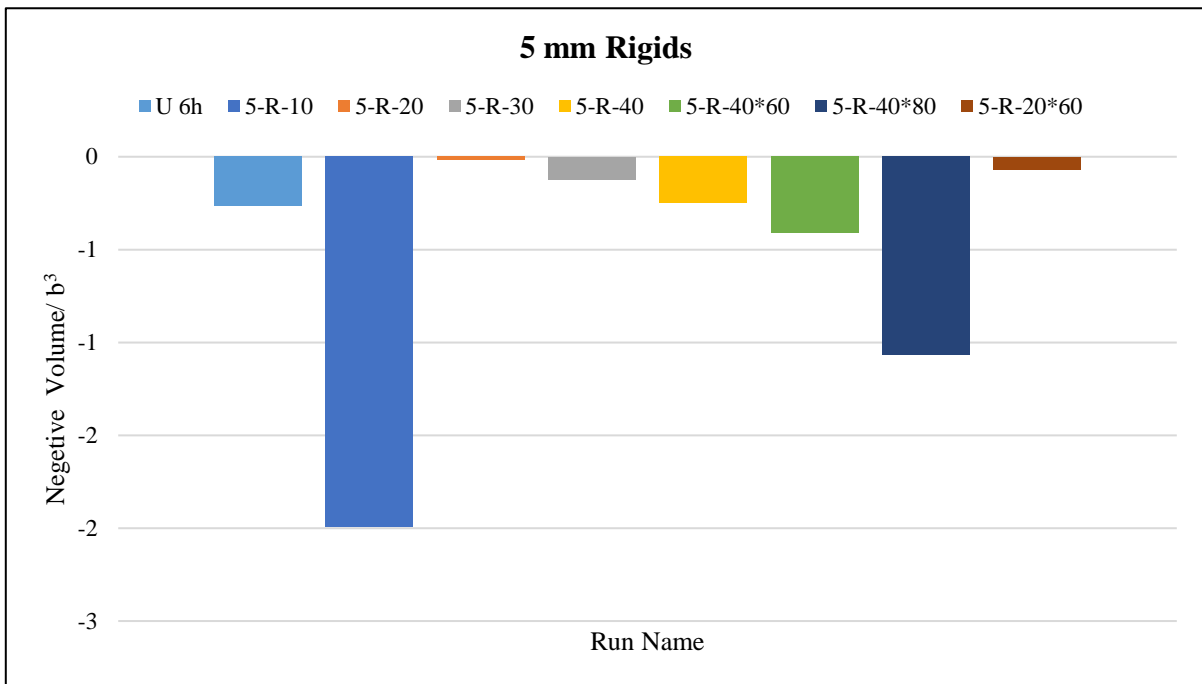


Figure 4.30. Histogram representation of the dimensionless negative scour volume.

- Downstream Scour Volume:

Based on Figure 4.31 and the previously mentioned observations, the downstream scour volume follows the same trend as the total scour volume and positive scour volume because the most volume changes happened in the downstream. Increased coverage leads to a decrease in downstream scour volume.

- Upstream Scour Volume:

Figure 4.32 reveals that the 10 cm by 10 cm (W/b=1.59) net, with minimal coverage, performs poorly in terms of upstream scour volume, showing higher scouring. As explained earlier, covering the entire width of the channel results in increased upstream scour volume, likely due to changes in flow patterns.

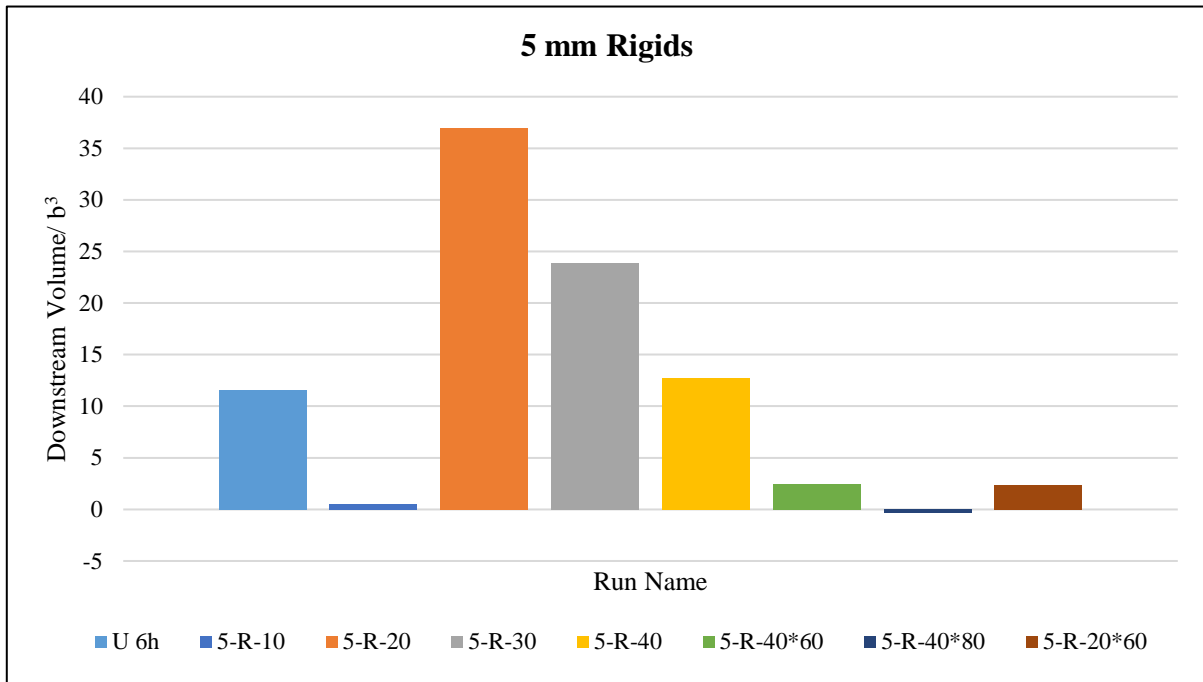


Figure 4.31. Histogram representation of the dimensionless downstream scour volume.

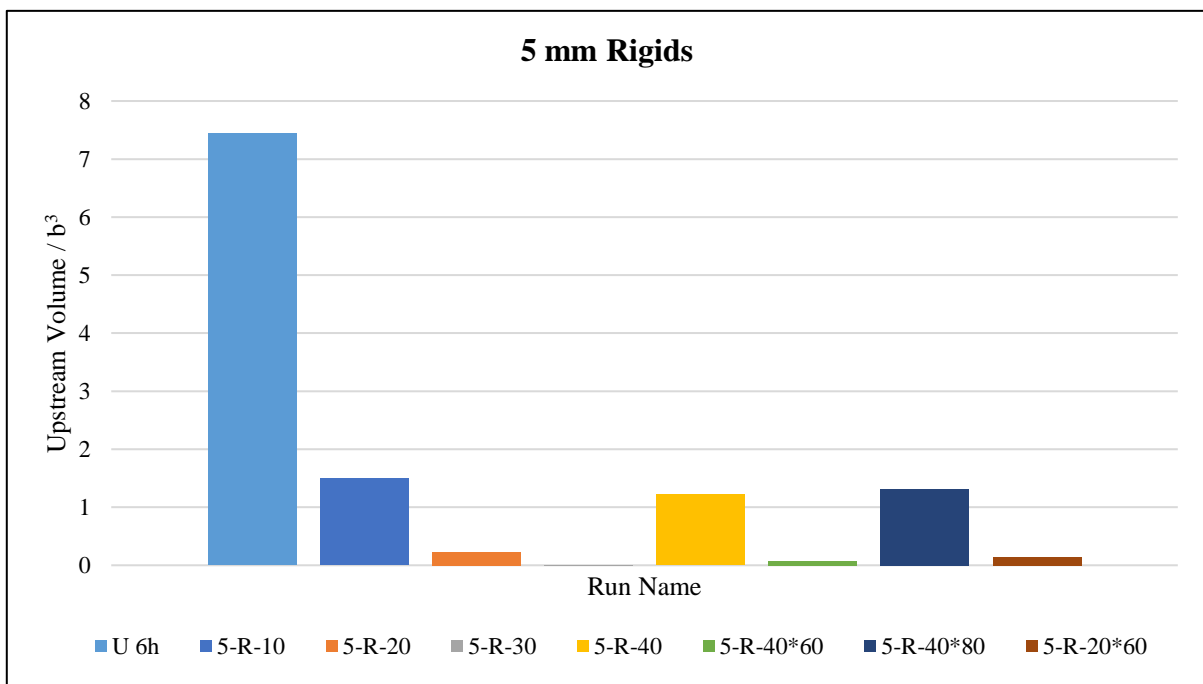


Figure 4.32. Histogram representation of the dimensionless upstream scour volume.

➤ Comparison between Upstream and Downstream Scour Volumes:

An analysis of upstream and downstream scour volumes indicates that these fine nets effectively reduce scouring near the upstream section of the pier. However, significant scouring is observed downstream beyond the nets, which can pose long-term issues and requires further discussion (see Figure 4.33).

In summary, the comparison and analysis of fine mesh nets and unprotected testing reveal important insights regarding their effectiveness in providing protection. The findings highlight a reduction in scour depth upstream, indicating a positive effect in mitigating scour. However, when considering sediment loss and downstream scour volume, the results were not as promising.

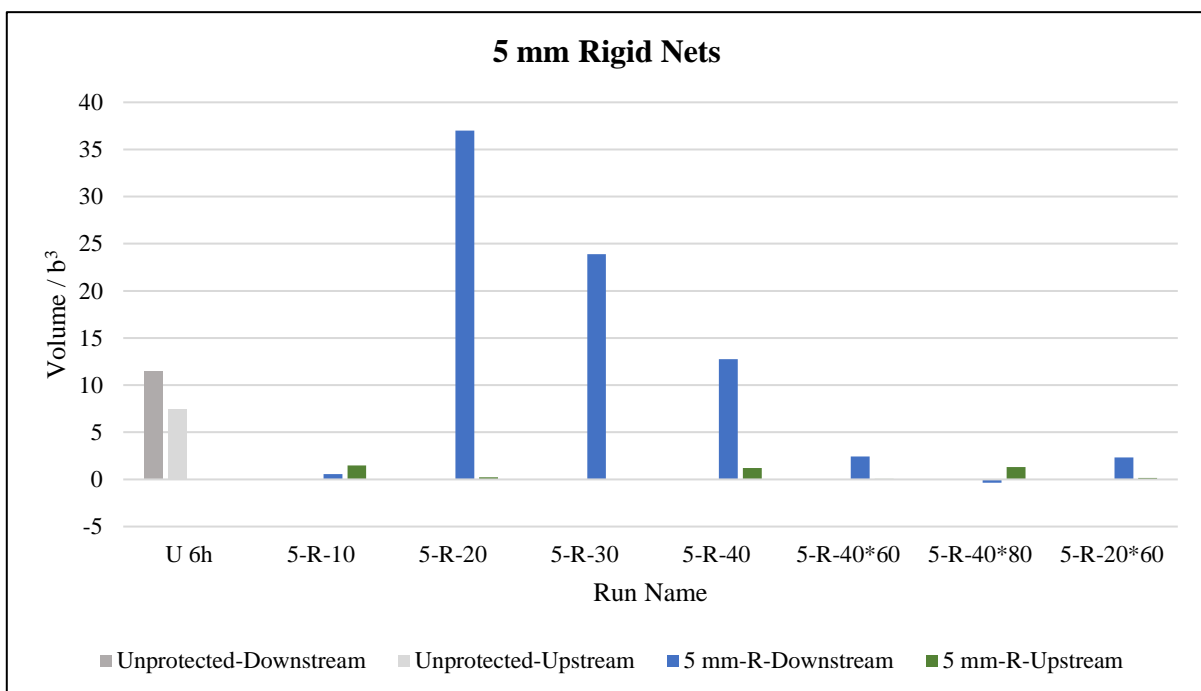


Figure 4.33. Histogram comparison of the dimensionless up and downstream scour volume.

4.2.1.5. Comparison among rigid (coarse and fine mesh) nets

In the previous sections, comparisons were made between coarse and fine rigid nets individually based on the coverage area criterion. Now, it is crucial to compare all these rigid nets and mention the most significant differences based on the impact of mesh size on protection.

It became evident that the fine rigid experiments exhibited superior performance in reducing upstream scouring during the experiments, with over two times less scouring observed, as shown in Figure 4.34.

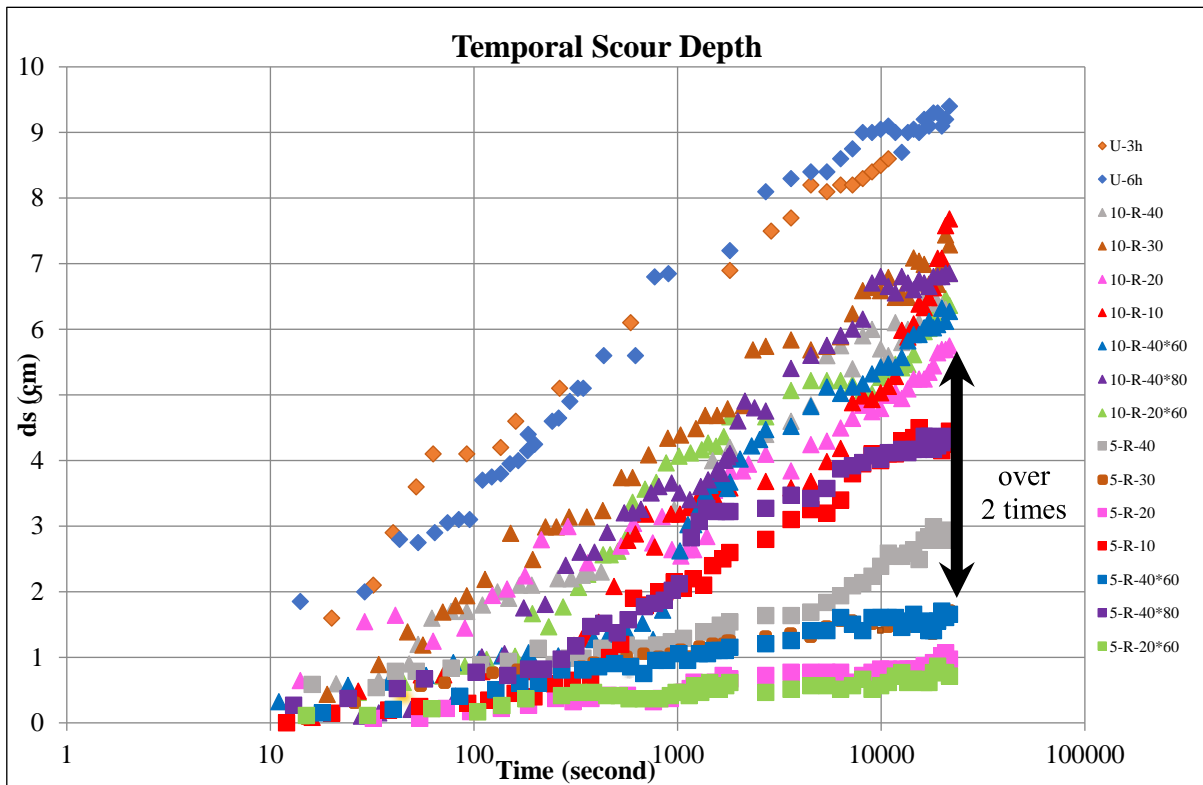


Figure 4.34. Visual comparison of rigid nets in terms of the temporal scour depth. The black arrow indicates over 2 times of difference btw coarse and fine recorded scour depth in the upstream.

The critical region for scouring is identified near the pier in the upstream for both coarse and fine experiments. In the downstream, for coarse nets, the critical scouring area is in the vicinity of the pier, while for fine nets, it occurs beyond the nets. In terms of coarse nets, accumulation of sediments on the nets and channel bed is observed downstream, whereas in the case of fine nets, this accumulation is minimal (Figure 4.35).

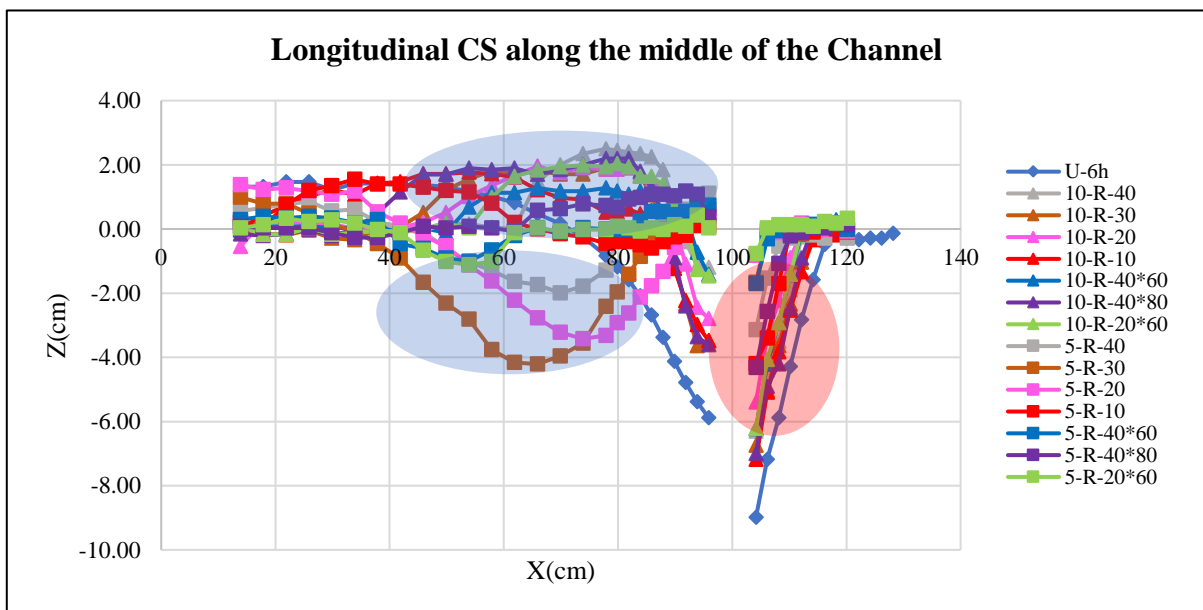


Figure 4.35. Visual comparison of the longitudinal profiles. The red circle indicates the same trend of scouring at upstream of the pier. the blue ovals are indicating the different trend of channel bed change in the downstream of the pier.

An analysis of upstream and downstream scour volumes (see Figure 4.36) indicates that the three mentioned fine nets [20 cm by 20 cm ($W/b=3.17$), 30 cm by 30 cm ($W/b=4.76$), and 40 cm by 40 cm ($W/b=6.35$)] exhibit a significant scour volume in the downstream compared to other nets of any mesh size and coverage area.

Moreover, based on the comparison graph, larger mesh sizes result in higher scour volumes in the upstream, which is reasonable due to the greater permeability of the net.

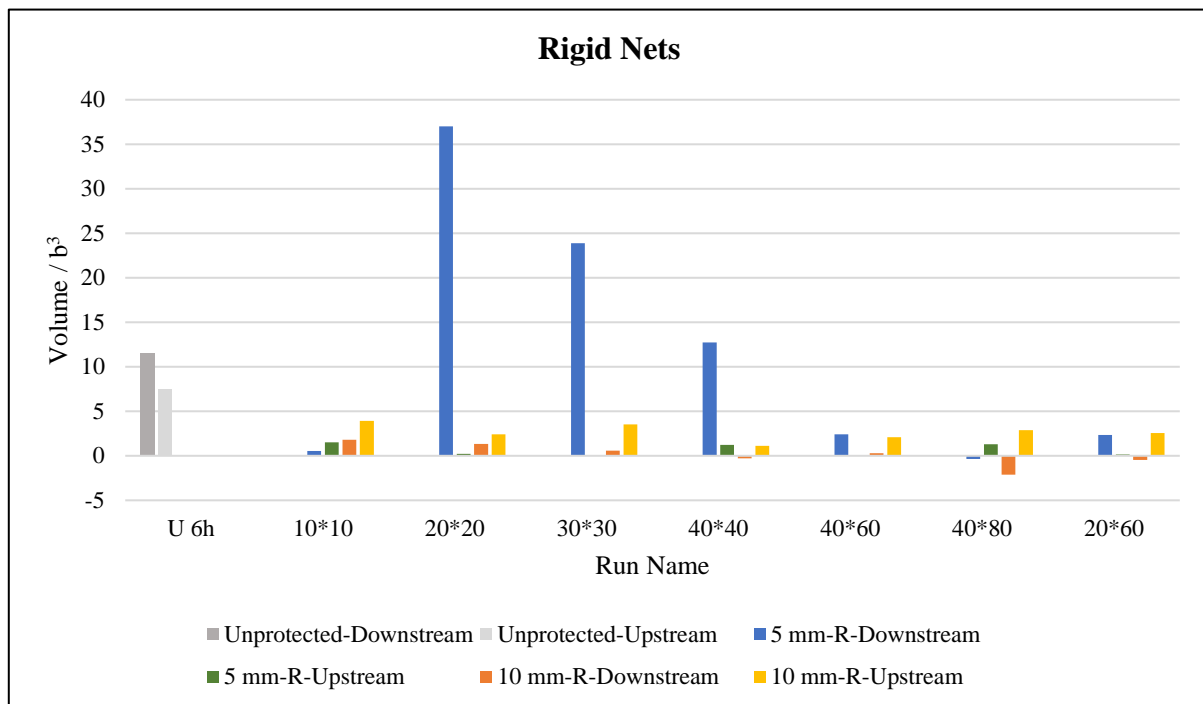


Figure 4.36. Histogram comparison of the dimensionless up and downstream scour volume.

In the end, the conclusion is that, for rigid nets, the coarse mesh is less effective than the fine one in the upstream, still furnishing some reduction. In the downstream the fine mesh produces apron scour beyond the edge of the carpet, while the coarse mesh creates a depositional plume that remains closer to the pier than in unprotected tests.

4.2.2. Flexible Geo-Carpets

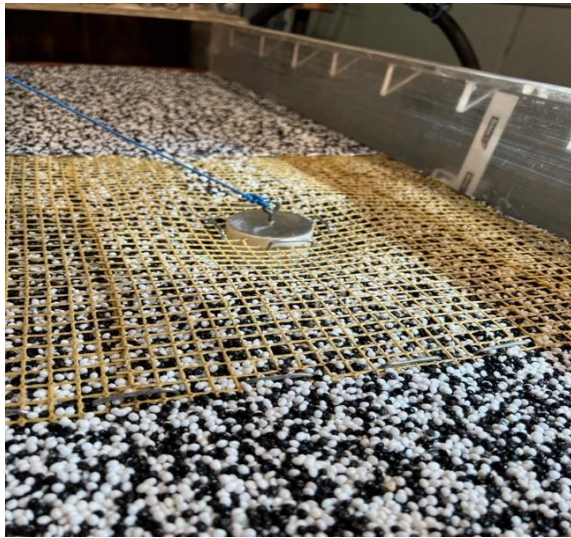
Consisting of two series of nets, both series have the same coverage areas and material flexibility, with the only difference being the mesh size. Furthermore, it should be noted that there are some irregularities in terms of the coverage areas of the extended nets, as mentioned earlier in the laboratory description chapter.

4.2.2.1. Coarse mesh nets

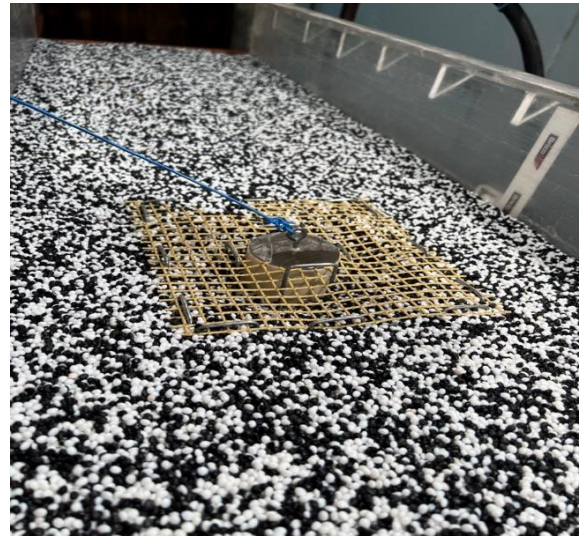
In this series of experiments, six coarse flexible nets were employed, consisting of four square-shaped nets with different coverage dimensions ranging from the entire width of the channel (40 cm by 40 cm) to a smaller size of 10 cm by 10 cm, as exemplified in Figure 4.37.

Moreover, two extended nets were employed, resembling the combined extended net that was utilized in previous series of experiments, as shown in Figure 4.37.

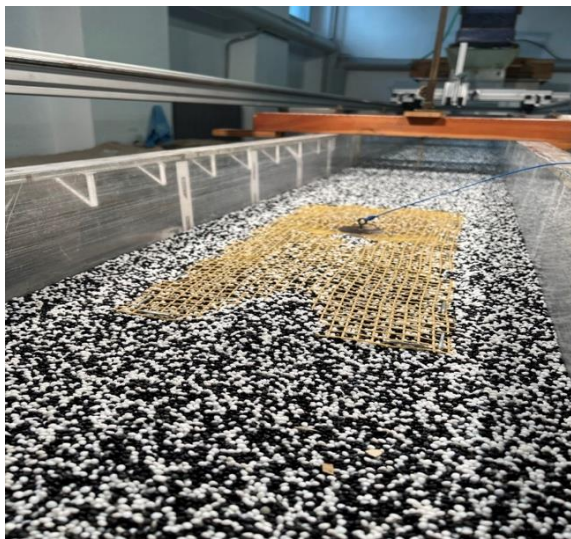
The 3D representation of these series of experiments can be find in Figure 4.38.



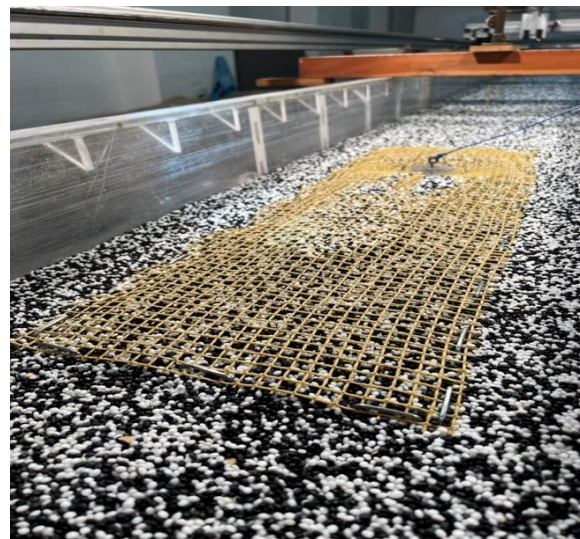
(a)



(b)



(c)



(d)

Figure 4.37. Exemplified applied coarse nets on the channel bed around the pier: (a) front view of the 40 cm by 40 cm net; (b) front view of the 20 cm by 20 cm net; (c) back view of the 25 cm by 60 cm net; (d) back view of the 25 cm by 80 cm net.

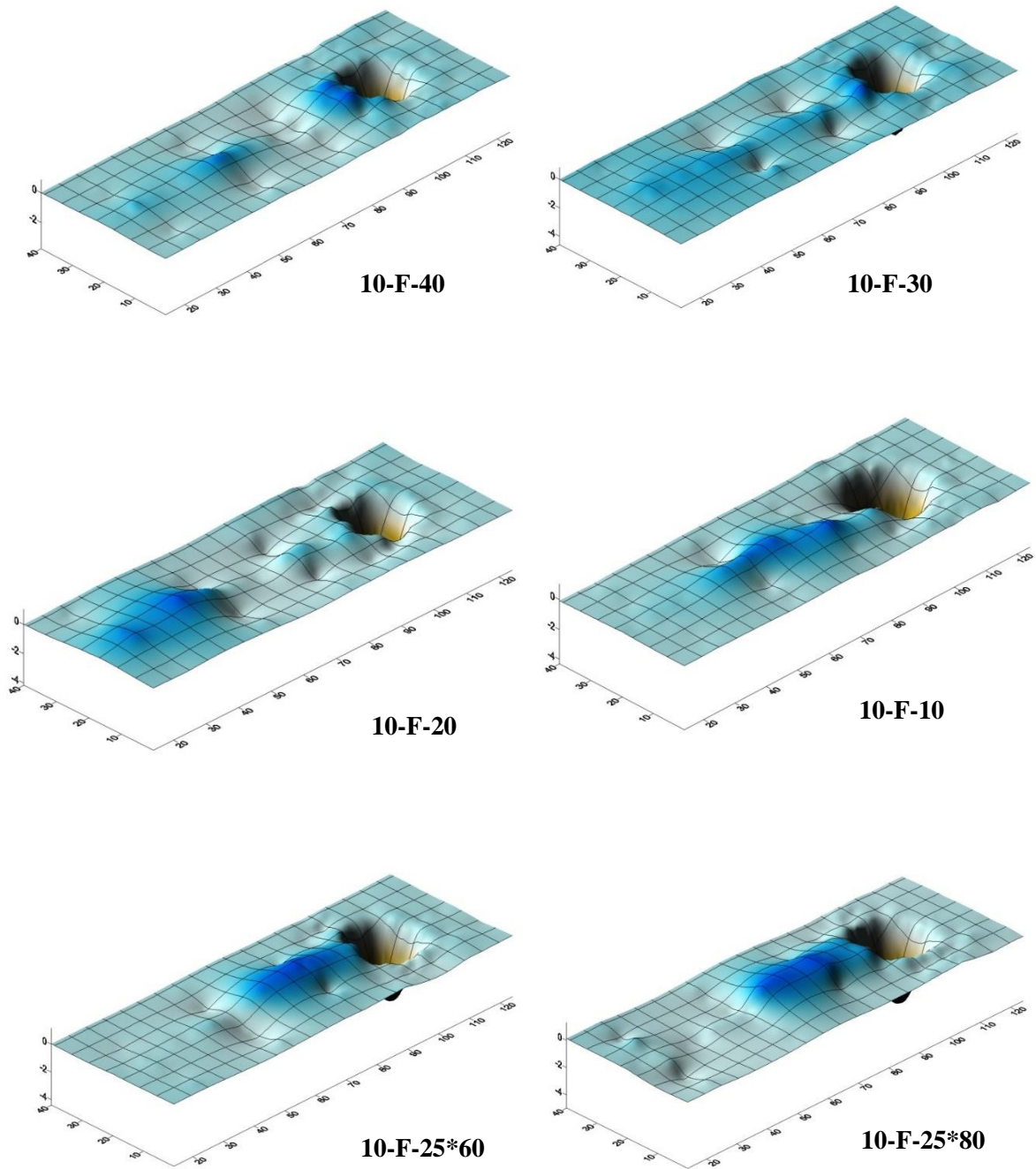


Figure 4.38. The sequence of maps presented 3D surface map.

4.2.2.2. Results, analysis, and comparison of coarse mesh nets and the reference test

In this section, the analysis of coarse flexible nets was performed by comparing them with unprotected reference test, focusing on the coverage area criterion.

The analysis is based on the results of specific graphical data, and a dimensionless framework, which are as follows:

➤ Temporal perspective

The upstream edge of the pier is considered the most critical section of the channel bed, as it is highly susceptible to deep scouring caused by the downward flow led to formation of horseshoe vortices.

By examining the temporal measurements obtained during the experiments with coarse flexible nets (see Figure 4.231), it becomes apparent that all six experiments exhibit a similar trend characterized by an increasing scour depth. The majority of the recorded scouring occurs within the initial hour of the experiments, followed by a gradual increase throughout the 6-hour duration. Comparing the unprotected case with the protected experiments, a significant reduction of approximately 4.5 cm in scour depth is observed.

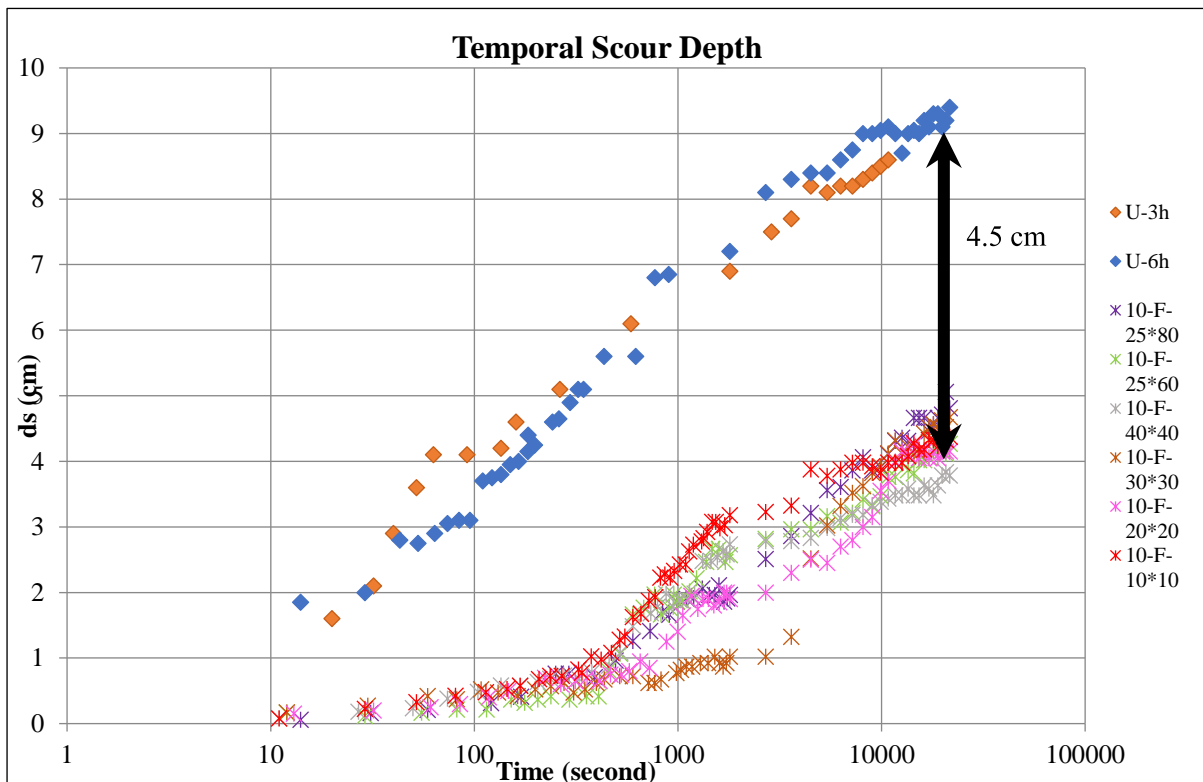


Figure 4.39. Temporal representation of the scour depth. The black arrow is indicating the mean scour depth difference btw the protected and unprotected tests.

➤ Longitudinal perspective:

A longitudinal analysis reveals that all experiments share the same trend in terms of longitudinal profiles (see Figure 4.40). The vicinity of the pier is identified as the most critical region for scouring in the upstream. In the downstream, an accumulation of sediment is observed, extending until the end of the nets. Beyond the nets, there is a slight scouring. While the extension of the nets does not result in a consistent trend, it helps disperse the accumulation and mitigate its concentration.

However, in the case of the 10 cm by 10 cm net, the accumulation extends until the end of the channel, resembling the unprotected scenario. The presence of coarse flexible nets

significantly reduces scouring in the critical region near the pier compared to the unprotected condition.

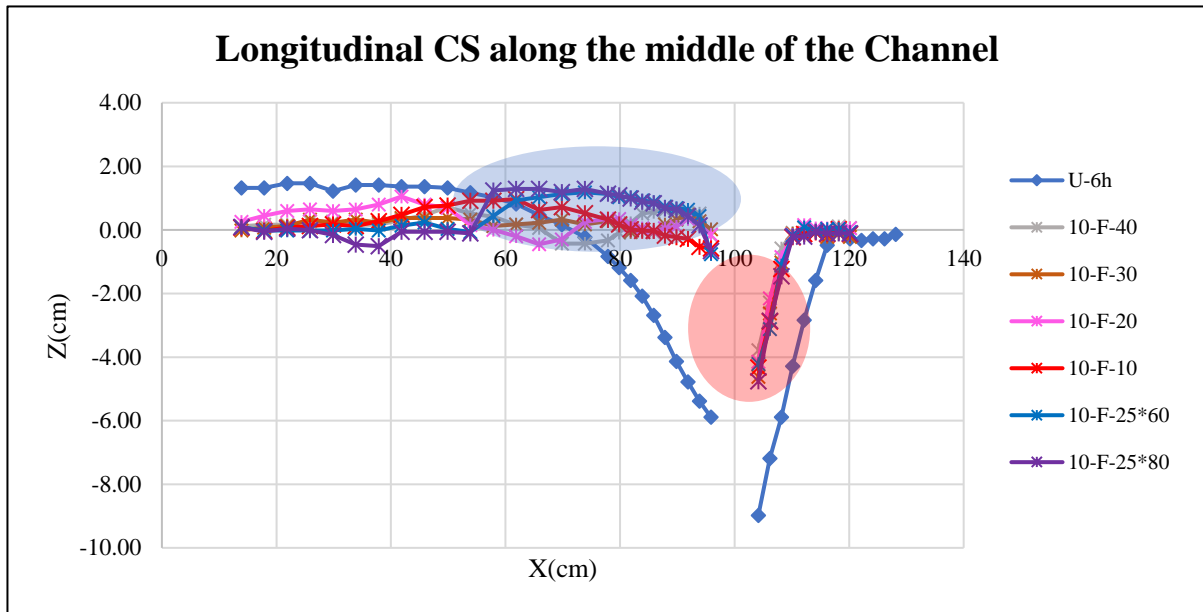


Figure 4.40. Visual representation of the longitudinal profiles. The red circle is indicating the critical area of scouring at upstream edge of the pier, the blue oval is indicating the accumulated eroded sediments in the downstream of the pier.

➤ Transversal perspective:

Figure 4.41 demonstrates that all experiments exhibit identical trend in terms of transversal profiles.

Among the tested scenarios, the 40 cm by 40 cm net yielded the least amount of scouring, while the 25 cm by 80 cm net resulted in the highest level of scouring.

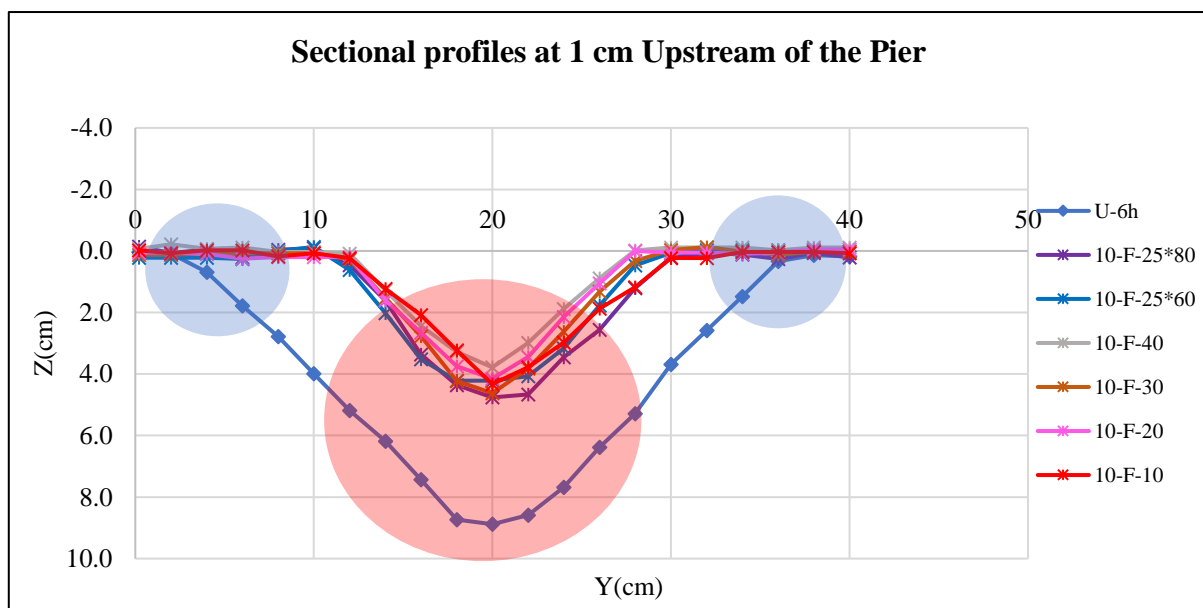


Figure 4.41. Visual representation of the transversal profiles. The blue circles are representing the side of the channel and the middle part of the channel is representing by the red circle.

➤ Location of Maximum Scouring in the Upstream and Downstream of the Pier:

Analyzing the longitudinal cross-section (see Figure 4.40) reveals that, in all cases of coarse flexible nets, the maximum scour depth is observed near the pier in the upstream. In the downstream, the location of maximum scouring does not follow a specific trend, as it varies between near the pier and beyond the net. This irregular distribution of maximum scouring in the downstream could be a result of connecting pieces of nets together to construct the desired coverage areas.

- Upstream Maximum Scour Depth:

Figure 4.42 demonstrates that the 40 cm by 40 cm ($W/b=6.35$) net exhibits the best performance in terms of reducing scouring near the upstream edge of the pier, while the 30 cm by 30 cm ($W/b=4.76$) and 25 cm by 80 cm ($L/W=3.2$) nets represent the worst cases. Generally, greater coverage with square-shaped nets leads to less scouring, except for the 30 cm by 30 cm ($W/b=4.76$) net, which may be due to incomplete installation. It is worth noting that extending the nets does not yield improvements in reducing upstream scouring. Nevertheless, in all cases, the scour depth is lower compared to the unprotected condition.

- Downstream Maximum Scour Depth:

Figure 4.43 illustrates that as the coverage around the pier increases, there is a corresponding decrease in scouring downstream near the pier. This reduction in scouring continues up to a certain point, beyond which the 40 cm by 40 cm ($W/b=6.35$) net exhibits a higher level of scouring compared to the 30 cm by 30 cm ($W/b=4.76$) net size. However, extending the nets downstream does not contribute to a further reduction in scouring. The 30 cm by 30 cm ($W/b=4.76$) net performs the best in terms of minimizing downstream scouring, while the 10 cm by 10 cm ($W/b=1.59$) net and two extended nets represent the worst cases. Importantly, all protected cases exhibit lower scouring compared to the unprotected scenario.

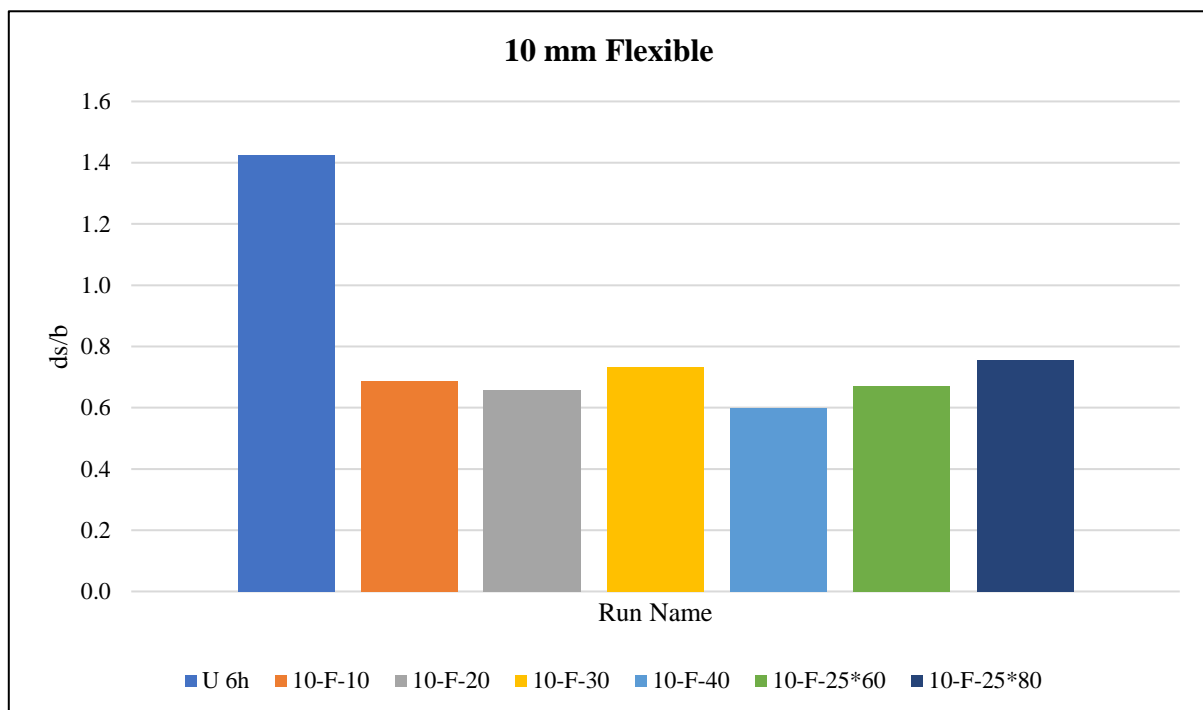


Figure 4.42. Histogram representation of the dimensionless upstream maximum scour depth.

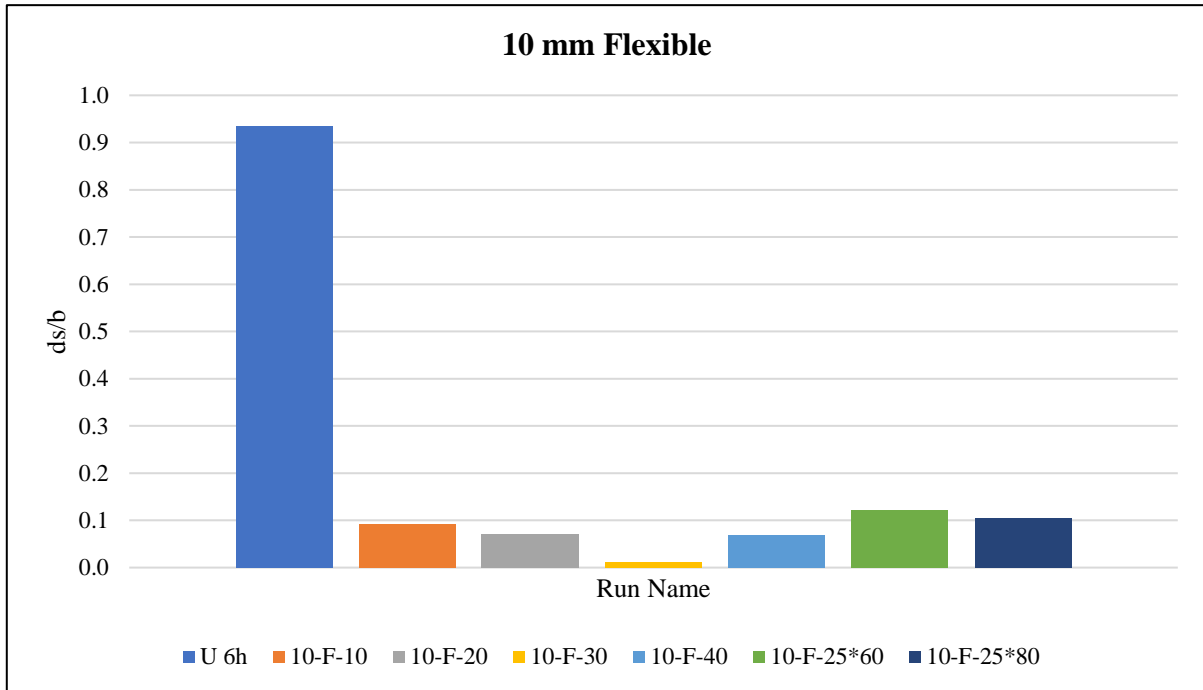


Figure 4.43. Histogram representation of the dimensionless downstream maximum scour depth.

➤ Scour Volumes Categorized into 5 Types:

- Total Scour Volume (Lost Sediments):

The total scour volume represents the cumulative sum of positive and negative volumes or the combined downstream and upstream volumes, indicating the sediment volume lost into the outlet tank. Figure 4.44 illustrates that increased coverage and extension of nets lead to a reduction in lost sediments, except for the 30 cm by 30 cm ($W/b=4.76$) and 25 cm by 80 cm ($L/W=3.2$) nets, which experience more sediment loss. However, it should be noted that the unprotected test, serving as the worst case, exhibits a significant difference with nine times more sediment loss compared to the cases where geo-carpets were employed as scouring countermeasures.

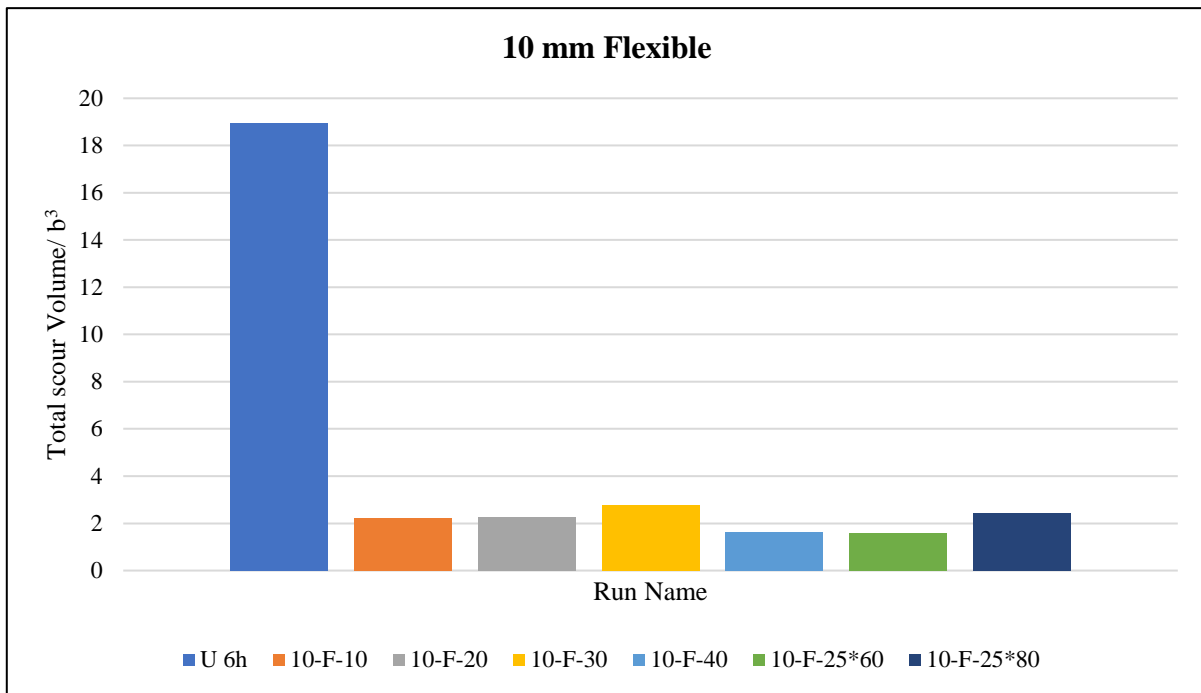


Figure 4.44. Histogram representation of the dimensionless total scour volume.

- Positive Scour Volume (Scoured Sediments):

Figure 4.45 demonstrates that the best-performing net in terms of minimizing positive scour volume (i.e., sediments scoured) is the 40 cm by 40 cm ($W/b=6.35$) net, while the 25 cm by 80 cm ($L/W=3.2$) net represents the worst case. Up to the 40 cm by 40 cm ($W/b=6.35$) net size, greater coverage leads to less positive scour volume, but extending the nets downstream does not help and results in more positive scour volume.

The unprotected test exhibits a substantial difference, with five times more sediment scouring compared to the other cases employing geo-carpets.

- Negative Scour Volume (Accumulated Sediments):

The unprotected test records a lower volume of sediment accumulation, as shown in Figure 4.46, which is expected considering the significant sediment loss during the experiment.

Overall, it can be stated that greater coverage leads to higher accumulation. However, it is worth mentioning that the 30 cm by 30 cm ($W/b=4.76$) geo-carpet demonstrates a low accumulation volume.

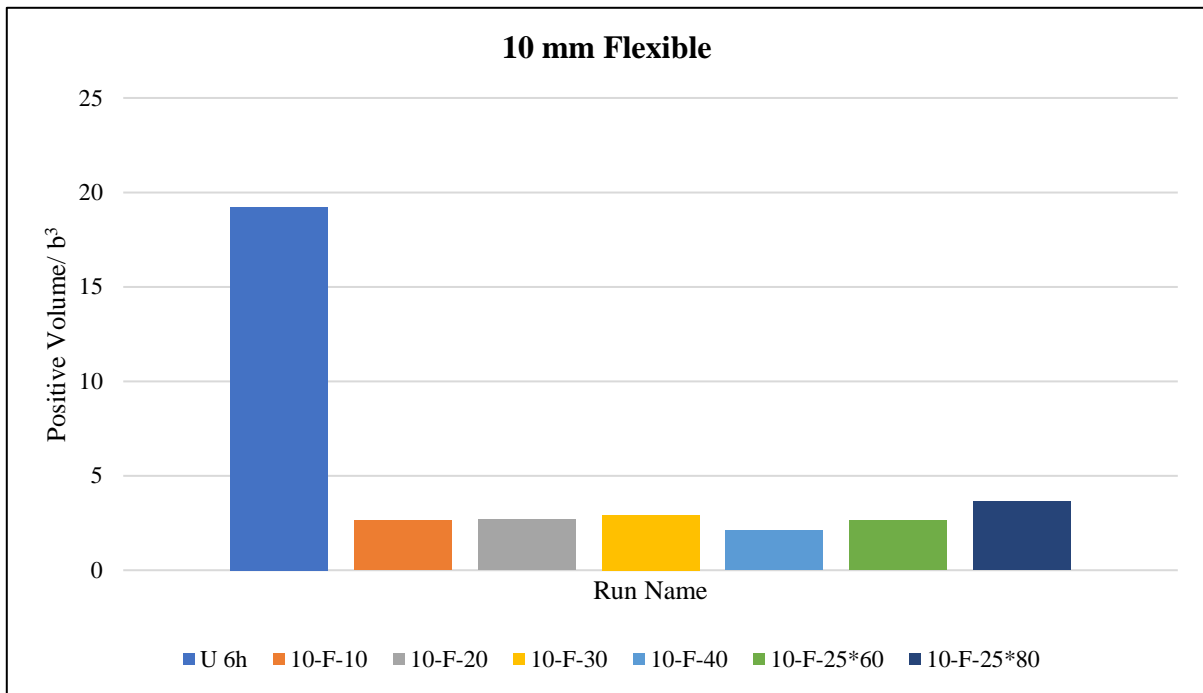


Figure 4.45. Histogram representation of the dimensionless positive scour volume.

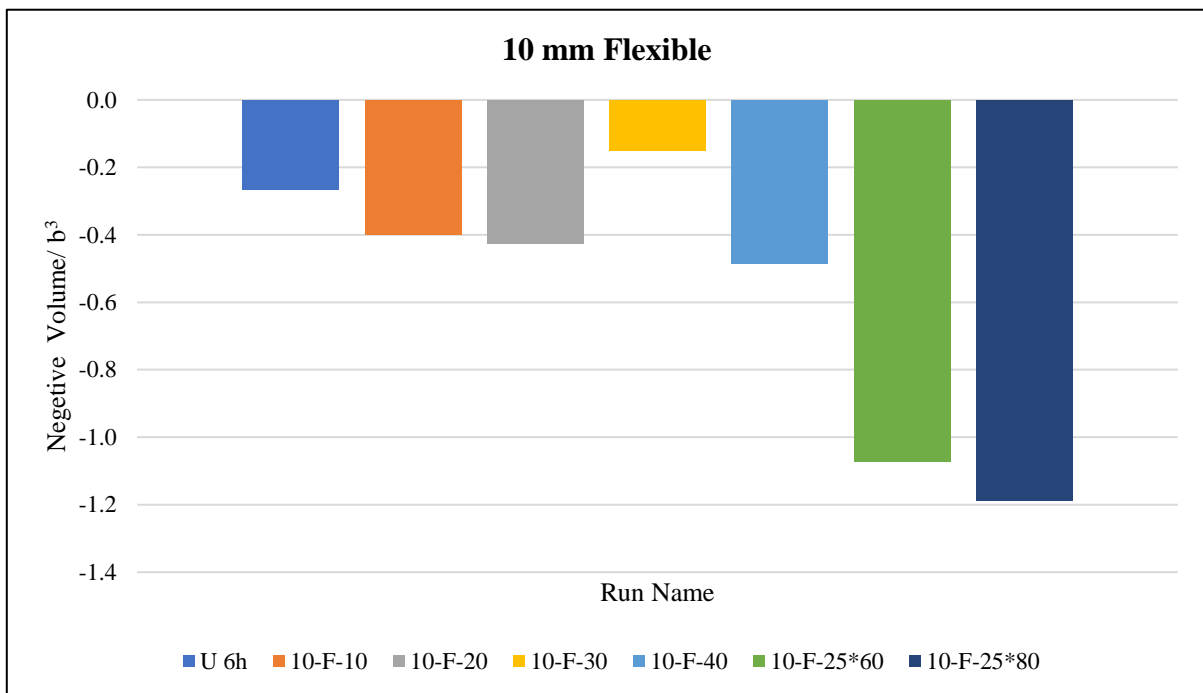


Figure 4.46. Histogram representation of the dimensionless negative scour volume.

- Downstream Scour Volume:

The downstream scour volume is the sum of positive and negative scour volumes from the middle of the pier to the end of the downstream surveyed area. Figure 4.47 indicates that less coverage results in a higher positive scour volume, leading to a positive downstream volume. On the other hand, extending the nets leads to a low downstream volume due to increased accumulation. The unprotected test exhibits a substantial downstream scour volume, six times higher than the protected cases, highlighting the effectiveness of the protection measures.

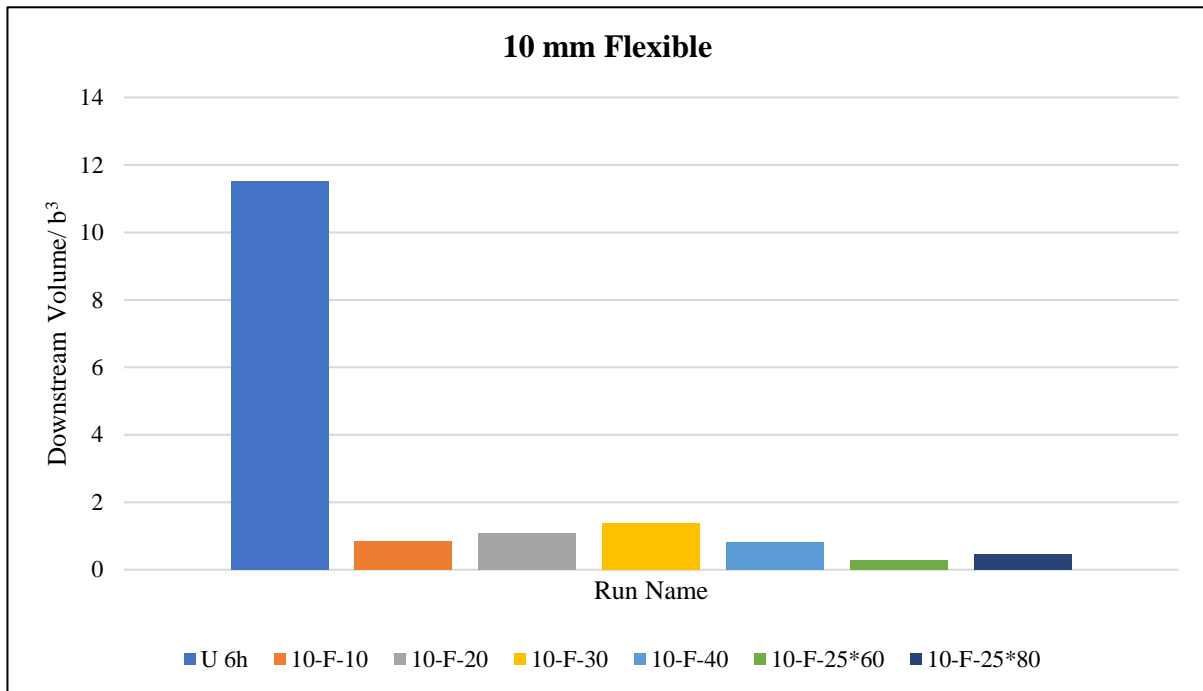


Figure 4.47. Histogram representation of the dimensionless downstream scour volume.

- Upstream Scour Volume:

The upstream scour volume represents the sum of positive and negative scour volumes from the middle of the pier to the end of the upstream surveyed area. Figure 4.48 reveals that greater coverage with square-shaped nets leads to a lower positive scour volume, resulting in a lower upstream volume. However, extending the nets results in worse performance, with an increase in upstream scour volume.

The unprotected test exhibits a significantly higher upstream scour volume, four times more than the protected cases, underscoring the effectiveness of the protection measures.

- Comparison between Upstream and Downstream Scour Volumes:

An analysis of upstream and downstream scour volumes does not reveal a clear trend (see Figure 4.49).

Nevertheless, it can be inferred that the 40 cm by 40 cm ($W/b=6.35$) nets provide the best protection for both upstream and downstream volumes of the pier due to their balanced

performance. Extending the net downstream contributes to the downstream volume of the pier and reduces scouring.

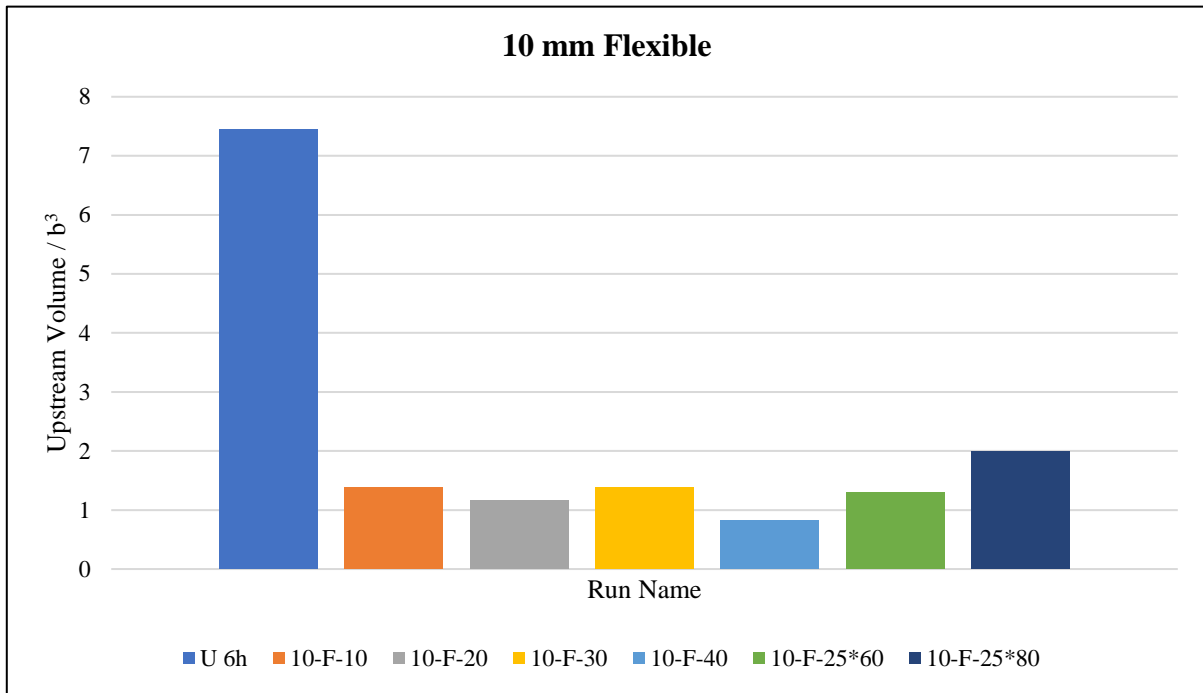


Figure 4.48. Histogram representation of the dimensionless upstream scour volume.

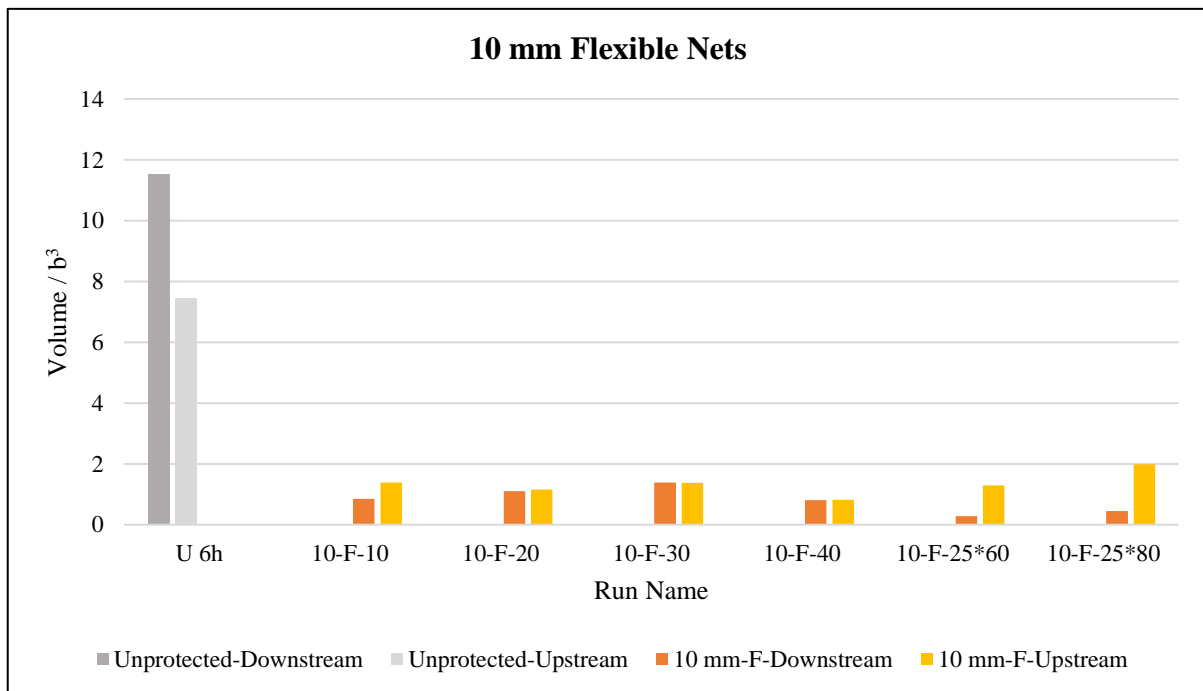


Figure 4.49. Histogram comparison of the dimensionless up and downstream scour volume.

4.2.2.3. Fine mesh nets

In this series of experiments, a total of seven fine flexible nets were utilized, with coverage areas identical to those of the previous series of experiments.

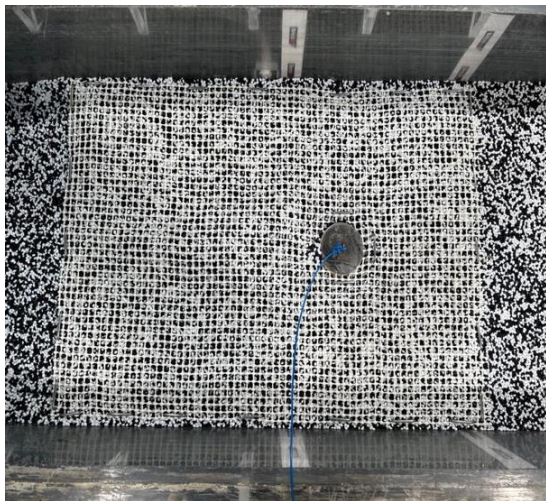
Examples of these fine flexible nets are presented in Figure 4.50, while the corresponding 3D schematics can be found in Figure 4.51.



(a)



(b)



(c)



(d)

Figure 4.50. Exemplified applied fine nets on the channel bed around the pier: (a) back view of the 30 cm by 30 cm net; (b) front view of the 10 cm by 10 cm net; (c) top view of the 40 cm by 60 cm net; (d) front view of the 20 cm by 60 cm net.

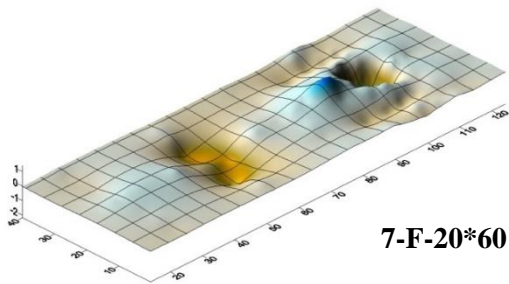
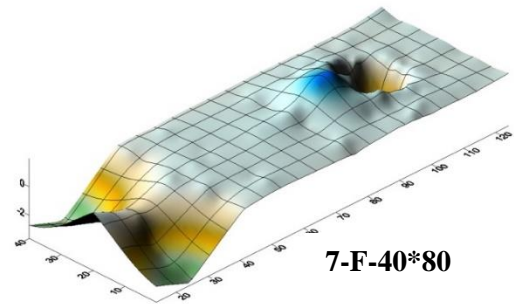
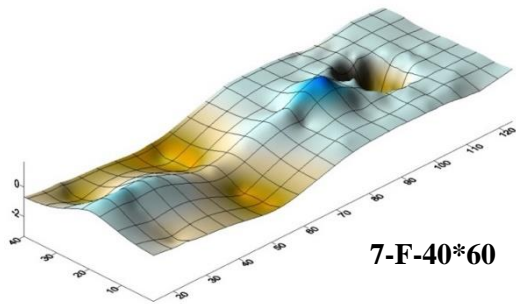
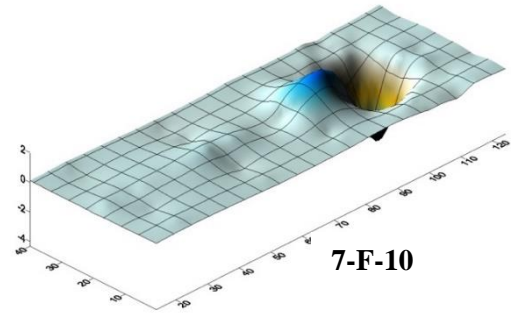
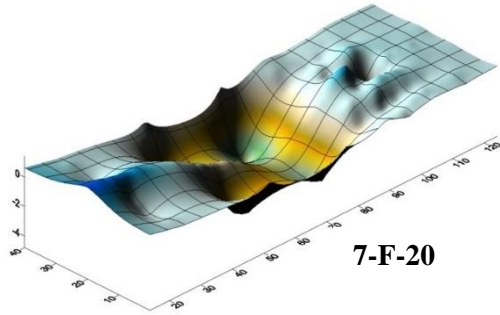
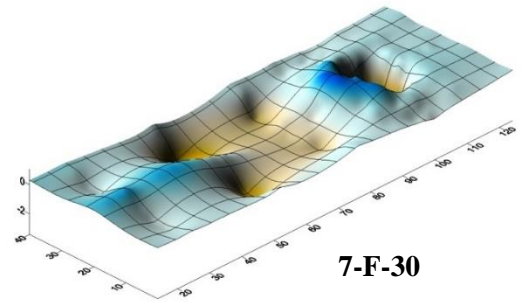
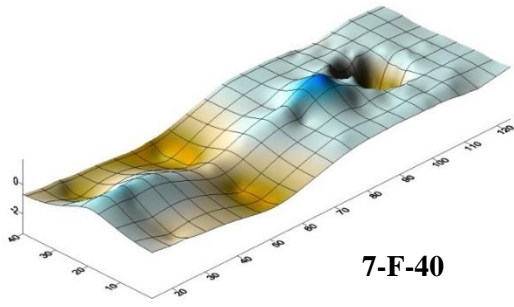


Figure 4.51. The sequence of maps presented 3D surface map.

4.2.2.4. Results, analysis, and comparison of fine mesh nets and the reference test

In this section, the analysis of fine flexible nets was performed by comparing them with unprotected reference test, focusing on the coverage area criterion.

The analysis is based on the results of specific graphical data, and a dimensionless framework, which are as follows:

➤ Temporal perspective

Analyzing the temporal measurements obtained from the fine flexible experiments (Figure 4.52) unveils a consistent trend across all seven experiments. This trend is characterized by an escalating scour depth over time. The majority of scouring occurs within the initial hour, followed by a gradual increase throughout the 6-hour duration. Notably, there is a significant average reduction of approximately 6 cm in scour depth.

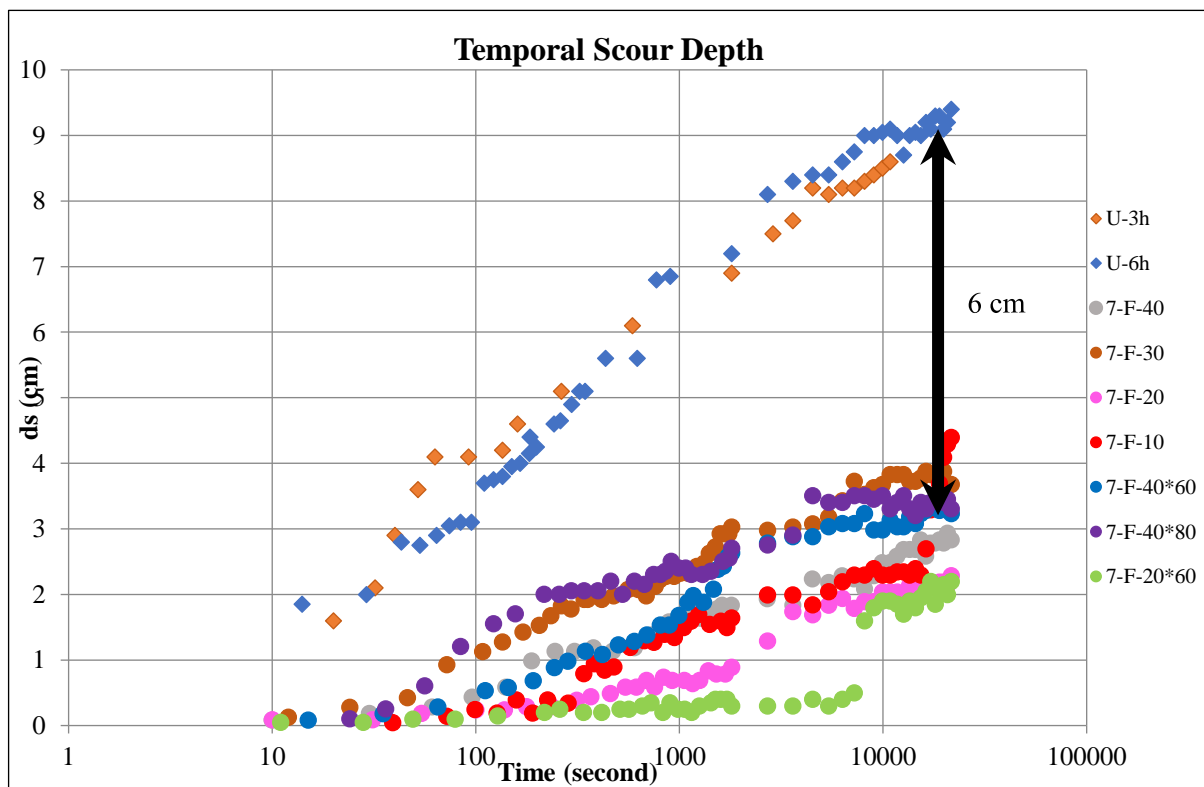


Figure 4.52. Temporal representation of the scour depth. The black arrow is indicating the mean scour depth difference btw the protected and unprotected tests.

➤ Longitudinal perspective:

Evaluation of the longitudinal cross-sections (see Figure 4.53) reveals that all experiments follow a common trend in terms of the shape of the longitudinal profile. The critical region for scouring is identified near the upstream section of the pier, followed by sediment accumulation downstream, extending until the end of the nets. Beyond the nets, noticeable scouring is observed in all cases. It is important to note that less coverage results in deeper scouring beyond

the net, while extending the nets downstream reduces the magnitude of scouring. However, the behavior of the 10 cm by 10 cm net differs and does not follow the aforementioned trend, resembling the unprotected scenario. The presence of fine flexible nets significantly reduces scouring near the pier compared to the unprotected condition.

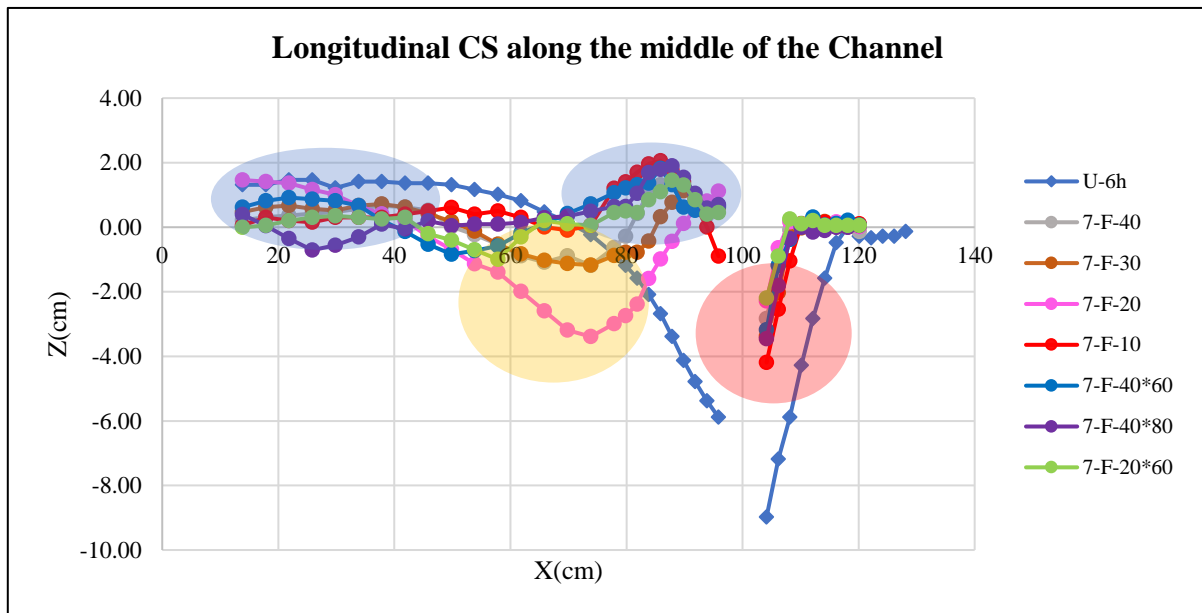


Figure 4.53. Visual representation of the longitudinal profiles. The red circle is indicating the critical area of scouring at 1 cm upstream edge of the pier, the blue ovals are indicating the accumulated eroded sediments in the downstream of the pier, the yellow circle is indicating the scouring beyond the nets.

➤ Transversal perspective:

Figure 4.54 demonstrates that all experiments exhibit identical trend in terms of transversal profiles. Among the tested scenarios, the 20 cm by 20 cm and 20 cm by 60 cm nets yielded the least amount of scouring, while the 10 cm by 10 cm net resulted in the highest level of scouring.

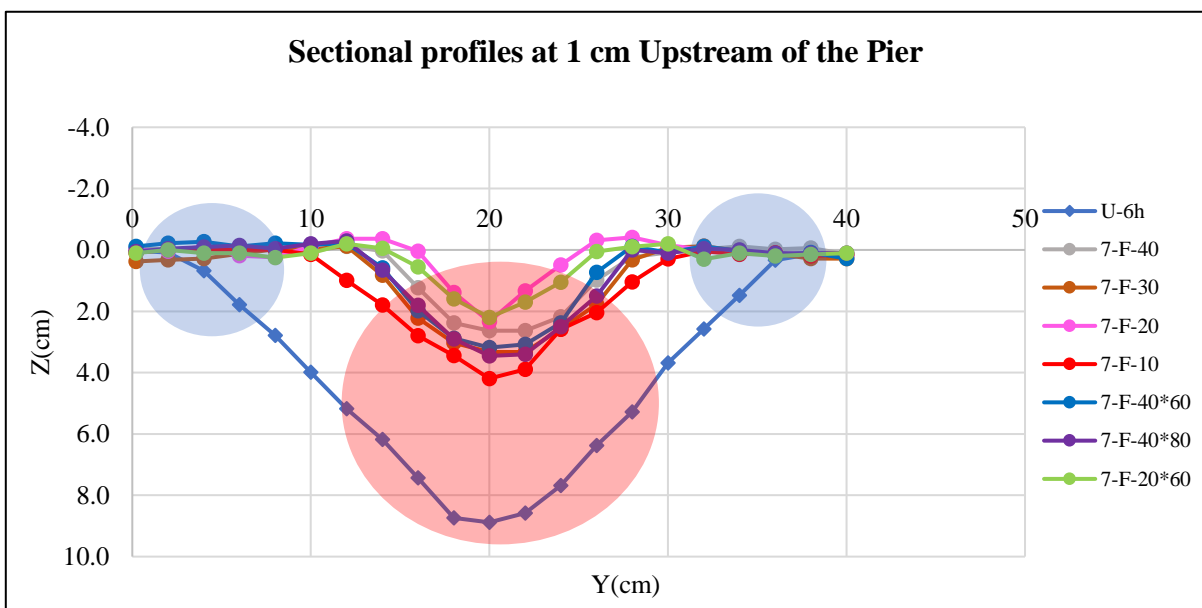


Figure 4.54. Visual representation of the transversal profiles. The blue circles are representing the side of the channel and the middle part of the channel is representing by the red circle.

➤ Location of Maximum Scouring in the Upstream and Downstream of the Pier:

Analyzing the longitudinal cross-sections (refer to Figure 4.53) reveals that in all cases of fine flexible nets, the maximum scour depth is observed near the pier in the upstream and beyond the net in the downstream.

- Upstream Maximum Scour Depth:

Figure 4.55 demonstrates that the 20 cm by 20 cm ($W/b=3.17$) and 20 cm by 60 cm ($L/W=3$) nets exhibit the most effective performance in reducing scouring near the upstream edge of the pier, while the 10 cm by 10 cm ($W/b=1.59$) and 40 cm by 80 cm ($L/W=2$) nets represent the least favorable scenarios. Extending the nets does not yield improvements in reducing upstream scouring, except for the 20 cm by 60 cm ($L/W=3$) net, which performs effectively. It is also worth noting that leaving the sides of the channel bed unprotected results in less upstream scouring, likely due to changes in flow patterns caused by covering the entire width of the channel. However, in all cases, the scour depth is significantly lower compared to the unprotected condition.

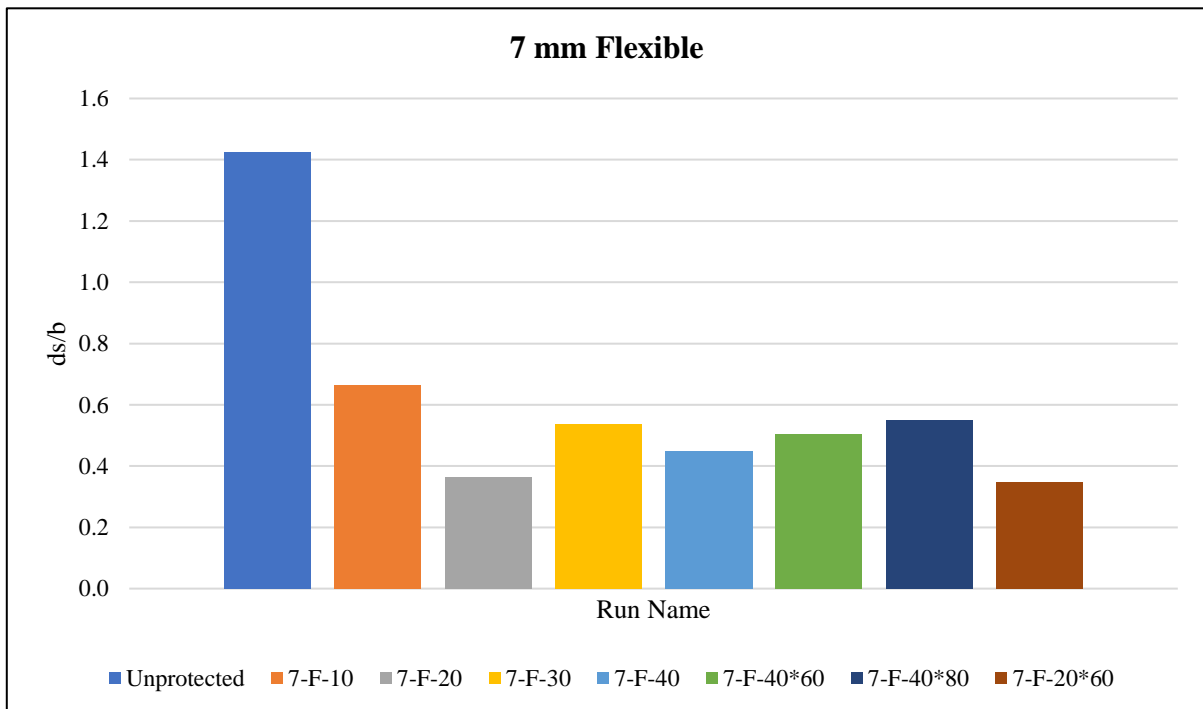


Figure 4.55. Histogram representation of the dimensionless upstream maximum scour depth.

- Downstream Maximum Scour Depth:

Figure 4.56 indicates that square-shaped coverage areas around the pier exhibit more downstream scouring near the pier compared to the extended nets. The 40 cm by 80 cm ($L/W=2$) net performs the best in terms of minimizing downstream scouring, while the 20 cm by 20 cm ($W/b=3.17$) net represents the least effective case, with a notable difference compared to other nets.

Importantly, all protected cases exhibit lower scouring compared to the unprotected scenario.

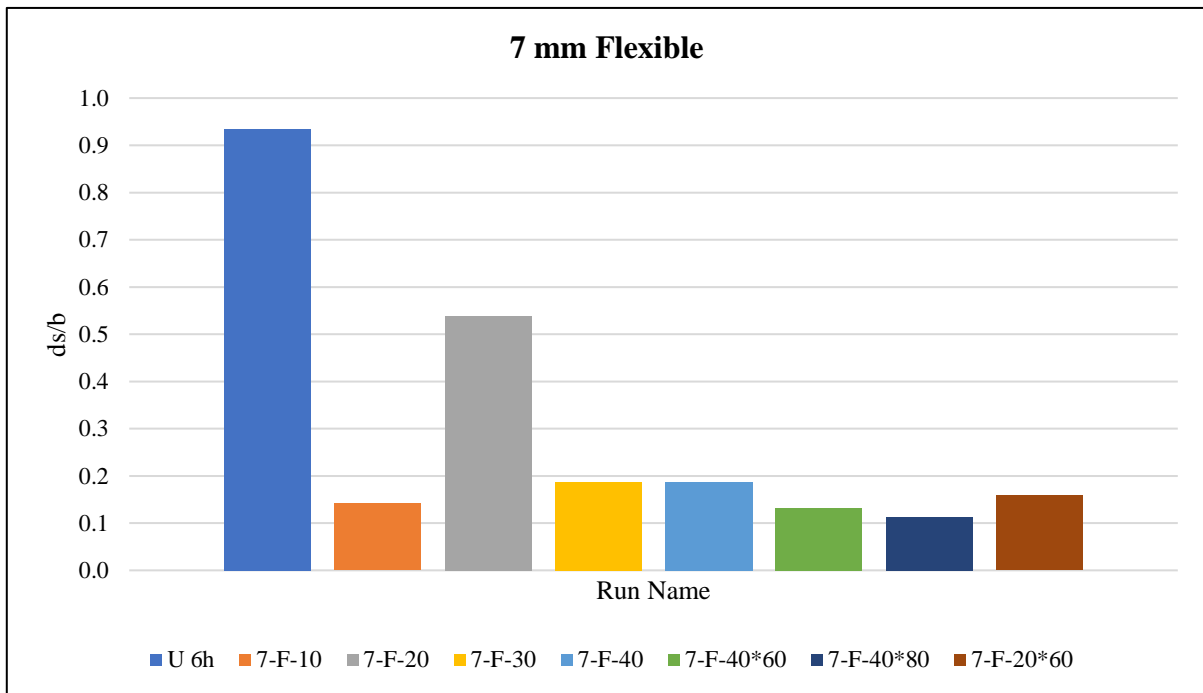


Figure 4.56. Histogram representation of the dimensionless downstream maximum scour depth.

➤ Scour Volumes Categorized into 5 Types:

- Total Scour Volume (Lost Sediments):

Figure 4.57 illustrates that increased coverage and extension of nets result in a reduction in lost sediments. However, it should be noted that the trend observed with the 10 cm by 10 cm ($W/b=1.59$) net is inconsistent with the other nets, showing significantly lower lost sediments. Notably, even the 20 cm by 20 cm ($W/b=3.17$) net experiences more sediment loss compared to the unprotected test, which is noteworthy. This suggests that sediment loss occurs even with the protection provided by the net.

- Positive Scour Volume (Scoured Sediments):

Figure 4.58 demonstrates that the positive scour volume follows the same trend as the total scour volume, with minimal negative scour volume observed in these fine flexible cases.

- Negative Scour Volume (Accumulated Sediments):

As mentioned previously, a small accumulation of sediment is observed in these protected cases, as shown in Figure 4.59. Among the comparisons, the 10 cm by 10 cm ($W/b=1.59$) and 40 cm by 80 cm ($L/W=2$) nets exhibit the highest accumulation.

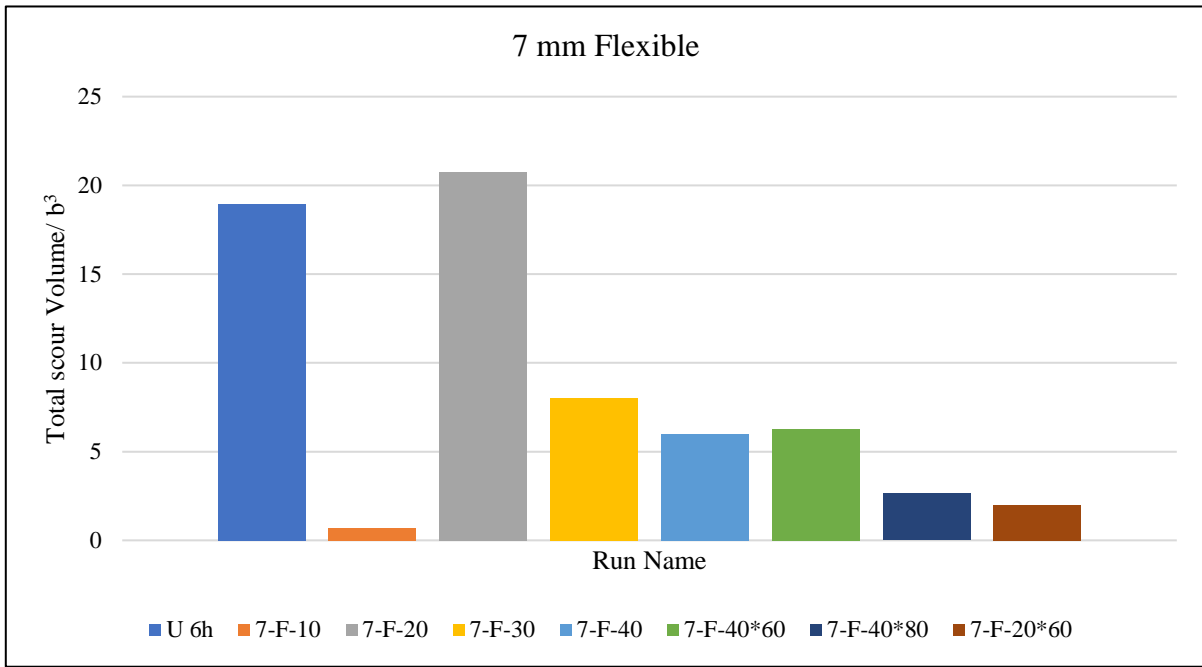


Figure 4.57. Histogram representation of the dimensionless total scour volume.

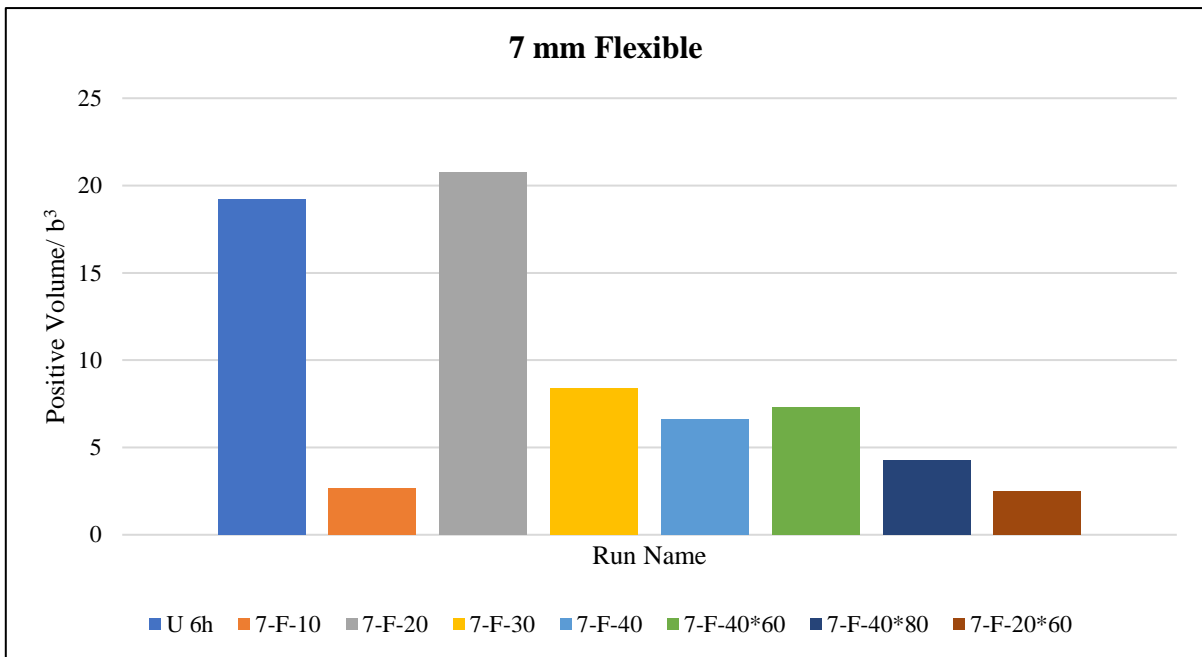


Figure 4.58. Histogram representation of the dimensionless positive scour volume.

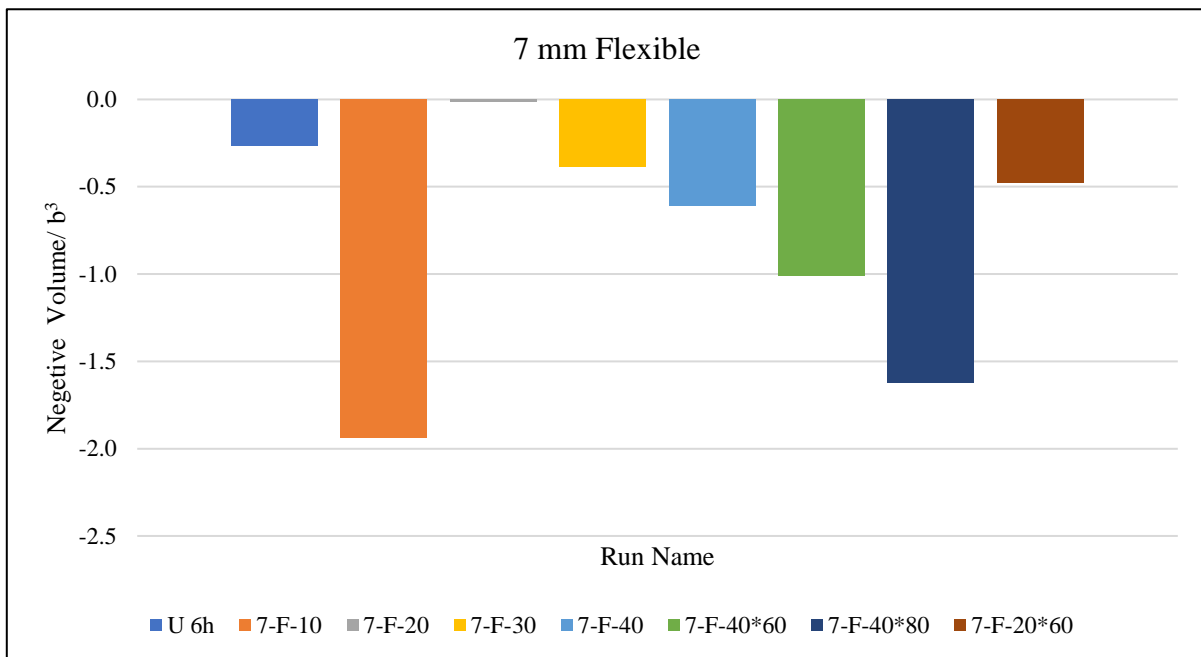


Figure 4.59. Histogram representation of the dimensionless negative scour volume.

- Downstream Scour Volume:

Based on Figure 4.60 and the previously mentioned observations, the downstream scour volume follows the same trend as the total scour volume and positive scour volume due to the significant volume changes occurring downstream. Increased coverage leads to a decrease in downstream scour volume. The 20 cm by 20 cm ($W/b=3.17$) net performs the worst, with a substantial difference compared to other nets.

- Upstream Scour Volume:

Figure 4.61 reveals that the 10 cm by 10 cm ($W/b=1.59$) net, with minimal coverage, performs poorly in terms of upstream scour volume, exhibiting higher scouring. As explained earlier, covering the entire width of the channel results in increased upstream scour volume, except for the 40 cm by 60 cm ($L/W=1.5$) net, likely due to changes in flow patterns.

- Comparison between Upstream and Downstream Scour Volumes:

An analysis of upstream and downstream scour volumes indicates that these fine nets effectively reduce scouring near the upstream section of the pier. However, significant scouring is observed downstream beyond the nets, which can pose long-term issues and requires further discussion (see Figure 4.62).

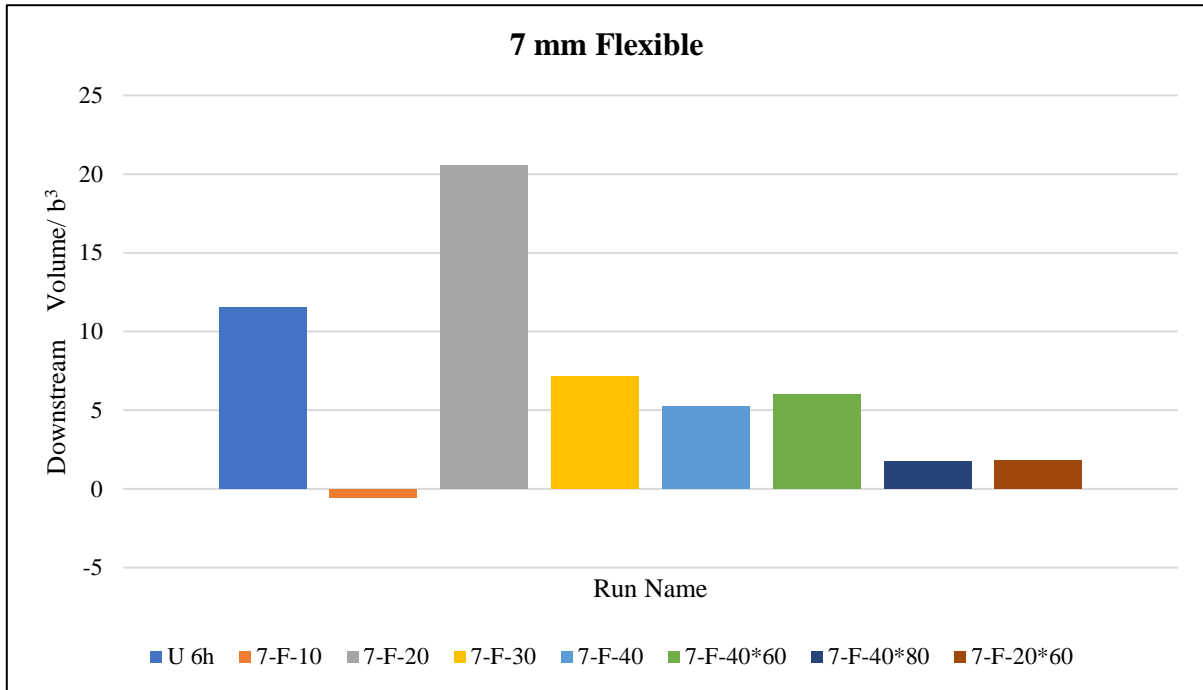


Figure 4.60. Histogram representation of the dimensionless downstream scour volume.

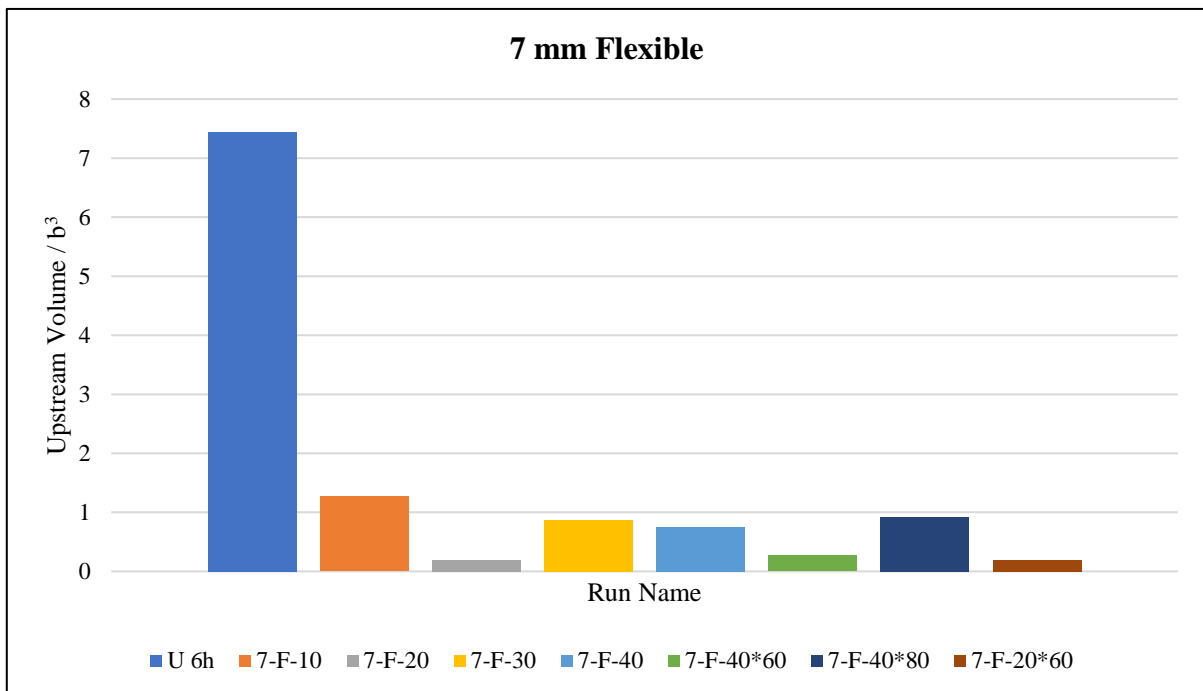


Figure 4.61. Histogram representation of the dimensionless upstream scour volume.

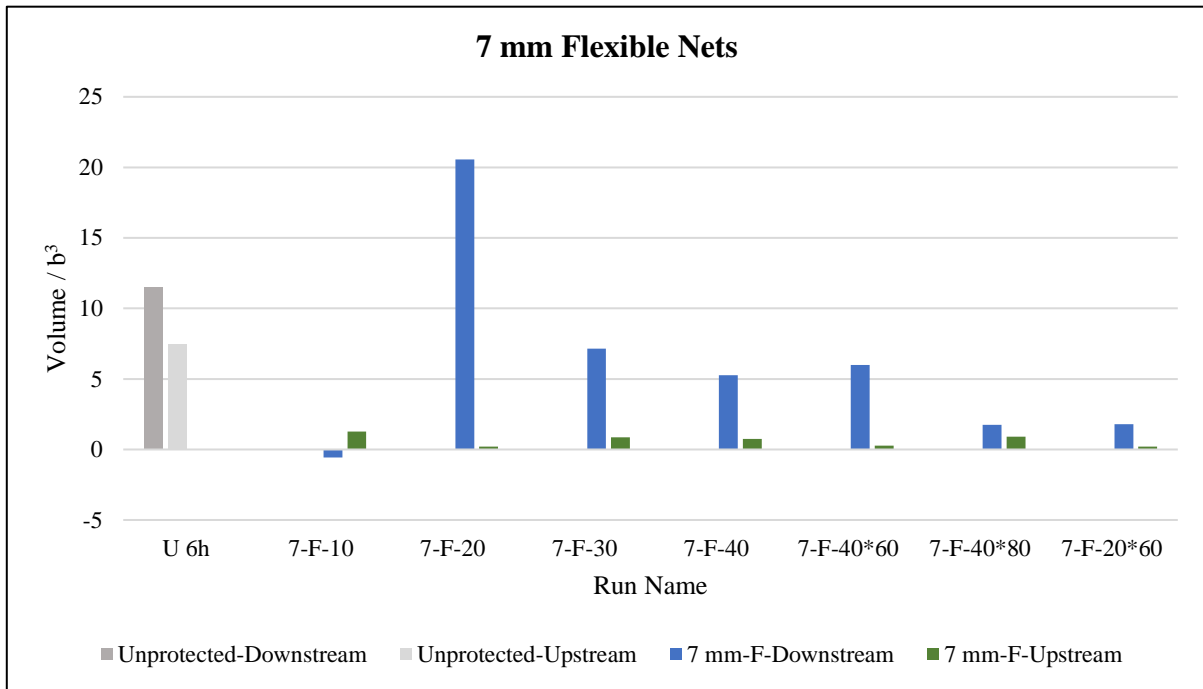


Figure 4.62. Histogram comparison of the dimensionless up and downstream scour volume.

4.2.2.5. Comparison among flexible (coarse and fine mesh) nets

It became evident that the fine flexible experiments exhibited superior performance in reducing upstream scouring during the experiments, with approximately one and a half times less scouring observed, as shown in Figure 4.63.

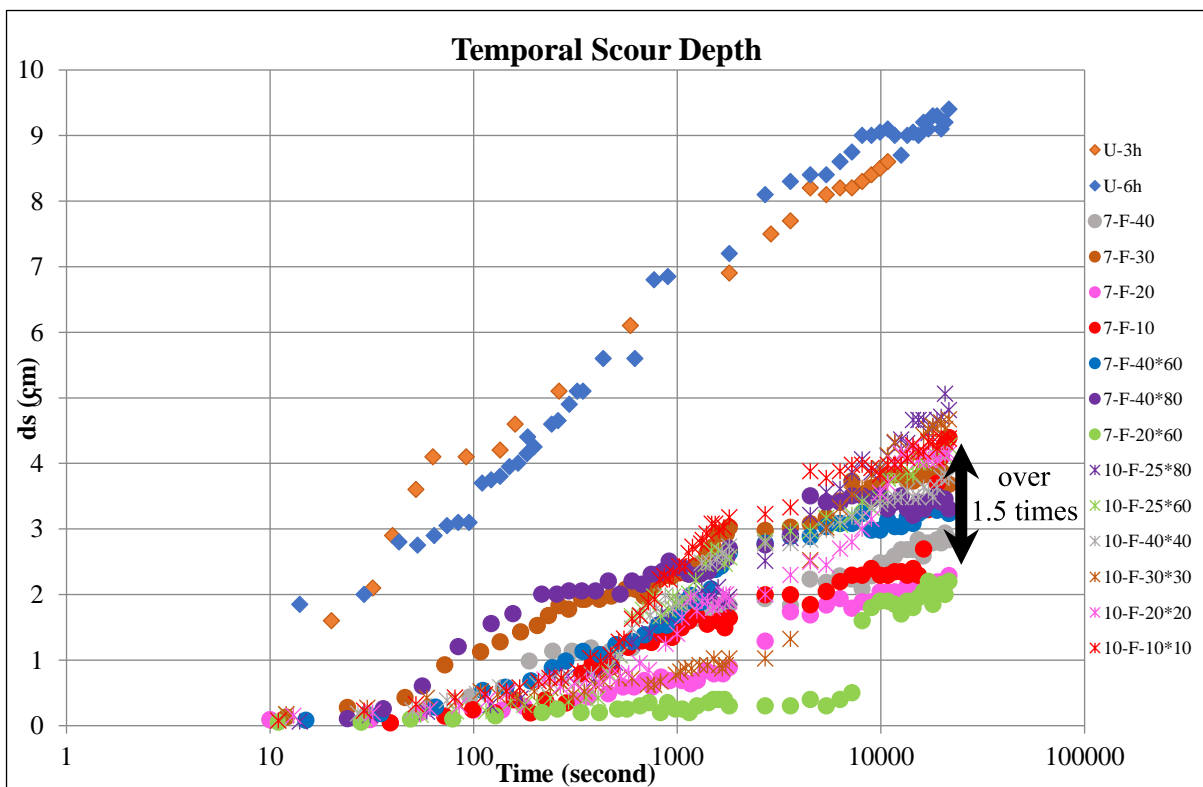


Figure 4.63. Visual comparison of flexible nets in terms of the temporal scour depth. The black arrow indicates over 2 times of difference btw coarse and fine recorded scour depth in the upstream.

The critical region for scouring is identified near the pier in the upstream for both coarse and fine nets. In the downstream, coarse nets do not follow a specific trend in the critical scouring area, while for fine nets, scouring occurs beyond the nets. Coarse nets experience sediment accumulation downstream, whereas fine nets show minimal accumulation (Figure 4.64)

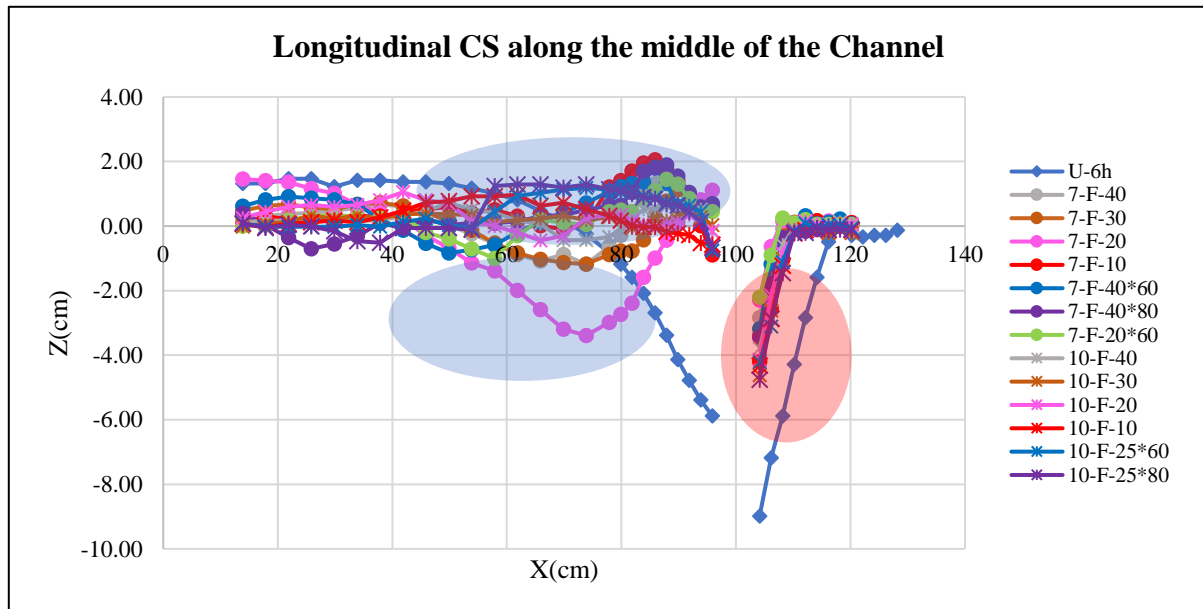


Figure 4.64. Visual comparison of the longitudinal profiles. The red circle indicates the same trend of scouring at upstream of the pier. the blue ovals are indicating the different trend of channel bed change in the downstream of the pier.

An analysis of upstream and downstream scour volumes (see Figure 4.65) indicates that the fine net with a size of 20 cm by 20 cm ($W/b=3.17$) exhibits a significant scour volume in the downstream compared to other nets of any mesh size and coverage area. Additionally, larger mesh sizes result in higher scour volumes in the upstream, which is reasonable due to the greater permeability of the net.

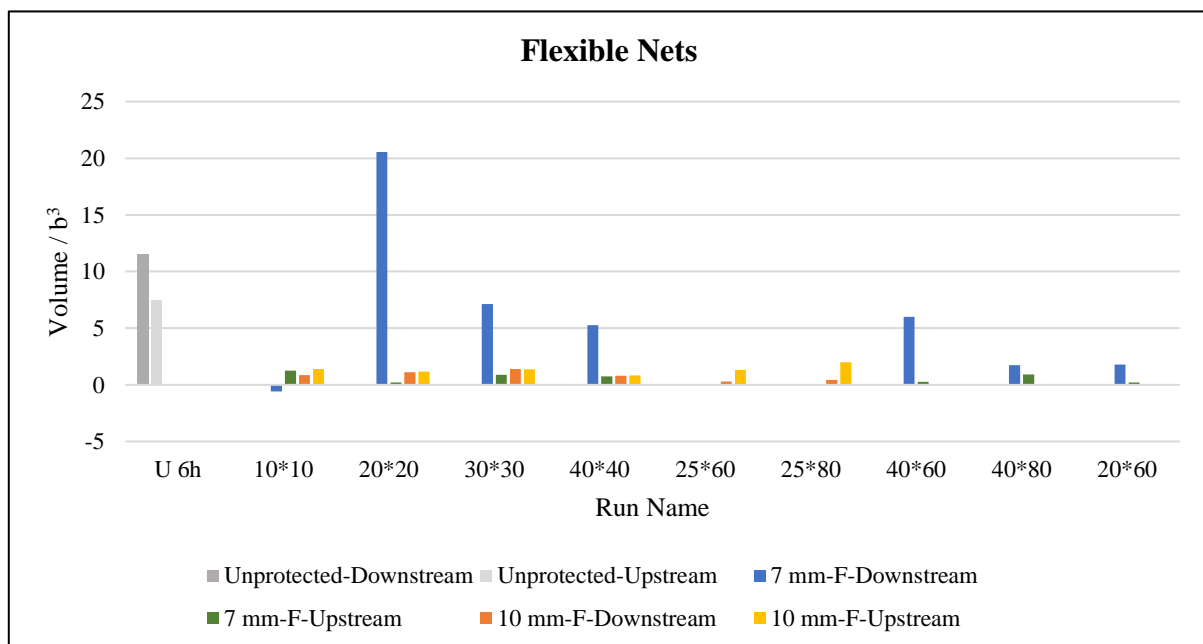


Figure 4.65. Histogram comparison of the dimensionless up and downstream scour volume.

The conclusion here, is similar to the one of rigid nets. However, the coarse fine nets performed better than its corresponding rigid one.

4.2.3. Rigid VS Flexible Geo-Carpets

Progressing further, an additional parameter to be considered for meticulous analysis and comparison is the material flexibility. The primary aim is to ascertain the material that exemplifies exceptional flexibility and manifests enhanced efficacy in mitigating and preventing scour phenomena.

4.2.3.1. Dimensionless analysis and comparison of the results from all performed tests.

During this stage, a thorough comparison of all the geo-carpets employed is carried out. In contrast to previous comparisons that focused on specific criteria, this analysis considers all three criteria—coverage area, mesh size, and material flexibility—to evaluate the overall effectiveness of the nets in providing protection. The objective is to assess the influence of these factors on protection by conducting a sensitivity analysis and comparing the different nets within a dimensionless framework.

The results of the comparisons are based on the analysis of specific graphical data, and a dimensionless framework, which are as follows:

➤ Temporal perspective

Upon examining the temporal measurements obtained from the experiments conducted by all the nets (Figure 4.66), it becomes evident that, in terms of reducing upstream scouring, the fine rigid nets exhibit superior performance in some cases. Notably, for all 27 experiments, the majority of recorded scouring occurs within the initial hour, followed by a gradual increase throughout the 6-hour duration. The representations may not be clearly legible, but for the sake of completeness, they have been presented.

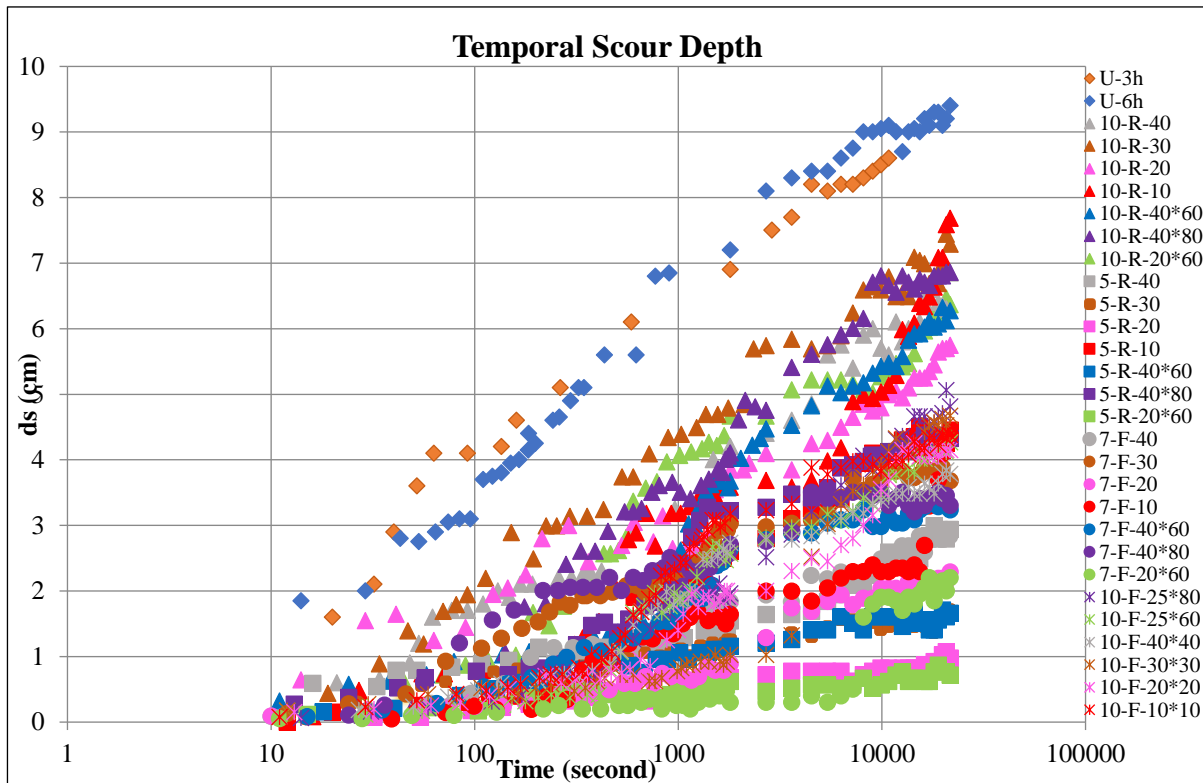


Figure 4.66. Temporal representation of the scour depth.

➤ Longitudinal perspective:

The analysis of longitudinal cross-sections (Figure 4.67) reveals that all fine nets exhibit the same longitudinal profile, and this observation holds true for all the coarse nets as well, although with some slight irregularities. The critical region for scouring is consistently identified near the upstream of the pier across all the nets. However, there is a notable difference in the downstream region near the pier between the fine and coarse nets. In the case of coarse nets, this region has been identified as the most critical area for scouring. Conversely, for fine nets, the most critical scouring region is located beyond the nets.

It is important to note that the presence of fine mesh nets has been observed to result in less scouring around the pier compared to the unprotected condition. On the other hand, in the case of coarse mesh nets, fewer changes in the channel bed have been observed in the downstream.

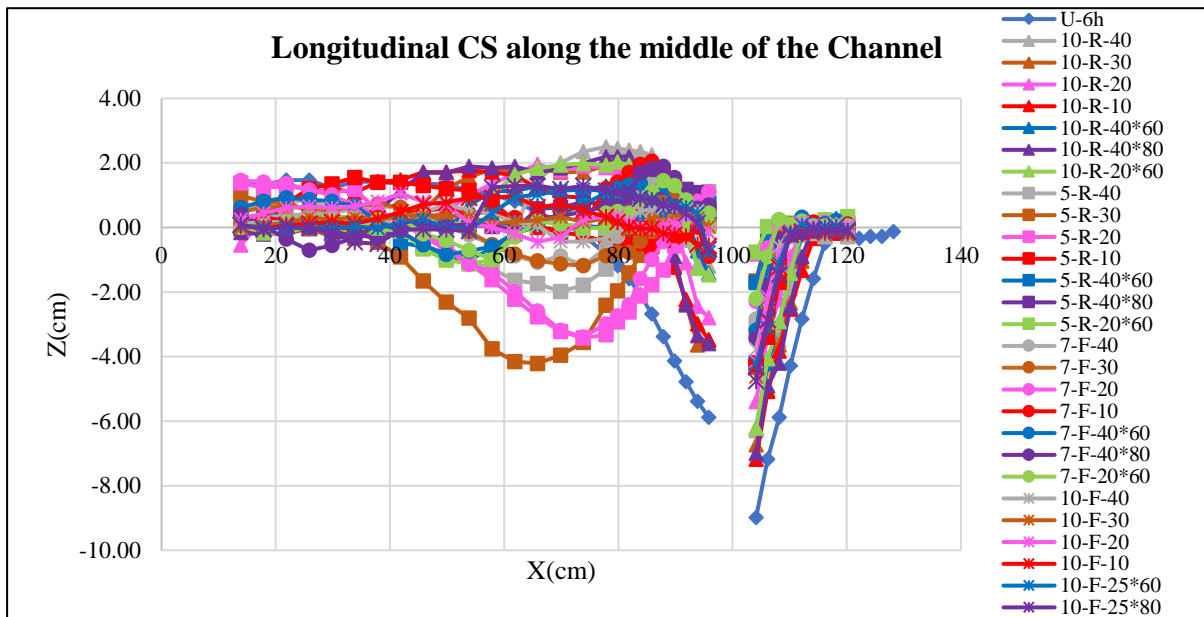


Figure 4.67. Visual representation of the longitudinal profiles.

➤ Transversal perspective:

Figure 4.68 illustrates that all experiments display an identical trend regarding the shape of transversal profiles.

Among the tested scenarios, the 20 cm by 20 cm and 20 cm by 60 cm fine rigid nets yielded the least amount of scouring, while the 10 cm by 10 cm coarse rigid net resulted in the highest level of scouring.

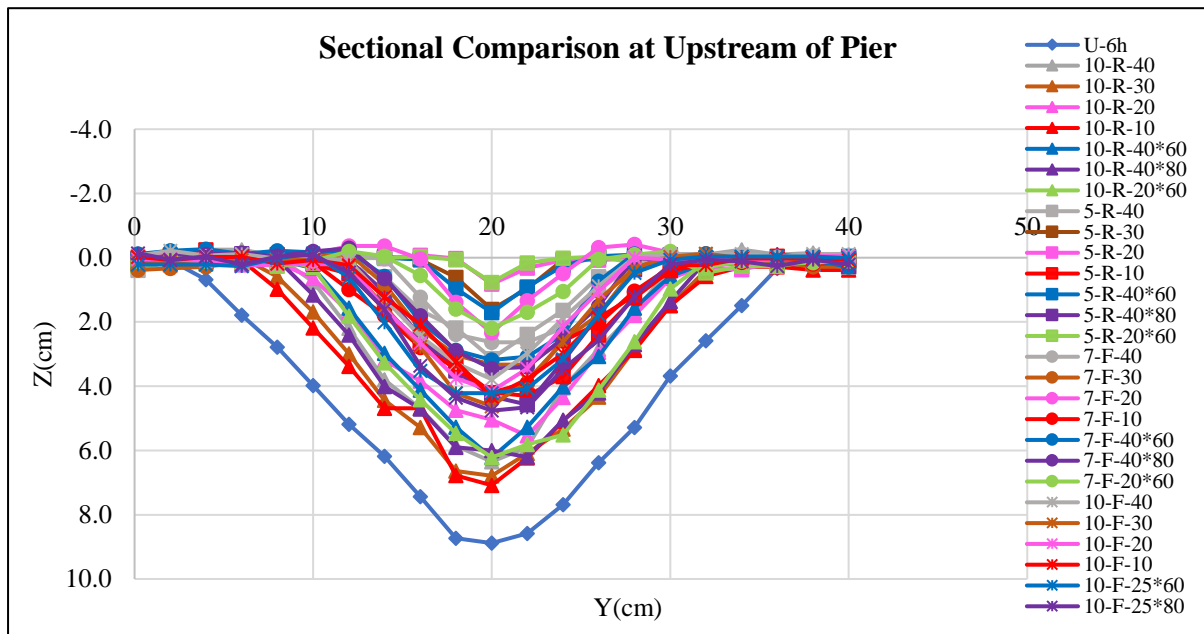


Figure 4.68. Visual representation of the transversal profiles.

➤ Location of Maximum Scouring in the Upstream and Downstream of the Pier:

Upon analyzing the longitudinal cross-sections (refer to Figure 4.67), it is evident that in all series of experiments, the maximum scour depth is consistently observed near the pier in the upstream region. However, there is a distinction between the coarse and fine mesh nets in the downstream region. For coarse nets, the maximum scouring occurs near the pier, whereas for fine mesh nets, it is observed beyond the net.

- Upstream Maximum Scour Depth:

The graphical data presented in Figure 4.69 differentiates between square-shaped geocarpet and extended ones, expressed by two different parameters, W/b , and L/W , respectively, as explained before, at the beginning of the coarse rigid nets analysis.

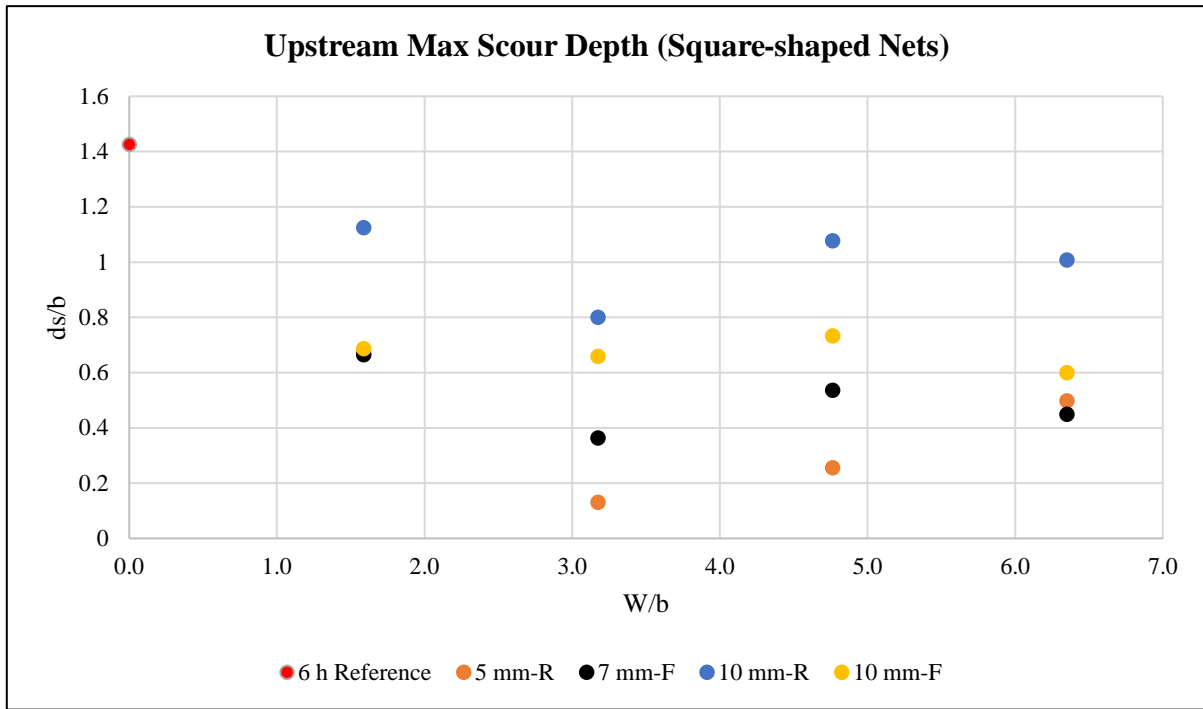
Figure 4.69 demonstrates a general trend among all the nets in terms of recording the maximum scour depth in the upstream, while accounting for the coverage area, mesh size, and material flexibility. Despite some inconsistencies, which are expected in any experiment, it is observed that:

- ❖ Increased flexibility leads to less scouring in the upstream of the pier.
- ❖ Smaller openings (mesh size) result in less scouring.
- ❖ When comparing coverage areas, the nets with ratios of $W/b=3.17$ and $L/W=3$ exhibit the best performance in terms of recording less scouring in the upstream region.

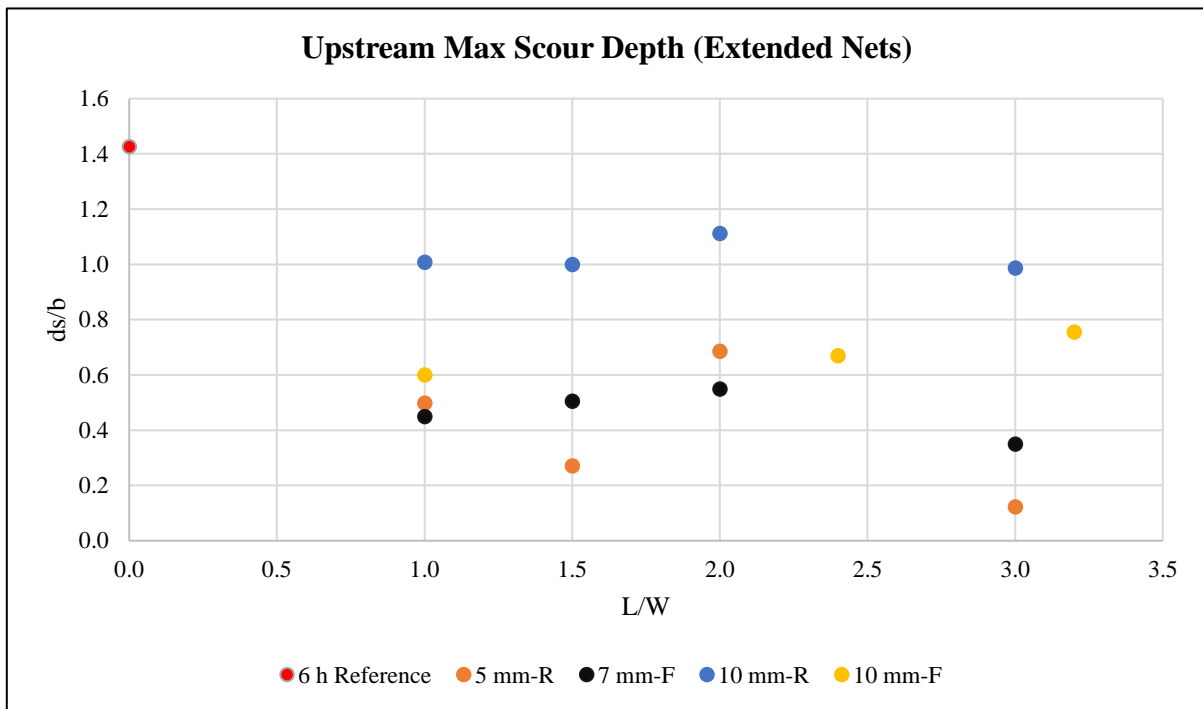
- Downstream Maximum Scour Depth:

Figure 4.70 illustrates that fine mesh and coarse mesh nets follow similar trends, respectively. By considering all three aspects simultaneously, it is evident that:

- ❖ Increased flexibility leads to less scouring in the downstream of the pier.
- ❖ Larger openings (mesh size) result in less scouring.
- ❖ Greater coverage and extension of the nets lead to less scouring. However, in the case of coarse rigid nets, there is a limitation. When the net is extended by a ratio of $L/W=2$, an inverse behavior is observed, resulting in higher scouring compared to less extended nets.

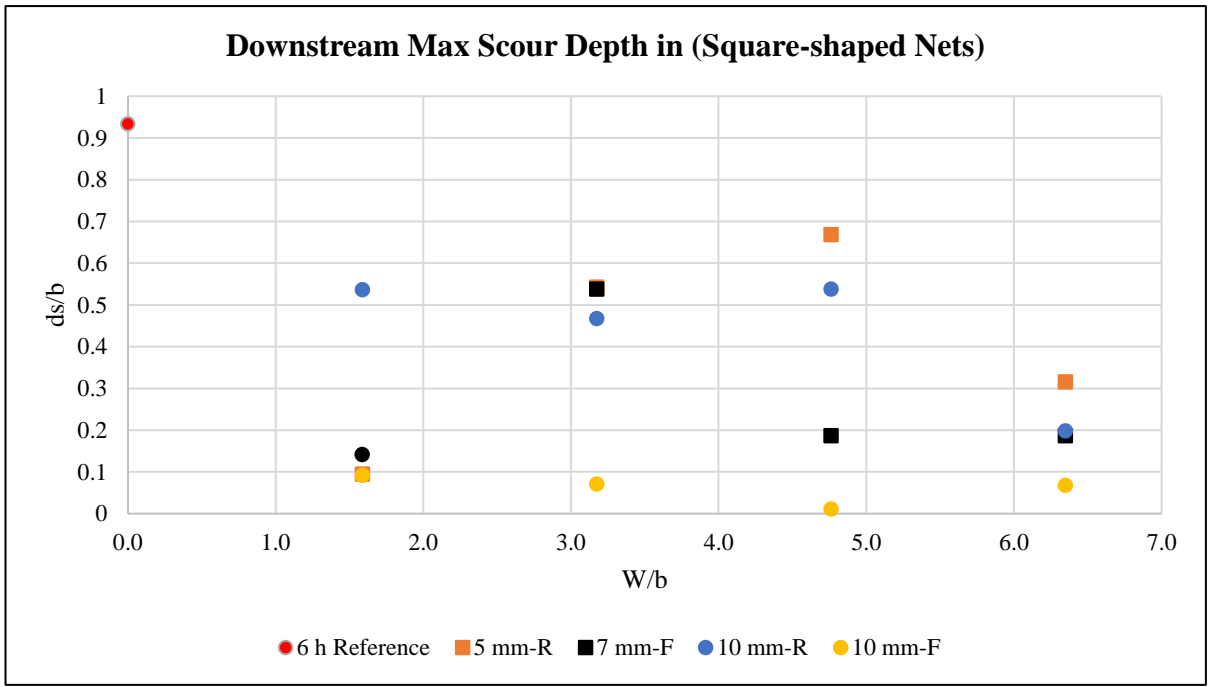


(a)

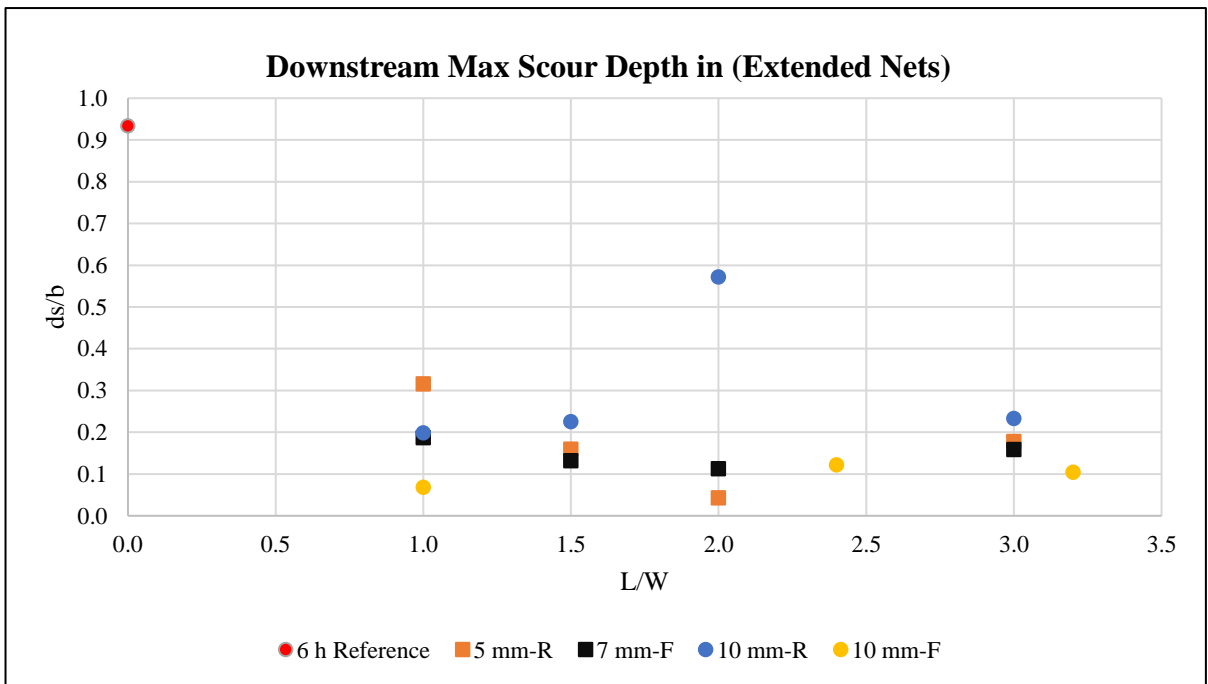


(b)

Figure 4.69. Representation of the dimensionless upstream maximum scour depth: (a) square-shaped nets; (b) extended nets.



(a)



(b)

Figure 4.70. Representation of the dimensionless downstream maximum scour depth: (a) square-shaped nets; (b) extended nets. In both graphs, the maximum scour depths which are indicated by squares (not circles), demonstrate that in those cases, the maximum scour depth happened beyond the nets in the downstream (not close to the pier).

➤ Total Scour Volume (Lost Sediments):

Figures 4.71 and 4.72 illustrate that both fine mesh and coarse mesh nets exhibit similar trends, respectively. Upon considering all three aspects concurrently, it has been unequivocally demonstrated that:

- ❖ The increased level of flexibility yields a reduction in the total scour volume (lost sediments).
- ❖ Larger mesh openings cause a decrease in the total scour volume.
- ❖ Concerning coverage area, with the exception of the nets with a ratio of $W/b=1.59$, which demonstrate lower sediment loss despite their diminutive size, greater coverage and extension of the nets lead to a decrease in the total scour volume (sediment loss). Notably, in certain cases such as the fine mesh nets with ratios of $W/b=3.17$ and 4.76 , a considerable sediment loss has been observed, surpassing that of the unprotected condition, which is noteworthy.

➤ Positive Scour Volume (Scoured Sediments):

Figures 4.73 and 4.74 depict that the positive scour volume follows a comparable pattern to the total scour volume, as the positive scour volume accounts for the majority of the total scour volume. Both fine mesh and coarse mesh nets exhibit similar trend, respectively. By considering all three aspects concurrently, it has been incontrovertibly established that:

- ❖ Increased flexibility results in a decrease in the positive scour volume (scoured sediments).
- ❖ Larger mesh openings lead to a reduction in the positive scour volume.
- ❖ With regards to coverage area, except for the nets with a ratio of $W/b=1.59$, which manifest lower sediment scouring despite their smaller size, greater coverage and extension of the nets contribute to a decrease.

➤ Negative Scour Volume (Accumulated Sediments):

Figures 4.75 and 4.76 depict that, As previously noted, the nets with ratios $W/b=1.59$ and $L/W=2$ exhibit the highest sediment accumulation. By considering all three aspects concurrently, it has been firmly established that:

- ❖ Enhanced flexibility results in a decrease in the negative scour volume (accumulated sediments).
- ❖ Larger mesh openings lead to a higher negative scour volume.
- ❖ Concerning coverage area, except for the nets with a ratio of $W/b=3.17$, which demonstrate lower sediment accumulation, likely due to a significant number of lost sediments, greater coverage and extension of the nets contribute to an increase in the negative scour volume (accumulated sediments).

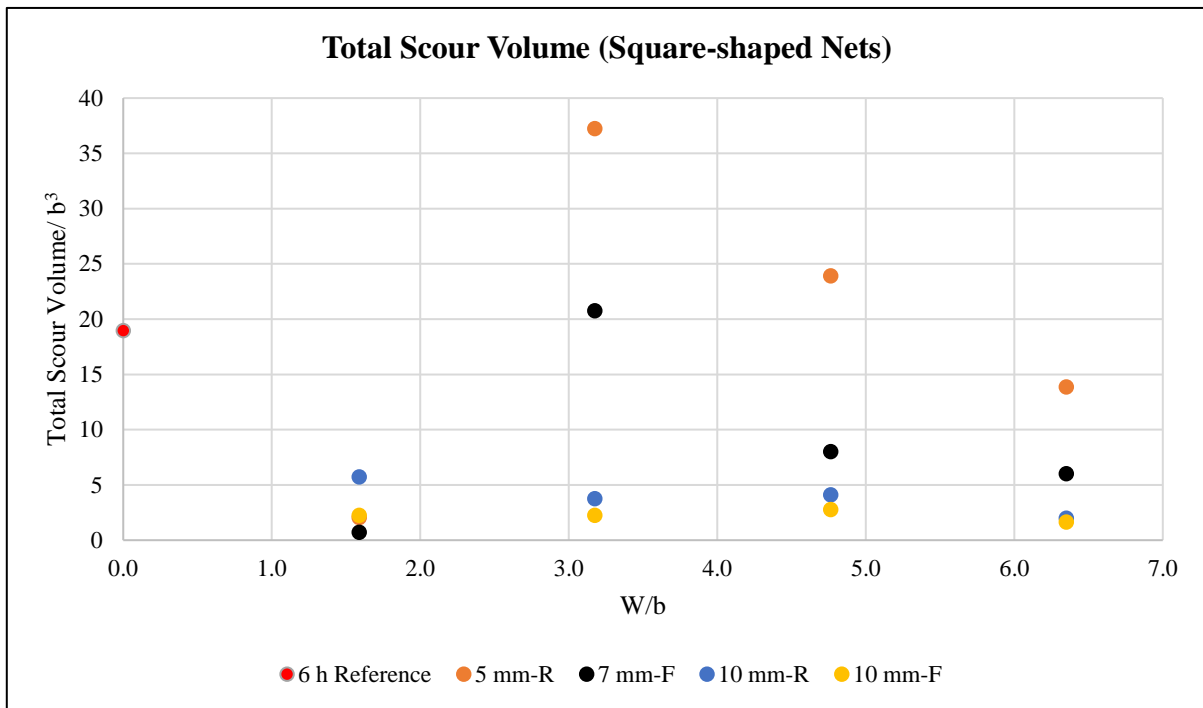


Figure 4.71. Representation of the dimensionless total scour volume of square-shaped nets.

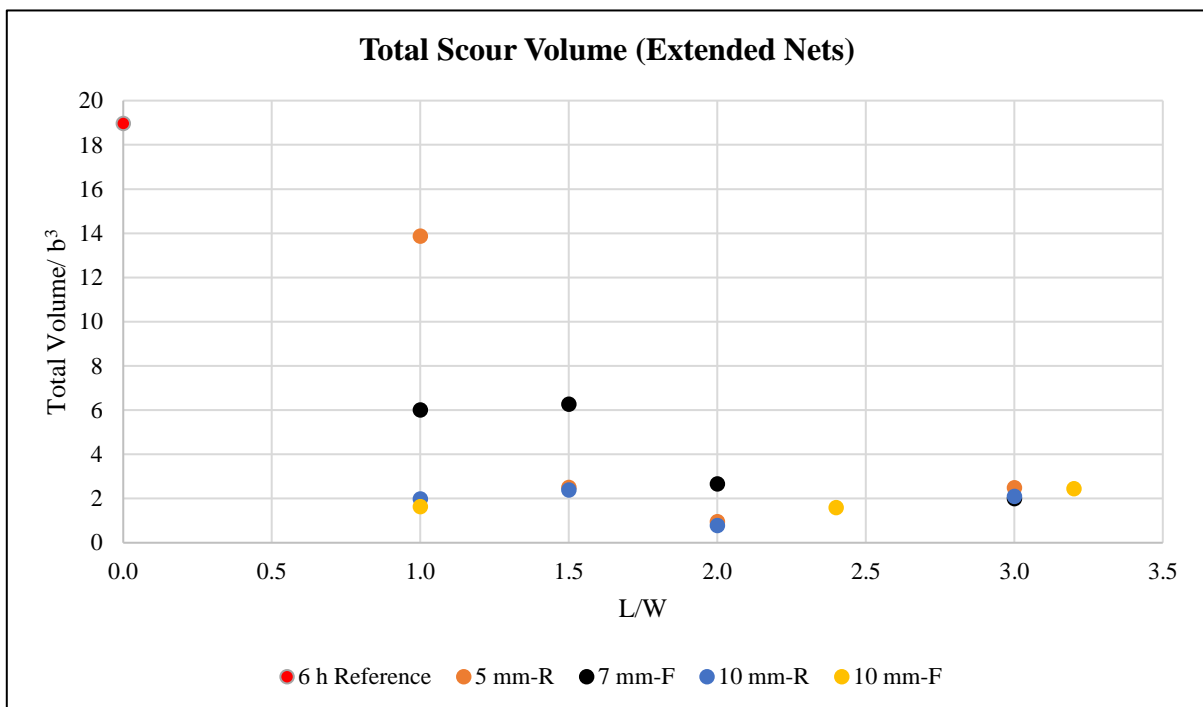


Figure 4.72. Representation of the dimensionless total scour volume of extended nets.

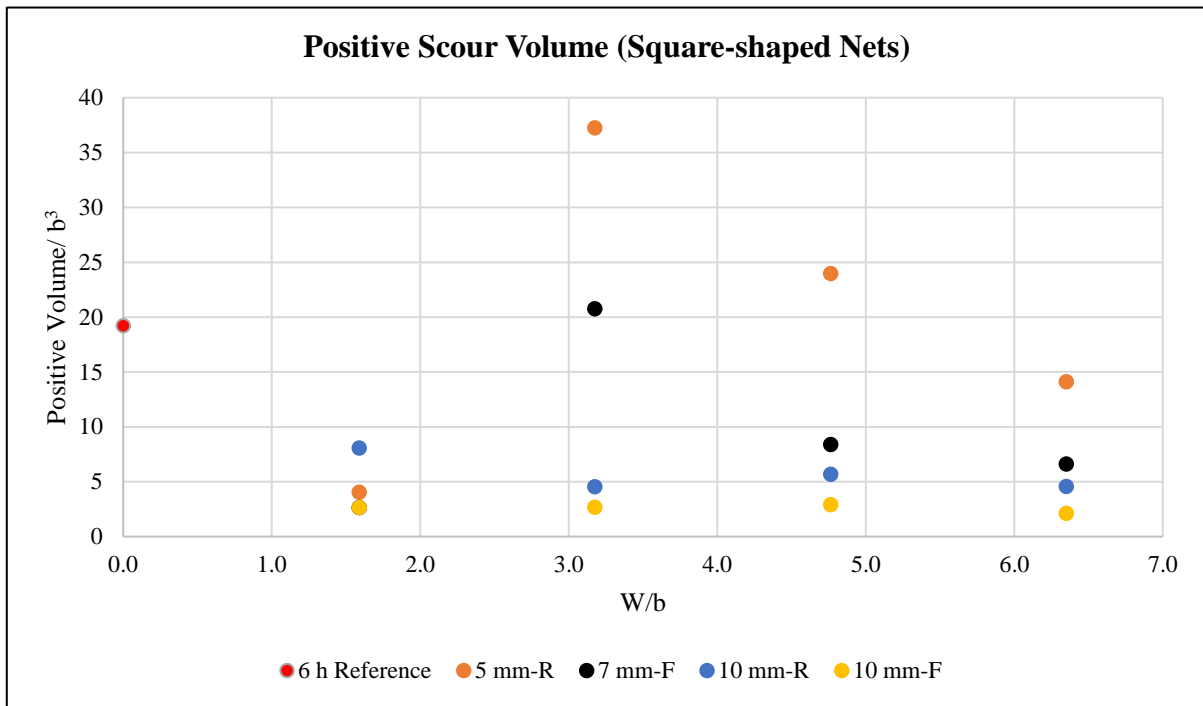


Figure 4.73. Representation of the dimensionless positive scour volume of square-shaped nets.

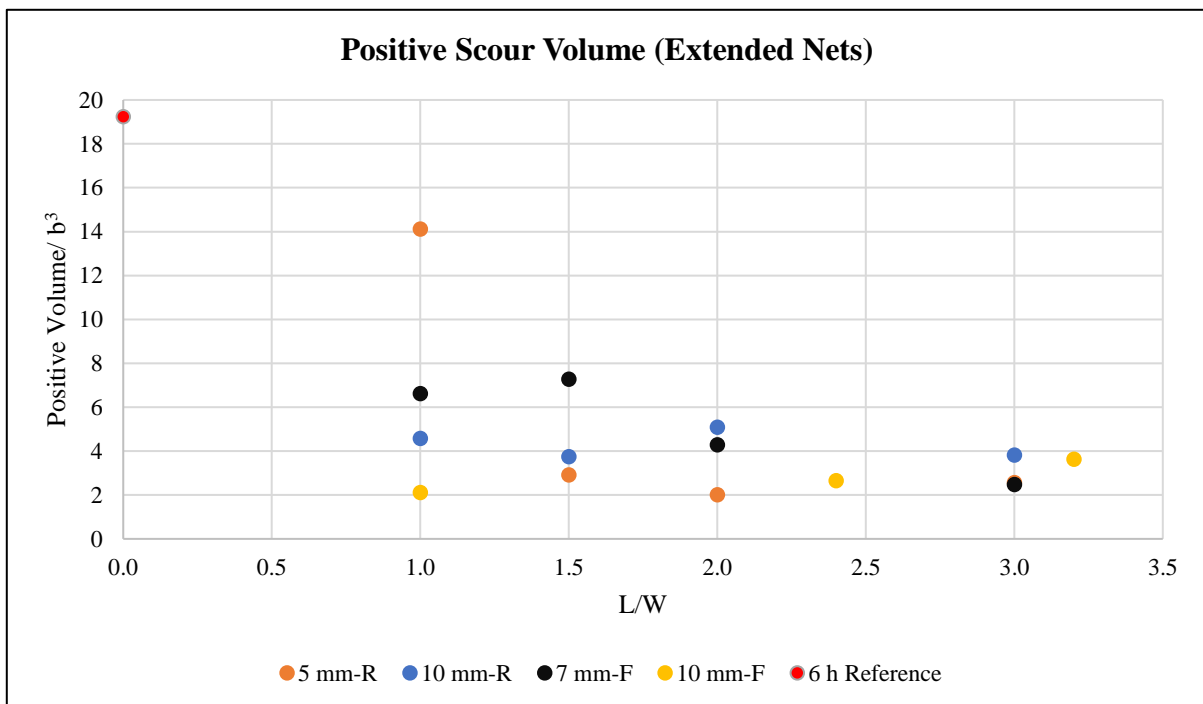


Figure 4.74. Representation of the dimensionless positive scour volume of extended nets.

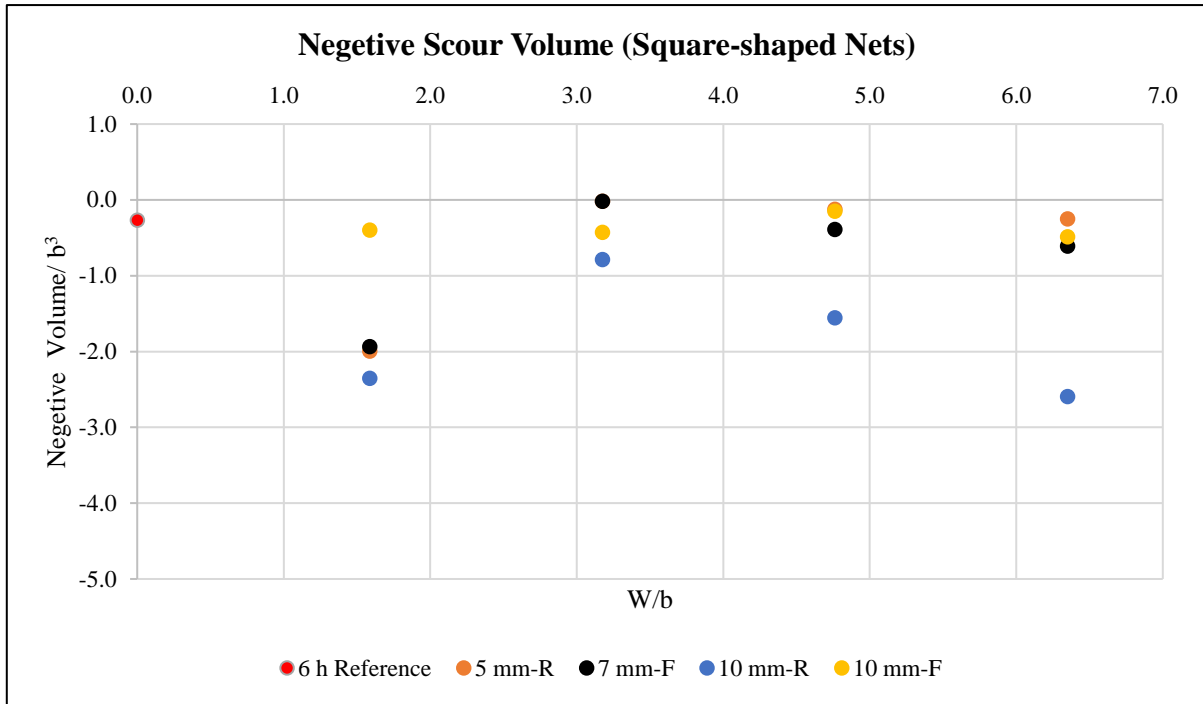


Figure 4.75. Representation of the dimensionless negative scour volume of square-shaped nets.

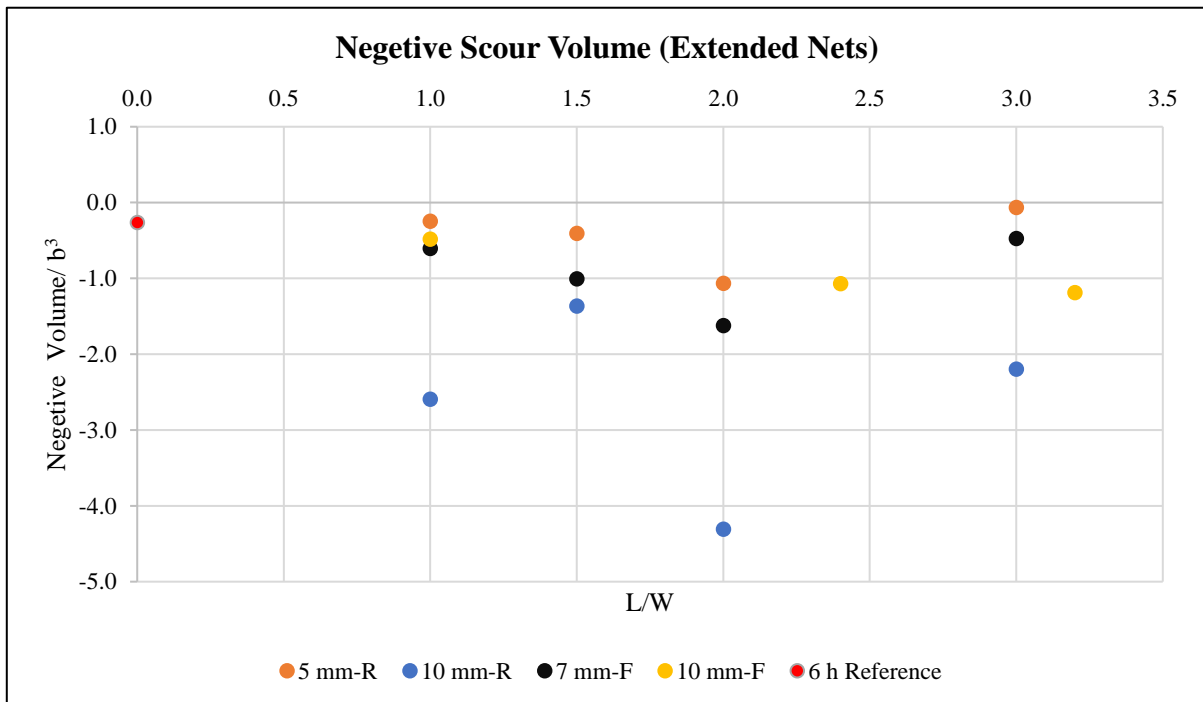


Figure 4.76. Representation of the dimensionless negative scour volume of extended nets.

➤ Downstream Scour Volume:

Based on Figures 4.77, 4.78 and the aforementioned observations, the downstream scour volume adheres to a similar trend as the total scour volume and positive scour volume, as the most substantial volume changes occur downstream. By considering all three aspects concurrently, it has been firmly established that:

- ❖ For coarse nets, increased flexibility yields a higher downstream scour volume. However, for fine nets, the trend is reversed, albeit with slight variations in mesh sizes.
- ❖ Smaller mesh openings result in a higher downstream scour volume.
- ❖ Regarding coverage area, except for the nets with a ratio of $W/b=1.59$, which exhibit lower downstream scour volume despite their smaller size, greater coverage, and extension of the nets lead to a decrease in the downstream scour volume.

➤ Upstream Scour Volume:

Figures 4.79 and 4.80 indicate that both fine mesh and coarse mesh nets follow similar trends, respectively. By considering all three aspects concurrently, it has been unequivocally demonstrated that:

- ❖ Increased flexibility leads to a reduction in the upstream scour volume.
- ❖ Smaller mesh openings result in a lesser upstream scour volume.
- ❖ With regards to coverage area, greater coverage and extension of the nets contribute to a decrease in the upstream scour volume. It is noteworthy that certain optimized configurations, with a ratio of $L/W=3$, have been observed as the most effective nets for protecting against upstream scour volume.

➤ Comparison between Upstream and Downstream Scour Volumes:

An examination of the changes in upstream and downstream scour volumes (refer to Figure 4.81) reveals that, overall, the fine flexible nets exhibit superior performance in terms of minimizing upstream scour volume compared to the other series of protected experiments. Conversely, the coarse flexible nets demonstrate better results in terms of reducing downstream scour volume compared to the other series of protected experiments.

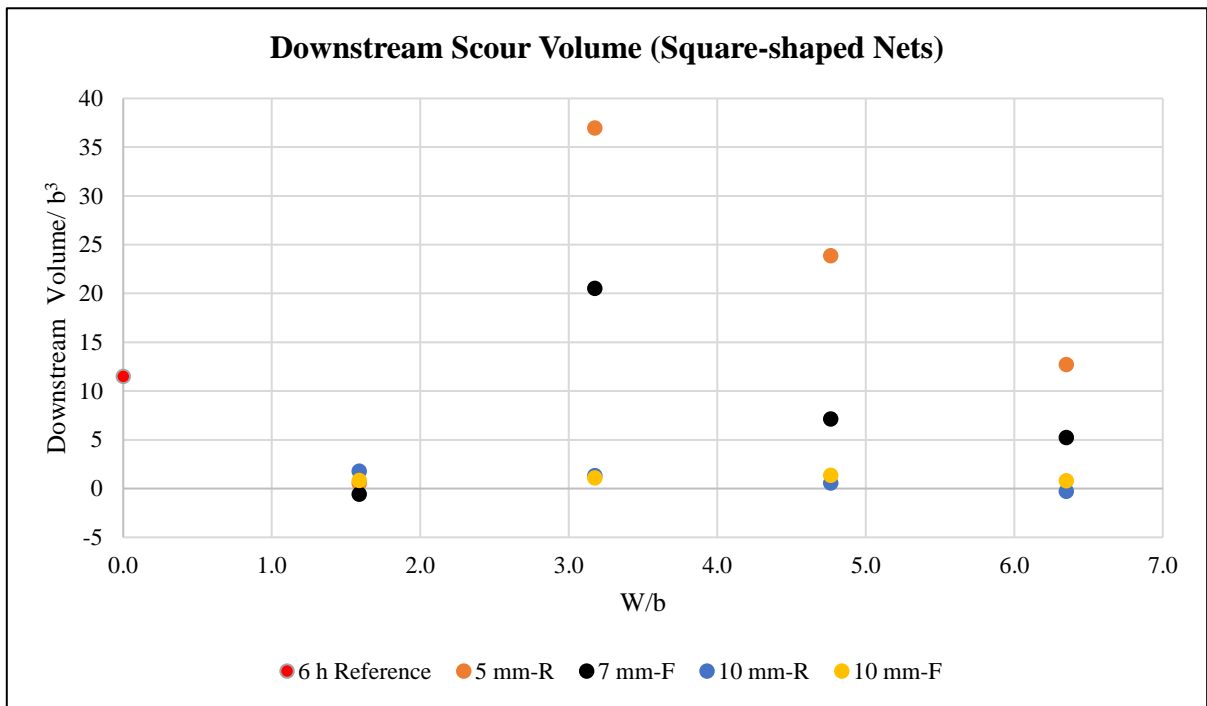


Figure 4.77. Representation of the dimensionless downstream scour volume of square-shaped nets.

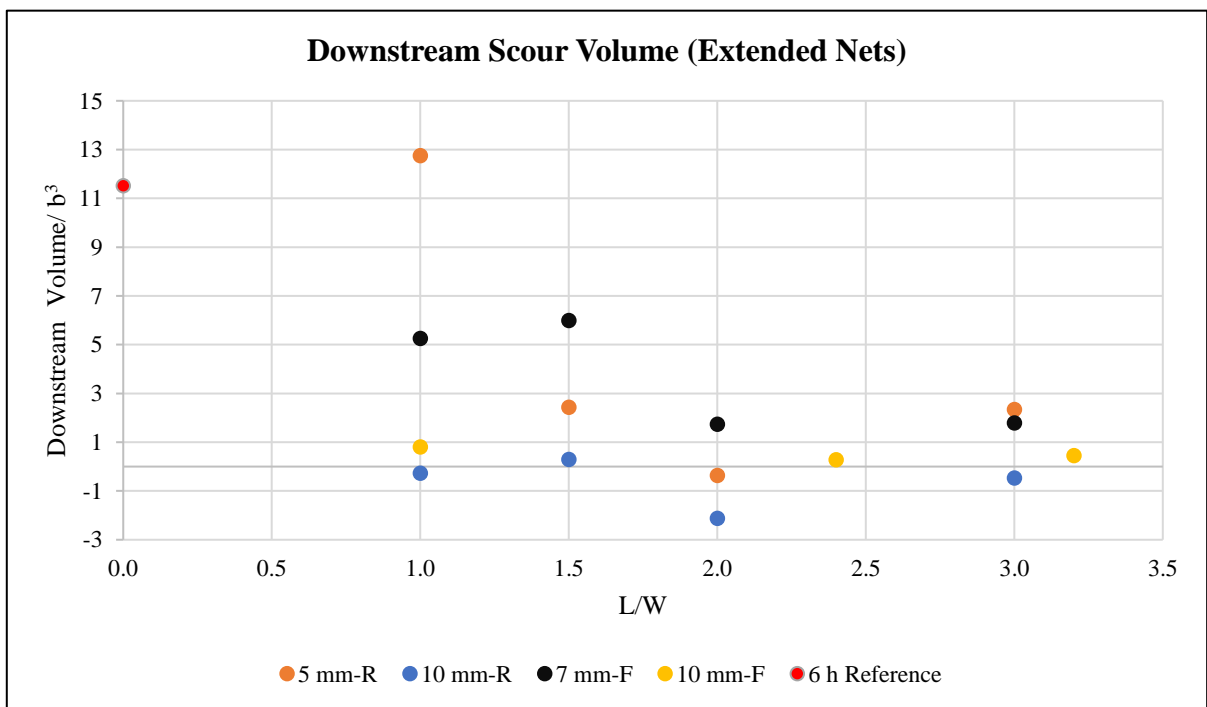


Figure 4.78. Representation of the dimensionless downstream scour volume of extended nets: (a) pointwise; (b) histogram.

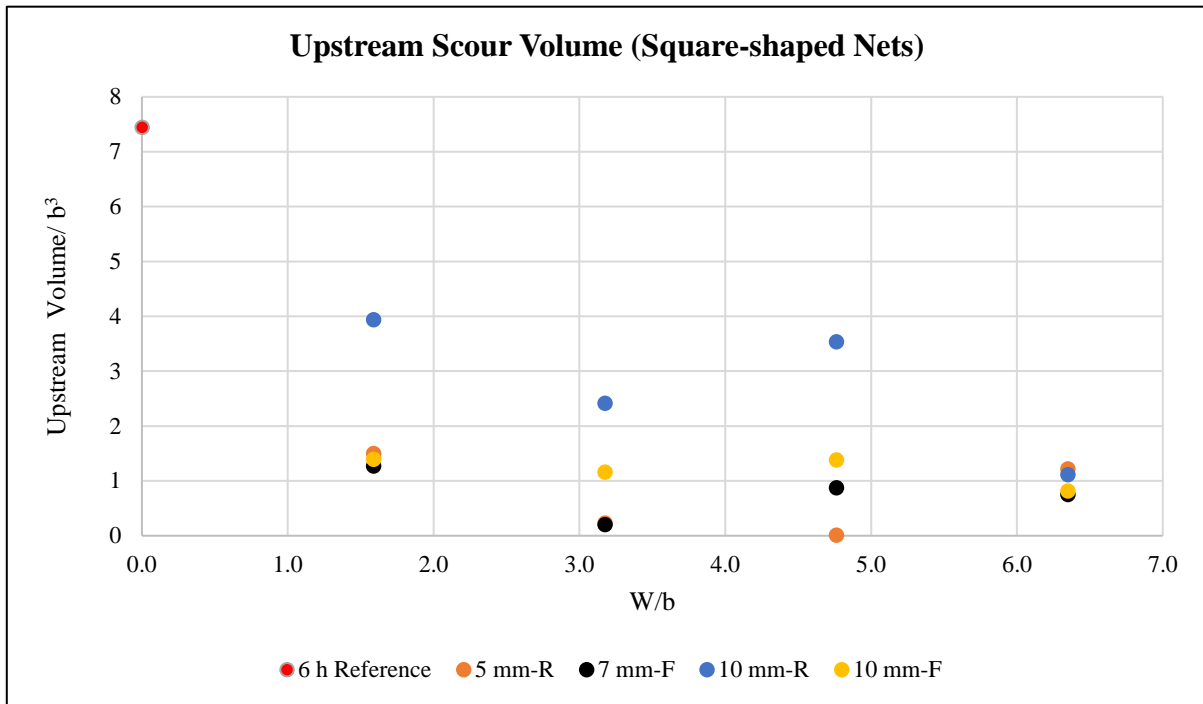


Figure 4.79. Representation of the dimensionless upstream scour volume of square-shaped nets.

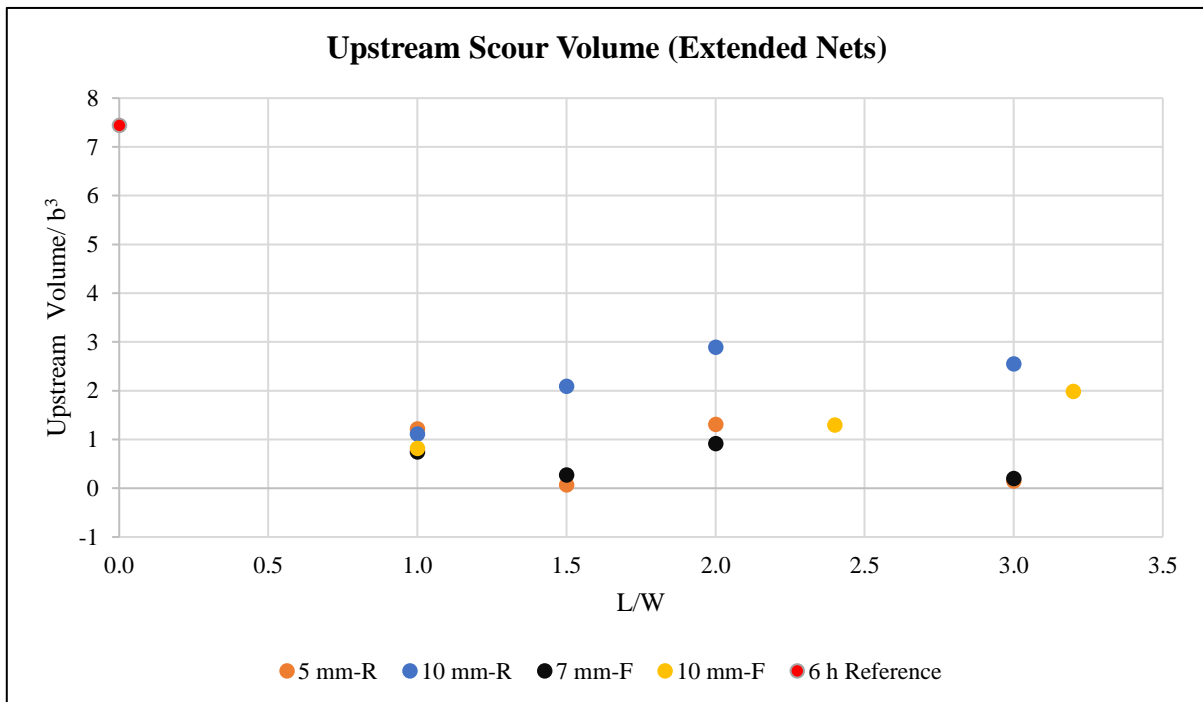
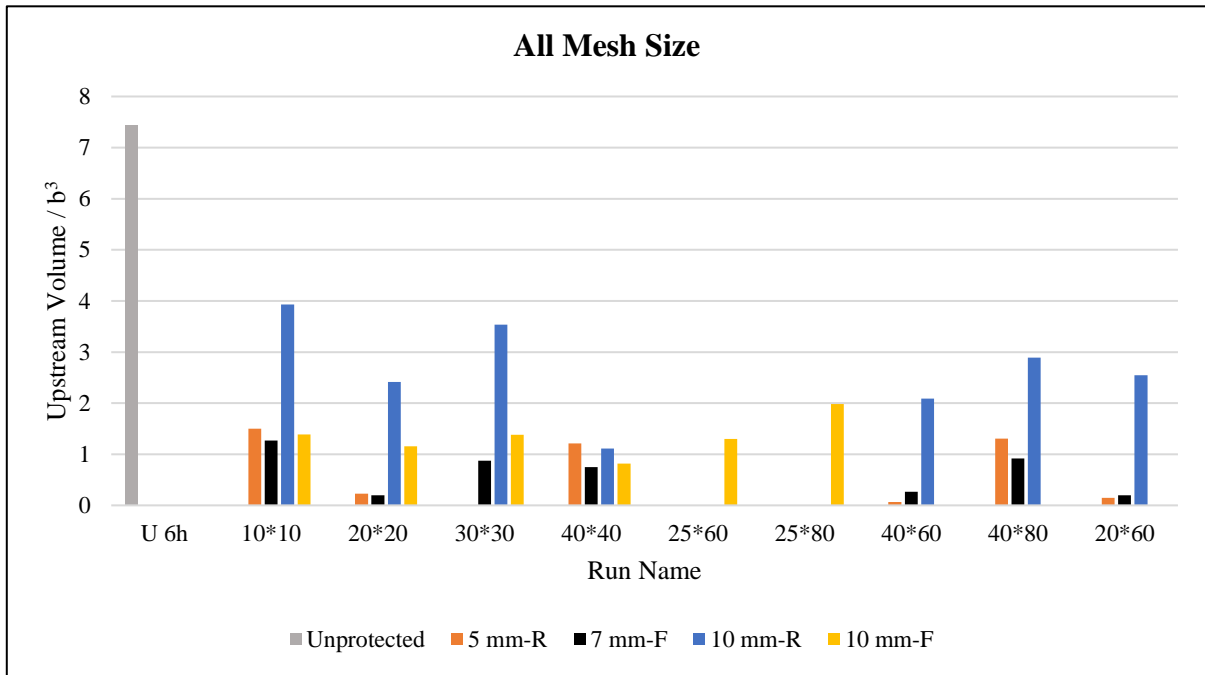
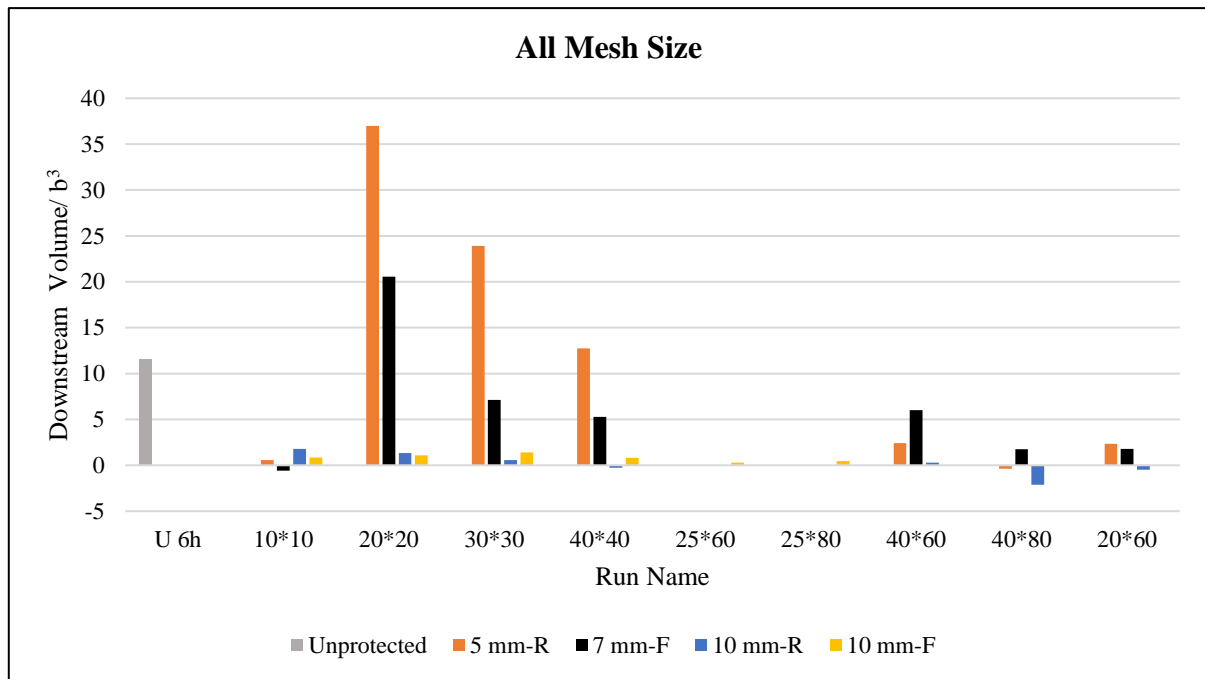


Figure 4.80. Representation of the dimensionless upstream scour volume of extended nets: (a) pointwise; (b) histogram.



(a)



(b)

Figure 4.81. Histogram representation of the dimensionless up and downstream scour volume: (a) upstream scour volume; (b) downstream scour volume.

In general, taking into account all the aspects of the dimensionless analysis and comparison of the results from all performed tests, it can be concluded that, the critical area affected by scouring and bed changes could be divided into two sections: upstream and downstream.

These two sections exhibit different behaviors when protected by geo-carpets, indicating that a particular type of net does not consistently yield the same desirable outcome for both sections. For instance, using a homogenous net in terms of all criteria (coverage area, mesh

size, and material flexibility) for protection may result in less scouring in the upstream section, while it may lead to poor performance in the downstream section.

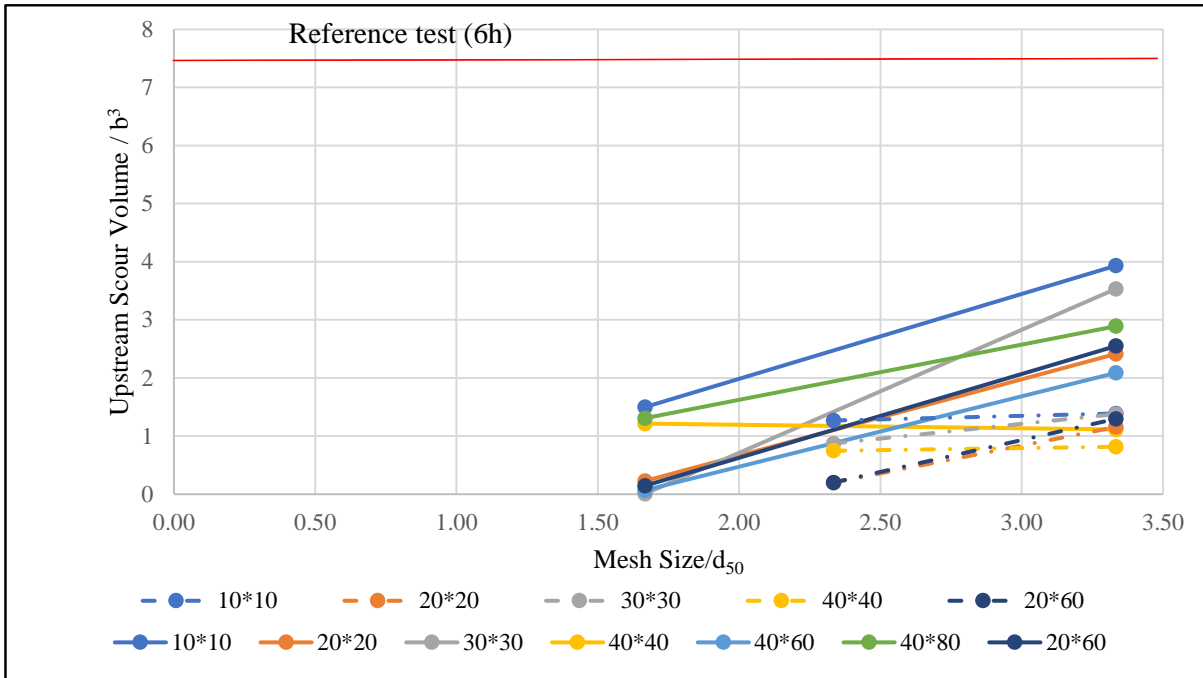
◆ Upstream section:

More flexibility, smaller mesh size, and an optimized coverage area ($W/b=3.17$ square-shaped net and $L/W=3$ extended net) contribute to less sediment scouring and channel bed changes (see Figure 4.82(a), continuous lines indicate rigid nets and dashed lines flexible nets).

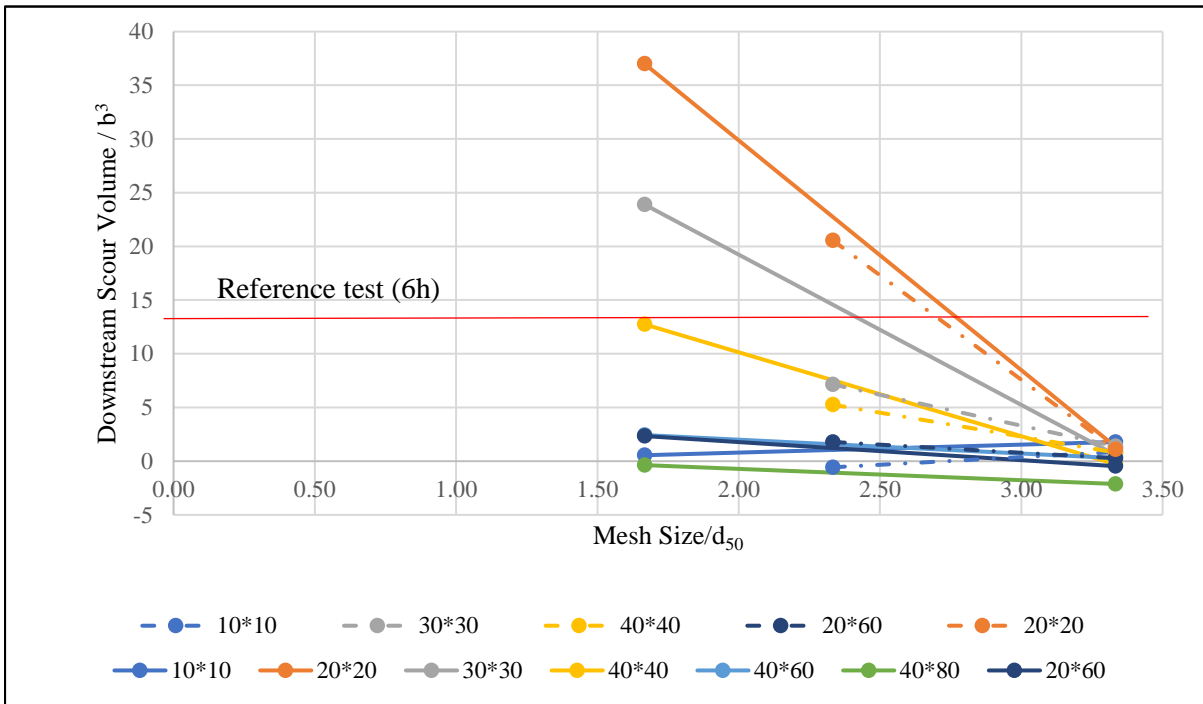
◆ Downstream section:

More flexibility, larger mesh size, and an extended coverage area towards the downstream of the pier ($L/W=2$ extended net), contribute to less sediment scouring and channel bed changes (see Figure 4.82(b), continuous lines indicate rigid nets and dashed lines flexible nets).

In conclusion, considering all the geo-carpets used in the conducted experiments and taking into account the variables of flexibility, mesh size, and coverage area, as well as the various analyses and comparisons conducted from different perspectives such as temporal upstream scour depth, longitudinal profiles, transversal profiles, and dimensionless analyses and comparisons from different viewpoints including maximum scour depths in upstream and downstream sections and scour volumes, it can be concluded that the most effective nets across all series of experiments were the nets with the ratios of $L/W=3$ and $W/b=6.35$, in addition, Table 4.4 reported that, mentioned effective nets, exhibited a significant reduction in scour volume compared to the unprotected reference test. The nets showed a range of 85 to 98 percent less upstream scour volume and 80 to 102 percent less downstream scour volume when compared to the unprotected reference test. These findings indicate the effectiveness of the nets in mitigating scouring effects both upstream and downstream of the test area.



(a)



(b)

Figure 4.82. General comparison of the scour volume based on all three variables (colors: various coverage area; line type: material flexibility; x-axis: mesh size): (a) upstream scour volume; (b) downstream scour volume.

#		Total Scour Volume		Positive Scour Volume		Negative Scour Volume		Upstream Scour Volume		Downstream Volume	
No	Run Name	Value (cm ³)	Change (%)	Value (cm ³)	Change (%)	Value (cm ³)	Change (%)	Value (cm ³)	Change (%)	Value (cm ³)	Change (%)
1	Unprotected	4741.23	-	4807.47	-	-66.24	-	1860.59	-	2880.64	-
2	R5-10*10	512.69	89.19%	1011.16	78.97%	-498.46	-652.54%	374.65	79.86%	138.04	95.21%
3	R5-20*20	9308.21	-96.32%	9312.57	-93.71%	-4.36	93.42%	56.83	96.95%	9251.38	-221.16%
4	R5-30*30	5977.47	-26.07%	5996.42	-24.73%	-30.51	53.94%	1.57	99.92%	5975.90	-107.45%
5	R5-40*40	3465.18	26.91%	3527.35	26.63%	-62.17	6.14%	303.72	83.68%	3186.63	-10.62%
6	R5-40*60	624.63	86.83%	726.97	84.88%	-102.34	-54.50%	17.13	99.08%	607.50	78.91%
7	R5-40*80	235.41	95.03%	502.44	89.55%	-267.03	-303.14%	326.96	82.43%	-91.55	103.18%
8	R5-20*60	621.36	86.89%	638.18	86.73%	-16.82	74.60%	36.29	98.05%	585.07	79.69%
9	R10-10-10	1430.47	69.83%	2018.18	58.02%	-587.71	-787.28%	983.41	47.15%	447.06	84.48%
10	R10-20*20	940.54	80.16%	1136.92	76.35%	-196.37	-196.47%	603.70	67.55%	336.85	88.31%
11	R10-30*30	1027.65	78.33%	1416.38	70.54%	-388.72	-486.86%	883.60	52.51%	144.05	95.00%
12	R10-40*40	493.23	89.60%	1142.14	76.24%	-648.90	-879.67%	278.54	85.03%	-69.17	102.40%
13	R10-40*60	594.06	87.47%	936.09	80.53%	-342.02	-416.36%	522.05	71.94%	72.01	97.50%
14	R10-40*80	191.99	95.95%	1269.98	73.58%	-1077.99	-1527.47%	722.77	61.15%	-530.78	118.43%
15	R10-20*60	521.10	89.01%	952.32	80.19%	-549.14	-729.06%	637.30	65.75%	-116.20	104.03%
16	F7-10*10	174.57	96.32%	658.78	86.30%	-484.21	-631.03%	316.90	82.97%	-142.33	104.94%
17	F7-20-20	5188.56	-9.43%	5193.02	-8.02%	-4.46	93.27%	49.63	97.33%	5138.93	-78.40%
18	F7-30-30	2003.45	57.74%	2101.02	56.30%	-97.57	-47.30%	218.24	88.27%	1785.22	38.03%
19	F7-40*40	1501.81	68.32%	1653.86	65.60%	-152.05	-129.56%	186.74	89.96%	1315.07	54.35%
20	F7-40*60	1566.17	66.97%	1818.59	62.17%	-252.43	-281.10%	67.11	96.39%	1499.06	47.96%
21	F7-40*80	663.66	86.00%	1069.60	77.75%	-406.22	-513.28%	229.12	87.69%	434.54	84.92%
22	F7-20*60	497.41	89.51%	616.31	87.18%	-118.90	-79.51%	50.13	97.31%	447.27	84.47%
23	F10-10*10	559.91	88.19%	659.48	86.28%	-99.57	-50.32%	347.26	81.34%	212.65	92.62%
24	F10-20*20	563.73	88.11%	670.47	86.05%	-106.74	-61.15%	288.95	84.47%	274.78	90.46%
25	F10-30*30	692.07	85.40%	729.67	84.82%	-37.60	43.24%	344.83	81.47%	347.24	87.95%
26	F10-40*40	405.77	91.44%	527.25	89.03%	-121.48	-83.41%	204.08	89.03%	201.68	93.00%
27	F10-25*60	394.60	91.68%	662.50	86.22%	-267.90	-304.46%	324.28	82.57%	70.31	97.56%
28	F10-25*80	608.62	87.16%	905.71	81.16%	-297.09	-348.53%	496.45	73.32%	112.16	96.11%

Table 4.4. A comparison, in terms of percentage, between the scour volumes of protected tests and the reference scour volumes without protection.

4.3. Comparing two analogous geosynthetic approaches

In light of our results presented within a dimensionless framework, we can conduct comparisons with other studies that provide comparable and consistent dimensionless results.

4.3.1. Comparing geo-carpets and geotextile layers

During this phase, the effectiveness of the utilized net system as a countermeasure can be assessed by comparing it to the findings of a reference study ([Nouri Imamzadehei et al., 2016](#)) that utilized geotextile layers instead of nets.

The primary focus of this comparison will be on temporal scour depth, which represents a crucial variable of interest. It would be beneficial if the dimensionless scour volumes were also provided by ([Nouri Imamzadehei et al., 2016](#)), as the scour volume perspective is crucial for making meaningful comparisons. This allows for deeper insights rather than solely considering temporal scouring at a specific point. It is important to highlight that, in our situation, the information regarding erosion in the downstream area was assessed only once at the end of the experiments and does not possess a temporal nature like the reference study. On the other hand, our data on erosion in the upstream region was collected continuously throughout the duration of the experiments, which the disparity in location introduces a significant difference between the two sets of data, making them incomparable in terms of their findings and conclusions.

4.3.1.1. Two general comparisons: coverage area and location of scour hole

➤ Coverage area:

The geotextile experiments conducted by ([Nouri Imamzadehei et al., 2016](#)) demonstrate that oval layers extended downstream exhibited the best performance in reducing scouring, as mentioned in the literature review. Interestingly, this pattern of scour reduction is similar to the performance observed in our extended nets, which have a coverage area with a width-to-length ratio of $L/W=3$ (20 cm by 60 cm). This observation is significant as it suggests that the specific shape and size of the net system can have a substantial impact on its effectiveness in mitigating scour around bridge piers. Recognizing this similarity provides further support for the potential efficacy of the extended nets in reducing scour depth.

➤ Location of scour hole

In the geotextile experiments conducted by ([Nouri Imamzadehei et al., 2016](#)), the placement of the protection layer resulted in a downstream shift of the scour hole. This can be attributed to the limited permeability of the geotextile, which hindered the flow patterns from easily passing through it. Consequently, scouring predominantly occurred downstream of the geotextile layer. In our study, however, the use of adequately permeable geo-carpets allowed for some scouring to occur in the vicinity of the pier. Flow patterns were able to pass through the nets more easily compared to the geotextiles. Among the 27 experiments carried out using different nets, only six nets displayed notable scouring downstream of the pier that extended beyond the nets. These findings were consistent with the tests conducted using geotextile layers. In the remaining cases, significant scouring was observed at the upstream edge of the pier.

4.3.1.2. Comparing scour depth downstream over a 6-hour time period

In line with the results of the current study and the reference study conducted by ([Nouri Imamzadehei et al., 2016](#)), a selection of six nets was made for a comparative analysis with geotextile layers. The comparison was carried out over a period of 6 hours, and both studies revealed a consistent trend in terms of substantial scouring downstream of the piers.

Two comparable geotextile cases were selected that did not have a delay exceeding the duration of our experiments. To conduct the comparison, three sets of experiments were chosen: the unprotected experiment without utilizing geotextile, and the two comparable experiments with geotextile.

Figure 4.83 illustrates that the two unprotected graphs exhibit slightly deviated scour depths but still follow a similar trend. According to the literature review by (Franzetti et al., 2022), a deviation of approximately 25% in terms of the dimensionless reported scour depth over time would be considered acceptable.

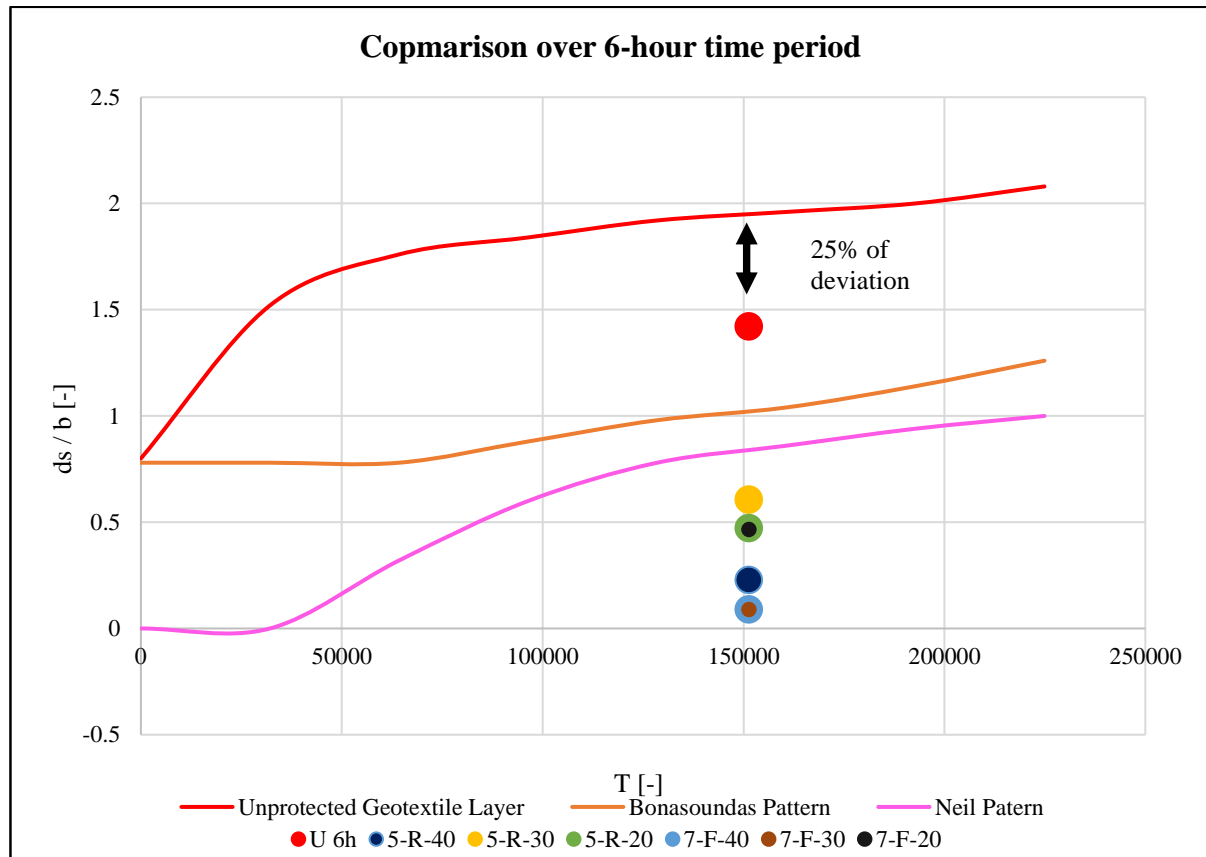


Figure 4.83. Comparative representation of the effective nets and geotextile layers (Nouri Imamzadehei et al., 2016) over 6 hours.

The analysis clearly indicates that all six nets selected for the study, with ratios of W/b (width-to-pier diameter ratio) at 3.17, 4.76, and 6.35, outperformed the two geotextile layers (Bonasoundas pattern in depth and Neil pattern). The graph visually demonstrates that the fine flexible nets with ratios of W/b at 4.76 and 6.35 exhibited the highest level of performance among all the six configurations.

4.4. Future research and improvements

It is important to acknowledge that our case study faced certain limitations in terms of material availability, as previously mentioned in the laboratory description. To ensure the completeness of the study and enhance the consistency of our comparisons, it is strongly advised to carry out the experiments, utilizing coarse flexible extended nets ($L/W=1.5, 2,$ and 3), that were conducted in this case with deviated ratios ($L/W=2.4$ and 3.2) than the other series of experiments utilized extended net. Additionally, for the fine flexible nets, we had to use a 7

mm mesh size instead of the desired 5 mm size. It is strongly recommended to rectify these limitations by conducting experiments with coarse flexible extended nets, which have the same coverage area as the coarse rigid extended nets. Similarly, redoing the fine flexible experiments with 5 mm mesh size nets would provide valuable insights into their performance. While previous findings have indicated that the fine rigid nets outperformed the coarse rigid nets in mitigating scouring near the pier, and a similar trend was observed for the flexible material. While the coarse flexible nets performed better than the coarse rigid nets, the fine rigid nets showed slightly superior performance compared to the fine flexible ones. However, this difference could be attributed to the disparity in mesh size between the fine nets. If the fine flexible nets had the same mesh size openings as the fine rigid nets, they might have exhibited even better performance than the fine rigid nets, similar to the cases where the flexible material outperformed the rigid material.

To gain a deeper understanding of the effects on flow patterns and sediment response, it is recommended to adjust the flexibility of the nets. Previous evidence has demonstrated that increased flexibility correlates with improved performance of the geo-carpets. Therefore, conducting future experiments with slightly more flexible carpets will validate if this correlation remains consistent and determine the potential benefits of extending flexibility within a certain range.

In order to further investigate the effectiveness of different coverage areas, it is recommended to incorporate a wider range of configurations. Among these, utilizing coverage areas such as a net with a ratio of $L/W=4$ would be a suitable choice, given the superior performance observed with the configuration with a ratio of $L/W=3$. By extending the coverage area slightly, we can evaluate how the geo-carpets respond and assess if there are additional benefits in terms of mitigating scouring.

Our study has provided evidence of contrasting responses of geo-carpets in the upstream and downstream areas of the pier. To further investigate this phenomenon, it is highly recommended to employ distinct types of nets in these respective locations. For instance, utilizing fine flexible mesh nets in the upstream section and coarse flexible nets in the downstream section will allow us to observe and analyze their performance. Additionally, it is advisable to implement different levels of flexibility simultaneously to explore the resulting flow patterns and their implications. Moreover, introducing varying coverage areas would be beneficial, such as leaving the sides of the channel uncovered in the upstream section, while covering them after the pier in the downstream section, or vice versa. By implementing these measures, we can gain a comprehensive understanding of how the geo-carpets function in different sections and determine the most effective configurations for each specific location.

It is crucial to emphasize once again that our case study conducted tests under a single hydrodynamic condition. Therefore, it is imperative to subject the geo-carpets to different hydrodynamic conditions to explore their behavior across a range of scenarios. Depending on the specific application, there can be a wide variety of hydrodynamic conditions in the real world, and relying solely on results from a single condition may not provide a comprehensive understanding of geo-carpets performance. By conducting experiments under various hydrodynamic conditions, we can gather valuable insights into how the geo-carpets respond and perform in different flow regimes, allowing for more accurate and reliable assessments of their effectiveness in real-world applications.

Given the duration of our experiments, which was limited to 6 hours, it is important to acknowledge that this timeframe may not have been sufficient to reach the equilibrium scour depth. Therefore, it is strongly recommended to conduct long-duration experiments to observe the results over an extended time span, like one or two weeks. These prolonged experiments would provide valuable insights into making the meaningful comparison with other consistent methods. Furthermore, the durability of the geo-carpets and their ability to maintain their effectiveness in mitigating scour over time could be simulated by so far extended experiments in terms of time period.

It is crucial to mention that the methodology employed for anchoring the geo-carpets remained consistent throughout all the experiments. Specifically, the carpets were anchored on the borders and using four nails around the pier. However, it is highly recommended to explore alternative arrangements for anchorage to observe how the nets respond to different flow patterns. Different nail configurations can significantly alter the stiffness and fixation of the carpets to the channel bed. This knowledge will contribute to optimizing the anchorage method, ensuring improved stability and performance of the geo-carpets in real-world scenarios.

Chapter 5

Summary and conclusions

The significance of civil infrastructure systems in reflecting societal progress and economic growth has been recognized since ancient times. However, the maintenance of these systems often receives inadequate attention, despite its crucial role in overall infrastructure management. Engineers have innovatively designed materials to address maintenance challenges and mitigate risks associated with infrastructure failures. Risk management is essential in addressing the consequences of failures, considering factors such as hazard, exposure, and vulnerability proposed by the United Nations International Strategy for Disaster Reduction (UNISDR) in 2017. Among the causes of bridge collapse, natural hazards are the primary culprits, with flooding and scour emerging as the most prominent contributors ([Imhof, 2004](#)). Extensive research has been conducted on clear-water scour, focusing on flow velocities within the range of $0.5 < v/v_c < 1.0$. Maximum scour depth (d_s) in relation to pier diameter (b) has been reported to vary widely from 0.75 to 2.5 in most cases, with a peak scour depth observed at $v/v_c = 1$.

To reduce vulnerability to flood events, scour protection systems for bridges in hostile environments such as rivers and coastal areas have been developed. These systems utilize both active and passive approaches, modifying flow patterns and reinforcing the bed against scour. By implementing such systems, engineers aim to enhance and sustain the performance of infrastructure elements over time.

The main goal of this thesis is to comprehensively investigate the effectiveness of a novel countermeasure system called the geo-carpet in mitigating scour. Experimental tests were conducted in a controlled environment, simulating clear-water scour conditions at a cylindrical pier in free-surface flow over a duration of 6 hours.

The comprehensive experimental campaign comprised a total of 30 conducted tests at the esteemed Hydraulic Lab G. Fantoli, situated within the Leonardo campus of Politecnico di Milano. The campaign commenced with a preliminary test, designed to attain the target discharge as prescribed by ([Radice and Ballio, 2008](#)). The target discharge, set at 95% of the critical flow rate associated with the maximum scour depth, was chosen to strike a balance. The objective was to minimize any potential disturbances to the upstream bed while remaining as close as possible to both the critical flow rate and the expected maximum scour depth. Subsequently, two unprotected tests were carried out, serving two crucial purposes. The initial test sought to validate the repeatability of the subsequent test, which spanned a duration of three hours. The second test, lasting six hours, was specifically designated as the reference test for this study. Notably, these two unprotected experiments also served the additional purpose of validating a novel scour predictor put forth by ([Franzetti et al., 2022](#)). The experimental campaign proceeded with conducting a total of 27 protected tests, each employing distinct

types of geo-carpets. These geo-carpets were varied based on three fundamental parameters: coverage area, mesh size, and material flexibility. By systematically manipulating these key parameters, the goal was to discern their individual impacts on the effectiveness of the scour countermeasure system. Concurrently, the observations of the scouring phenomenon were made during the tests, alongside the comprehensive collection of quantitative data.

This study serves as a continuation of the previous thesis conducted by Manuel Felipe Martin Moya in 2021. Building upon the previous research, our study maintains the same experimental conditions while introducing some updated and consistent characteristics. While the previous thesis primarily focused on two key parameters, namely coverage area and mesh size, our study incorporates an additional significant factor: material flexibility. In contrast to the previous thesis, which conducted 12 trials, our study extends the experimental campaign to encompass a total of 30 trials. This expanded scope provides us with a more comprehensive and nuanced insight into the functionality and performance of the employed countermeasure.

The experiments in our current study were conducted with a constant water discharge of 7.25 l/s and a consistent water depth of 8 cm. The measured section-averaged flow velocity (v) was determined to be 0.23 m/s, while the critical velocity for the incipient motion of sediment particles (v_c) was established as 0.24 m/s. To systematically explore the effects of different factors, we organized the experiments into four distinct series, utilizing different types of nets, including coarse rigid, fine rigid, coarse flexible, and fine flexible nets. Each series comprised various coverage areas, which included both square-shaped and extended nets. It is worth noting that the nets referred to in this context are the geo-carpets mentioned above.

By conducting thorough data collection and utilizing comprehensive surveys, we were able to generate a range of valuable information, including temporal scour depth, longitudinal and transversal profiles. These data were further visualized through 2-dimensional representations and transformed into 3-dimensional figures using Surfer software. Additionally, scour volumes were calculated using the midpoint method, providing quantitative measurements of the scour phenomenon. To facilitate analysis and comparison of the results, we employed a dimensionless framework. This allowed us to assess changes in the channel bed, depths of maximum scouring, and alterations in scour volumes across all the tests. Through this analysis, we were able to identify highly effective configurations of geo-carpets that exhibited superior performance in mitigating scour-related issues.

A significant observation from the experiments was that the major scouring in the upstream of the pier occurred during the initial hour, while bed changes in the downstream occurred gradually over the course of the experiments. All the tested protections demonstrated their effectiveness in reducing scour depth upstream compared to the reference unprotected case. However, it was found that finer and more flexible nets exhibited superior performance in preventing scouring in the upstream section. In the downstream section, coarse nets showed sediment accumulation, whereas fine nets exhibited significant scouring beyond the nets were installed. Based on the analysis of dimensionless scour volumes and considering all aspects of the comparison, it is evident that the critical area affected by scouring and bed changes should be divided into two sections: upstream and downstream. These sections exhibit distinct behaviors when protected by different geo-carpets configurations, indicating that a single type of net may not consistently yield desirable outcomes for both sections. In the upstream section, it was found that greater flexibility, smaller mesh size, and an optimized coverage area (such as a square-shaped net with a coverage area ratio (Width-to-pier diameter) of $W/b=3.17$ and an

extended net with a length-to-width ratio of $L/W=3$) contribute to reduced sediment scouring and minimal channel bed changes. On the other hand, in the downstream section, higher flexibility, larger mesh size, and an extended coverage area towards the downstream (such as an extended net with a length-to-width ratio of $L/W=2$) contribute to mitigating sediment scouring and channel bed changes. Considering all the geo-carpets employed in the conducted experiments and taking into account the three variables (flexibility, mesh size, and coverage area), as well as the various dimensional and non-dimensional analyses and comparisons conducted from different perspectives (including temporal upstream scour depth, longitudinal profile, maximum scour depths in upstream and downstream sections, and changes in scour volume), it can be concluded that the most effective configurations across all series were the nets with dimensionless ratios of ($L/W=3$) and ($W/b=6.35$). These configurations exhibited a significant reduction in scour volume when compared to the unprotected reference test. Specifically, the nets resulted in a range of 85 to 98 percent less upstream scour volume and 80 to 102 percent less downstream scour volume compared to the unprotected reference test.

In addition to the comparison of geo-carpet configurations within our study, a comparison was also made with another geosynthetic approach described in the work of ([Nouri Imamzadehei et al., 2016](#)). This comparison revealed interesting outcomes, particularly in terms of coverage area. The oval geotextile layers extended downstream demonstrated the best performance in reducing scouring, which is similar to the performance observed in our suggested 20 cm by 60 cm nets, with a coverage area ratio of ($L/W=3$). In the geotextile experiments, the placement of the protection layer resulted in a downstream shift of the scour hole. This phenomenon can be attributed to the limited permeability of the geotextile, which hindered the flow patterns from easily passing through it. In our study, however, the use of adequately permeable geo-carpets allowed for some scouring to occur in the vicinity of the pier. It was observed that in the case of 6 fine nets, significant scouring occurred beyond the nets in the downstream section. By conducting dimensionless analysis and comparisons, it was found that all six chosen cases of geo-carpet configurations outperformed the two comparable geotextile layer configurations (Bonasoundas pattern in depth and Neil pattern). Unfortunately, due to a delay exceeding the duration of our experiments, it was not possible to make comparisons with the other configurations from the reference study.

Our case study has identified several limitations and proposes future experiments to enhance the completeness and consistency of the findings. The recommendations for further research include conducting experiments with extended configurations using coarse flexible nets and redoing the fine flexible experiments with the desired 5 mm mesh size. It is suggested to adjust the flexibility of the nets to explore its impact on flow patterns and sediment response. Increasing the coverage area and using different types of nets in the upstream and downstream sections can provide further insights. Testing under various hydrodynamic conditions is essential to understand the behavior of geo-carpets in different flow regimes. Long-duration experiments are recommended to observe the durability and long-term effectiveness of the geo-carpets. Exploring alternative anchorage arrangements can optimize the stability and performance of the nets. Implementing these recommendations will contribute to a more comprehensive understanding of the performance of geo-carpets and their suitability for real-world applications.

References

- Akib, S., Jahangirzadeh, A., Wei, L. H., Shirazi, S. M., and Rahman, S. (2012). Experimental study on the skewed integral bridge by using crushed concrete geobags as scour protection. Proceedings of the 6th International Conference on Scour and Erosion, <https://www.researchgate.net/publication/264125162>.
- Akib, S., Liana Mamat, N., Basser, H., and Jahangirzadeh, A. (2014). Reducing local scouring at bridge piles using collars and geobags. The Scientific World Journal, 2014. <https://doi.org/10.1155/2014/128635>.
- Ansari, S. A., and Qadar, A. (1994). Ultimate depth of scour around bridge piers. Hydraulic Engineering, ASCE. <https://cedb.asce.org/>.
- Bonasoundas, M. (1973). Strömungsvorgang und Kolkproblem am runden Brückenpfeiler. Bericht nr 28, <http://resolver.tudelft.nl/uuid:fcbbca18-5dd7-439a-ba3c-ee966320f01>.
- Brandimarte, L., Paron, P., and Di Baldassarre, G. (2012). Bridge pier scour: A review of processes, measurements and estimates. Environmental Engineering and Management Journal, 11(5), 975-989. <https://doi.org/10.30638/eemj.2012.121>.
- Brath, A., and Montanari, A. (2000). Vulnerabilità idraulica dei ponti. Soluzioni innovative nella manutenzione dei corsi d'acqua con forte trasporto solido. Numero Spec. Della Riv. L'Acqua, 3, 45-60. <https://www.idrotecnicaitaliana.it/sommari/vulnerabilita-idraulica-dei-ponti/>.
- Breusers, H. (1965). Scouring around drilling platforms. J. Hydraul Res. IAHR, Bull., 19, 276. <https://cir.nii.ac.jp/crid/1581980076303321856>.
- Breusers, H., Nicollet, G., and Shen, H. (1977). Local scour around cylindrical piers. Journal of Hydraulic Research, 15(3), 211-252. <https://doi.org/10.1080/00221687709499645>.
- Breusers, H., and Raudkivi, A. J. (1991). International Association for Hydraulic Research.

Scouring, Balkema, Rotterdam, The Netherlands,
<https://doi.org/10.1201/9781003079477>.

Brice, J., and Blodgett, J. (1978). Countermeasures for hydraulic problems at bridges, volume II: case histories for sites 1-283. <https://rosap.nrl.bts.gov/view/dot/25312>.

Chang, W.-Y., Lai, J.-S., and Yen, C.-L. (2004). Evolution of scour depth at circular bridge piers. *Journal of Hydraulic Engineering*, 130(9), 905-913. [https://doi.org/10.1061/\(asce\)0733-9429\(2004\)130:9\(905\)](https://doi.org/10.1061/(asce)0733-9429(2004)130:9(905)).

Chanson, H. (2004). Hydraulics of open channel flow. <https://doi.org/10.1016/b978-075065978-9/50013-1>.

Chee, R. K. W. (1982). Live-bed scour at bridge piers. Publication of: Auckland University, New Zealand, <https://trid.trb.org/view/217201>.

Chiew, Y.-M. (1992). Scour protection at bridge piers. *Journal of Hydraulic Engineering*, 118(9), 1260-1269. [https://doi.org/10.1061/\(asce\)0733-9429\(1992\)118:9\(1260\)](https://doi.org/10.1061/(asce)0733-9429(1992)118:9(1260)).

Chiew, Y.-M. (1995). Mechanics of riprap failure at bridge piers. *Journal of Hydraulic Engineering*, 121(9), 635-643. [https://doi.org/10.1061/\(asce\)0733-9429\(1995\)121:9\(635\)](https://doi.org/10.1061/(asce)0733-9429(1995)121:9(635)).

Chiew, Y.-M., and Lim, F.-H. (2000). Failure behavior of riprap layer at bridge piers under live-bed conditions. *Journal of Hydraulic Engineering*, 126(1), 43-55. [https://doi.org/10.1061/\(asce\)0733-9429\(2000\)126:1\(43\)](https://doi.org/10.1061/(asce)0733-9429(2000)126:1(43)).

Chiew, Y.-M., and Melville, B. W. (1987). Local scour around bridge piers. *Journal of Hydraulic Research*, 25(1), 15-26. <https://doi.org/10.1080/00221688709499285>.

Chitale, S. (1988). Estimation of scour at bridge piers. *Water and Energy International*, 45(1), 57-68. <https://www.indianjournals.com>.

Chris, S., and Norbert, D. (2003). Lessons from the Collapse of the Schoharie Creek Bridge.

- Proceedings of the Forensic Engineering Congress, San Diego, CA, USA, [https://doi.org/10.1061/40692\(241\)18](https://doi.org/10.1061/40692(241)18).
- Coleman, N. (1972). Analyzing laboratory measurements of scour at cylindrical piers in sand beds. in: hydraulic research and its impact on the environment, <https://repository.tudelft.nl/islandora/object/uuid:7ae20959-482d-40bc-876f-c06bc3691493/datastream/OBJ>.
- Coleman, N. L. (1981). Velocity profiles with suspended sediment. *Journal of Hydraulic Research*, 19(3), 211-229. <https://doi.org/10.1080/00221688109499516>.
- Deng, L., and Cai, C. (2010). Bridge scour: Prediction, modeling, monitoring, and countermeasures. *Practice periodical on structural design and construction*, 15(2), 125-134. [https://doi.org/10.1061/\(asce\)sc.1943-5576.0000041](https://doi.org/10.1061/(asce)sc.1943-5576.0000041).
- Ettema, R. (1980). Scour at bridge piers. <https://trid.trb.org/view/171850>.
- Ettema, R., Constantinescu, G., and Melville, B. W. (2017). Flow-field complexity and design estimation of pier-scour depth: Sixty years since Laursen and Toch. *Journal of Hydraulic Engineering*, 143(9), 03117006. [https://doi.org/10.1061/\(asce\)hy.1943-7900.0001330](https://doi.org/10.1061/(asce)hy.1943-7900.0001330).
- Ettmer, B., Orth, F., and Link, O. (2015). Live-bed scour at bridge piers in a lightweight polystyrene bed. *Journal of Hydraulic Engineering*, 141(9), 04015017. [https://doi.org/10.1061/\(asce\)hy.1943-7900.0001025](https://doi.org/10.1061/(asce)hy.1943-7900.0001025).
- Foti, S., and Sabia, D. (2011). Influence of foundation scour on the dynamic response of an existing bridge. *Journal of bridge engineering*, 16(2), 295-304. [https://doi.org/10.1061/\(asce\)be.1943-5592.0000146](https://doi.org/10.1061/(asce)be.1943-5592.0000146).
- Franzetti, S., MALAVASI, S., and Piccinin, C. (1994). Sull'erosione alla base delle pile di ponte in acque chiare. <https://hdl.handle.net/11311/542558>.
- Franzetti, S., Radice, A., Rebai, D., and Ballio, F. (2022). Clear Water Scour at Circular Piers:

- A New Formula Fitting Laboratory Data with Less Than 25% Deviation. *Journal of Hydraulic Engineering*, 148(10), 04022021. [https://doi.org/10.1061/\(asce\)hy.1943-7900.0002009](https://doi.org/10.1061/(asce)hy.1943-7900.0002009).
- Gales, S. R., and Bell, J. (1938). The principles of river-training for railway bridges, and their application to the case of the hardinge bridge over the lower ganges at sara.(appendix by jr bell, reprinted from 1890). *Journal of the Institution of Civil Engineers*, 10(2), 136-200. <https://doi.org/10.1680/ijoti.1938.14557>.
- Ghorbani, B., and Kells, J. (2008). Effect of submerged vanes on the scour occurring at a cylindrical pier. *Journal of Hydraulic Research*, 46(5), 610-619. <https://doi.org/10.3826/jhr.2008.3003>.
- Graf, W., and Istiarto, I. (2002). Flow pattern in the scour hole around a cylinder. *Journal of Hydraulic Research*, 40(1), 13-20. <https://doi.org/10.1080/00221680209499869>.
- Graf, W., and Yulistiyanto, B. (1998). Experiments on flow around a cylinder; the velocity and vorticity fields. *Journal of Hydraulic Research*, 36(4), 637-654. <https://doi.org/10.1080/00221689809498613>.
- Hancu, S. (1971). Computation of local scour in the vicinity of bridge piers. Proc., 14th Int. Association of Hydraulic Research (IAHR) Congress, <https://doi.org/10.1139/cjce-2022-0237>.
- Heibaum, M. (2006). The use of geosynthetics in scour protection. Proceedings 3rd International Conference on Scour and Erosion (ICSE-3). November 1-3, 2006, Amsterdam, The Netherlands, <https://hdl.handle.net/20.500.11970/100030>.
- Heibaum, M. H. (2000). Scour countermeasures using geosynthetics and partially grouted riprap. *Transportation Research Record*, 1696(1), 244-250. <https://doi.org/10.3141/1696-70>.
- Hong, J.-H., Goyal, M. K., Chiew, Y.-M., and Chua, L. H. (2012). Predicting time-dependent pier scour depth with support vector regression. *Journal of Hydrology*, 468, 241-248.

<https://doi.org/10.1016/j.jhydrol.2012.08.038>.

Imhof, D. (2004). Risk assessment of existing bridge structures. University of Cambridge Dissertation, Kings College]. <https://doi.org/10.17863/CAM.19092>.

Jain, S. C. (1981). Maximum clear-water scour around circular piers. Journal of the Hydraulics Division, 107(5), 611-626. <https://doi.org/10.1061/jyceaj.0005667>.

Jia, Y., Altinakar, M., and Guney, M. S. (2018). Three-dimensional numerical simulations of local scouring around bridge piers. Journal of Hydraulic Research, 56(3), 351-366. <https://doi.org/10.1080/00221686.2017.1356389>.

Johnson, P. A. (1992). Reliability-based pier scour engineering. Journal of Hydraulic Engineering, 118(10), 1344-1358. [https://doi.org/10.1061/\(asce\)0733-9429\(1992\)118:10\(1344\)](https://doi.org/10.1061/(asce)0733-9429(1992)118:10(1344)).

Johnson, P. A., and Ayyub, B. M. (1992). Assessing time-variant bridge reliability due to pier scour. Journal of Hydraulic Engineering, 118(6), 887-903. [https://doi.org/10.1061/\(asce\)0733-9429\(1992\)118:6\(887\)](https://doi.org/10.1061/(asce)0733-9429(1992)118:6(887)).

Korkut, R., Martinez, E. J., Morales, R., Ettema, R., and Barkdoll, B. (2007). Geobag performance as scour countermeasure for bridge abutments. Journal of Hydraulic Engineering, 133(4), 431-439. [https://doi.org/10.1061/\(asce\)0733-9429\(2007\)133:4\(431\)](https://doi.org/10.1061/(asce)0733-9429(2007)133:4(431)).

Kothyari, U. C., Garde, R. C. J., and Ranga Raju, K. G. (1992). Temporal variation of scour around circular bridge piers. Journal of Hydraulic Engineering, 118(8), 1091-1106. [https://doi.org/10.1061/\(asce\)0733-9429\(1992\)118:8\(1091\)](https://doi.org/10.1061/(asce)0733-9429(1992)118:8(1091)).

Lagasse, P., Richardson, E., Schall, J., and Price, G. (1997). NCHRP report 396: instrumentation for measuring scour at bridge piers and abutments. TRB, National Research Council, Washington, DC, <https://hdl.handle.net/20.500.11970/100398>.

Larras, J. (1963). Profondeurs Maximales d'Erosion des Fonds Mobiles Autour des Piles en

Rivere. Ann. Ponts Chaussees, 133, 411-424.
<https://cir.nii.ac.jp/crid/1571135651373190016>.

Lauchlan, C., Coleman, S., and Melville, B. (2001). Temporal scour development at bridge abutments. IAHR congress proceedings, hydraulics of rivers, water words and machinery, Tsinghua University Press.
<https://research.tudelft.nl/en/publications/temporal-scour-development-at-bridge-abutments>.

Lauchlan, C. S., and Melville, B. W. (2001). Riprap protection at bridge piers. Journal of Hydraulic Engineering, 127(5), 412-418. [https://doi.org/10.1061/\(ASCE\)0733-9429\(2001\)127:5\(412\)](https://doi.org/10.1061/(ASCE)0733-9429(2001)127:5(412)).

Laursen, E. M., and Toch, A. (1956). Scour around bridge piers and abutments. 4. <https://publications.iowa.gov/id/eprint/20237>.

Lebeau, K. H., and Wadia-fascetti, S. J. (2007). Fault tree analysis of Schoharie Creek Bridge collapse. Journal of Performance of Constructed Facilities, 21(4), 320-326. [https://doi.org/10.1061/\(asce\)0887-3828\(2007\)21:4\(320\)](https://doi.org/10.1061/(asce)0887-3828(2007)21:4(320)).

Macky, G. (1990). Survey of roading expenditure due to scour-a report for the Road Research Unit. <https://trid.trb.org/view/1198799>.

Mashahir, M. B., Zarrati, A. R., and Rezayi, M. (2004). Time development of scouring around a bridge pier protected by collar. Proceedings 2nd International Conference on Scour and Erosion (ICSE-2). November 14.-17., 2004, Singapore, <https://hdl.handle.net/20.500.11970/99986>.

Melville, B., and Sutherland, A. (1988). Design method for local scour at bridge piers. Journal of Hydraulic Engineering, 114(10), 1210-1226. [https://doi.org/10.1061/\(asce\)0733-9429\(1988\)114:10\(1210\)](https://doi.org/10.1061/(asce)0733-9429(1988)114:10(1210)).

Melville, B. W. (1984). Live-bed scour at bridge piers. Journal of Hydraulic Engineering, 110(9), 1234-1247. [https://doi.org/10.1061/\(asce\)0733-9429\(1984\)110:9\(1234\)](https://doi.org/10.1061/(asce)0733-9429(1984)110:9(1234)).

- Melville, B. W. (1997). Pier and abutment scour: integrated approach. *Journal of Hydraulic Engineering*, 123(2), 125-136. [https://doi.org/10.1061/\(asce\)0733-9429\(1997\)123:2\(125\)](https://doi.org/10.1061/(asce)0733-9429(1997)123:2(125)).
- Melville, B. W., and Coleman, S. E. (2000). *Bridge scour*. Water Resources Publication, <https://www.wrpllc.com/books/bsr.html>.
- Neill, C. R. (1973). Guide to bridge hydraulics. <https://www.semanticscholar.org/paper/Guide-to-bridge-hydraulics-Neill/e8acb3f1a889d8f86c678e448759f10776756392>.
- Nouri Imamzadehei, A., Heidarpour, M., Nouri Imamzadehei, M., Ghorbani, B., and Haghiabi, A. (2016). Control of the local scouring around the cylindrical bridge pier using armed soil by geotextile. *International Journal of Geosynthetics and Ground Engineering*, 2, 1-8. <https://doi.org/10.1007/s40891-016-0045-7>.
- Oliveto, G., and Hager, W. H. (2002). Temporal evolution of clear-water pier and abutment scour. *Journal of Hydraulic Engineering*, 128(9), 811-820. [https://doi.org/10.1061/\(asce\)0733-9429\(2002\)128:9\(811\)](https://doi.org/10.1061/(asce)0733-9429(2002)128:9(811)).
- Radice, A., and Ballio, F. (2008). Double-average characteristics of sediment motion in one-dimensional bed load. *Acta Geophysica*, 56, 654-668. <https://doi.org/10.2478/s11600-008-0015-0>.
- Radice, A., Franzetti, S., and Ballio, F. (2002). Local scour at bridge abutments. <https://re.public.polimi.it/handle/11311/248634>.
- Radice, A., and Lauva, O. (2017). Live-bed pier scour in a covered flow. *Journal of Hydraulic Engineering*, 143(10), 06017016. [https://doi.org/10.1061/\(asce\)hy.1943-7900.0001359](https://doi.org/10.1061/(asce)hy.1943-7900.0001359).
- Rasaei, M., Nazari, S., and Eslamian, S. (2020). Experimental investigation of local scouring around the bridge piers located at a 90 convergent river bend. *Sādhanā*, 45(1), 87. <https://doi.org/10.1007/s12046-020-1314-7>.

- Richardson, E., and Davis, S. (2001). Evaluating scour at bridges, Forth Edition, Rep. <https://rosap.nrl.bts.gov/view/dot/50281>.
- Shen, H. W., Schneider, V. R., and Karaki, S. (1969). Local scour around bridge piers. Journal of the Hydraulics Division, 95(6), 1919-1940. <https://doi.org/10.1061/jyceaj.0002197>.
- Shirole, A., and Holt, R. (1991). Planning for a comprehensive bridge safety assurance program. Transportation Research Record, 1290, 39-50. <https://onlinepubs.trb.org/Onlinepubs/trr/1991/1290vol1/1290.pdf#page=52>.
- Wu, H., Yao, C., Li, C., Miao, M., Zhong, Y., Lu, Y., and Liu, T. (2020). Review of application and innovation of geotextiles in geotechnical engineering. Materials, 13(7), 1774. <https://doi.org/10.3390/ma13071774>.
- Xiong, W., Tang, P., Kong, B., and Cai, C. (2017). Computational simulation of live-bed bridge scour considering suspended sediment loads. Journal of Computing in Civil Engineering, 31(5), 04017040. [https://doi.org/10.1061/\(asce\)cp.1943-5487.0000689](https://doi.org/10.1061/(asce)cp.1943-5487.0000689).
- Yoon, T. H. (2005). Wire gabion for protecting bridge piers. Journal of Hydraulic Engineering, 131(11). [https://doi.org/10.1061/\(asce\)0733-9429\(2005\)131:11\(942\)](https://doi.org/10.1061/(asce)0733-9429(2005)131:11(942)).
- Zarrati, A. R., Chamani, M. R., Shafaie, A., and Latifi, M. (2010). Scour countermeasures for cylindrical piers using riprap and combination of collar and riprap. International Journal of Sediment Research, 25(3), 313-322. [https://doi.org/10.1016/s1001-6279\(10\)60048-0](https://doi.org/10.1016/s1001-6279(10)60048-0).
- Zarrati, A. R., Gholami, H., and Mashahir, M. (2004). Application of collar to control scouring around rectangular bridge piers. Journal of Hydraulic Research, 42(1), 97-103. <https://doi.org/10.1080/00221686.2004.9641188>.
- Zhang, Q., Zhou, X.-L., and Wang, J.-H. (2017). Numerical investigation of local scour around three adjacent piles with different arrangements under current. Ocean Engineering, 142, 625-638. <https://doi.org/10.1016/j.oceaneng.2017.07.045>.